ABSTRACT

Title of Dissertation: MODELING HELICOPTER NEAR-HORIZON HARMONIC NOISE DUE TO TRANSIENT MANEUVERS

Richard Sickenberger, Doctor of Philosophy, 2013

Dissertation directed by: Professor Fredric Schmitz
Department of Aerospace Engineering

A new first principles model has been developed to estimate the external harmonic noise radiation for a helicopter performing transient maneuvers in the longitudinal plane. This model, which simulates the longitudinal fuselage dynamics, main rotor blade flapping, and far field acoustics, was validated using in-flight measurements and recordings from ground microphones during a full-scale flight test featuring a Bell 206B-3 helicopter. The flight test was specifically designed to study transient maneuvers.

The validated model demonstrated that the flapping of the main rotor blades does not significantly affect the acoustics radiated by the helicopter during maneuvering flight. Furthermore, the model also demonstrated that Quasi-Static Acoustic Mapping (Q-SAM) methods can be used to reliably predict the noise radiated during transient maneuvers.

The model was also used to identify and quantify the contributions of main rotor thickness noise, low frequency loading noise, and blade-vortex interaction (BVI) noise during maneuvering flight for the Bell 206B-3 helicopter. Pull-up and push-over

maneuvers from pure longitudinal cyclic and pure collective control inputs were investigated. The contribution of thickness noise and low frequency loading noise during maneuvering flight was found to depend on the orientation of the tip-path plane relative to the observer. The contribution of impulsive BVI noise during maneuvering flight was found to depend on the inflow through the main rotor and the orientation of the tip-path plane relative to the observer.

MODELING HELICOPTER NEAR-HORIZON HARMONIC NOISE DUE TO TRANSIENT MANEUVERS

by

Richard D. Sickenberger

Dissertation submitted to the Faculty of the Graduate School of the
University of Maryland, College Park in partial fulfillment
of the requirements for the degree of
Doctor of Philosophy
2012

Advisory Committee:

Professor James Baeder, Chair/Advisor
Professor Fredric Schmitz, Advisor
Professor Christopher Cadou
Professor Inderjit Chopra
Professor Anya Jones
Professor Ramani Duraiswami, Dean's Representative

Dedication

for Gaurav

Acknowledgments

This dissertation marks the culmination of nearly eight years of research, but it would not have been possible without the support and encouragement of so many people. First and foremost, I would like to express the utmost gratitude to my technical advisor, Dr. Fredric Schmitz. Dr. Schmitz introduced me to the field of rotorcraft acoustics early in my graduate school career, and I am eternally grateful for all of the opportunities that I have had while working with Dr. Schmitz.

I would also like to specially thank Dr. Baeder for acting as the chair and the remaining members of my dissertation committee, Dr. Cadou, Dr. Chopra, Dr. Jones, and Dr. Duraiswami for their time, their advice, their guidance, and their support.

This dissertation would also not have been possible without the assistance of the rest of Dr. Schmitz's aeroacoustics research group: Dr. Gaurav Gopalan, Dr. Sudarshan Koushik, Dr. Eric Greenwood, Dr. Cal Sargent, Ben May, and Chris Sutton. Your support during the flight tests and in discussing various research challenges is truly appreciated.

The Gilroy flight test described in this dissertation was a large effort, and it was made possible by many people. I would like to thank ARIS Helicopters for providing the Bell 206B-3 for acoustic flight testing. Specifically, I would like to thank maintenance officer Eric Mouritsen, pilots Paul Dexter and Sam Nowden, and ARIS Helicopters founder Steve Sullivan. These individuals were instrumental in the development, testing, and debugging of the tip-path plane tracking system that was developed as a part of this research. I would also like to thank everyone from Bell Helicopter, the U.S. Army Aeroflightdynamics Directorate, and NASA Ames Research Center who ensured the success of the flight test. In particular, Mr. Royce Snyder and Mr. Tim Samuels of Bell

Helicopter, Mr. Bill Decker of NASA Ames, and Mr. Ernie Morales and Dr. Ben Sim of the U.S. Army.

I also wish to thank David Conner, Gary Fleming, and Mike Watts from NASA Langley for their support in the development of the tip-path plane tracking system. And I would also like to express my appreciation to the Vertical Lift Consortium and the National Rotorcraft Technology Center for their support of my research involving transient maneuvering flight.

Last, but certainly not least, I would like to express my thanks to my friends and my family; especially my parents, Dave and Debbie, and my sister, Rebecca, for their unwavering love, encouragement, support, and patience over the years. And a special thank you to Pamela Mood, Robert Watts, Alicia Farrell, and everyone at Sean Bolan's for standing beside me and helping to keep me grounded when I needed it the most.

Table of Contents

List of Tables

List of Figures

Abbreviations and Nomenclature

A	Rotor disk area, m2
A_1	Lateral cyclic coefficient, rad
a_0	Blade pre-cone angle, rad
a_1	Longitudinal flapping coefficient, rad
B	Body reference point at the center of gravity
B_1	Longitudinal cyclic coefficient, rad
b_1	Lateral flapping coefficient, rad
C_D	Mean drag coefficient
$C_{L\alpha}$	Lift curve slope (2π), rad^{-1}
C_l	Sectional lift coefficient
c	Speed of sound, m/s
	Chord length, m
D	Fuselage drag, N
E	Beddoes' empirical correction to wake skew angle
$\hat{e}$	Coordinate system unit vector
F_P	Aerodynamic load normal to the hub plane, N
F_T	Aerodynamic load tangent to the hub plane, N
f	Equivalent flat plate area, m^2
H	Hub reference point
H_{HP}	In-plane H-force (in shaft coordinate system), N
I_b	Blade mass moment of inertia, $kg \cdot m^2$

I_β	Blade mass moment of inertia about flapping hinge, kg·m^2
I_{yy}	Pitching moment of inertia, kg·m^2
$\hat{i}, \hat{j}, \hat{k}$	Basis of unit vectors
L	Sum of rolling body moments, N·m
M	Sum or pitching body moments, N·m
M_r	Relative mach number
M_{TR}	Trace Mach number
M_x	Main rotor rolling moment, N·m
M_y	Main rotor pitching moment, N·m
m	Aircraft mass, kg
N	Sum of yawing body moments, N·m
N_b	Number of blades
$\hat{n}$	Blade surface unit normal vector
O	Origin of inertial coordinate system
P	Reference point on elastic axis
p	Body roll rate, rad/s
	Pressure on the blade surface, Pa
p'	Acoustic pressure, Pa
Q_{HP}	Main rotor torque (in shaft coordinate system), N·m
q	Body pitch rate, rad/s
R	Blade radius, m

r	Body yaw rate, rad/s
	Radial position measured from root, m
	Distance from acoustic source to observer, m
$\hat{r}$	Unit vector from acoustic source to the observer
$\overrightarrow{r_{y/x}}$	Position vector from "x" to "y"
s	Relative distance traveled by airfoil in semi-chords
S	Elemental blade surface area
T	Thrust, N
T_{HP}	Thrust (in shaft coordinate system), N
$T^{x/y}$	Coordinate transformation matrix from system "x" to system "y"
t_0	Observer time, s
t_s	Source time, s
U_P	Component of air velocity relative to the blade element perpendicular to the hub plane, m/s
U_T	Component of air velocity relative to the blade element tangential to the hub plane, m/s
U	Total sectional flow velocity, m/s
u	Body longitudinal velocity, m/s
$\vec{u}$	Control vector
V	Velocity of the air relative to the blade element, m/s
	Reference point on the trailed wake
$\overrightarrow{V_i}$	Induced inflow velocity vector, m/s

$\overrightarrow{V_{x/Y}}$	Velocity of the "x" relative to the "Y" coordinate system, m/s
V_x	Longitudinal velocity of the aircraft (in shaft coordinate system)
V_y	Lateral velocity of the aircraft (in shaft coordinate system)
V_z	Vertical velocity of the aircraft (in shaft coordinate system)
V_∞	Free stream velocity
v	Body lateral velocity, m/s
v_i	Induced inflow, m/s
v_n	Velocity normal to the blade surface, m/s
W	Aircraft weight, N
w	Body vertical velocity, m/s
X	Sum of longitudinal body forces, N
	Recurrence function
x	Non-dimensional radial position, *r/R*
	Non-dimensional position from the leading edge of the airfoil
x_H	Longitudinal offset between the center of gravity and the hub, m
Y	Sum of lateral body forces, N
	Recurrence function
Y_{HP}	In-plane Y-force (in shaft coordinate system), N
$\vec{y}$	State vector
Z	Sum of vertical body forces, N
z_H	Vertical offset between the center of gravity and the hub, m

α	Angle of attack, rad
α_e	Effective angle of attack, rad
β	Blade flapping angle relative to the hub plane, rad
Γ	Circulation, m^2/s
Γ_b	Bound circulation, m^2/s
γ	Lock number, $\rho c C_{L\alpha} R^4 / I_b$
γ_D	Descent angle, rad
ΔC_P	Differential pressure coefficient on the airfoil
θ	Blade pitch angle, rad
	Local angle between the surface normal vector and the radiation direction, rad
θ_B	Body pitch angle, rad
θ_S	Shaft tilt angle, rad
θ_{TW}	Blade twist, rad
θ_0	Collective angle, rad
λ	Nondimensional total inflow ratio $\lambda_i - \mu_z$
λ_i	Nondimensional induced inflow ratio
$\lambda_{i,0}$	Nondimensional induced inflow from momentum theory
λ_{HP}	Nondimensional total inflow ratio through the hub plane
μ	Advance ratio
μ_x	Longitudinal advance ratio (in shaft coordinate system)
μ_y	Lateral advance ratio (in shaft coordinate system)

μ_z	Vertical advance ratio (in shaft coordinate system)
ρ	Fluid density, kg/m^3
ρ_0	Density of the undisturbed medium, kg/m^3
ϕ_B	Body roll angle, rad
ψ	Blade azimuth, rad
ψ_B	Body yaw angle, rad
ψ_w	Wake age, rad
Ω	Angular velocity of the main rotor, rad/s
$\overrightarrow{\omega^{y/x}}$	Angular velocity vector of the "y" frame relative to the "x" frame
$\overrightarrow{\dot{\omega}^{y/x}}$	Angular acceleration vector of the "y" frame relative to the "x" frame

Superscripts and Subscripts

$(\dot{})$	First derivative with respect to time
$(\ddot{})$	Second derivative with respect to time
$(\ )_A$ *or* $^A(\ )$	Aerodynamic coordinate system
$(\ )_B$ *or* $^B(\ )$	Body (fuselage)-fixed coordinate system
$(\ )_I$ *or* $^I(\ )$	Inertial coordinate system
$(\ )_L$ *or* $^L(\ )$	Local blade coordinate system
$(\ )_R$ *or* $^R(\ )$	Shaft-rotating coordinate system
$(\ )_S$ *or* $^S(\ )$	Shaft-fixed coordinate system
$(\ )_T$ *or* $^T(\ )$	Tip-path plane coordinate system

Abbreviations

AEDT	Aviation Environmental Design Tool
BVI	Blade-Vortex Interaction
BVISPL	BVI Sound Pressure Level
CG	Center of Gravity
DLR	Deutsches Zentrum fur Luft und Raumfahrt
FAR	Federal Aviation Regulation
FRAME	Fundamental Rotorcraft Acoustic Modeling from Experiments
HNM	Heliport Noise Model
HP	Hub Plane
HSI	High Speed Impulsive
INM	Integrated Noise Model
IRIG	Inter-Range Instrumentation Group
MR	Main Rotor
NIST	National Institute of Standards and Technology
NOE	Nap-of-the-Earth
OASPL	Overall Sound Pressure Level
ODE	Ordinary Differential Equation
ONERA	Office National d'Etudes et Recherches Aerospatiales
PAVE	Pilot Assist in the Vicinity of Helipads
PPGD	Portable Programmable Guidance Display
RONAP	Rotorcraft Operational Noise Abatement Procedure
Q-SAM	Quasi-Static Acoustic Mapping

RNM	Rotorcraft Noise Model
SPL	Sound Pressure Level
TPP	Tip-Path Plane

Chapter 1 Introduction

1.1 Background

The acoustic signature radiated by aircraft is an important concern in both civil and military operations. For civil applications, noise generated by aircraft is a source of annoyance to ground populations. In the United States, various government guidelines have been created to address noise pollution radiated by aircraft near populated areas. Such regulations include the Federal Aviation Administration's Federal Aviation Regulation 36 (FAR 36) in 1969, and the Noise Control Act of 1972. In Europe, EU Directive 2002/30/EC established similar regulations for aircraft noise emissions.

For military applications, noise generated by aircraft can adversely affect the detectability, or observability, of the aircraft. Military aircraft must be capable of approaching a target and completing an objective without alerting the enemy. This is particularly true for low-speed aircraft that can be vulnerable to attack from ground personnel for long periods of time [1]. This vulnerability was exploited by Great Britain around the Second World War with the installation of concrete acoustic mirrors that were used to detect aircraft approaching the coastline. While more advanced radar systems have surpassed the capabilities of the acoustic mirrors, the aural detectability of aircraft is still a concern for many present day missions.

The problems of aircraft aural detection are further compounded for rotorcraft by the aerodynamic environment of the rotor system and their unique operational missions. During steady flight, the directivity of the main rotor noise sources are generally related to the orientation of the tip-path plane of the main rotor. The tip-path plane is defined by

the path traced by the tip of the main rotor blade over a complete revolution. Noise sources that propagate below the tip-path plane tend to annoy civilian observers as aircraft fly overhead. Noise sources that propagate parallel to the tip-path plane tend to set the detection distance of incoming aircraft to observers in the horizon (see top frame in Figure 1.1). However, because helicopters often fly nap-of-the-earth patterns, the orientation of the tip-path plane can be altered when executing transient maneuvers such as pull-ups, dives, and rolls. These transient maneuvers can result in out-of-plane noise sources propagating towards the horizon (see bottom frame in Figure 1.1). The importance of transient maneuver noise on community annoyance and aural detection is a current research topic.

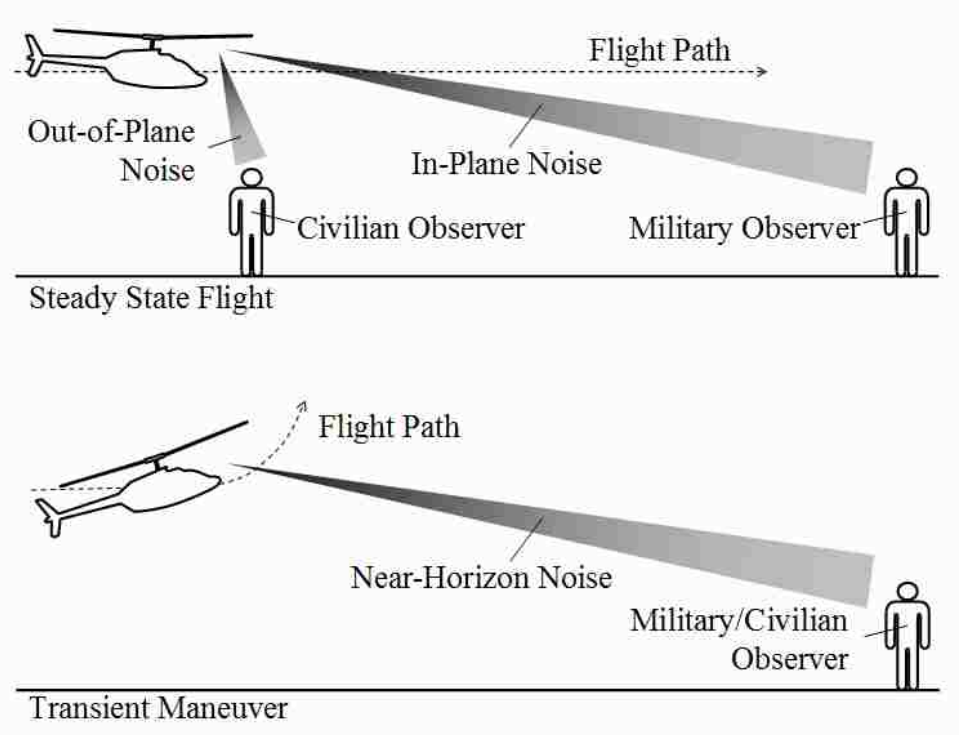

Figure 1.1. Directivity characteristics of main rotor noise during steady-state and transient maneuvering flight.

In order to understand how transient maneuvering flight affects the observability of the aircraft, it is first important to identify the dominant noise sources associated with these maneuvers. Second, it is important to be able to model these sources to develop mitigation strategies. And lastly, it is important to be able to predict and relay the acoustic state of the aircraft to the pilot since noise in the cabin is frequently a poor indicator of the true acoustic state of the helicopter [2].

1.2 Rotorcraft Noise Sources

At the highest level, rotorcraft noise sources are generally classified into two types. The first type, rotor harmonic noise, is any noise generated by the rotor systems on the aircraft. It is caused by steady and unsteady aerodynamic forces that can be represented by harmonic thickness and loading noise. The second type, non-rotor harmonic noise, is composed of rotor broadband noise and all of the other non-rotor noise sources on the helicopter. Rotor broadband noise is aperiodic and can be caused by random loadings due to atmospheric turbulence, inflow disturbances, turbulence from blade boundary layer effects, vortex shedding, and flow separation. Additional non-rotor noise sources usually include, but are not limited to, the engine, the gear box, and the airflow around the fuselage. It has been shown that typically the external noise radiation of the helicopter is dominated by rotor harmonic noise [2]. Therefore, this dissertation will focus on discrete harmonic noise levels associated with the main rotor.

Main rotor harmonic noise is largely made up of four noise sources – thickness and loading noise, which are mostly low to mid-frequency noise sources, and high-speed impulsive (HSI) and blade-vortex interaction (BVI) noise, which are impulsive noise

sources. When present, the impulsive HSI and BVI sources are often the dominant source of noise radiated by the rotorcraft [3].

Thickness noise is generated by the displacement of the air as the rotor passes through the medium. This source is largely governed by the blade thickness and the tip Mach number of the blades. Below the transonic regime, thickness noise of the main rotor has a negative, almost symmetrical shape that is dominated by low frequency content at the first few harmonics of the main rotor operational frequency. Thickness noise can become large at high advancing tip Mach numbers. Thickness noise is loudest when the far-field observer is located near the plane of the rotor in the direction of forward flight.

Loading noise is generated by the application of the aerodynamic force of the rotor to the fluid medium. As with thickness noise, loading noise is mostly made of low frequency content. In a rotor system, thrust and drag are the dominant aerodynamic forces. Lifting forces create noise normal to the tip-path plane while pressure drag forces create noise near the tip-path plane of the rotor.

High-speed impulsive (HSI) is an impulsive version of thickness noise that occurs when the blade operates in the transonic regime. Local shocks form in this region that propagate near the tip-path plane of the rotor and, due to their directivity pattern, cannot be heard inside the cabin. In the past, HSI has been a major concern for detection, but since modern helicopters feature thinner blade sections and operate at low tip speeds, HSI has become less of a problem.

Blade-vortex interaction (BVI) is the impulsive counterpart to loading noise. BVI occurs when the rotor blade passes through, or in close proximity to, trailed vortices

released from preceding blades (see Figure 1.2). These interactions result in a rapid change of the blade aerodynamic loads, and generate impulsive waves that are most intense out of the plane of the rotor. The intensity of BVI is driven by the wake geometry, the wake strength, and the miss distance between the rotor tip-path plane and the trailed wake.

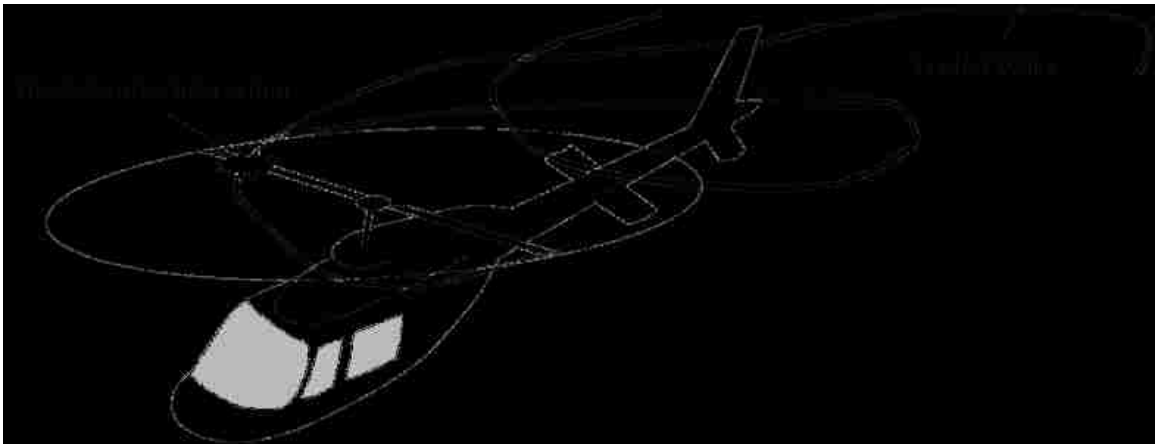

Figure 1.2. Illustration of a blade-vortex interaction.

The four primary main rotor harmonic noise sources and their general directivity patterns relative to the tip-path plane are shown in Figure 1.3.

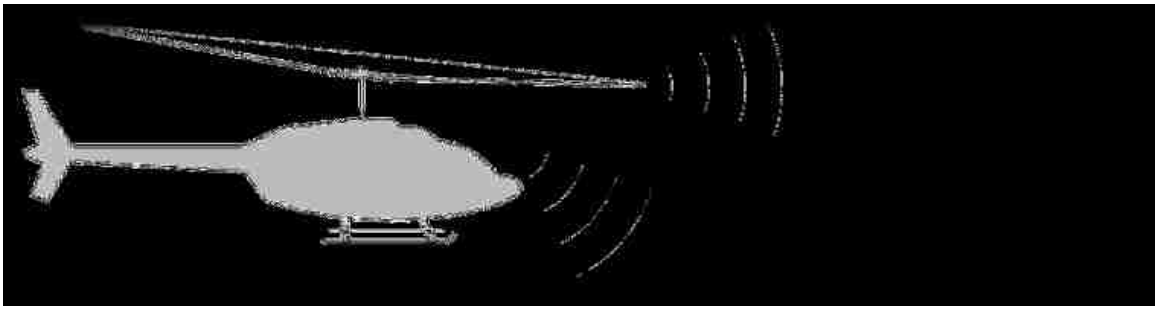

Figure 1.3. Main rotor harmonic noise sources.

Recently, it has been shown that when executing transient pull-up and roll maneuvers in a Bell 206B-3 helicopter, the attitude of the main rotor tip-path plane relative to the wake trailed by the main rotor introduced BVI noise into the near horizon

noise radiated by the aircraft [4]. This was found to markedly increase the relative detection distance of the helicopter. In environments with low ambient backgrounds, the detection distance was set by the 80-150 Hz band; in environments with moderate ambient backgrounds, the detection distance was set by the 400-500 Hz band. For the Bell 206B-3, both critical bands lie within the BVI sound pressure level (BVISPL) band which spreads from the 6^{th} main rotor harmonic to the 40^{th} (78 Hz to 521 Hz). Perceived low frequency loading noise directed towards the horizon was also found to rise as the maneuver changed the attitude of the tip-path plane and exposed the underside of the rotor to the horizon.

This study also indicates that it may be possible to fly special combination maneuvers that mitigate BVI radiation and thereby reduce detection distance. These maneuvers would be designed to increase the miss distance between the tip-path plane and the trailed wake. For example, prior to executing a maneuver, the inflow can be increased by increasing the collective control. Combination maneuvers such as these were attempted in 2011 and showed promise in reducing BVI emissions during transient pull-ups and rolls [5].

1.3 Helicopter Noise Modeling

The ultimate goal of helicopter noise modeling is to be able to adequately predict the acoustics radiated by the helicopter during flight. These models provide a means of quantifying the contributions of noise sources and can be used for developing methodologies for flying quietly and avoiding detection. Over the past few decades, these models have been developed and applied to steady state maneuvers with varying degrees

of success. More recently, some of these models have been applied to maneuvering flight, but many have yet to be validated.

Helicopter noise modeling can be divided into two categories – first-principles models and empirical models. First-principles models attempt to capture the basic physics of the helicopter system including the dynamics, aerodynamics, and wake structure. These models are typically computationally expensive and many models have not been validated with flight testing. Empirical methods incorporate acoustic and other physical measurements into the modeling and are typically faster, but are limited to the set of flight conditions used to generate the data. While extrapolation is possible for empirical methods, they too require validation.

1.3.1 First-Principles Models

The ultimate objective of the first-principles model is to mathematically model the acoustics radiated by the various sources on the aircraft. A variety of methods are available, but some of the most widely used models are based around solving the Ffowcs Williams-Hawkings equation, which describes sound generated by surfaces in arbitrary motion through a medium [6]. The Ffowcs Williams–Hawkings equation is broken into three terms: monopoles which use sources and sinks to emulate how the blade passes through the medium; dipoles that model the aerodynamic loading of the blade; and quadrupoles which model complex noises such as those associated with HSI noise.

One of the most well known implementations of the Ffowcs Williams–Hawkings equation is the WOPWOP code developed by Langley Research Center [7]. Featuring the subsonic Farassat Formulation 1A of the Ffowcs Williams–Hawkings equation, WOPWOP computes the solution for a prescribed blade motion and aerodynamic time

history which is imported from additional computational models. In order to obtain these additional data, the WOPWOP acoustics model is coupled with various dynamic, blade structural, aerodynamic, and wake models.

NASA Langley Research Center initially combined the aeroacoustics WOPWOP model with the CAMRAD.Mod1 performance, trim, and wake code and the HIRES high resolution blade loads post-processor to compare BVI noise with wind tunnel data [8]. The results showed good agreement with the wind tunnel, but highlighted the dependence on accurate aerodynamic loading and wake modeling. Improvements were later made by incorporating CAMRAD II into the model which featured better wake modeling [9].

An improved version of WOPWOP, known as PSU-WOPWOP, was developed at Penn State to model the acoustics of rotorcraft in maneuvering flight [10], [11], and [12]. PSU-WOPWOP was used under DARPA's Helicopter Quieting Program which used computational fluid dynamics (CFD) and computational structural dynamics (CSD) to develop a more robust physics-based design tool [13]. To facilitate quicker computations, the CAMRAD dynamics model was eventually replaced with the GENHEL non-linear flight dynamics model [14]. Despite these improvements, real-time modeling was only attainable for coarse time steps, and the early maneuvering models were not designed to capture BVI.

The University of Maryland has also more recently incorporated a free-wake model into the PSU-WOPWOP and GENHEL model [15]. This model was used to predict the acoustics of hyper-aggressive pull-up maneuvers that featured rates as high 40 deg/s. Results indicated that these maneuvers caused a bundling of the trailed wake that

led to “Super-BVI.” However, these results, which were also modeled with coarse time steps, have not been verified with flight testing.

Presently, first-principles models have two challenges. First, they need to be able to accurately model all of the aerodynamic source terms during maneuvering flight. This requires adequate modeling of the rotor aerodynamic environment and the wake structure. These models must also be validated with physical flight testing to ensure that all of the important noise sources are adequately captured for transient maneuvers. Second, they must be able to compute solutions in a timely manner if they are to be used for flight simulators and on-board piloting displays. While high-order aerodynamic, structural, and wake models may produce accurate results, they do so at the expense of computational time.

1.3.2 Empirical and Semi-Empirical Models

An alternative to first-principles models are empirical models based on flight test data and ground acoustic measurements. This approach reduces the necessity of modeling the complete physics of the problem.

One of the simplest models is the Integrated Noise Model (INM) developed by the Federal Aviation Administration [16]. Based on the procedure described in SAE-AIR-1845, the noise radiated by an aircraft is recorded by a single microphone for three basic trajectories: take-offs, approaches, and cruising flight (see Figure 1.4). These measurements are then used to estimate the noise generated by aircraft in a specific operational mode. Later, two additional microphones, 150 m off each side of the flight path, were incorporated to capture some helicopter noise directivity characteristics. The INM was also later expanded to the Heliport Noise Model to determine the impact of

helicopter noise in the vicinity of terminal operations. While these integrated models do an adequate job of calculating the noise generated from commonly repeated flight trajectories, they do not capture the individual noise sources radiated by the aircraft.

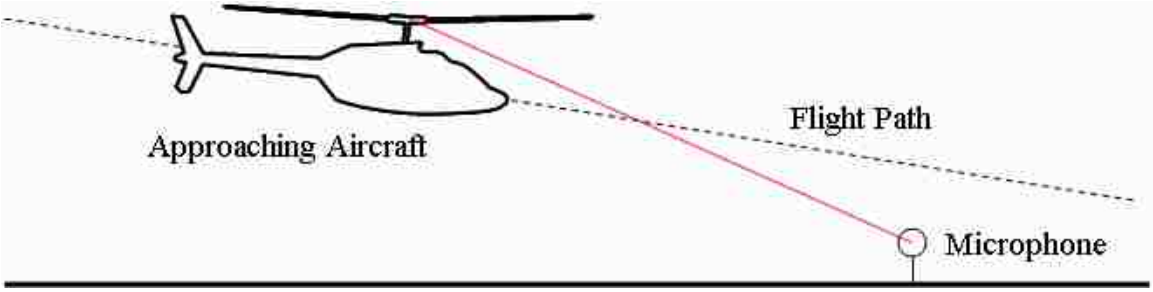

Figure 1.4. Approach pattern measurement under SAE-AIR-1845.

The Rotorcraft Noise Model (RNM) was created by NASA Langley Research Center and Wyle Laboratories [17]. This model incorporates source noise hemispheres which are obtained by flying rotorcraft in steady state flight over an array of microphones perpendicular to the flight path. These microphones recordings are used to de-propagate the rotorcraft noise to a hemisphere surrounding the aircraft (see Figure 1.5). As the aircraft passes over the array, the various microphones trace the sound pressure levels over the surface of the hemisphere. Various interpolation schemes can be used to fill in the regions of the sphere not captured directly by the microphones. A database of these spheres is generated by flying the aircraft at various airspeeds and flight path angles.

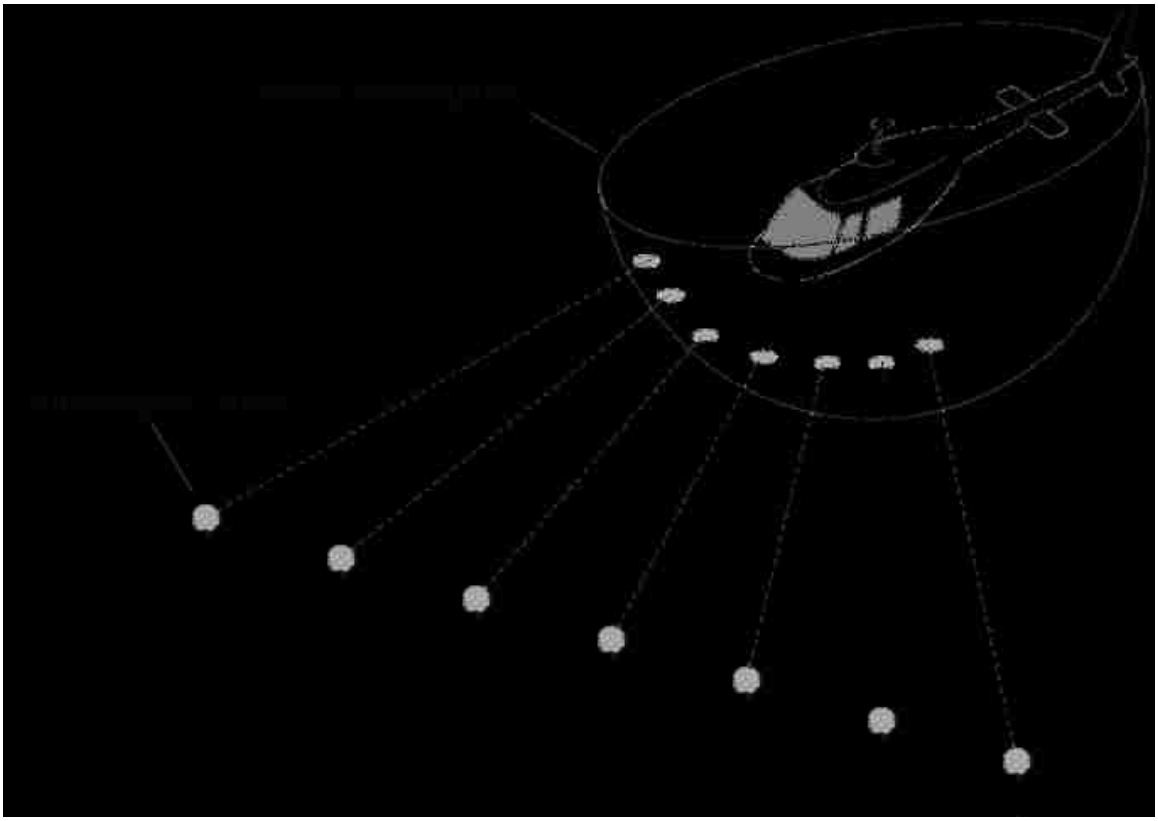

Figure 1.5. Array flyover for hemisphere generation.

RNM predicts the acoustic radiation of a helicopter by breaking a trajectory into a series of straight-line segments and interpolating the sound hemispheres from the available database. Though turns are not explicitly modeled, the original RNM would rotate the sound hemispheres by the bank angle.

Gopalan extended the RNM model to accommodate moderate accelerations and decelerations below 0.1 g [18]. Instead of using a database of airspeeds and descent angles, the RNM Quasi-Static Acoustic Mapping (Q-SAM) model determines an equivalent steady condition based on the tip-path plane angle of attack and the advance ratio. Greenwood further extended the RNM Q-SAM model to accommodate turns and moderate accelerations and decelerations by incorporating the thrust coefficient as a parameter in the database [19].

The European models, Sound Exposure Level Starting from Emitted Noise Evaluation (SELENE) and the Helicopter Environmental Noise Analysis (HELENA), operate similar to RNM, but the noise hemispheres are generated using a two-dimensional microphone array [20], [21].

One limitation of the pure empirical models is that they require a complete database of flight conditions for all aircraft of interest. Furthermore, while it is relatively straight forward to interpolate between source hemispheres based on the flight condition, extrapolation becomes a challenging task. To address this, Greenwood developed the Fundamental Rotorcraft Acoustic Modeling from Experiments (FRAME) model [22]. FRAME incorporates some first principles models of the dominant noise sources with analytical models from wind tunnel experiments and flight tests to form a semi-empirical model. In Greenwood's model, noise sources for a 2-bladed main rotor system, including BVI, are generalized based on non-dimensional parameters and each source is modeled separately. While the model was developed for steady maneuvers, FRAME has recently been applied to transient pull-up maneuvers and predicted BVI noise well when compared to ground microphone acoustics recorded during a flight test [23]. However, FRAME is still largely driven by empirical models that are tuned to match measurements made for a particular aircraft.

1.3.3 Previous Flight Tests

Over the years, multiple helicopter acoustics flight test campaigns have been performed to identify the acoustic sources on rotorcraft and to develop and validate acoustic models. While wind tunnel experiments may seem like an attractive option for obtaining this acoustic data, they do not always yield accurate measurements for a full-

scale aircraft in flight. Wind tunnel experiments using scaled rotors have compared well with full-scale flight test measurements at low to moderate advance ratios, but at higher advance ratios discrepancies begin to appear – likely due to the sensitivity of the wake structure to the Reynolds number and flow turbulence [24]. However, even full-scale wind tunnel testing has been shown to be an inadequate representation of the free-air environment at high advance ratios [25]. Therefore, the only way to capture all of the acoustic sources of the helicopter in forward flight is to conduct full-scale helicopter acoustic flight test programs.

One of the earliest full scale acoustic flight tests was performed by the Army Air Mobility R&D Laboratory and the Army Engineering Flight Activity at Edwards Air Force Base in 1975 [26]. During this test, a UH-1H helicopter was flown in formation with an OV-1C Mohawk aircraft fitted with microphones. Under a wide range of steady-state flight conditions, the OV-1C was maneuvered to various positions relative to the UH-1H to quantify the directivity of impulsive noise sources (see Figure 1.6). The results of this test also illustrated that cabin noise was not always a good indicator of the acoustic state of the aircraft, especially for noise sources that propagate in the plane of the rotor.

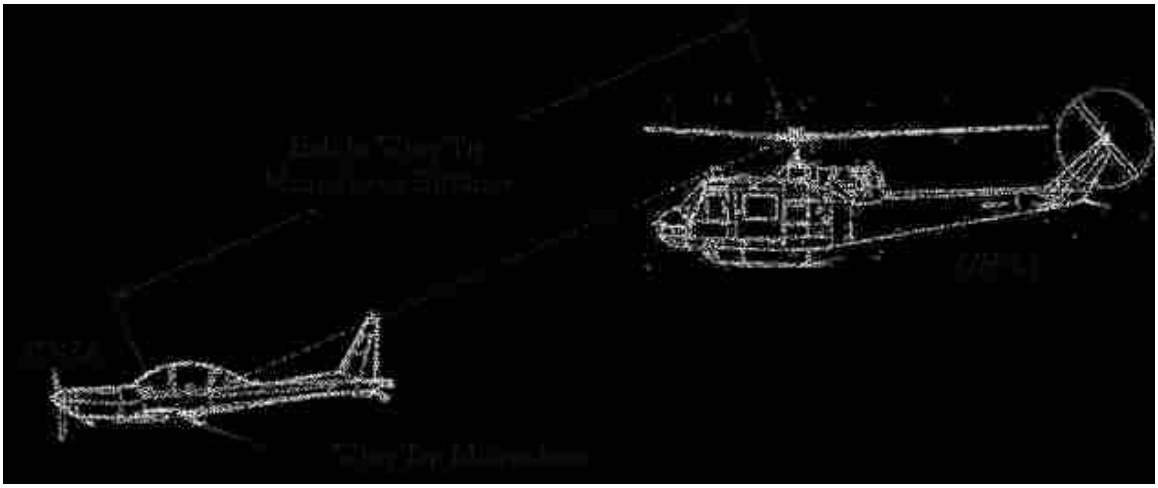

Figure 1.6. Acoustic test formation flight.

Following the success of the first test, a similar test was later performed replacing the OV-1C with a YO-3A "Quiet" aircraft [27]. Various helicopters were evaluated using the formation flying technique including a UH-1H, UH-60, UH-61, AH-63, AH-64, and AH-1S. The In-Flight Rotorcraft Acoustics Program at NASA Ames Research Center later expanded this test to study the acoustics of an S-76C to compare full-scale measurements with those obtained in a wind tunnel [25]. The results of this flight test campaign related the impulsive BVI noise to the advance ratio and the tip-path plane angle of the main rotor.

In 2001, at Cochstedt Airport in Germany, the Deutsches Zentrum fur Luft und Raumfahrt (DLR) and the Office National d'Etudes et Recherches Aerospatiales (ONERA) conducted a thorough acoustics flight test campaign as part of the "Quiet Rotorcraft" program [28]. The objectives of the Rotorcraft Operational Noise Abatement Procedure (RONAP) test were to generate high quality aerodynamic data for designing low noise flight procedures, validate aerodynamic and acoustic prediction codes, and verify of the equivalence of scaled rotor wind tunnel and full scale flight tests. Featuring

a Messerschmitt-Bolkow-Blohm (MBB) BO-105, the test focused on descents at various airspeeds and descent angles, but also included some climbing flight, level flight, transient maneuvers, and accelerating/decelerating flight.

The DLR test was expanded in 2004 as part of the Pilot Assistant in the Vicinity of Helipads (PAVE) program [29]. Featuring a BO-105 and a Eurocopter EC-135 Flying Helicopter Simulator (FHS), 243 different maneuvers were flown over a two-dimensional array of microphones. These maneuvers include steady flight, steady descents, turns, accelerations, decelerations, and transitions to-and-from descents.

In 2006, NASA, Army, Bell Helicopter, and the University of Maryland conducted an acoustics flight test at Moffet Field, CA with an instrumented Bell 206B-3 helicopter [30]. In addition to an onboard inertial measurement system, a custom spray rig fitted with microphones was installed to record the acoustics directly below the rotor, and an optics-based longitudinal tip-path plane tracking system, developed by the author, was installed to track the orientation of the tip-path plane [31], [32]. A range of steady maneuvers, accelerations, decelerations, descents, and steady turns were used to validate the RNM-QSAM model.

During the 2006 test, it was observed that when the pilot was maneuvering the helicopter into the desired flight condition, impulsive noise events similar to BVI were radiated by the helicopter. To investigate this, the same group conducted a follow-up test at Gilroy, CA in 2007 using the same aircraft without the in-flight microphone rig. In addition to the typical matrix of steady state maneuvers, this test also flew transient pull-up and roll maneuvers at various rates. Further details of this flight test are discussed in Chapter 2.

More recently, NASA, Army, Bell Helicopter, and the University of Maryland conducted an acoustics test campaign at Eglin Air Force Base, FL in the summer of 2011 [5]. Featuring an instrumented Bell 430 helicopter, this test focused on capturing the acoustics radiated when executing compound transient maneuvers. This aircraft was also fitted with a more advanced optics-based tip-path plane tracking system, developed by the author, capable of recording the complete three-dimensional orientation of the tip-path plane during the maneuvers. The Eglin Air Force Base campaign illustrated that by executing maneuvers designed to mitigate BVI, it was possible to avoid radiating impulsive noise towards the horizon.

1.4 Dissertation Objectives

The following describes the objectives of this dissertation.

- *Conduct a flight test to capture near-horizon harmonic noise during transient maneuvers*. The purpose of the 2007 flight test campaign at Gilroy, CA was to capture the impulsive noise common to transient maneuvering flight. During this test, the aircraft executed a series of pull-up maneuvers at various rates. Onboard instrumentation during these maneuvers is correlated with ground-based microphones to identify the impulsive noise sources that radiated towards the horizon. Proper monitoring of the tip-path plane attitude was critical to this campaign.
- *Develop a dynamic model that captures the governing physics of near horizon noise during these maneuvers*. The next objective develops a first-principles model that accurately captures the dynamic behavior of the aircraft, the orientation of the tip-path plane, the aerodynamic environment, and the

acoustics of the helicopter. The aerodynamic model is to be designed to predict both low frequency loading noise and high frequency loading noise.

- *Quantitatively compare the results from modeling with experimental data*. The results of the first principles model will be compared to the data recorded by instruments onboard the helicopter and acoustic time histories from ground-based microphones. This dataset includes the dynamics of the helicopter, the attitude of the tip-path plane, and the noise radiated by the helicopter.
- *Develop a reduced order model that provides a good estimation of detection distance in real time*. The ultimate objective of this dissertation is to develop a model that is sufficient in predicting impulsive noise generated by the helicopter during transient maneuvers. This model can be used for pilot guidance, land use planning, and developing trajectories that minimize detection distance. A major emphasis of this reduced order model is the incorporation of quasi-steady assumptions wherever possible and the impact of these assumptions on the accuracy of the model. Quasi-steady models are preferable as they can be referenced from look-up tables and are ideal for real-time systems.

1.5 Dissertation Roadmap

The first chapter of this dissertation provides an overview of the problem and gives a brief history on acoustic modeling techniques and relevant acoustic flight test campaigns.

The second chapter provides a thorough review of the acoustic flight test campaign held at Gilroy, CA in 2007. This chapter details the test environment, the

matrix of flight conditions, the data reduction, and a preliminary investigation of the dominant noise sources during transient maneuvering flight.

The third chapter discusses the development of the first-principles model used to emulate the dynamics of the aircraft, the dynamics of the tip-path plane, the aerodynamic environment, and the radiated acoustics. This chapter also describes the development of the quasi-steady models used to expedite model computation.

The fourth chapter compares the results of the model with the measurements made during the flight test campaign. These comparisons are applied for steady-state flight and longitudinal cyclic pull-up maneuvers.

The fifth chapter applies the mathematical model to study the contributions of low frequency main rotor sources to the far field acoustics. This includes an investigation of the directivity characteristics and the relationship between the loading noise distribution and the estimation of low frequency loading noise. Additionally, this chapter also explores additional longitudinal maneuvers to identify trends between the piloting input, the relative distance of the wake to the tip-path plane, and the attitude of the tip-path plane relative to the observer.

The sixth chapter summarizes the dissertation, lists the important conclusions of this research, and proposes new research avenues for future investigation.

Chapter 2 Transient Maneuver Flight Test and Data Reduction

2.1 Background

In 2006, NASA, the U.S. Army, Bell Helicopter, and the University of Maryland conducted an acoustics flight test at Moffet Field, CA with a heavily instrumented Bell 206B-3 helicopter. Acoustic measurements were made for a variety of steady-flight maneuvers including level flight, descents, and accelerations. The purpose of this test was to verify the RNM Q-SAM model.

During this campaign, it was observed that the helicopter would generate large levels of impulsive noise that radiated towards the horizon when setting up and exiting the steady maneuvers; especially when pulling up at the end of the descent maneuvers and when rolling into each leg of the flight corridor. The intensity of this radiation was, in some cases, similar to that experienced when the aircraft flew steady conditions known to generate large levels of BVI noise.

To study the acoustic characteristics during these transient maneuvers, a second test program was conducted in the summer of 2007 using the same aircraft.

2.2 2007 Gilroy, CA Flight Test

The 2007 flight test campaign was performed at a farm in Gilroy, CA. This location was chosen due to the low levels of ambient background noise and the favorable wind conditions. To take advantage of these conditions, the flights were conducted just after dawn from June 13 to June 25 when there were “low-to-no” winds.

2.2.1 Test Site

The test site was arranged such that the microphone array was aligned perpendicular to the flight path. The center microphone was located along with the flight path, and additional microphones were positioned 150 m on either side (see Figure 2.1). Each microphone station featured a B&K microphone installed on a 1.2 m tower and was recorded on a Sony PC208/PC208Ax data recorder at a 65,536 Hz sample rate. An Inter-Range Instrumentation Group (IRIG) time code was simultaneously recorded with the acoustics to synchronize the microphone recordings with other measurements.

Figure 2.1. Gilroy test site layout.

2.2.2 Aircraft

A Bell 206B-3 aircraft was used during the Gilroy test campaign. To ensure similar thrust levels for repeat test cases, all maneuvers were flown between 95% and 100% of the gross mass (1451 kg).

Figure 2.2. Bell 206B-3 aircraft stationed at Gilroy.

The Bell 206B-3 features a 10.16 m diameter 2-bladed teetering main rotor. The blades feature an 11.3% Modified "Droop Snoot" airfoil with a 0.33 m chord, a -11.1° twist from root to tip, and a 2.25° pre-cone angle. Based on measurements made by onboard instrumentation, the main rotor angular velocity is 6.51 Hz. The mast of the main rotor is tilted forward 5 degrees.

The Bell 206B-3 also features a conventional 1.58 m diameter 2-bladed tail rotor. The tail rotor features a NACA 0012.5 airfoil with a chord of 0.13 m. Based on

measurements made by onboard instrumentation, the tail rotor angular velocity is 42.13 Hz.

2.2.3 In-Flight Instrumentation

The test aircraft was equipped with a suite of sensors for recording the state of the aircraft (see Figure 2.3). All of these systems were equipped with accurate time keeping devices so that all of the measurements could be synchronized with the ground based microphone recordings.

Figure 2.3. Bell 206B-3 in-flight instrumentation package.

Inertial and navigation data was recorded using NASA's Portable Programmable Guidance Display (PPGD) [33]. The heart of the PPGD system is the Honeywell H-765GU embedded GPS/INS system which features sensors for measuring acceleration, pitch, roll, and yaw rates, velocity, body attitude, and heading. The PPDG system also

includes an Apollo/Garmin CNX80 GPS receiver and an Ashtech Z-Sensor GPS receiver with a Radio Technical Commission for Maritime Services (RTCM) differential receiver to provide position data accurate to 1.6 cm. The PPDG system is integrated with an on-board heads up display in the cockpit that provides piloting cues for each maneuver. This system ensures that the pilot maintains the desired flight condition and remains along the prescribed flight path. Any deviations from the nominal flight condition are observed in the air and the maneuver can be repeated to ensure good quality data.

A Nicolet Vision Data Acquisition System (see Figure 2.4) was also installed inside the aircraft to record measurements from a SpaceAge Control, Inc. Model 100510 Swivel-Head Air Data Boom. The Air Data Boom provides angle of attack, angle of sideslip, total pressure, and static pressure measurements. The output of a CNS Systems Clock II TAC 32 IRIG Receiver is also fed into the Nicolet Vision system to record the time of day. Main rotor and tail rotor blade positions are monitored using once-per-revolution sensors that were also fed to the Nicolet Vision system.

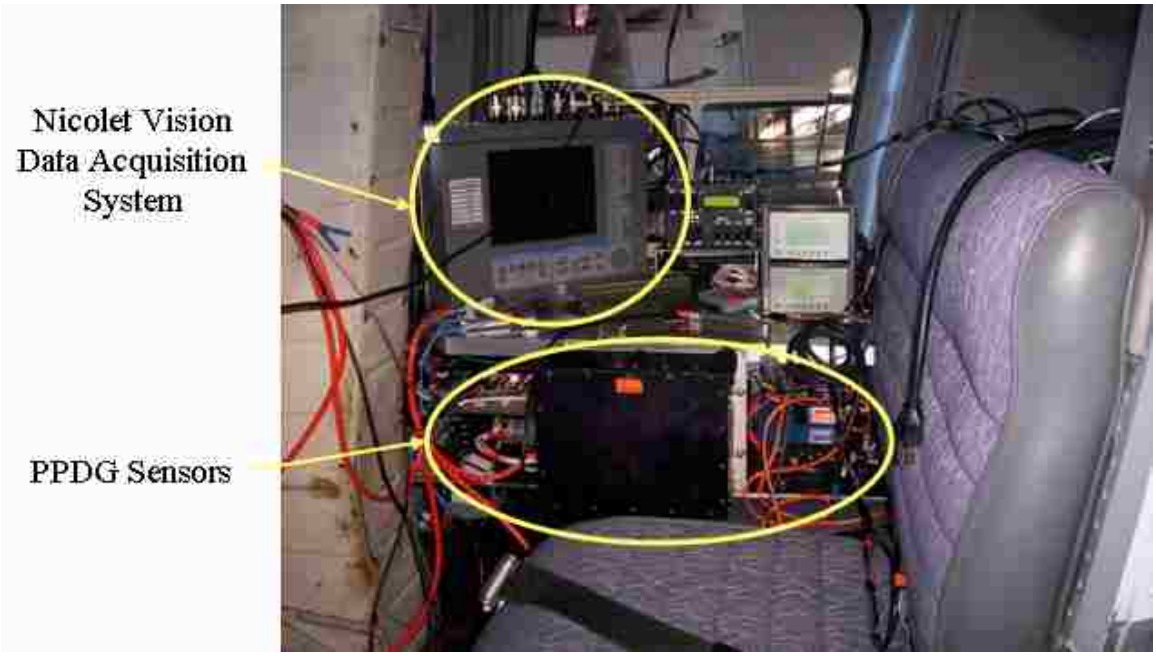

Figure 2.4. In-flight measurement pallet.

The tip-path plane tracking system makes up the final in-flight measurement device on the aircraft. This system features a custom camera and laser assembly mounted to the fuselage of the aircraft that acquires images of the main rotor blades as they pass overhead each revolution [31], [32]. Tip targets, attached to the blade tips of each blade, illuminate as the blades pass through a vertical line generated by focusing a green laser through a convex lens (see Figure 2.5). These illuminated targets are captured by the cameras and translated into a relative flapping angle. When combined with the angle of attack data recorded by the air-data boom, this system provides a means of tracking the tip-path plane angle of attack. As this system only features forward and aft-facing cameras, it is only capable of measuring the longitudinal flapping of the tip-path plane.

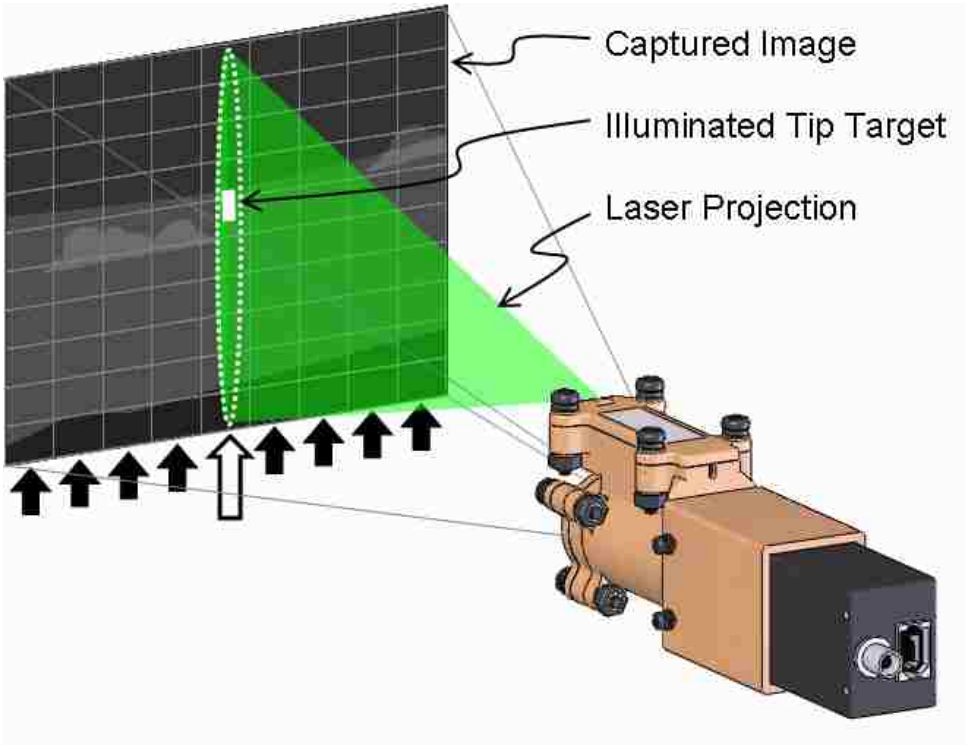

Figure 2.5. TPP tracking system camera.

2.2.4 Maneuvers

Overall, 450 maneuvers were flown during the 2007 flight test. The longitudinal maneuvers included steady level flight cases at various velocities, steady ascents and descents at various velocities and flight path angles, and steady accelerations and decelerations at various velocities and flight path angles. To expand RNM Q-SAM capabilities for turns, various level and descending turns were also executed. As with the longitudinal maneuvers, these were performed at various velocities and descent angles. All of these maneuvers were executed following patterns programmed into the PPDG.

In addition to the steady cases, transient pull-ups and rolls to the left and right were also studied. When performing these maneuvers, the pilot maintained a steady level flight condition of 75 knots and an altitude of 150 feet along the flight path. When the

aircraft was 1500 ft from the center microphone array, the pilot would execute a pure cyclic pull-up maneuver or a pure cyclic roll maneuver (see Figure 2.6). These were performed at slow, moderate, and fast rates as deemed by the flight crew. The purpose of the maneuver was to capture and record the near-horizon noise associated with the initial transient.

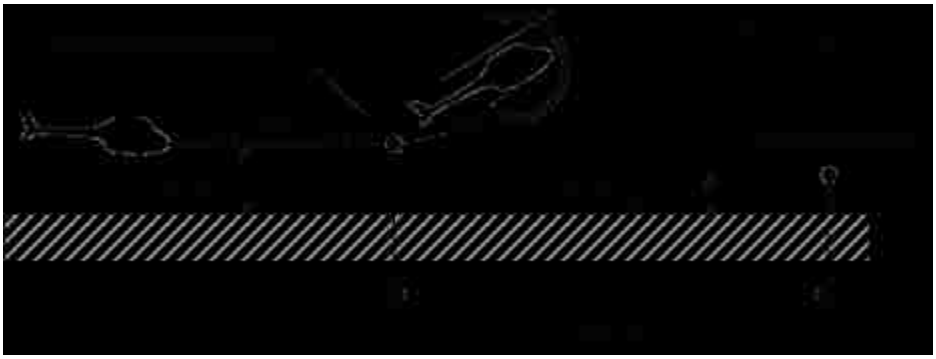

Figure 2.6. Transient maneuver flight pattern.

As will be shown later in this dissertation, the acoustics generated during these maneuvers is extremely sensitive to the orientation of the tip-path plane, the positioning of the wake, and the loading distribution on the advancing side of the rotor disk. Since lateral measurements of the tip-path plane were not available during this test program, only the transient pull-up maneuvers will be investigated.

2.3 Data Reduction

The data reduction process can be broken into two synchronization processes. The first process is used to synchronize all of the data to a common time. As mentioned above, data from all of the various scientific instrument pallets were equipped to receive an accurate time signal. Analog instruments simultaneously recorded the IRIG time format of the National Institute of Standards and Technology (NIST) broadcast signal. Digital instruments stored the serial timestamp message transmitted by the GPS receivers.

The second process is used to account for the retarded time between when noise was emitted by the aircraft, the source time, and when it was received by the microphones, the observer time. This process is shown graphically in Figure 2.7. The relationship between the observer time, t_o, and the source time, t_s, is given by the retarded time equation:

$$t_o = t_s + \frac{|\vec{r}|}{c} \tag{2.1}$$

Where $\vec{r}$ is the position vector from the observer to the source and c is the speed of the wave through the medium – in this case the speed of sound. The source position vector must also take into account the motion of the medium in the presence of wind.

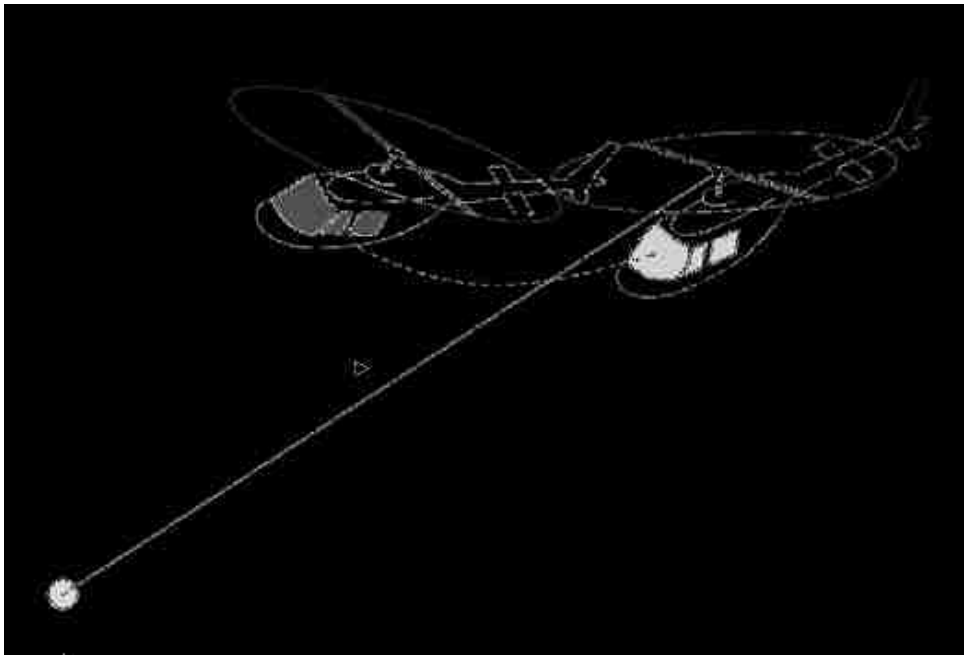

Figure 2.7. Retarded time diagram.

By converting all of the measurements into observer time, it is possible to correlate the acoustic trends with the state of the aircraft.

2.3.1 Slow Pull-up

This section will discuss the reduced data set for the slow pure cyclic pull-up maneuver. All data is shown relative to the source time so that the ground microphone trends can be correlated to the state of the helicopter. For clarity, all time is measured relative to the start of the data record and most of the steady state data prior to executing the pull-up maneuver is not shown. In-flight measurements indicate that this maneuver produced a maximum pitch rate of 4.4°/s and that the pull-up was executed approximately 46.5 seconds into the run (see Figure 2.8). The pitch rate data indicates the pull-up was held at a fairly constant rate of 2.5°/s over the duration of the record. Also note that the in-flight measurements suggest that the pilot performed a slight nose-down transient just prior to executing the pull up.

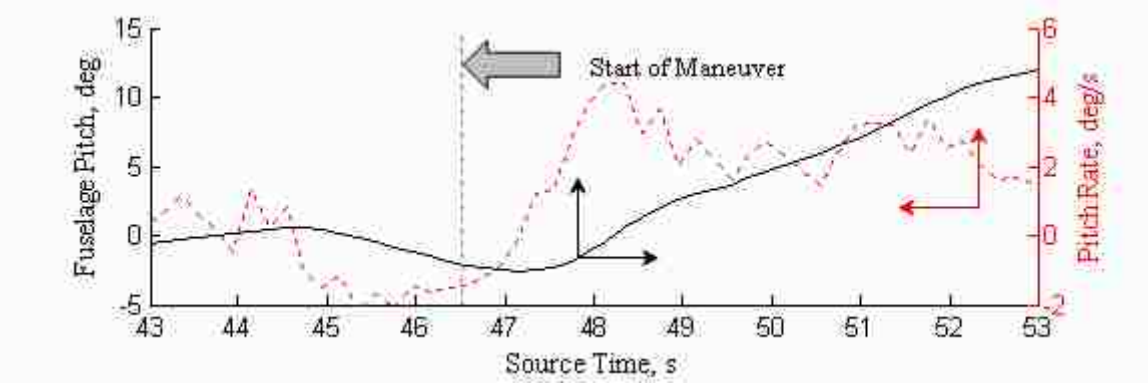

Figure 2.8. Body response during slow pull-up maneuver.

The time histories of the three microphones are shown in Figure 2.9. At a source time of 48 seconds, both the center and retreating-side microphones begin to experience increased levels of impulsive noise. This initial increase also coincides with when the fuselage begins to pitch-up at a steady rate. These levels increase over the first 1 to 1.5 seconds. These levels then remain higher than the steady condition over the duration of

the maneuver. This suggests that during the maneuver, the wake remains in close proximity to the tip-path plane.

The lack of a notable increase in impulsive noise levels on the advancing side microphone suggest that the noise radiation was not directed towards the microphone on the advancing side.

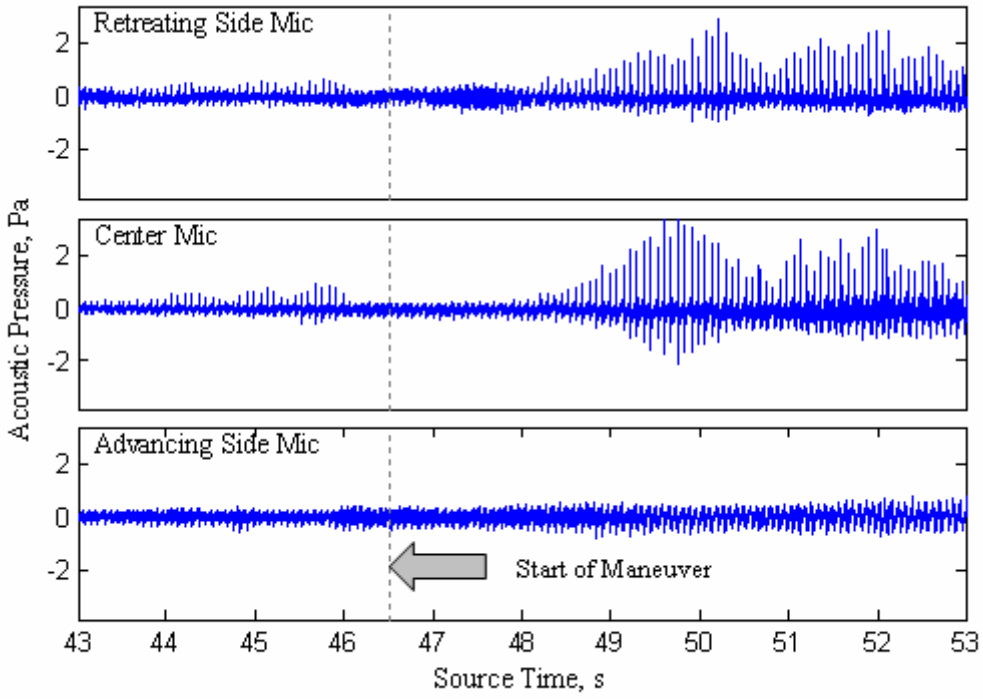

Figure 2.9. Acoustic time history during slow pull-up maneuver.

The time history of multiple sound pressure metrics is presented in Figure 2.10 for each microphone. These metrics include the overall sound pressure level (OASPL) over the entire frequency range, the BVI sound pressure level (BVISPL) which contains content from the 6th main rotor harmonic to the 40th main rotor harmonic (78 Hz to 521 Hz for the Bell 206B-3), and the sound pressure level between the 1st and the 6th main rotor harmonic (13 Hz to 78 Hz for the Bell 206B-3). As observed from the acoustic time

histories, BVI captured by the center and retreating-side microphones results in an increase in the BVISPL during the course of the maneuver while levels stay relatively low on the advancing side. However, the low frequency noise below the 6th main rotor harmonic shows an increase on all three microphones. This indicates that during the maneuver, the tilt of the tip-path plane, in addition to radiating BVI noise to the horizon, also exposes the far field observer to low frequency loading noise.

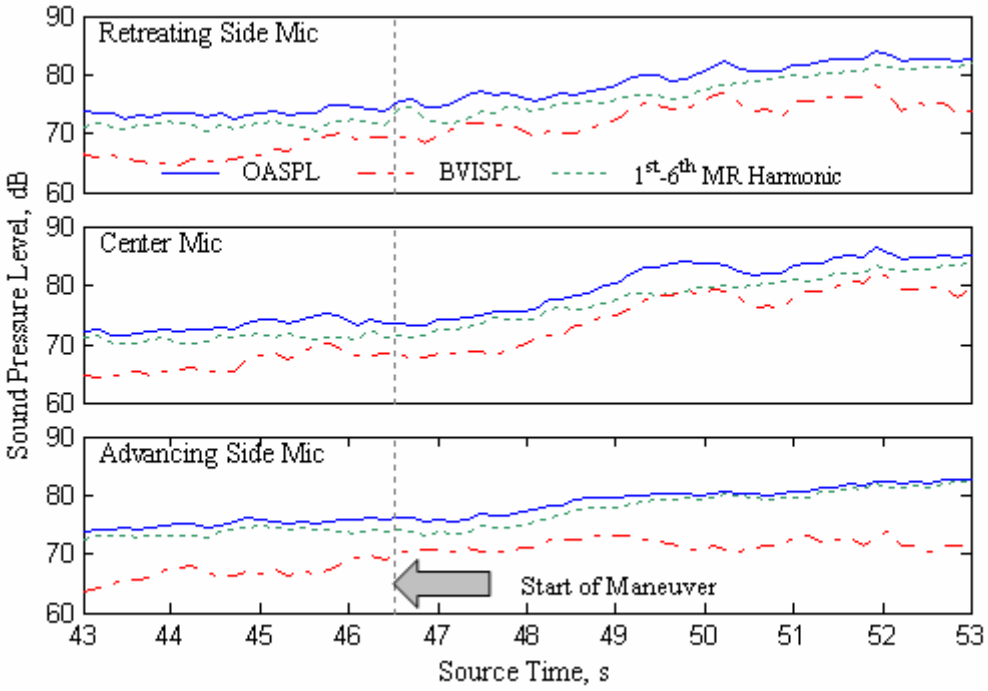

Figure 2.10. Sound level metrics during slow pull-up maneuver.

Additional in-flight measurements are provided in Figure 2.11. During the steady region, the initial advance ratio and tip-path plane angle of attack were 0.19 and -1.4° respectively. Over the execution of the maneuver, the aircraft decelerates rapidly, which will have important implications in the number and locations of the blade-vortex interactions. As the aircraft begins to pitch-back, the tip-path plane angle of attack

becomes positive and the normal acceleration felt within the aircraft increases. The tip-path plane angle of attack reaches a maximum value of 0.8°; the maximum normal acceleration 127% over nominal g-loading. Peaks in the tip-path plane attitude and normal acceleration both occur approximately 49 seconds into the record; approximately 2.5 seconds after the slow pull-up maneuver is executed.

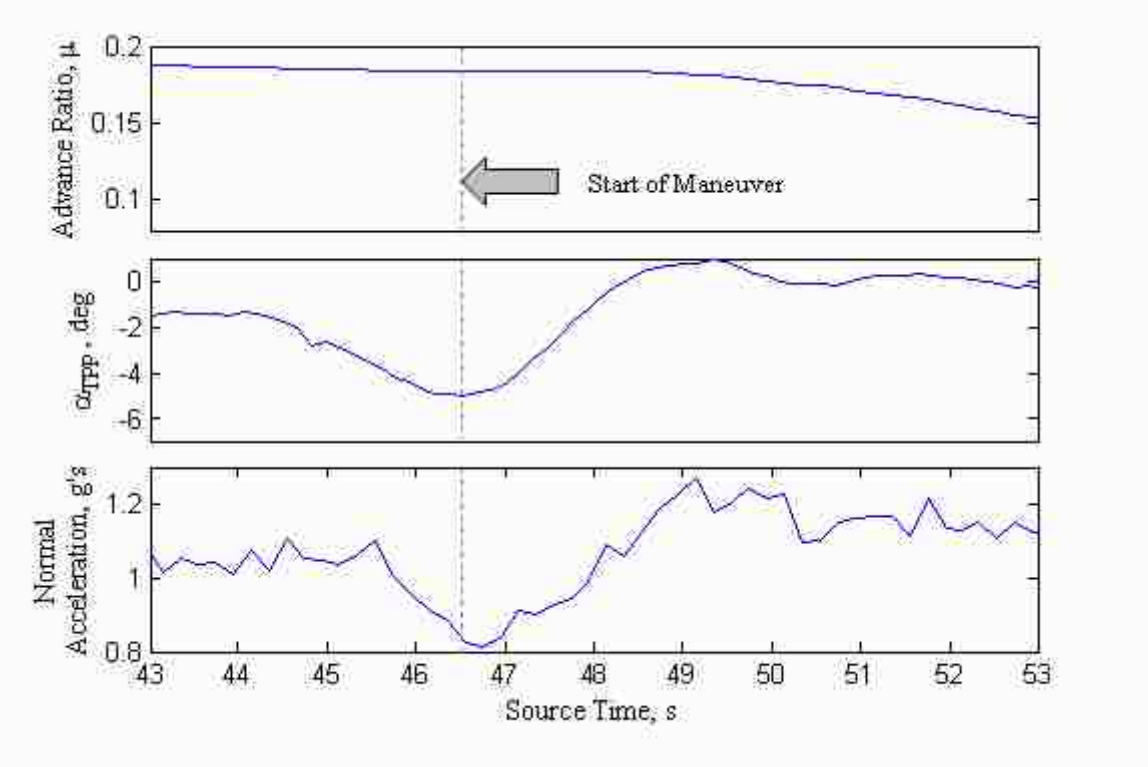

Figure 2.11. Additional in-flight measurements during slow pull-up maneuver.

2.3.2 Moderate Pull-up

The second reduced data set is for the moderate pure cyclic pull-up maneuver. In-flight measurements indicate that the maneuver was executed around 36.5 seconds into the data record, experienced a maximum pitch rate of 6.8°/s, and was held around 5°/s over the duration of the maneuver (see Figure 2.12).

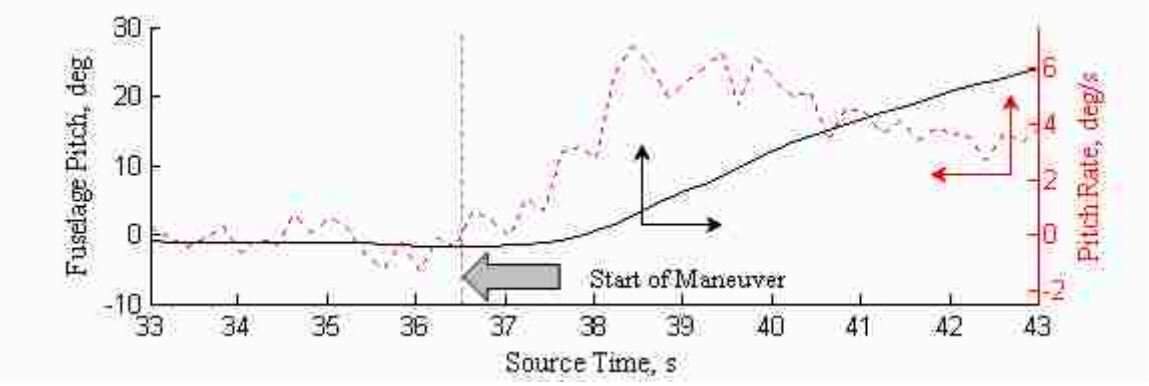

Figure 2.12. Body response during moderate pull-up maneuver.

The acoustic time histories of the three microphones for the moderate pull-up maneuver are shown in Figure 2.13. Increased levels of impulsive noise are detected by the center and retreating-side microphones around 38 seconds into the record; again coinciding with when the notable increases in fuselage pitch begins. As with the slow pull-up maneuver, these data suggest that the wake approaches and remains in close proximity to the tip-path plane during the maneuver. This time, the pull-up maneuver is executed in a location that permits the advancing side microphone to also pick up increased impulsive noise. However, the sensitivity of the directivity is indicated by the short duration of the increased impulsive noise on the advancing-side microphone as compared to the other two channels.

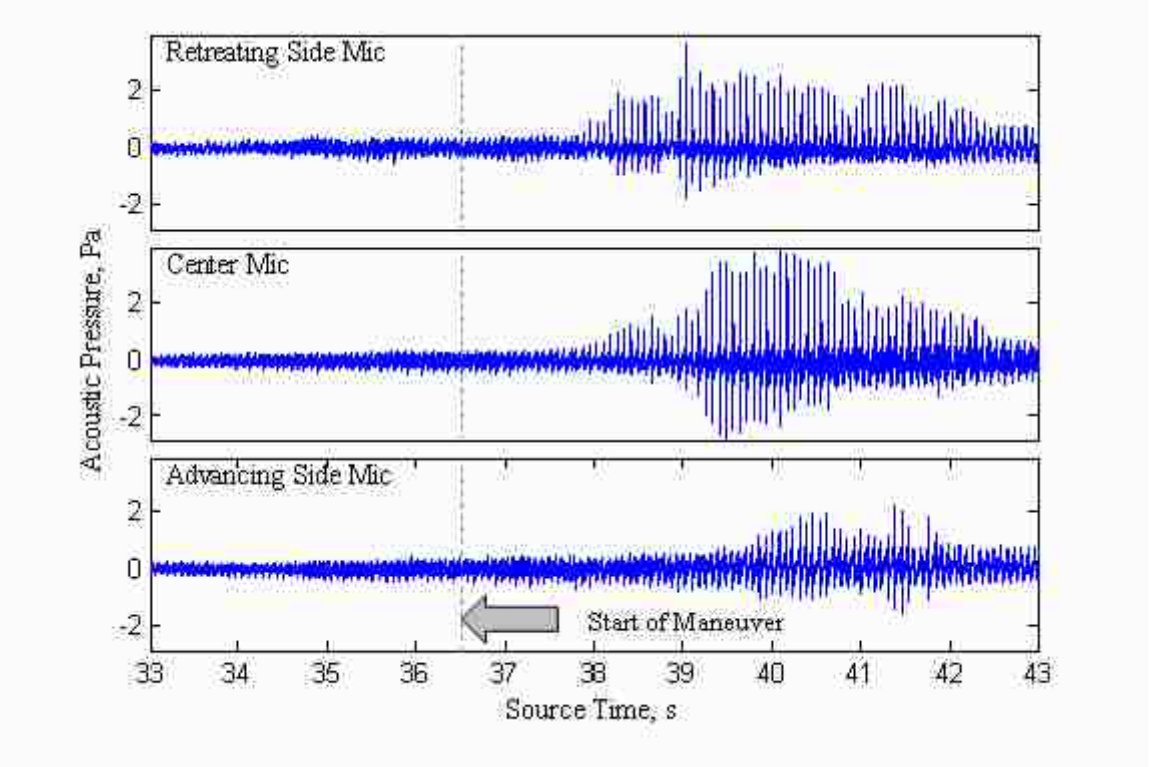

Figure 2.13. Acoustic time history during moderate pull-up maneuver.

The time histories of multiple sound pressure metrics is presented for the moderate pull-up maneuver in Figure 2.14. In this maneuver, all three microphones captured an increase in BVISPL noise. Furthermore, all three microphones show an increase in the low frequency noise as the tip-path plane exposes the observer to the low frequency loading noise projected out of the plane of the rotor. Though BVISPL levels surpass the levels between the 1st and 6th main rotor harmonics for the center microphone during the maneuver, the low frequency noise remains the largest contributor to the overall acoustic levels on the retreating and advancing-side microphones.

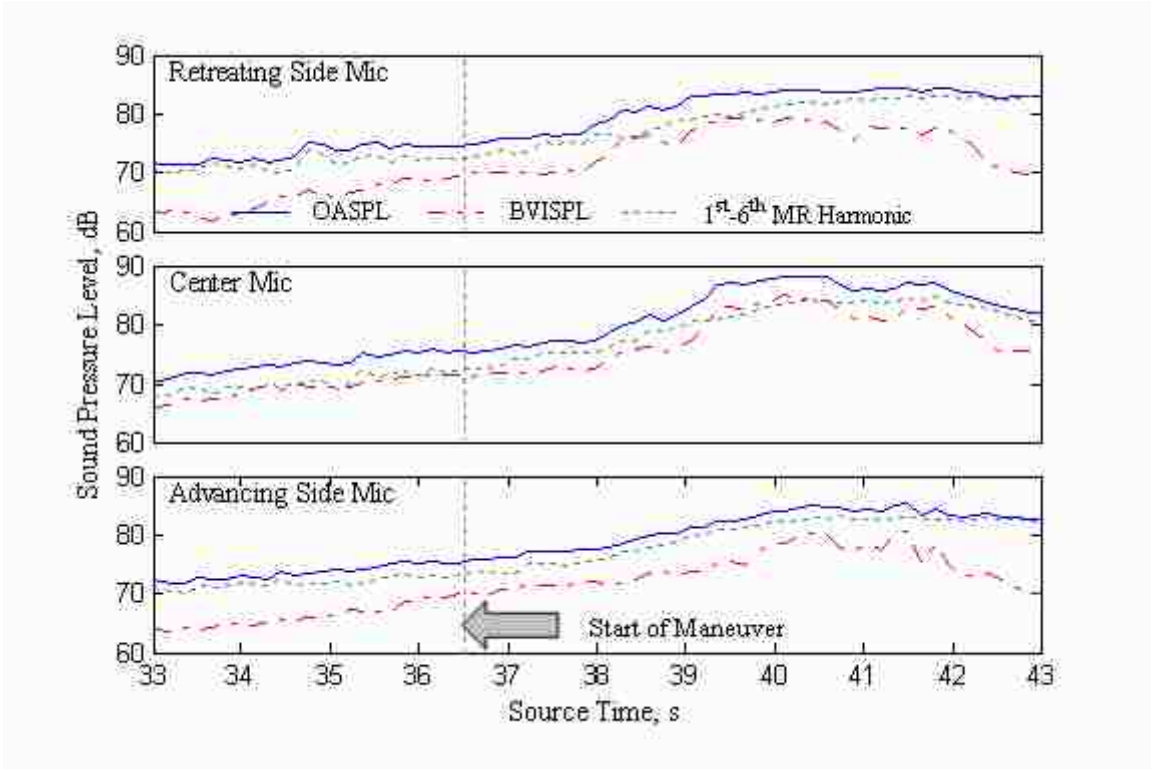

Figure 2.14. Sound level metrics during moderate pull-up maneuver.

Additional in-flight measurements for the moderate pull-up maneuver are shown in Figure 2.15. During the steady region, the initial advance ratio and tip-path plane angle of attack were 0.19 and -2.6° respectively. Over the execution of the maneuver, the aircraft decelerates faster than in the previous case. As the aircraft begins to pitch-back, the tip-path plane angle of attack becomes positive and the normal acceleration felt within the aircraft increases. The tip-path plane angle of attack reaches a maximum value of 2.7°; the maximum normal acceleration 145% over nominal g-loading. Peaks in the tip-path plane attitude and normal acceleration both occur approximately 40 seconds into the record; approximately 3 seconds after the moderate pull-up maneuver is executed.

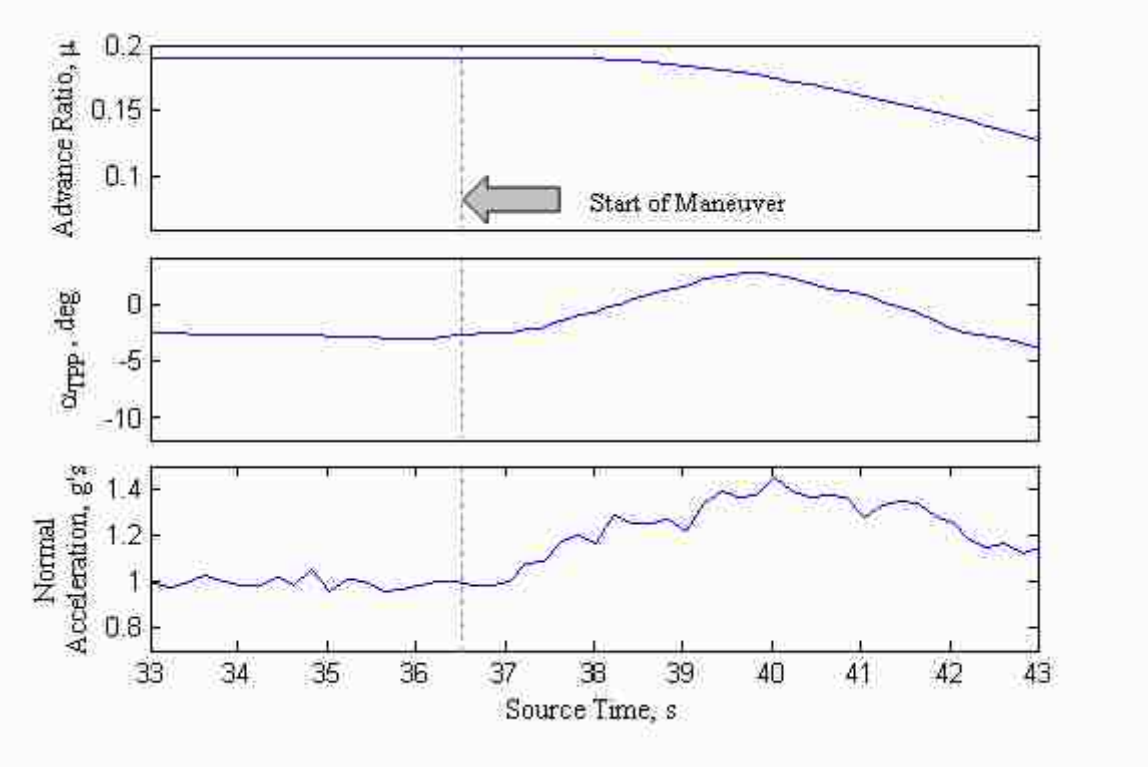

Figure 2.15. Additional in-flight measurements during moderate pull-up maneuver.

2.3.3 Fast Pull-up

The final reduced data set is for the fast pure cyclic pull-up maneuver. In-flight measurements indicate that the maneuver was executed around 40.7 seconds into the data record and the aircraft experienced a maximum pitch rate of 17.6°/s at 42.5 seconds. Unlike the other two pull-up maneuvers, the pitch rate was not held constant after execution, and began to decrease over the course of the maneuver (see Figure 2.16).

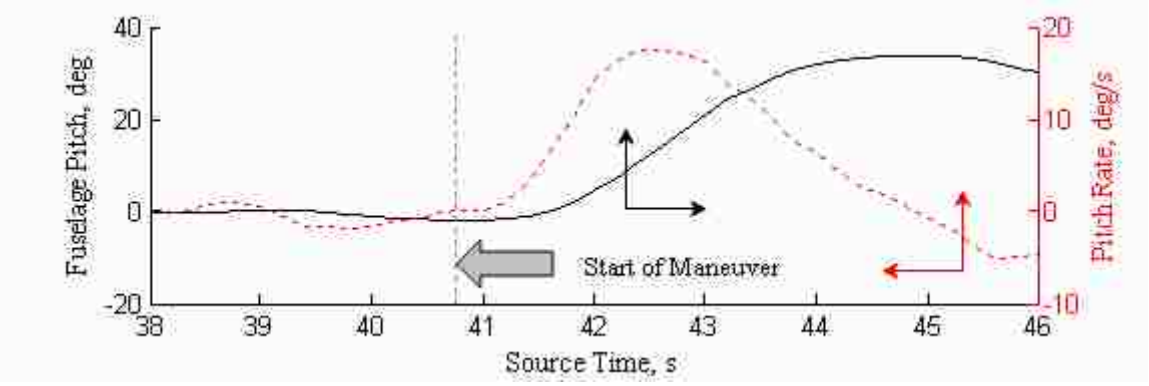

Figure 2.16. Body response during fast pull-up maneuver.

The acoustic time histories of the three microphones during the fast pull-up maneuver are shown in Figure 2.17. The center and retreating-side microphones first observe increases in impulsive noise at 42 seconds into the data record, roughly the same time that the fuselage begins to pitch up. However, unlike the previous maneuvers, there are two distinguished amplitude peaks over the course of the maneuver – likely due to the wake passing through the tip-path plane twice. The first occasion is likely due to the wake passing through the tip-path plane as the aircraft pitches up. However, instead of remaining in close proximity during the entire maneuver, the pull-up is severe enough that the wake passes through and moves above the tip-path plane where the impulsive noise levels temporarily decrease. Then, as the pitch rate drops, the wake likely passes through the tip-path plane a second time creating the second rise in impulsive noises. As in the case of the moderate pull-up, the advancing-side microphone is in a suitable place to observe an increase in impulsive noise, but due to the directivity of the advancing side BVI, the duration is not sufficient enough to feature the multiple peaks seen on the other channels.

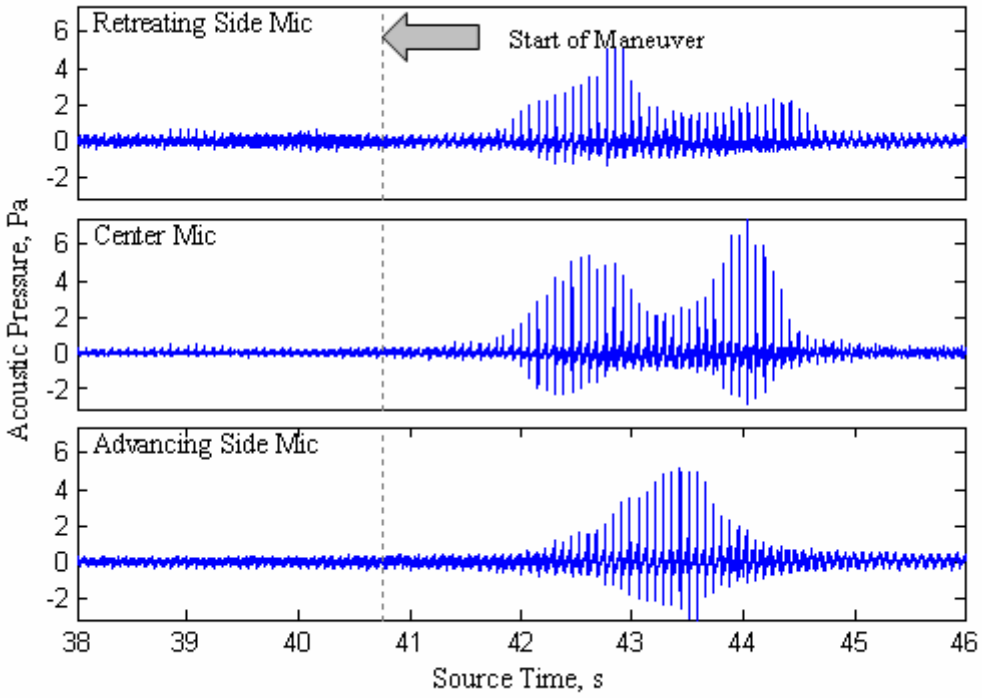

Figure 2.17. Acoustic time history during fast pull-up maneuver.

The sound level metrics for the fast pull-up maneuver are presented in Figure 2.18. All three microphones witness increases in the BVISPL band and all feature moments where the BVISPL is the largest contributor to the overall acoustic levels. However, the center and retreating side microphones both contain dips in the BVISPL. As pointed out previously, this is likely due to the wake passing through the tip-path plane twice. During the momentary dip in BVISPL, the low frequency noise continues to increase as the tip-path plane exposes the out-of-plane loading noise towards the horizon. These levels eventually drop as the tip-path plane begins to tilt forward at the end of the maneuver.

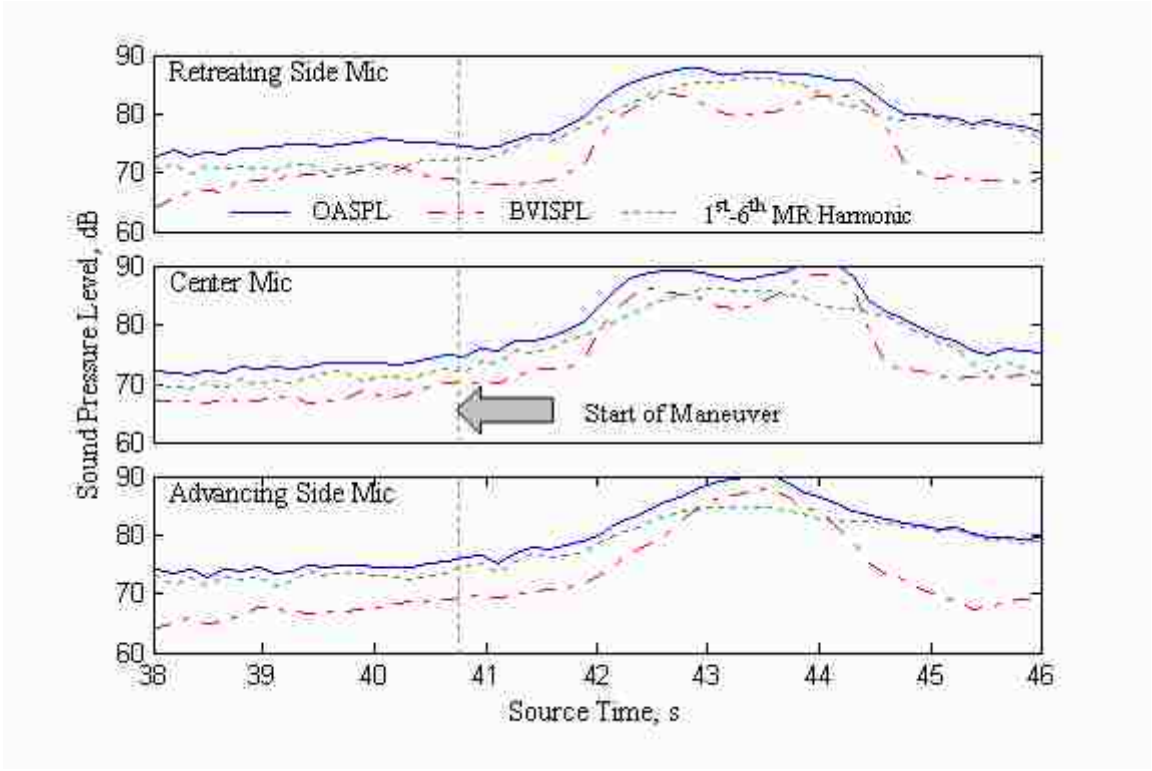

Figure 2.18. Sound level metrics during moderate pull-up maneuver.

Additional in-flight measurements for the fast pull-up maneuver are shown in Figure 2.19. During the steady region, the initial advance ratio and tip-path plane angle of attack were 0.19 and -2.5° respectively. Over the execution of the maneuver, the aircraft decelerates faster than in the other pull-up maneuvers. As the aircraft begins to pitch-back, the tip-path plane angle of attack becomes positive and the normal acceleration felt within the aircraft increases. The tip-path plane angle of attack reaches a maximum value of 9.7°; the maximum normal acceleration 173% over nominal g-loading. Peaks in the tip-path plane attitude and normal acceleration both occur approximately 43 seconds into the record; approximately 2 seconds after the moderate pull-up maneuver is executed.

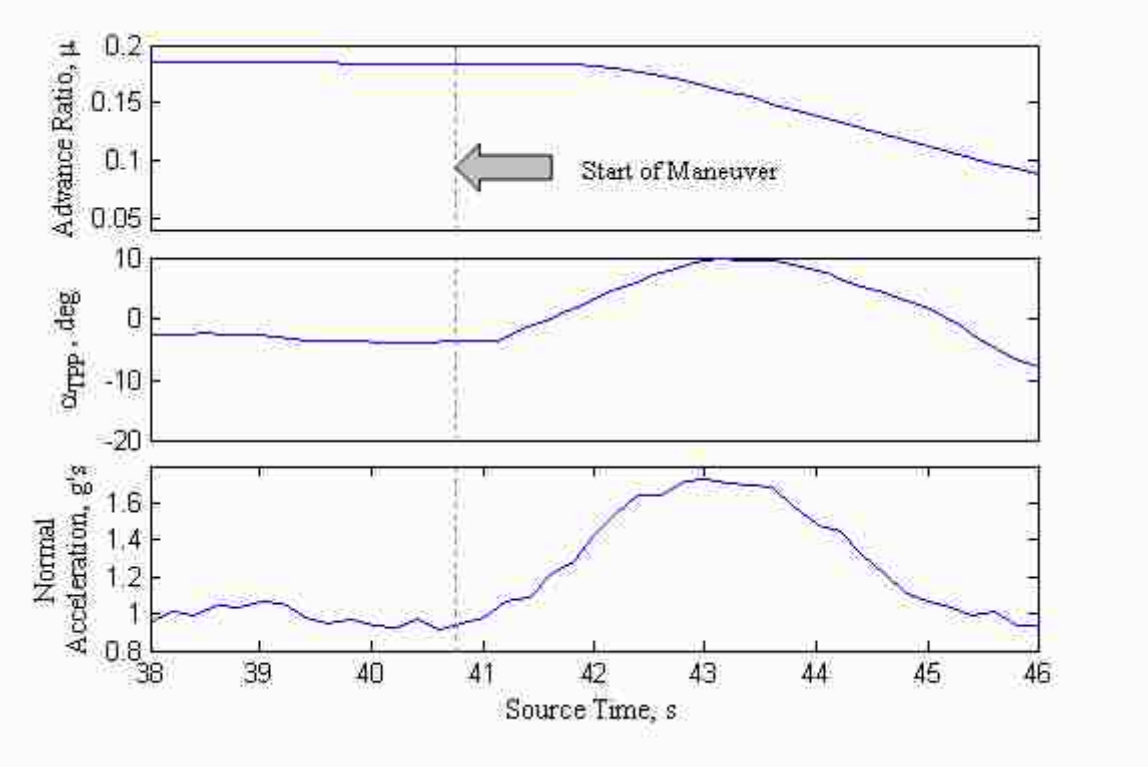

Figure 2.19. Additional in-flight measurements during fast pull-up maneuver.

2.3.4 Summary of Maneuvers

Below is a summary of the initial and peak in-flight measurements for the three maneuvers.

Table 2.1. Summary of Maneuvers

Maneuver	Initial μ	Initial α_{TPP}	Peak Pitch Rate	Peak α_{TPP}	Peak Normal Acceleration
Slow	0.19	-1.4°	4.4°/s	0.8°	1.27 g's
Moderate	0.19	-2.6°	6.8°/s	2.7°	1.45 g's
Fast	0.19	-2.5°	17.6°/s	9.7°	1.73 g's

2.4 Preliminary Analysis of Fast Pull-up Maneuver

Once the data reduction is complete and the acoustic trends synchronized to the state of the aircraft, it is possible to focus on the characteristics of the impulsive noise. The first task compares the general shapes of the impulse to known classical BVI forms. The second task investigates the sequence of the individual blade-vortex interactions. The later task will address the presence and severity of the wake bundling before introducing the more complicated first principles analysis. This preliminary analysis will focus on the data set for the most aggressive pure cyclic pull-up maneuver.

2.4.1 Impulse Pulse Shape Investigation

The acoustic time histories shown in Figure 2.20 presents the raw microphone recordings for one full blade revolution from the Bell 206B-3 during a steady 4.5° descent at 60 knots – a condition known to generate severe BVI noise for the aircraft.

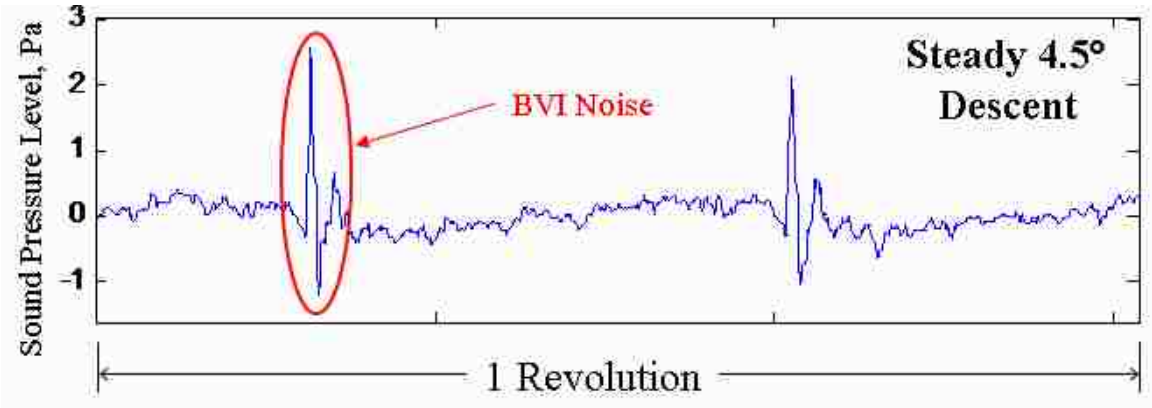

Figure 2.20. Acoustic time history during a known BVI condition.

As each blade passes through the advancing-side region of the rotor, it comes into close proximity to the trailed wake and generates several impulsive interactions that radiate into the far field. Each of these interactions includes an initial negative pulse followed by a positive pulse. The quantity and directivity of these pulses is largely a

function of the wake geometry. For high advance ratios, the wake is stretched out behind the aircraft and only a few interactions occur; at lower advance ratios, the wake is contracted and more interactions can occur. This concept is shown for advance ratios of 0.2 and 0.1 in Figure 2.21. Recall that during the fast pull-up maneuver, the range of advance ratios is similar to that shown in Figure 2.21. This illustrates the range of possible interactions that can be experienced over the duration of the pull-up maneuver.

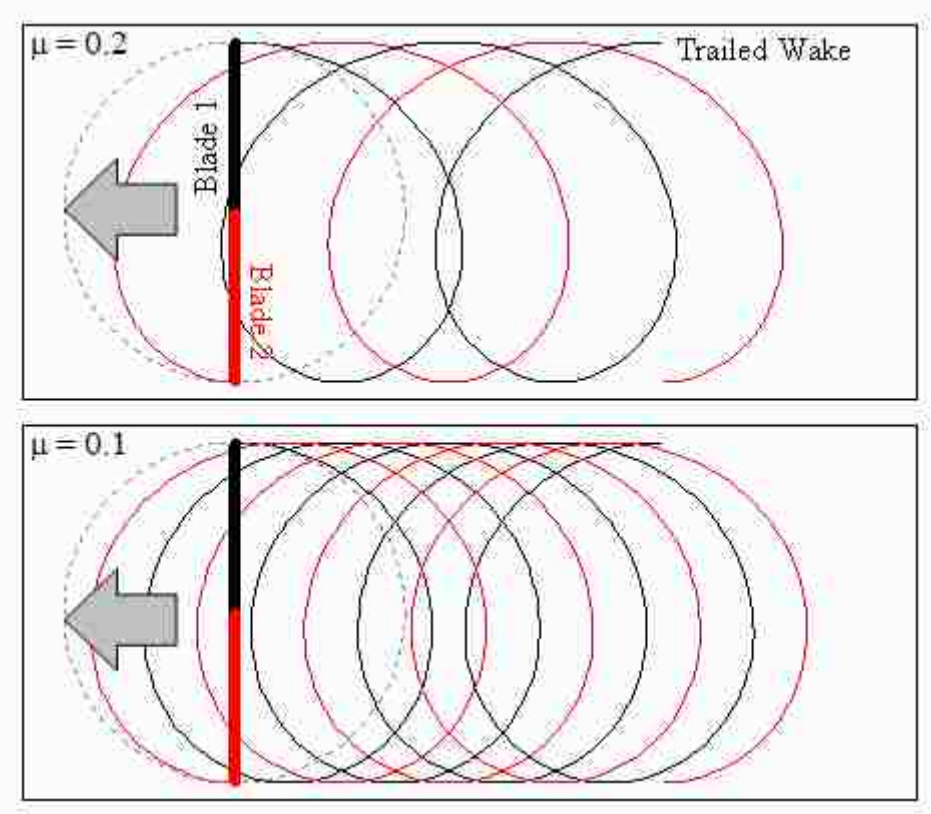

Figure 2.21. Overhead view of helical wake at different advance ratios.

The raw acoustic time history for a complete revolution during the fast pull-up maneuver is presented in Figure 2.22. This sample is taken for the center microphone around 42.6 seconds into the maneuver when the maximum impulsive noise is observed. For convenience, the time history for the 4.5° descent known to produce BVI is plotted in

the top frame and the time axis aligned for comparison. Note that the helicopter was at a different distance away from the microphone array when these samples were taken and the amplitudes have not been adjusted to account for this difference.

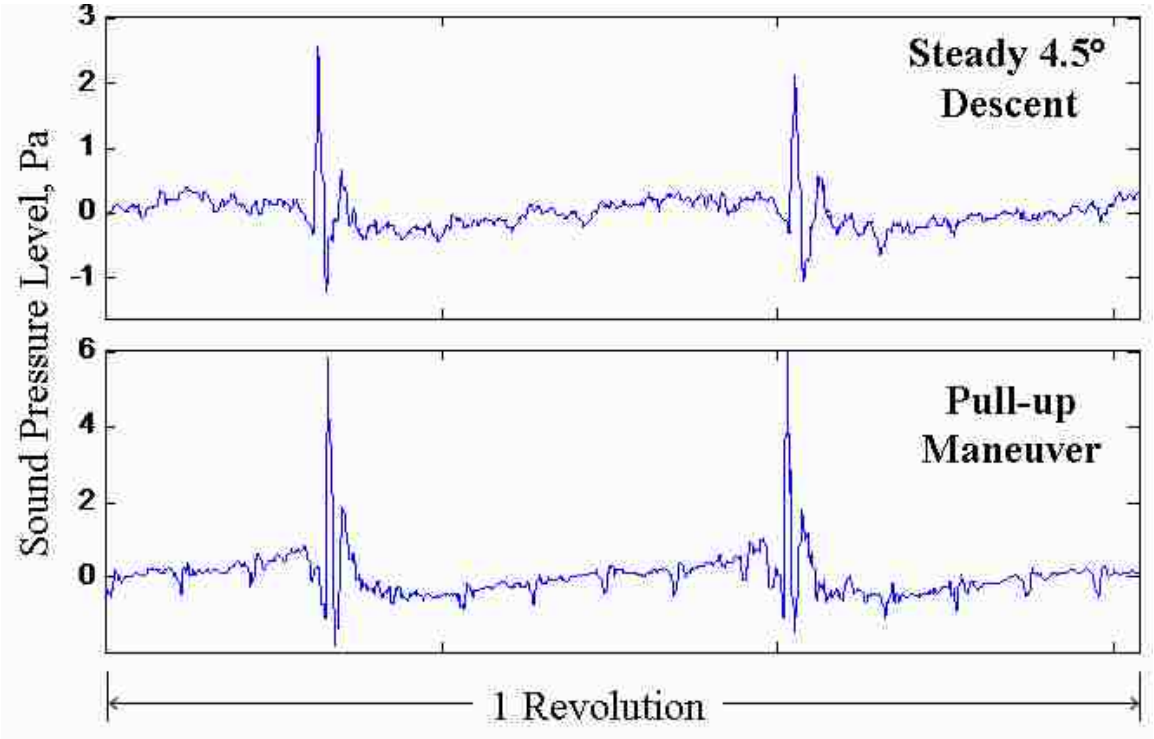

Figure 2.22. Acoustic time history for the 4.5° steady descent (top) and the fast pull-up maneuver (bottom).

These data indicate that the impulsive noise captured during even the most extreme pull-up maneuvers is extremely similar in shape to the classical BVI pattern. This qualitative analysis of the pulse shape suggests that the impulsive noise experienced during the maneuvers is attributed to BVI as the wake passes through the tip-path plane. Next, a general model will be discussed to investigate the sequencing of expected BVI events.

2.4.2 Blade-Vortex Interaction Acoustic Phasing

In this section, a model that treats the BVI interactions as uniformly weighted omni-directional disturbances will be applied. This model features the same technique developed by Schmitz and Sim [34], [35], but with adjustments made to account for maneuvering flight. These models were developed to capture the grouping of BVI disturbances and can be used to predict when BVI should be captured in the far field. Adequately modeling the aerodynamics and acoustics of the BVI events require more sophisticated models which will be developed in the following chapter.

2.4.2.1 Wake Geometry Update

Because the tip-path plane orientation is changing dynamically during maneuvering flight, steady-state expressions that describe the wake position relative to the tip-path plane like those derived in reference [36] cannot be used. Instead, a time stepping procedure is used to account for variations in velocity, flight trajectory, body attitude, and tip-path plane attitude.

Consider the general diagram shown in Figure 2.23. In this diagram, the point O, represents a fixed inertial point in space, the point B represents the center of gravity of the helicopter, the point H represents the main rotor hub, and the point V represents a point on the trailed wake. The absolute velocity of V is then simply the time derivative of the absolute position vector from O to V. Since V is a point in the medium, the absolute velocity of V is simply the velocity of the medium at that location.

For the purposes of developing a simple omni-directional disturbance model, the following assumptions will be made when updating the wake. First, the inertial velocity of the medium will only be the inflow through the tip-path plane, V_i. Second, the inflow

through the tip-path plane will be uniform. Third, no blade flapping will be considered; the tip-path plane will be normal to the shaft. Fourth, the trailed wake will be modeled as a prescribed helical wake.

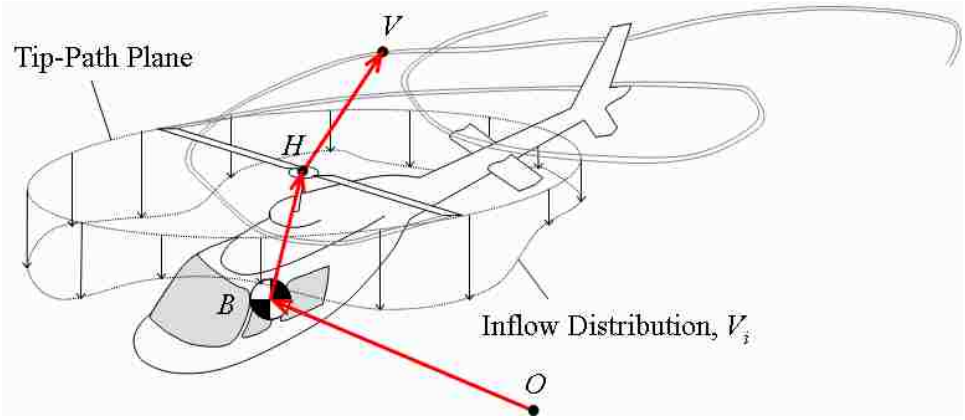

Figure 2.23. Wake geometry and position vector diagram.

The velocity of a point on the wake relative to the hub in the tip-path plane, $\overrightarrow{V_{V/T}}$, is found to be:

$$\overrightarrow{V_{V/T}} = \vec{V}_i - \overrightarrow{V_{B/I}} - \overrightarrow{\omega^{B/I}} \times \overrightarrow{r_{H/B}} - \left(\overrightarrow{\omega^{B/I}} + \overrightarrow{\omega^{T/S}}\right) \times \overrightarrow{r_{V/H}} \tag{2.2}$$

Where $\overrightarrow{V_{B/I}}$ is the velocity of the center of gravity relative to the inertial frame, $\overrightarrow{\omega^{B/I}}$ is the angular velocity of the body relative to the inertial frame, $\overrightarrow{\omega^{T/S}}$ is the angular velocity of the tip-path plane relative to the shaft frame (zero for the simplified case of no blade flapping), $\overrightarrow{r_{H/B}}$ is the position vector from the center of gravity to the hub, and $\overrightarrow{r_{V/H}}$ is the position vector from the hub a point on the trailed wake. Each point on the wake is advanced using a forward Euler scheme with time step Δt:

$$\overrightarrow{r_{V/H}^{n+1}} = \overrightarrow{r_{V/H}^{n}} + \overrightarrow{V_{H/T}} \Delta t \tag{2.3}$$

2.4.2.2 Omni-Directional Disturbance Model

Following the "Level A" modeling developed by Sim [34], a unit strength disturbance is radiated omni-directionally wherever the blade intersects the projection of the prescribed wake in the tip-path plane. These omni-directional spheres radiate towards the far-field at the speed of sound and are assumed to be non-decaying. An illustration of this model is shown in Figure 2.24. The circles near the intersection of the reference blade and the wake are the boundary of the omni-directional disturbances as seen if looking at the tip-path plane from above. The diameter of the circle is indicative of how far the disturbance has propagated since it was created. Accumulation of the disturbance boundaries is indicative of the strength of the pressure wave.

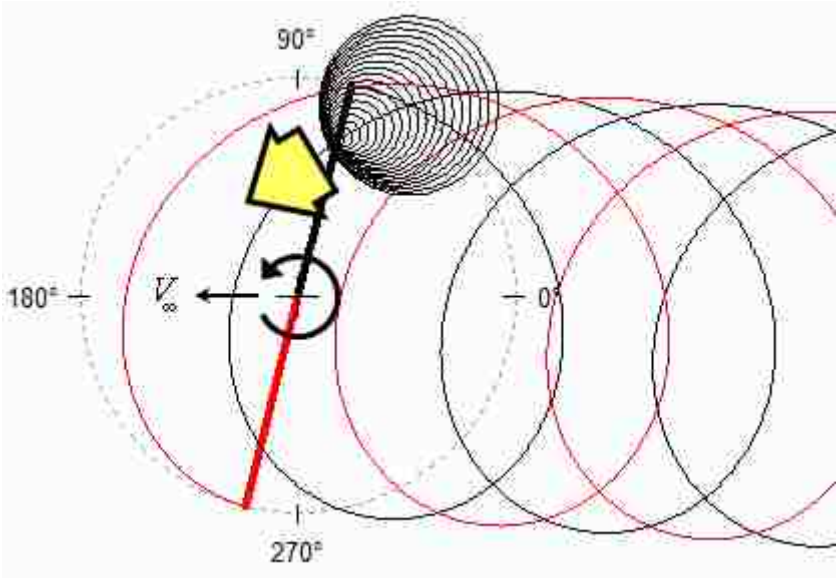

Figure 2.24. Omni-directional modeling of an oblique interaction.

When describing BVI interactions, it is beneficial to also consider the trace Mach number. This is the speed at which a trace of the blade-vortex intersection moves relative to the stationary medium [37]. The trace Mach number is defined as:

$$M_{TR} = \frac{U}{c \sin \gamma} \tag{2.4}$$

Where U is the velocity of the blade at the intersection, c is the speed of sound, and γ is the blade-vortex intersection angle (see Figure 2.25).

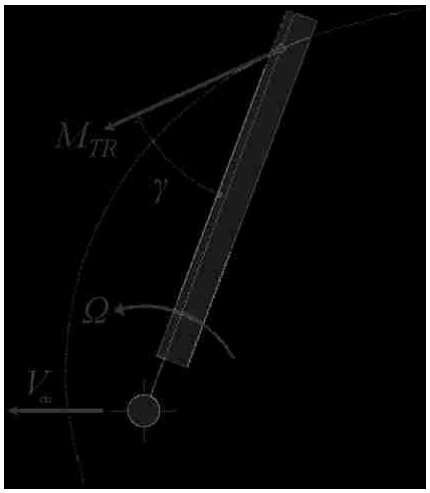

Figure 2.25. Trace Mach number geometry.

This level of modeling also provides a means of characterizing the types of BVI interactions. Generally, these are classified as either oblique interactions or parallel interactions. A graphical representation of an oblique interaction was shown previously in Figure 2.24. Oblique interactions occur when the blade intersects the wake at oblique angles and are localized to a single part of the blade during the interaction. In this example, the oblique interaction creates an accumulation of acoustic pressure waves that radiate forward and towards the retreating-side of the tip-path plane.

A graphical representation of a parallel interaction is shown in Figure 2.26. Parallel interactions occur when the blade is nearly parallel to the wake at the time of intersection. This simultaneously triggers disturbances over the length of the blade. In

this example, the parallel interaction creates an acoustic pressure front that propagates forward and to the advancing-side of the tip-path plane.

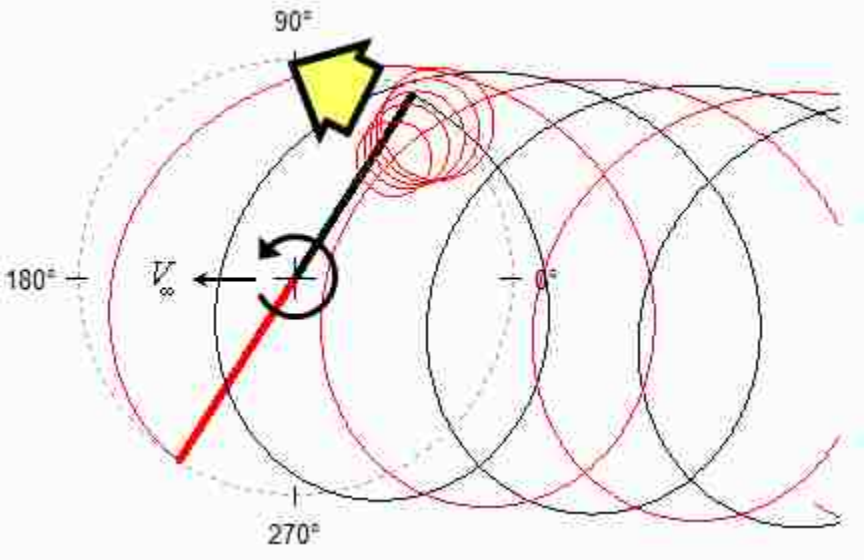

Figure 2.26. Parallel interaction.

Figure 2.27 displays the six interactions that occur for a 2-bladed main rotor traveling at an advance ratio of 0.19 – the same advance ratio flown prior to the execution of the transient maneuvers during the Gilroy flight test. Because inboard portions of the blade contribute little to acoustics [35], only the interactions occurring on the outer 50% of the reference blade are illustrated. The gray arcs indicate the location in the tip-path plane of all of the intersections between the blade and the projection of the wake over one full revolution. Note that there are four interactions on the advancing side of the tip-path plane (labeled #1 through #4) and there are two interactions on the retreating side (labeled #R1 and #R2).

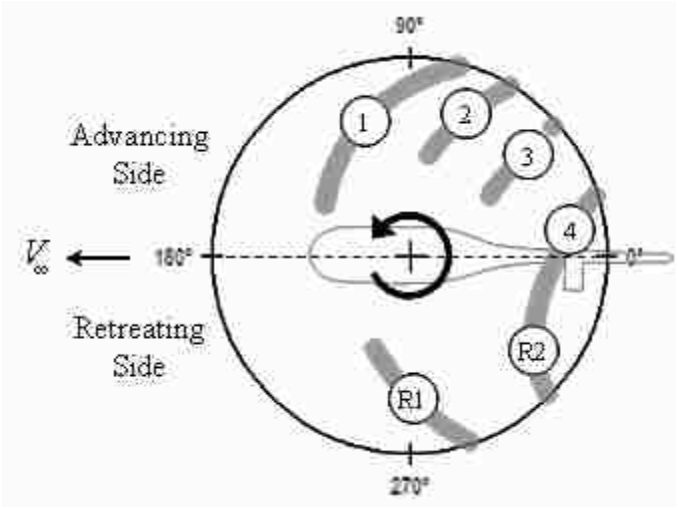

Figure 2.27. BVI interaction locations in tip-path plane at μ = 0.19.

Details of the individual interactions are provided in Figure 2.28. In each frame, the left image displays the interaction geometry and the boundaries of the radiated omni-directional disturbances. The large gray arrow in the geometry plots indicates the direction that the dominant acoustic pressure wave front propagates. The right image in each frame plots the trace Mach number of each intersection versus the blade station where the intersection occurs. The arrow above each trace Mach number curve indicates the direction that the trace Mach number changes over the course of the interaction. Note that interactions #1 and #R1 are essentially the same continuous interaction, but have been divided to separate advancing and retreating-side features. The same is true for #4 and #R2.

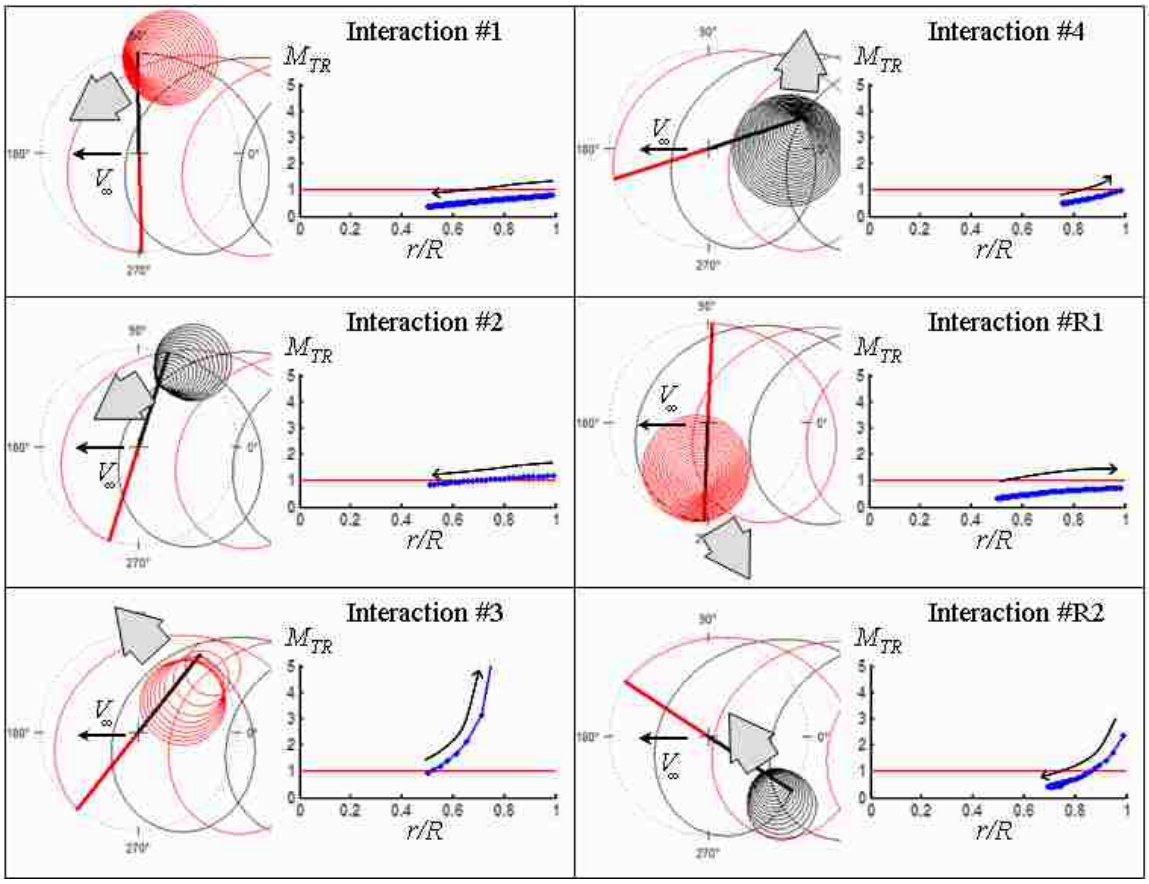

Figure 2.28. Details of interactions at μ = 0.19.

Interactions #1 and #2 on the advancing side are both oblique interactions that propagate forward and slightly towards the retreating-slide of the tip-path plane. The interaction of #1 begins at the blade tips and moves towards the root. Over the course of this interaction, the trace Mach number is always subsonic. The interaction of #2 also begins at the blade tip and moves towards the root, but the trace Mach number associated with this interaction is initially supersonic. Therefore, the initial disturbances associated with interaction #2 are likely to group together and create a strong pressure wave. Interaction #3 on the advancing side is a nearly parallel interaction that propagates forward and towards the advancing-side of the tip-path plane. The #3 interaction begins near the middle of the blade and rapidly propagates towards the tip at a supersonic trace

Mach number. As with the supersonic #2 oblique interaction, this interaction will also produce a strong grouping of focused disturbances. The final interaction on the advancing-side, #4, is oblique and radiates to the advancing-side of the aircraft. This interaction begins inboard and radiates towards the tip accelerating over the course of the maneuver.

Interaction #R1 on the retreating-side is an oblique interaction that radiates aft and towards the retreating-side of the tip-path plane. This interaction starts inboard and accelerates towards the tip, but the trace Mach number remains subsonic over the course of the interaction. The other interaction on the advancing side, #R2, is an oblique interaction that radiates forwards and to the advancing-side of the tip-path plane. The #R2 interaction is initially supersonic, but rapidly decelerates as the interaction moves inboard. It is important to point out that both retreating-side interactions occur substantially later than the advancing-side interactions and are typically more benign when compared to their advancing-side counterparts [38]. Furthermore, these interactions are all specific to a 2-bladed rotor and an advance ratio of 0.19. Under maneuvering flight, the quantity of interactions, the directivity patterns, and the trace Mach numbers will change.

2.4.2.3 Application to the Fast Pull-up Maneuver

The omni-directional modeling technique was applied to the fast pull-up maneuver using a prescribed helical wake. These synthetic time histories are compared with the actual time histories. If notable wake bundling was present during the maneuver, then the wake distortions would create a misalignment between the groupings of the omni-directional disturbances in the synthetic time histories and the acoustic time histories measured by the ground microphones. If, however, the two time histories do

align, then the wake structure must be similar to the prescribed model and wake distortions are minimal.

Comparisons between the omni-directional model and the acoustic measurements made at the microphone along the flight path are provided in Figure 2.29 and Figure 2.30. At the top of each figure is the total acoustic time history over the maneuver. This top frame also features six shaded regions corresponding to a complete rotor revolution taken at three-revolution increments. The triangle over each region labels the subsequent detailed snapshots.

The details of the shaded regions appear below the total time history. The right frame of each detail is a top view of the tip-path plane indicating the locations of the BVI intersections. The top left frame of each detail is the acoustic time history recorded by the microphone along the flight path. The bottom-left frame of each detail is the synthetic wave generated by the accumulation of the omni-directional disturbances at the same location. Each interaction is labeled in the tip-path plane overhead view and identified in the synthetic time history. Vertical guidelines are included to compare notable groupings from the omni-directional model with the acoustic time histories. For clarity, only disturbances on the outer 50% of the reference blade span are displayed. Note that because of the nature of the discretization in the omni-directional model, oblique interactions are generally captured better than parallel interactions.

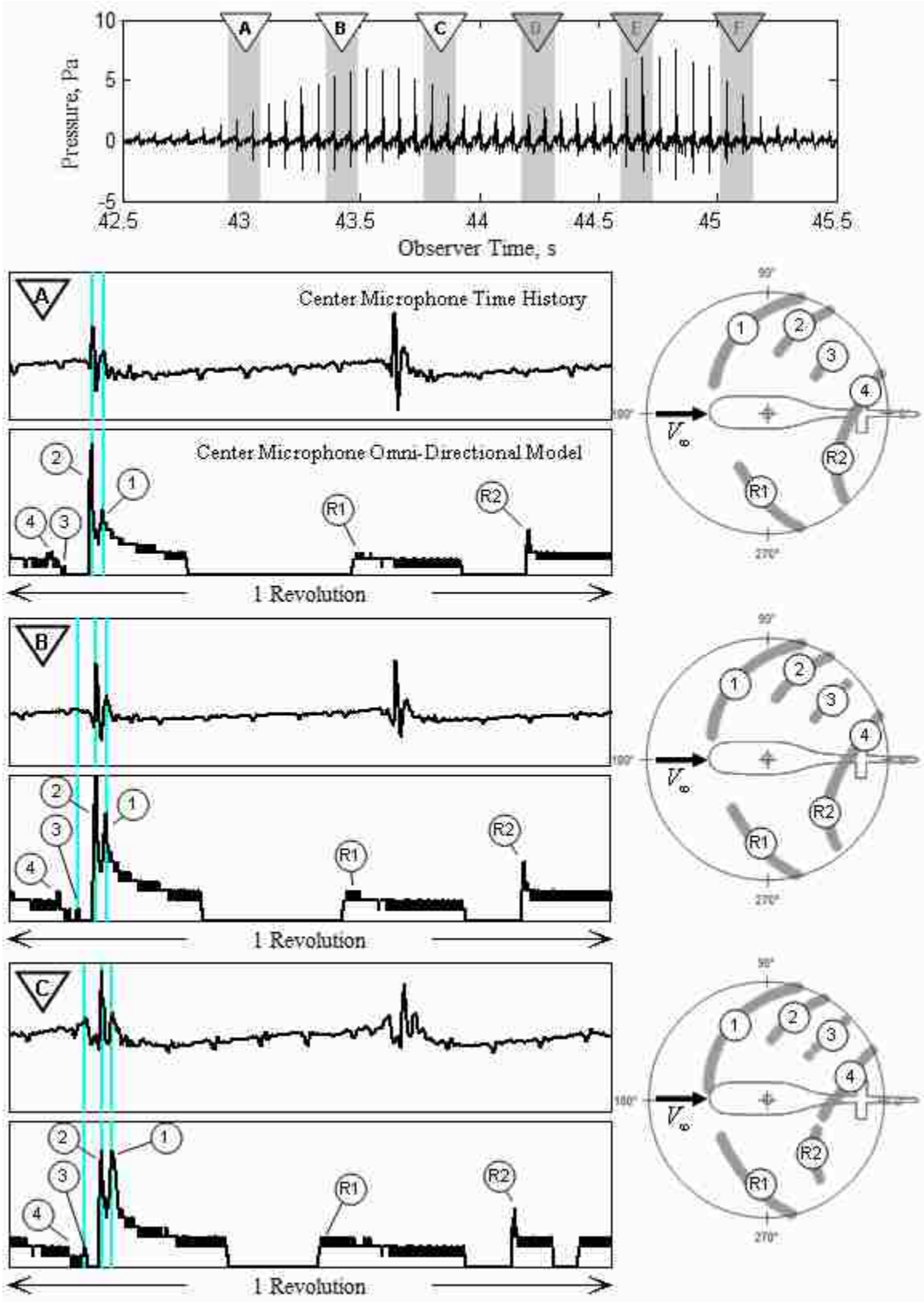

Figure 2.29. BVI details for revolutions the first half of the pull-up maneuver.

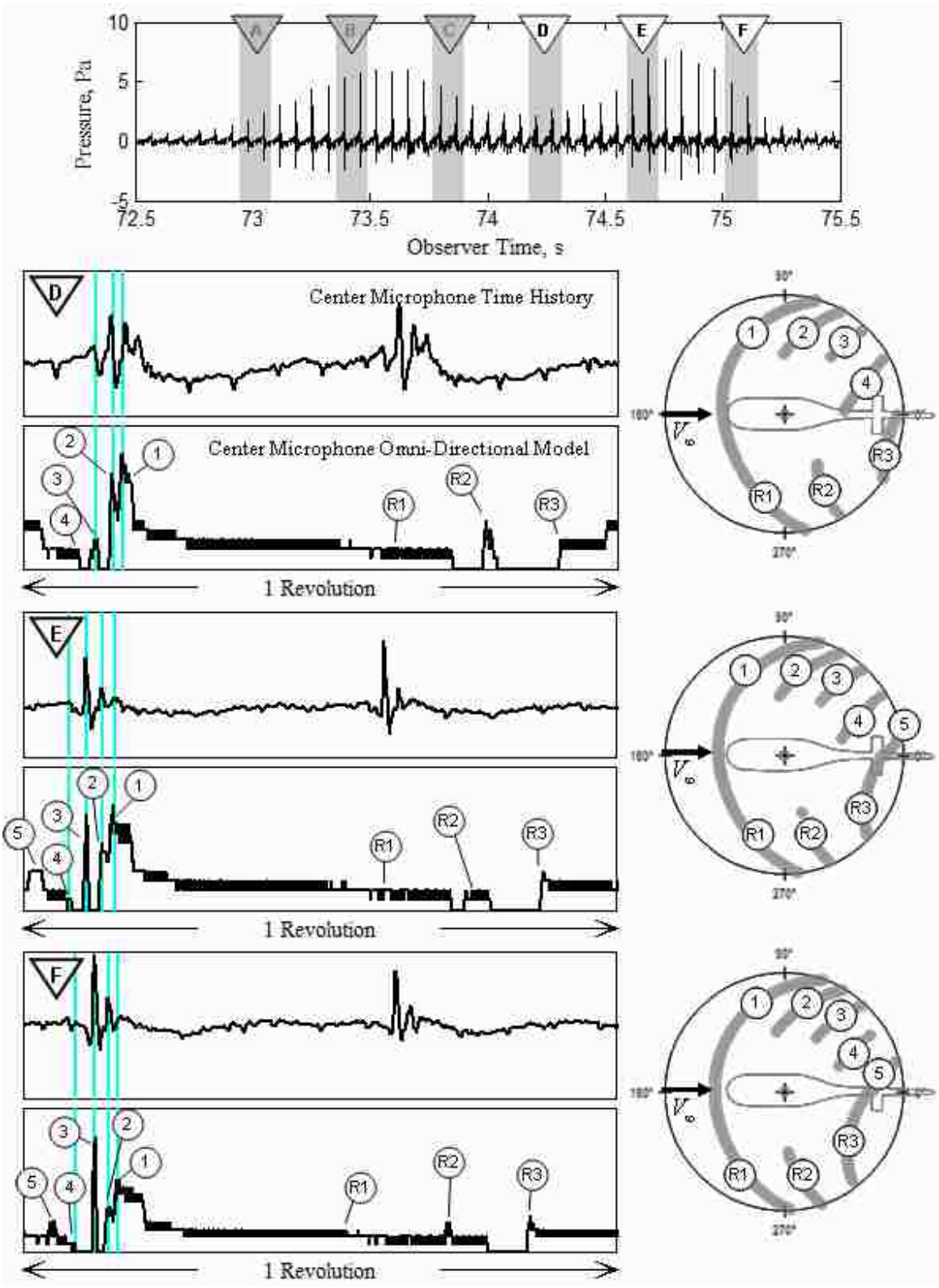

Figure 2.30. BVI details for the second half of the pull-up maneuver.

In general, the alignment of the groupings from the omni-directional model matches well with the impulsive spikes observed in the recordings from the ground microphone. The basic wake model adequately captures the transition of the #3 interaction from a parallel interaction to an oblique interaction as the helicopter decelerates, the steady weakening of the #1 and #2 interactions, and the formation of additional interactions near the aft region of the tip-path plane. All of these trends are also captured by the ground microphones. This suggests that there is no significant wake distortion during the most aggressive pull-up maneuver executed during the flight test campaign.

2.4.3 Summary

Three preliminary conclusions were drawn by dissecting the acoustic time history from the pull-up maneuvers.

1. The individual pulse shape of the impulsive noise matches very well with the impulsive noise captured during a condition known to produce large levels of BVI noise. Therefore the impulsive noise content of the near-horizon harmonic noise observed when executing the transient pure cyclic pull-up maneuvers is likely attributed to blade-vortex interactions as the wake passes through or in close proximity to the tip-path plane.

2. The groupings of an omni-directional disturbance model featuring a prescribed helical wake are coincident with the impulsive spikes present in the microphone time histories. This suggests that there was no significant wake bundling when executing even the most aggressive of the pull-up maneuvers. Furthermore, most of the acoustic energy radiated forward of the aircraft appears to be generated by oblique interactions on the advancing side of the rotor.

3. Low frequency noise is related to the attitude of the tip-path plane during the maneuver. As the tip-path plane tilts back, increased acoustic levels of low frequency loading noise are radiated towards the horizon.

Chapter 3 Governing Equations

3.1 Overview

Many helicopter acoustic prediction codes follow a procedure similar to the block diagram in Figure 3.1. A control input sequence is passed into a model that captures the dynamics and aerodynamics of the aircraft. The output of the dynamics and aerodynamics model, which typically includes the trajectory of the aircraft, the motions of the main rotor blades, and the blade loads, are then passed into an acoustic model that predicts the acoustics radiated by the helicopter.

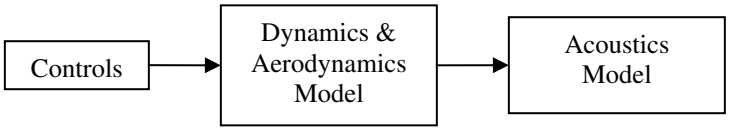

Figure 3.1. Classic flow diagram for acoustic prediction codes.

The fidelity of the dynamics and aerodynamics modeling can be tailored to meet the requirements of the modeler. For example, dynamics models may incorporate blade bending modes and aerodynamics models may incorporate free wake models for sophisticated loading calculations. Many available models couple the high fidelity dynamics and aerodynamics computations together and require advanced iterative solvers to obtain solutions.

A consequence of this approach is that the solvers tend to be extremely computationally expensive to operate while many of the details featured in the high fidelity models contribute little to the overall behavior of the aircraft in flight. As the

objective of this dissertation is to capture the general trends of the dynamics and acoustics during pull-up maneuvers, a simplified first-principles model is developed in this chapter.

Consider an alternative acoustic prediction model, outlined in Figure 3.2. A control sequence is passed into a dynamics model where the blade loads, blade flapping, and aircraft trajectory are found for longitudinal flight assuming rigid main rotor blades and uniform inflow through the tip-path plane. These data are processed using two paths to compute the radiated acoustics. The low-frequency loading path passes the low-frequency blade loads through a refinement model that makes corrections for unsteady aerodynamics. These refined low frequency blade loads and the blade geometry are lastly passed into an acoustics model responsible for calculating the low-frequency loading and the thickness noise of the helicopter. Alternatively, the high-frequency loading path passes the trajectory and flapping data into a trailed wake model that is necessary to predict high frequency blade-vortex interaction (BVI) noise. High frequency blade loads are found by integrating the induced velocity along the trailed wake using the incompressible form of the Biot-Savart law. After correcting for unsteady aerodynamics, the blade loads are passed into an acoustics model to compute the BVI noise.

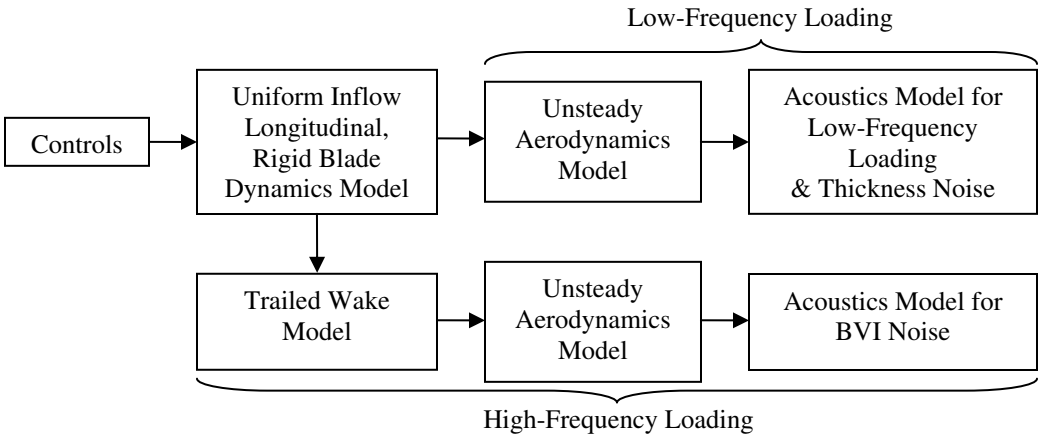

Figure 3.2. Modified block diagram for acoustic prediction code.

A major assumption in this model is that the high frequency loads from the wake used to calculate BVI noise have a negligible contribution to the motion of the aircraft and the flapping of the main rotor blades. Therefore the refined aerodynamic loads are not fed back into the dynamics model. Flight test data will later be used to validate this assumption.

The details of each block and the governing equations of the models are addressed in the following subsections.

3.2 Dynamics Model

The dynamics model handles the governing equations for the motion of the aircraft and flapping for a two-bladed teetering rotor. The inputs to the dynamics model include the collective and cyclic control positions. The outputs include the motion of the aircraft, the flapping response of the main rotor blades, and blade loads for uniform inflow. The derivation of the set of closed-form dynamics expressions is similar to the technique used by Chen to develop a simplified mathematical model for flight simulation [39], [40]. A benefit of using closed-form expressions is that they can be computed on the

fly at a relatively low computational expense; a feature ideal for real-time in-flight systems.

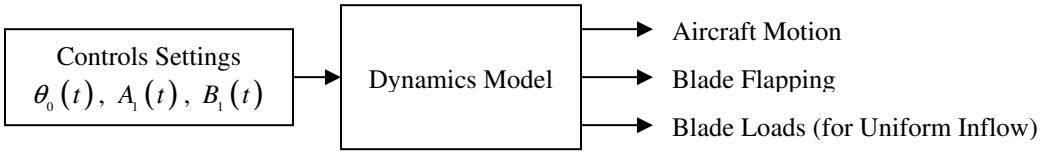

Figure 3.3. Dynamics model diagram.

3.2.1 Dynamics Model Assumptions

In order to obtain closed form expressions that govern the general low-frequency motion of the aircraft and the tip-path plane during the initial transient of the pull-up maneuvers, several simplifying assumptions are made. As a consequence of these simplifications, the governing equations are valid over a limited range of flight conditions. Fortunately, these assumptions have been shown to be valid for performance and stability calculations for advance ratios below 0.3 [41], [42]. A summary of the assumptions are listed below.

Controller Assumptions:

The Blade pitch for the Bell 206B-3 is described by a first harmonic series and the blade features a linear twist from the root to the tip:

$$\theta(t) = \theta_0 - A_1 \cos\psi - B_1(t)\sin\psi + \frac{r}{R}\theta_{TW} \tag{3.1}$$

Dynamic Modeling Assumptions:

- Longitudinal and lateral helicopter motions are assumed to be independent and only longitudinal motion is considered. Though the flight test data

does indicate that some coupling exists, these effects are weak during the initial pull-up transient where longitudinal motion dominates.

- The individual blades are rigid in bending, torsion, and lag. These simplifications are made to capture the general blade motion but are generally valid for blades where the elastic axis, center of gravity, and aerodynamic center are coincident.
- Blade flapping is assumed to follow a first harmonic series:

$$\beta(t) = a_0 - a_1(t)\cos\psi - b_1(t)\sin\psi \tag{3.2}$$

$$\dot{\beta}(t) = -\left[\dot{a}_1(t) + b_1(t)\Omega\right]\cos\psi - \left[\dot{b}_1(t) - a_1(t)\Omega\right]\sin\psi \tag{3.3}$$

$$\ddot{\beta}(t) = -\left[\ddot{a}_1 + 2\dot{b}_1(t)\Omega - a_1(t)\Omega^2\right]\cos\psi - \left[\ddot{b}_1(t) - 2\dot{a}_1(t)\Omega - b_1\Omega^2\right]\sin\psi \tag{3.4}$$

- Higher harmonic flapping terms are assumed small and are neglected.
- Main rotor RPM remains constant during the maneuver. On the Bell 206B-3 this is accomplished using a governor on the engine. It is assumed that the governor response instantaneously.

<u>Aerodynamic Modeling Assumptions</u>

- Inflow through the tip-path plane is assumed uniform. In forward flight, there is a notable longitudinal variation in the inflow, but this primarily affects the lateral blade flapping. Furthermore, the uniform inflow through the tip-path plane is calculated from momentum theory using the quasi-steady thrust and tip-path plane angle of attack. This assumption is generally valid since the aircraft motion is slow compared to the response time of the inflow.

- In accordance with blade element methods, quasi-steady aerodynamic strip theory is used to obtain the blade loads acting at the quarter chord of each blade segment.
- Reverse flow and compressibility effects are neglected. These effects have been shown to be important for blade vibration and strength calculations, but have a minor influence on stability and control characteristics.

3.2.2 Dynamics Model Governing Equations

The dynamics model can be divided into two coupled sets of equations: those that govern the motion of the aircraft body, and those that govern the motion of the rotor blades.

3.2.2.1 Fuselage Equations of Motion

An aircraft is illustrated in longitudinal flight in Figure 3.4. Two coordinate systems used to obtain the governing equations for the fuselage motion are shown in this diagram: the body coordinate system and the shaft coordinate system. The body coordinate system is fixed to the center of gravity of the aircraft, B, and is aligned such that the longitudinal body unit vector, $\hat{i}_B$, points towards the nose of the aircraft parallel to the waterline, and the vertical body unit vector, $\hat{k}_B$, points downwards normal to the waterline. The fuselage pitch attitude, θ_B, is the angle of the longitudinal body unit vector measured relative to the horizon. The body coordinate system is used to derive the body equations of motion since the products of inertia remain constant in this reference frame.

The shaft coordinate system is fixed to the center of the hub, H, and is aligned such that the unit vector $\hat{i}_S$ points towards the nose of the aircraft and lies in the hub plane and the unit vector $\hat{k}_S$ points downwards parallel to the shaft. The hub is offset from the center of gravity longitudinally by x_H and vertically by z_H, and the shaft is tilted back from the vertical body unit vector by θ_S. It is convenient to derive the rotor loads acting at the hub in the shaft coordinate system. Further details regarding these and other coordinate systems used in the model can be found in Appendix A.

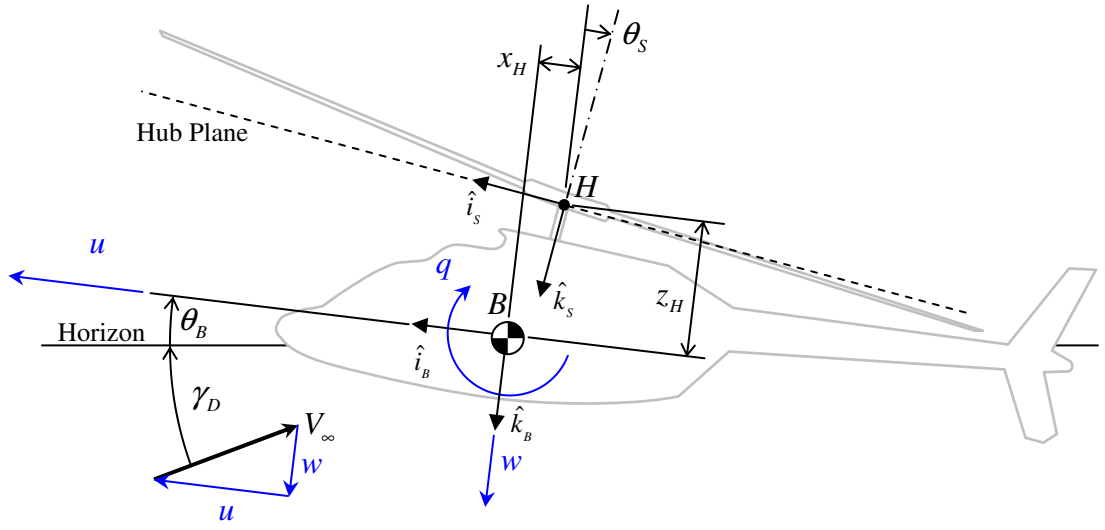

Figure 3.4. Motion diagram for a helicopter in longitudinal flight. All measurements are shown positive.

Referring to Figure 3.4, the longitudinal motion includes a longitudinal component, u, acting along $\hat{i}_B$, a vertical component, w, acting along $\hat{k}_B$, and pitch rate, q, about the center of gravity. For no-wind conditions, the free stream velocity, V_∞, is the resultant of the longitudinal and vertical velocity components. For no-wind conditions,

the descent angle, γ_D, is the angle of the horizon measured relative to the free stream velocity vector.

The free body diagram of the same aircraft in longitudinal flight is shown in Figure 3.5. In this model, the primary external loads acting on the aircraft include the weight of the aircraft, W, the drag of the fuselage, D, the aerodynamic pitching moment of the fuselage, M_y, and the rotor loads acting at the hub. Rotor loads are shown decomposed into a term normal to the hub plane, T_{HP}, and a term that lies in the hub plane, H_{HP}. The directions of the rotor loads are assumed positive when acting in the same direction as the shaft coordinate system unit vectors.

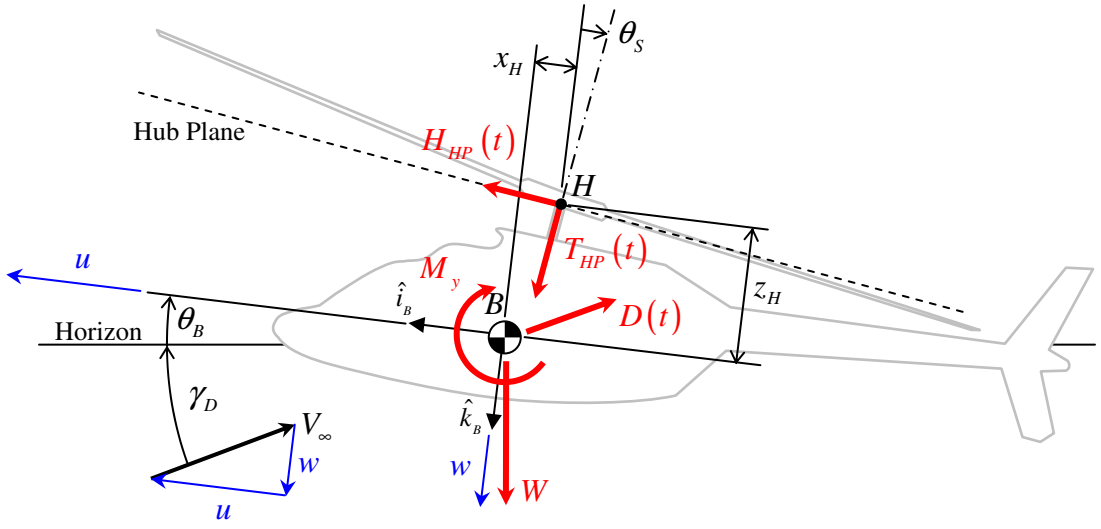

Figure 3.5. Free body diagram for longitudinal flight.

The equations of motion for the rigid fuselage symmetric about the $\hat{i}_B - \hat{k}_B$ plane for longitudinal flight, derived in Appendix B, are given below.

$$X = m(\dot{u} + qw) \tag{3.5}$$

$$Z = m\left(\dot{w} - qu\right) \tag{3.6}$$

$$M = I_{yy}\dot{q} \tag{3.7}$$

Where m is the mass of the body, and I_{yy} is the pitching moment of inertia of the body.

Referring again to Figure 3.5, X is the sum of external loads acting along body unit vector $\hat{i}_B$:

$$X = T_{HP}\sin\theta_S + H_{HP}\cos\theta_S - D\cos\left(\gamma_D + \theta_B\right) - W\sin\theta_B \tag{3.8}$$

Z is the sum of external loads acting along body unit vector $\hat{k}_B$:

$$Z = T_{HP}\cos\theta_S - H_{HP}\sin\theta_S - D\sin\left(\gamma_D + \theta_B\right) + W\cos\theta_B \tag{3.9}$$

And M is the sum of pitching moments about the center of gravity:

$$M = T_{HP}\cos\theta_S x_H - T_{HP}\sin\theta_S z_H - H_{HP}\cos\theta_S z_H - H_{HP}\sin\theta_S x_H + M_y \tag{3.10}$$

The fuselage drag, D, acts parallel to the free-stream velocity and is defined as:

$$D = \frac{1}{2}\rho V_\infty^2 f \tag{3.11}$$

Where f is the equivalent flat plate area of the fuselage.

Expressions for the rotor loads, T_{HP} and H_{HP}, are found by integrating the aerodynamic loads over the span of each rotor blade. These terms, which are derived in Appendix D, are summarized below for longitudinal flight.

$$H_{HP} = \frac{1}{2}\rho c C_{L\alpha} R\left(\Omega R\right)^2 \left\{\theta_0 A_{H_{HP}} + \theta_{TW} B_{H_{HP}} - A_1 C_{H_{HP}} - B_1 D_{H_{HP}} + E_{H_{HP}}\right\} \tag{3.12}$$

Where,

$$A_{H_{HP}} = \left(-\mu_x \lambda_{HP} - \frac{2}{3}a_1 + \frac{1}{3}\frac{\dot{b}_1}{\Omega}\right)$$

$$B_{H_{HP}} = \left(-\frac{1}{2}\mu_x \lambda_{HP} - \frac{1}{2}a_1 + \frac{1}{4}\frac{\dot{b}_1}{\Omega} \right)$$

$$C_{H_{HP}} = \left(\frac{1}{8}\mu_x \frac{q}{\Omega} + \frac{1}{3}a_0 + \frac{1}{8}\mu_x \frac{\dot{a}_1}{\Omega} \right)$$

$$D_{H_{HP}} = \left(-\frac{1}{2}\lambda_{HP} - \frac{1}{2}\mu_x a_1 + \frac{3}{8}\mu_x \frac{\dot{b}_1}{\Omega} \right)$$

$$E_{H_{HP}} = \begin{pmatrix} \frac{1}{3}\frac{q}{\Omega}a_0 + \frac{3}{2}\lambda_{HP}a_1 + \frac{1}{8}\mu_x \frac{q}{\Omega}b_1 - \frac{1}{2}\mu_x a_0^2 - \frac{1}{2}\mu_x a_1^2 + \frac{1}{3}a_0 b_1 \\ -\lambda_{HP}\frac{\dot{b}_1}{\Omega} + \frac{1}{3}\frac{\dot{a}_1 a_0}{\Omega} + \frac{1}{8}\mu_x \frac{\dot{a}_1 b_1}{\Omega} + \frac{1}{8}\mu_x \frac{\dot{b}_1 a_1}{\Omega} - \frac{C_D}{C_{L\alpha}}\mu_x \end{pmatrix}$$

$$T_{HP} = \frac{1}{2}\rho c C_{L\alpha} R(\Omega R)^2 \left\{ \theta_0 A_{T_{HP}} + \theta_{TW} B_{T_{HP}} - A_1 C_{T_{HP}} - B_1 D_{T_{HP}} + E_{T_{HP}} \right\} \qquad (3.13)$$

Where

$$A_{T_{HP}} = -\left[\frac{2}{3} + \mu_x^2 \right]$$

$$B_{T_{HP}} = -\left[\frac{1}{2} + \frac{1}{2}\mu_x^2 \right]$$

$$C_{T_{HP}} = 0$$

$$D_{T_{HP}} = -\mu_x$$

$$E_{T_{HP}} = \left(\lambda_{HP} - \frac{1}{2}\mu_x \frac{\dot{b}_1}{\Omega} \right)$$

The advance ratio term, μ_x, in the above expressions is the advance ratio relative to the hub plane:

$$\mu_x = \frac{u\cos\theta_S - w\sin\theta_S}{\Omega R} \qquad (3.14)$$

Inflow through the hub plane, λ_{HP}, is related to the inflow through the tip-path plane, λ_{TPP}, as follows:

$$\lambda_{HP} = \lambda_{TPP} - \mu_x a_1 \tag{3.15}$$

Where λ_{TPP} is found using quasi-steady momentum theory (see Appendix D).

3.2.2.2 Main Rotor Equations of Motion

The blade flapping motion is found by the equilibrium of inertial and aerodynamic moments about the flapping hinge [43]. A diagram of flapping motion for forward flight is provided in Figure 3.6. If the aerodynamic loads are assumed to act at the elastic axis, the only external force acting on the blade that contributes to the flapping motion is the sectional aerodynamic force perpendicular to the elastic axis, dF_P. If the center of gravity of the blade segment is assumed to lie on the elastic axis, the only inertial load that contributes to the flapping motion is that produced by the product of the component of the absolute acceleration perpendicular to the elastic axis, a_P, and the mass of the blade element. By using the absolute acceleration of the blade element to describe the inertial load, the pseudo forces (i.e. centrifugal and Coriolis forces) do not have to be treated as external loads.

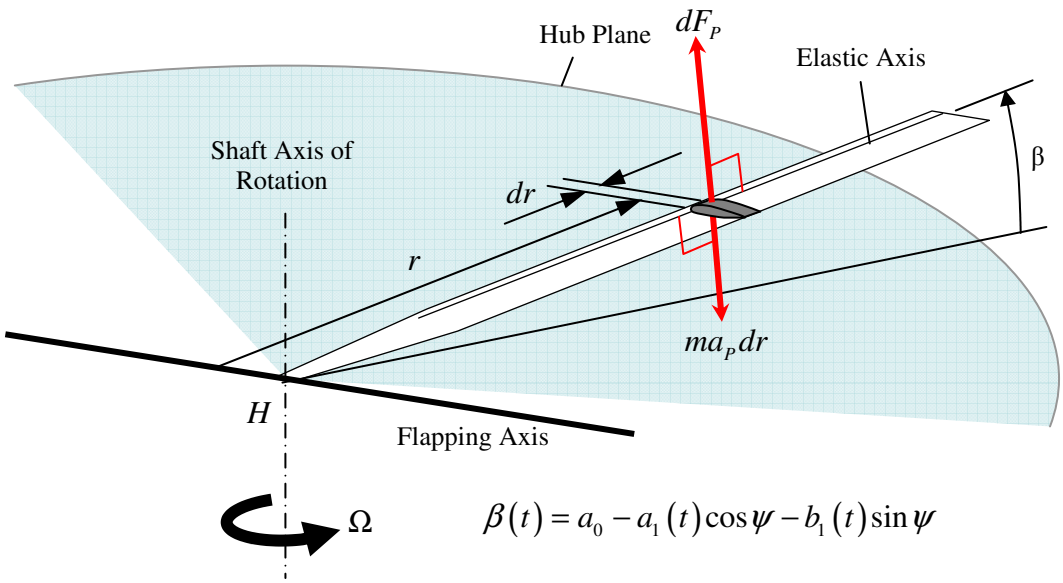

Figure 3.6. Rotor blade flapping diagram.

Integrating the elemental flapping moments along both blades and assuming flapping motion follows a first harmonic series produces a system of second order differential equations that describes the blade flapping (see Appendix F for the complete derivation).

Harmonically matching cosine terms of the second order differential equation for flapping yields:

$$\ddot{a}_1 = -\Omega\left(\frac{\gamma}{8}\dot{a}_1 + 2\dot{b}_1\right) + \Omega^2\frac{\gamma}{6}\left[\mu_x a_0 - \frac{3}{4}\left(1+\frac{1}{2}\mu_x^2\right)b_1 + \frac{3}{4}\left(1+\frac{1}{2}\mu_x^2\right)A_1\right] - \Omega\frac{\gamma}{8}q \qquad (3.16)$$

Harmonically matching the sine terms of the second order differential equation for flapping yields:

$$\ddot{b}_1 = \Omega\left(2\dot{a}_1 - \frac{\gamma}{8}\dot{b}_1\right) + 2\Omega q + \Omega^2\frac{\gamma}{8}\left[\left(1-\frac{1}{2}\mu_x^2\right)a_1 - \frac{8}{3}\mu_x\theta_0 + \left(1+\frac{3}{2}\mu_x^2\right)B_1 - 2\mu_x\theta_{TW} + 2\mu_x\lambda_{HP}\right] \qquad (3.17)$$

Where, γ, is the Lock number of the blade.

Two alternative flapping models are also considered in this dissertation that further reduces computational cost. The first approximates blade flapping as a system of first order differential equations by neglecting the acceleration of the flapping coefficients (i.e. $\ddot{a}_1 = \ddot{b}_1 = 0$). This essentially neglects the inertial moment of the blade about the hinge. In this model, the first order differential equations for main rotor flapping become:

$$\dot{a}_1 = \frac{\Omega\gamma\left[\begin{array}{l}\frac{4\gamma}{3}\mu_x a_0 - 16\left(1-\frac{1}{2}\mu_x^2\right)a_1 - \gamma\left(1+\frac{1}{2}\mu_x^2\right)b_1 + \frac{128}{3}\mu_x\theta_0 \\ +\gamma\left(1+\frac{1}{2}\mu_x^2\right)A_1 - 16\left(1+\frac{3}{2}\mu_x^2\right)B_1 + 32\mu_x\theta_{TW} - 32\mu_x\lambda_{HP}\end{array}\right]}{\gamma^2+256} - q \tag{3.18}$$

$$\dot{b}_1 = \frac{\Omega\gamma\left[\begin{array}{l}\frac{64}{3}\mu_x a_0 + \gamma\left(1-\frac{1}{2}\mu_x^2\right)a_1 - 16\left(1+\frac{1}{2}\mu_x^2\right)b_1 - \frac{8\gamma}{3}\mu_x\theta_0 \\ +16\left(1+\frac{1}{2}\mu_x^2\right)A_1 + \gamma\left(1+\frac{3}{2}\mu_x^2\right)B_1 - 2\gamma\mu_x\theta_{TW} + 2\gamma\mu_x\lambda_{HP}\end{array}\right]}{\gamma^2+256} \tag{3.19}$$

The second approximates the blade flapping as a quasi-steady system by neglecting the angular acceleration and velocity of the flapping coefficients (i.e. $\ddot{a}_1 = \ddot{b}_1 = \dot{a}_1 = \dot{b}_1 = 0$). This model essentially assumes an instantaneous balance of aerodynamic and centrifugal moments about the flapping hinge. In this model, the flapping coefficients are found to be:

$$a_1 = \frac{\frac{8}{3}\mu_x\theta_0 + 2\mu_x\theta_{TW} - \left(1+\frac{3}{2}\mu_x^2\right)B_1 - 2\mu_x\lambda_{HP} - \frac{16}{\gamma}\frac{q}{\Omega}}{\left(1-\frac{1}{2}\mu_x^2\right)} \tag{3.20}$$

$$b_1 = \frac{\frac{4}{3}\left(\mu_x a_0 + \frac{3}{4}\left(1+\frac{1}{2}\mu_x^2\right)A_1\right) - \frac{q}{\Omega}}{\left(1+\frac{1}{2}\mu_x^2\right)} \tag{3.21}$$

The dynamic response of the tip-path plane under a 1° step input in collective and longitudinal cyclic are shown in Figure 3.7 and Figure 3.8 respectively for the Bell 206B-3 traveling in level flight at $\mu = 0.20$. For reference, the responses of the reduced order model and the quasi-steady model are also provided. The longitudinal and lateral responses curves indicate the deviation of the flapping coefficients from their initial values. These plots also include reference lines for determining the settling time of the system. The settling time criteria require that the amplitudes of the oscillations be within 5% of the final quasi-steady value.

For the applied step function, the longitudinal flapping settles within 1.4 rotor revolutions; the lateral flapping settles within 2.4 revolutions. However, under both input perturbations, the overall flapping response of the tip-path plane is largely driven by the response of the longitudinal flapping coefficient. Note that both the 2nd order and 1st order flapping models reach the settled values at similar times.

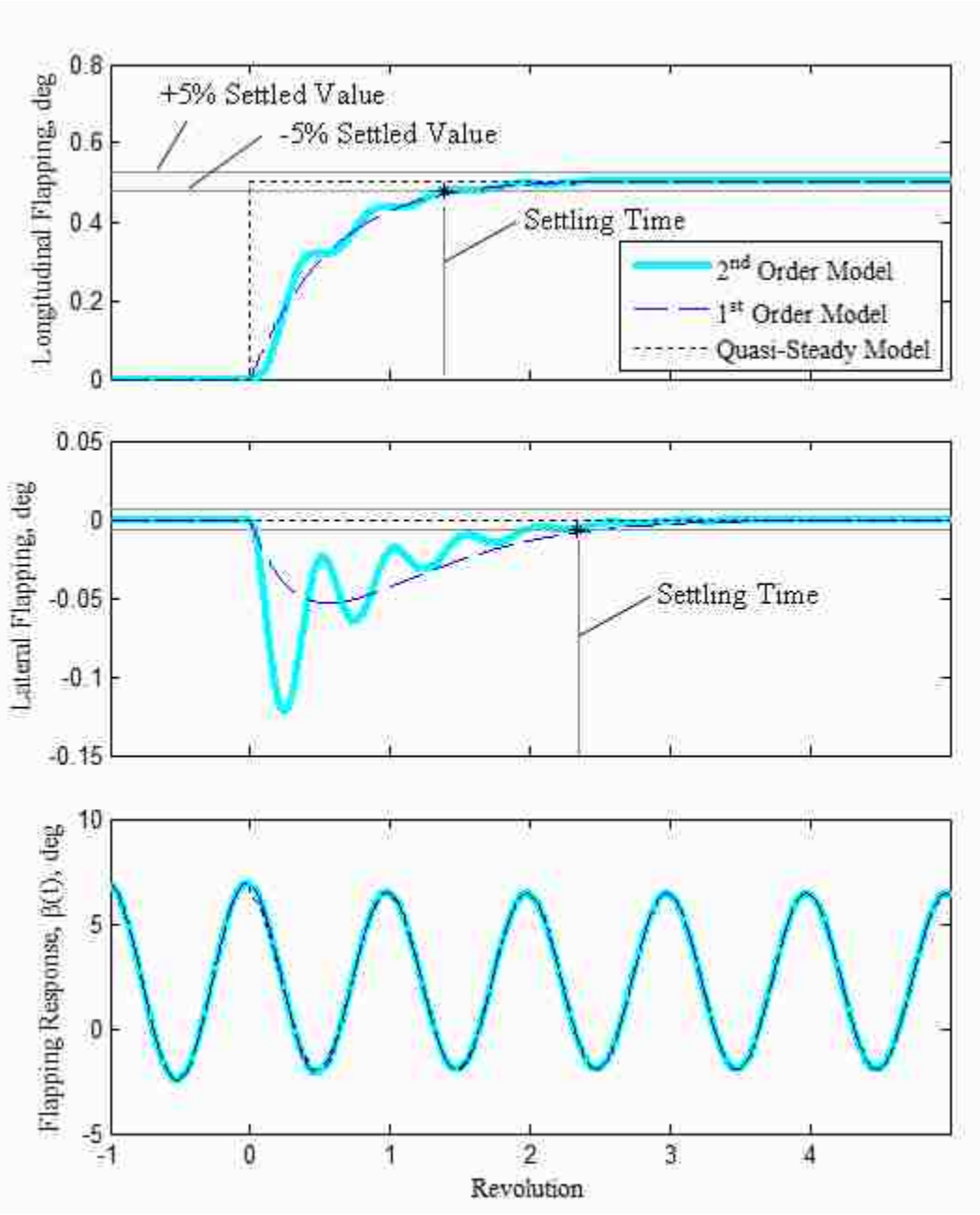

Figure 3.7. Tip-path plane dynamic response to a 1° step input in collective applied at revolution #0 (Bell 206B-3 at $\mu = 0.20$). Lateral and longitudinal flapping values are measured relative to their initial conditions.

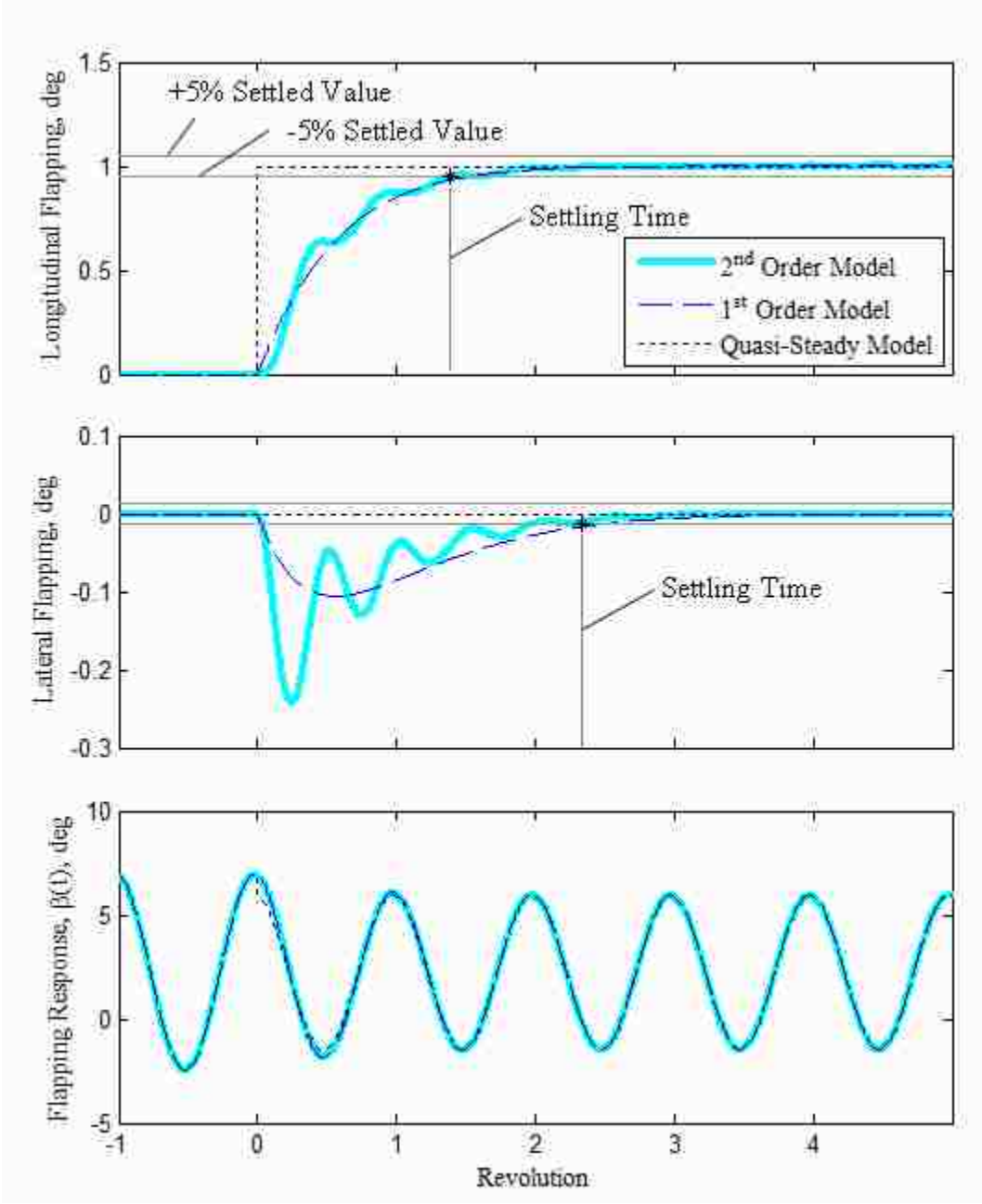

Figure 3.8. Tip-path plane dynamic response to a 1° step input in longitudinal cyclic applied at revolution #0 (Bell 206B-3 at $\mu = 0.20$). Lateral and longitudinal flapping values are measured relative to their initial conditions.

3.2.2.3 Combined Equations of Motion

Combining the body and main rotor equations of motion yields a set of 8 coupled, nonlinear differential equations for maneuvering flight typically represented in the form:

$$\dot{\vec{y}} = g\left(\vec{y}, \vec{u}, t\right) \tag{3.22}$$

Where, $\vec{y}$ is the state vector, $\vec{u}$ is the control vector, and t is time. In the derived dynamics model:

$$\begin{aligned} \vec{y} &= \left\{u, w, q, a_1, b_1, \dot{a}_1 \dot{b}_1 \theta_b\right\} \\ \vec{u} &= \left\{\theta_0, A_1, B_1\right\} \end{aligned} \tag{3.23}$$

The governing equations derived in this section for the fuselage and blade motion are summarized below.

$$\dot{u} = \frac{-W \sin\theta_B + T_{HP} \sin\theta_S + H_{HP} \cos\theta_S - D\cos\left(\gamma_D + \theta_B\right)}{m} - qw \tag{3.24}$$

$$\dot{w} = \frac{W \cos\theta_B + T_{HP} \cos\theta_S - H_{HP} \sin\theta_S - D\sin\left(\gamma_D + \theta_B\right)}{m} + qu \tag{3.25}$$

$$\dot{q} = \frac{\left(T_{HP} \cos\theta_S - H_{HP} \sin\theta_S\right) x_H - \left(T \sin\theta_S + H \cos\theta_S\right) z_H + M_y}{I_{yy}} \tag{3.26}$$

$$\dot{a}_1 = \frac{d}{dt}\left(a_1\right) \tag{3.27}$$

$$\dot{b}_1 = \frac{d}{dt}\left(b_1\right) \tag{3.28}$$

$$\ddot{a}_1 = -\Omega\left(\frac{\gamma}{8}\dot{a}_1 + 2\dot{b}_1\right) + \Omega^2 \frac{\gamma}{6}\left[\mu_x a_0 - \frac{3}{4}\left(1 + \frac{1}{2}\mu_x^2\right) b_1 + \frac{3}{4}\left(1 + \frac{1}{2}\mu_x^2\right) A_1\right] - \Omega\frac{\gamma}{8} q \tag{3.29}$$

$$\ddot{b}_1 = \Omega\left(2\dot{a}_1 - \frac{\gamma}{8}\dot{b}_1\right) + 2\Omega q$$
$$+\Omega^2\frac{\gamma}{8}\left[\left(1-\frac{1}{2}\mu_x^2\right)a_1 - \frac{8}{3}\mu_x\theta_0 + \left(1+\frac{3}{2}\mu_x^2\right)B_1 - 2\mu_x\theta_{TW} + 2\mu_x\lambda_{HP}\right] \tag{3.30}$$

$$\dot{\theta}_B = q \tag{3.31}$$

The solution to the above set is found by applying a numerical integrating method. In this dissertation, a 4th order Runge-Kutta iterative method is applied [44]. This concept is shown graphically in Figure 3.9 for a single time step.

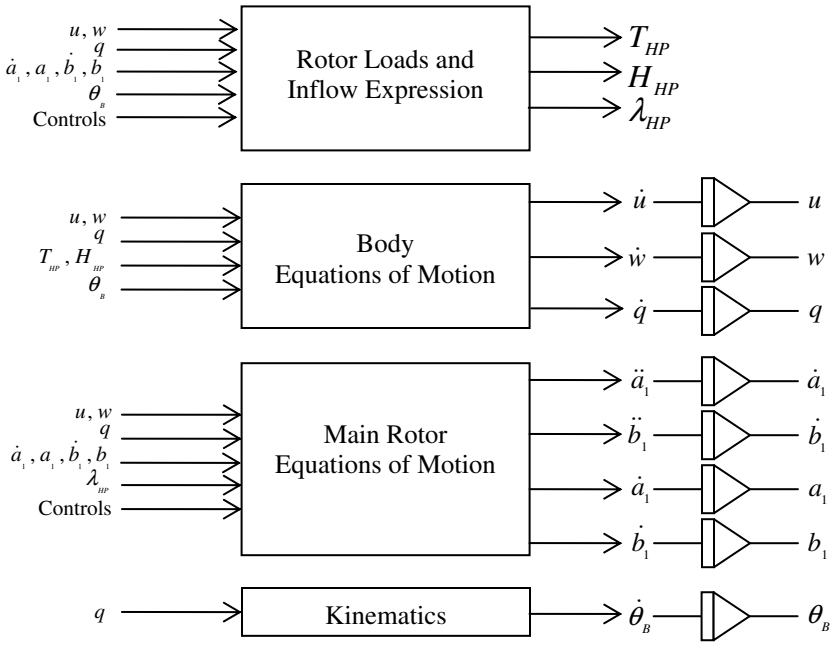

Figure 3.9. Block diagram for equations of motion and blade flapping for a single time step.

For the simplified case of flapping described by the set of first order differential equations, the governing equations for main rotor flapping become:

$$\dot{a}_1 = \frac{\Omega\gamma\left[\begin{array}{l}\frac{4\gamma}{3}\mu_x a_0 - 16\left(1-\frac{1}{2}\mu_x^2\right)a_1 - \gamma\left(1+\frac{1}{2}\mu_x^2\right)b_1 + \frac{128}{3}\mu_x\theta_0 \\ +\gamma\left(1+\frac{1}{2}\mu_x^2\right)A_1 - 16\left(1+\frac{3}{2}\mu_x^2\right)B_1 + 32\mu_x\theta_{TW} - 32\mu_x\lambda_{HP}\end{array}\right]}{\gamma^2+256} - q \tag{3.32}$$

$$\dot{b}_1 = \frac{\Omega\gamma\left[\begin{array}{l}\frac{64}{3}\mu_x a_0 + \gamma\left(1-\frac{1}{2}\mu_x^2\right)a_1 - 16\left(1+\frac{1}{2}\mu_x^2\right)b_1 - \frac{8\gamma}{3}\mu_x\theta_0 \\ +16\left(1+\frac{1}{2}\mu_x^2\right)A_1 + \gamma\left(1+\frac{3}{2}\mu_x^2\right)B_1 - 2\gamma\mu_x\theta_{TW} + 2\gamma\mu_x\lambda_{HP}\end{array}\right]}{\gamma^2+256} \tag{3.33}$$

$$\ddot{a}_1 = 0 \tag{3.34}$$

$$\ddot{b}_1 = 0 \tag{3.35}$$

For the case of flapping described by the quasi-steady model, the governing equations for main rotor flapping become:

$$\dot{a}_1 = 0 \tag{3.36}$$

$$\dot{b}_1 = 0 \tag{3.37}$$

$$\ddot{a}_1 = 0 \tag{3.38}$$

$$\ddot{b}_1 = 0 \tag{3.39}$$

And the quasi-steady flapping coefficients are calculated directly:

$$a_1 = \frac{\frac{8}{3}\mu_x\theta_0 + 2\mu_x\theta_{TW} - \left(1+\frac{3}{2}\mu_x^2\right)B_1 - 2\mu_x\lambda_{HP} - \frac{16}{\gamma}\frac{q}{\Omega}}{\left(1-\frac{1}{2}\mu_x^2\right)} \tag{3.40}$$

$$b_1 = \frac{\frac{4}{3}\left(\mu_x a_0 + \frac{3}{4}\left(1+\frac{1}{2}\mu_x^2\right)A_1\right) - \frac{q}{\Omega}}{\left(1+\frac{1}{2}\mu_x^2\right)} \tag{3.41}$$

3.3 High Frequency Aerodynamic Loading Model

In the derivation of the dynamics model, several simplifying assumptions were made regarding the aerodynamic environment of the blades and the wake structure. The first major assumption was that the inflow induced by the wake through the rotor was uniform. The second major assumption incorporated quasi-steady two-dimensional strip theory and ignored the effects of unsteady aerodynamics. In reality, the wake structure is more complicated and a better representation of it is required for adequate prediction of BVI noise.

For a main rotor in forward flight, the vortex wake structure is a combination of two sources: the trailed wake and the shed wake (see Figure 3.10). The trailed wake, results from the spanwise distribution of lift (and therefore spanwise distribution of circulation) over the rotor blade. These trailed vortices tend to form perpendicular to the elastic axis [36]. The overall induced inflow is largely related to the trailed wake.

For rotor blades, the lift and bound circulation tend to be concentrated at the blade tips resulting in very strong trailed vortices on the outboard portion of the blade. These outboard vortices quickly roll up to produce a trailed tip vortex of circulation equal to the maximum bound circulation on the blade and are the dominant feature of the rotor wake [43]. A similar vortex circulating in the opposite direction is also generated at the root, but because the bound circulation gradient is smaller on the inboard section of the blade, the root vortex tends to be weaker and more diffuse than the tip vortex [43]

The shed wake results from temporal variations of the spanwise distribution of lift. From Kelvin's Theory of Circulation, any change in circulation results in the shedding of a counteracting vortex [45]. This vortex tends to form parallel to the elastic axis. Shed

wake elements closest to the blade tend to delay the effects of changes in the induced velocity on the rotor blade. Therefore the shed wake is important for unsteady aerodynamics.

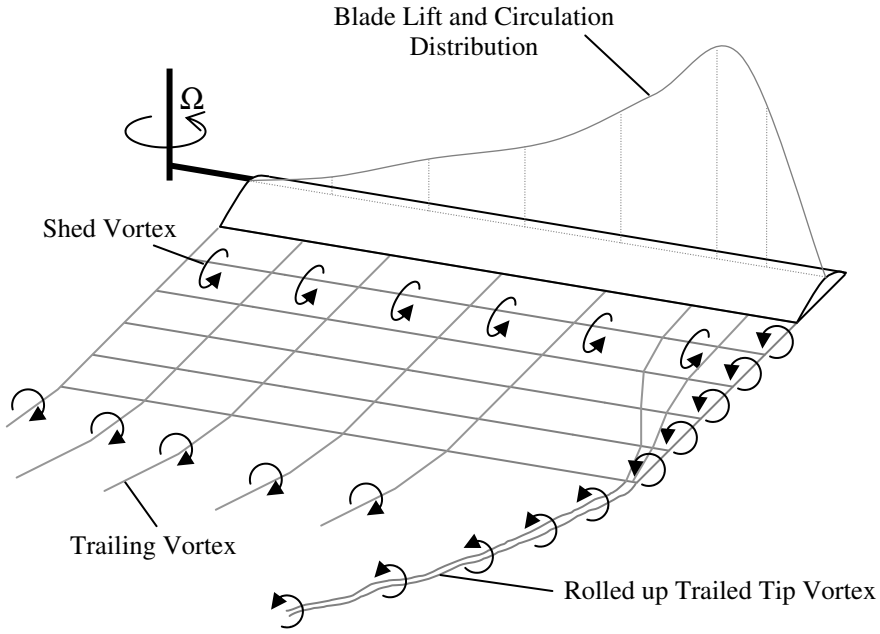

Figure 3.10. Wake vortex structure.

This section discusses the implementation of the wake model and the computation of refined aerodynamic loads.

3.3.1 High Frequency Aerodynamics Model Assumptions

The following assumptions made within the high-frequency aerodynamics models are summarized below.

- Aircraft motion and blade flapping is governed by low frequency dynamic and aerodynamic loading. Contributions from the high frequency aerodynamics model are assumed negligible and are not fed back into the dynamics model.

- The trailed wake vortex filaments are rolled up and released from the tip. The strength of the vortex filament is equal in magnitude to the maximum bound circulation found from the blade loads predicted in the dynamics model. The weaker inboard vortices are ignored.
- The vortex filaments are approximated as straight lines. This approximation is made to simplify integration of the Biot-Savart equation along the wake, but is generally valid for small filaments with low curvature.
- The vortex is a Vatistas model with a fixed core radius and does not change over time.
- Motion of the tip vortex nodes with respect to the tip-path plane is prescribed by an inflow model and the motion of the tip-path plane.

3.3.2 Trailed Wake Model

The addition of the trailed wake is used to obtain more accurate high frequency blade loadings for the computation of BVI noise. This is accomplished by incorporating a prescribed wake and integrating the Biot-Savart law along the wake to compute the induced velocity at a blade station. It is assumed that the trailed wake vortices are instantaneously bundled at the tip of the blade. The wake itself is modeled as a series of straight-line filaments released from the tip of each blade (see Figure 3.11). All of the outboard trailed vortices are rolled up at the tip.

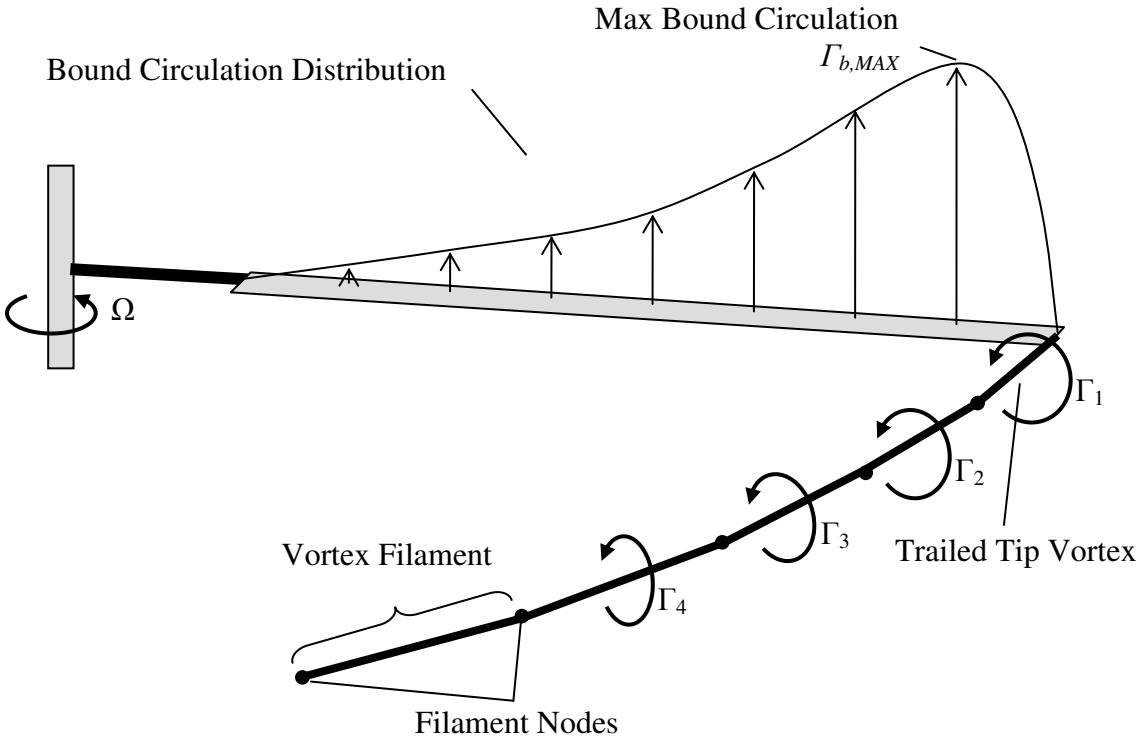

Figure 3.11. Trailed wake structure.

3.3.2.1 Trailed Wake Strength

The strength of the vortex filament rolled up and released from each blade is assumed to be equal in magnitude to the maximum bound circulation strength of the blade. This assumption is generally valid for lightly uniformly twisted blades like those featured on the Bell 206B-3. The Kutta-Joukowski theorem provides a link between the bound circulation, Γ_b, and the lift [46]:

$$\Gamma_b = \frac{1}{2} V_\infty c C_l \tag{3.42}$$

Using the general loading expression from the dynamics model, the location of the maximum circulation can be calculated by taking the first derivative of the circulation

expression with respect to span location and equating the result to zero. After expansion, the non-dimensional span location of maximum bound circulation is found to be:

$$x_{\Gamma_{max}} = \frac{-\theta_0 - \left(\frac{q}{\Omega} - A_1 + \theta_{TW}\mu_y + b_1 + \frac{\dot{a}_1}{\Omega}\right)\cos\psi - \left(\frac{p\cos\theta_s}{\Omega} - B_1 + \theta_{TW}\mu_x - a_1 + \frac{\dot{b}_1}{\Omega}\right)\sin\psi}{2\theta_{TW}} \quad (3.43)$$

This radial station is substituted into the low-frequency loading expression to obtain the magnitude of the maximum bound circulation on each blade.

3.3.2.2 Trailed Wake Motion

The geometry of the trailed wake filaments is updated based on the motion of the tip-path plane and a prescribed Beddoes inflow model. Consider Figure 3.12. Under no-wind conditions, the velocity of a vortex node, V, relative to the tip-path plane is:

$$\overrightarrow{V_{V/H}} = \Omega R\overrightarrow{\lambda_{i,TPP}} - \overrightarrow{V_{B/I}} - \overrightarrow{\omega^{B/I}} \times \overrightarrow{r_{H/B}} - \left(\overrightarrow{\omega^{B/I}} + \overrightarrow{\omega^{T/S}}\right) \times \overrightarrow{r_{V/H}} \quad (3.44)$$

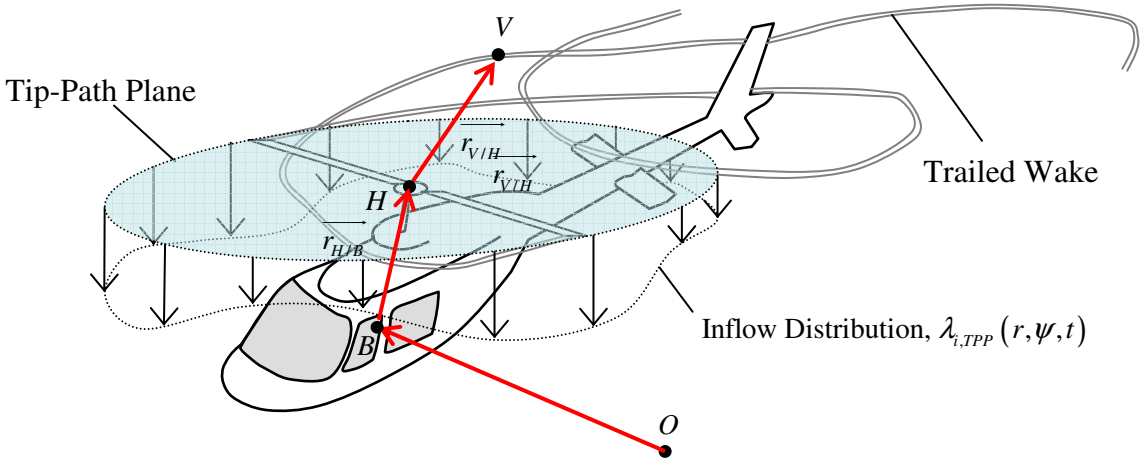

Figure 3.12. Wake geometry.

Where $\overrightarrow{\lambda_{i,TPP}}$ is the inflow through the tip-path plane – which may be a function of radial location, azimuth location, and time, $\overrightarrow{V_{B/I}}$ is the absolute velocity of the body, $\overrightarrow{r_{H/B}}$ is the position vector from the center of gravity, B, to the hub, H, $\overrightarrow{r_{V/H}}$ is the

position vector from the hub to a vortex filament node in the trailed wake, $\overrightarrow{\omega^{B/I}}$ is the absolute angular velocity vector of the fuselage, and $\overrightarrow{\omega^{T/S}}$ is the angular velocity vector of the tip-path plane relative to the shaft.

The nodes of each wake filament convect through the medium by a prescribed inflow distribution. In this dissertation, the Beddoes' inflow distribution is used which has been shown to agree well with both experimental results and the free vortex wake model [36].

$$\lambda_{i,TPP} = \begin{cases} \lambda_{i0,TPP}\left(1 + E\frac{x_{TPP}}{R} - E\left|\left(\frac{y_{TPP}}{R}\right)^3\right|\right) & \text{under the rotor disk} \\ 2\lambda_{i0,TPP}\left(1 - E\left|\left(\frac{y_{TPP}}{R}\right)^3\right|\right) & \text{outside the rotor disk} \end{cases} \tag{3.45}$$

Where $\lambda_{i0,TPP}$ is the rotor induced inflow from momentum theory for forward flight, x_{TPP} is the $\hat{i}_T$ coordinate of the node in the tip-path plane, y_{TPP} is the $\hat{j}_T$ coordinate of the node in the tip-path plane, and E is the Beddoes suggested empirical value equal to half of the wake skew angle [36].

The location of each wake node relative to the tip-path plane is updated by numerically integrating the relative velocity of the vortex node relative to the tip-path plane over the time step (see Figure 3.13).

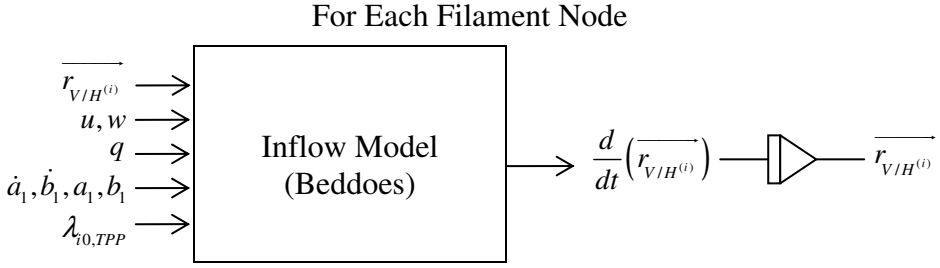

Figure 3.13. Wake geometry update block diagram.

With the wake geometry and strength known, the induced velocity at each blade segment is found by integrating the induced velocity from each of the individual vortex filaments. The induced velocity from each filament is calculated using the incompressible Biot-Savart law integrated along a straight segment (see Figure 3.14):

$$\overrightarrow{V_{ind}} = \frac{\Gamma_v}{4\pi r_p}\left(\cos\theta_1 - \cos\theta_2\right)\hat{e} \tag{3.46}$$

Where

$$r_p = \frac{\left|\vec{r_1} \times \vec{r_2}\right|}{\left|\vec{r_0}\right|}$$

$$\cos\theta_1 = \frac{\vec{r_0} \bullet \vec{r_1}}{\left|\vec{r_0}\right|\left|\vec{r_1}\right|}$$

$$\cos\theta_2 = \frac{\vec{r_0} \bullet \vec{r_2}}{\left|\vec{r_0}\right|\left|\vec{r_2}\right|}$$

$$\hat{e} = \frac{\vec{r_1} \times \vec{r_2}}{\left|\vec{r_1} \times \vec{r_2}\right|}$$

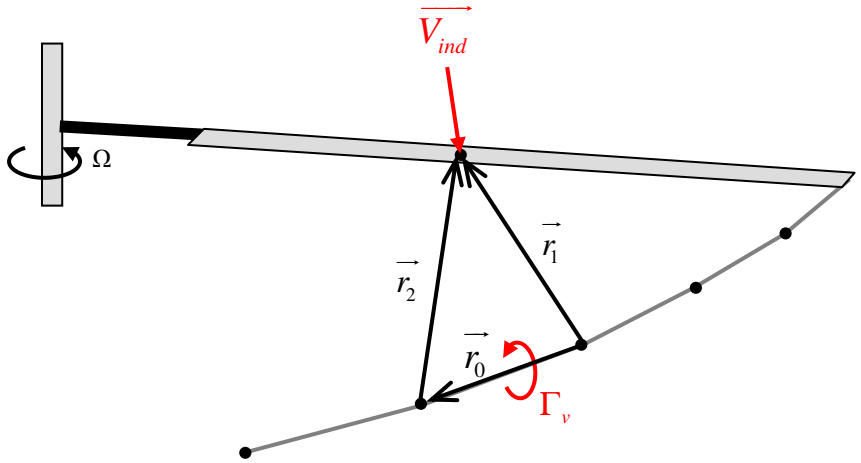

Figure 3.14. Induced velocity from a straight-line vortex at a point on the blade.

The total induced velocity at a point on the blade is found by summing the induced velocity from all of the filaments for all of the blades.

In this vortex model, a singularity occurs as the blade approaches the vortex filament. To prevent this numerical anomaly, the Vatistas model featuring a finite core size, r_c, is introduced:

$$\overrightarrow{V_{ind}} = \frac{\Gamma_v}{4\pi} \frac{r_p}{\left(r_c^{2n} + r_p^{2n}\right)^{1/n}} \left(\cos\theta_1 - \cos\theta_2\right) \hat{e} \tag{3.47}$$

This form of the Biot-Savart law is a general form to accommodate a variety of vortex models. In the case of $n = 1$, the model reduces to the Scully vortex model. The Rankine vortex model is obtained as $n \to \infty$. In this dissertation, the Bagai-Leishman model is used where $n = 2$. This model has been shown to agree well with experimental measurements [36].

From here, the geometric angle of attack is found by replacing the uniform induced velocity with the integrated induced velocity from the trailed wake.

3.3.3 Unsteady Aerodynamics

As with the trailed wake, direct incorporation of the shed wake to account for unsteady aerodynamics is possible at the added cost of additional computations of the Biot-Savart law. Fortunately, unsteady aerodynamic effects can also be captured through the Leishman-Beddoes 2D incompressible indicial aerodynamics model. This indicial model is then used to calculate the effective angle of attack using the one-step recursive approximation to the Duhamel's integral:

$$X(s) = X(s-\Delta s)e^{-b_1\Delta s} + A_1\Delta\alpha_s \tag{3.48}$$

$$Y(s) = Y(s-\Delta s)e^{-b_2\Delta s} + A_2\Delta\alpha_s \tag{3.49}$$

$$\alpha_e(s) = \alpha(s) - X(s) - Y(s) \tag{3.50}$$

Where s is the reduced time:

$$s = \frac{2}{c}\int_0^t V dt \tag{3.51}$$

The empirical constants used in the preceding equations are the same values as used by Leishman in reference [36]. Two dimensional airfoil strip theory with the effective angle of attack is used to compute the updated unsteady sectional blade loads.

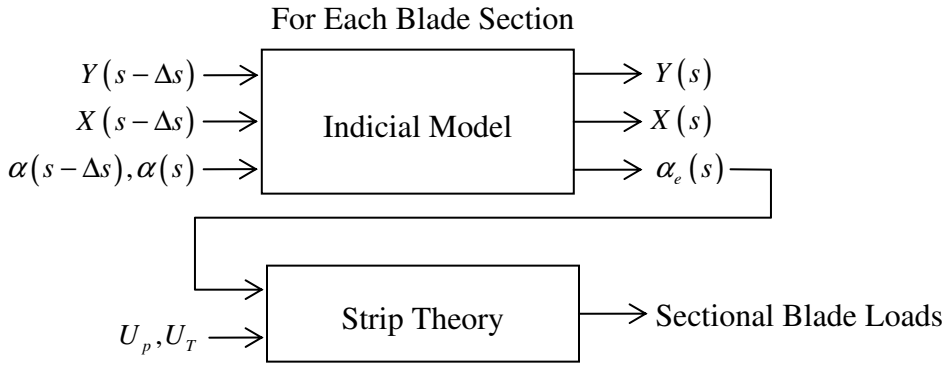

Figure 3.15. Unsteady aerodynamics block diagram.

3.3.4 Quasi-Steady Wake Model

By far the greatest computational expense is the repeated calculation of the Biot-Savart law when finding the induced velocity at the blades from the trailed wake. Because the motion of the helicopter and the tip-path plane is arbitrary during maneuvering flight, the induced velocity of all of the trailed vortex filaments must be calculated at each time step.

One possible means of expediting these calculations would be to replace the time-integrated wake position model with a quasi-steady model based on a snapshot of the advance ratio, inflow through the tip path plane, and orientation of the tip-path plane. The wake positions reduce to a set of closed-form expressions that relate the position of the filament nodes as a function of wake age. Assuming a Beddoes inflow distribution, the wake positions as a function of wake age are:

$$x_T = R\cos\left(\psi_b - \psi_w\right) + R\mu\psi_w \tag{3.52}$$

$$y_T = R\sin\left(\psi_b - \psi_w\right) \tag{3.53}$$

$$z_T = -R\mu_z\psi_w - \begin{cases} R\lambda_{0i,TPP}\left(1 + E\left(\cos\left(\psi_b - \psi_w\right) + 0.5\mu\psi_w - \left|\left(\frac{y_{TPP}}{R}\right)^3\right|\right)\right) & x_{TPP} < -R\cos\left(\psi_b - \psi_w\right) \\ 2R\lambda_{0i,TPP}\left(1 - E\left|\left(\frac{y_{TPP}}{R}\right)^3\right|\right)\psi_w & \cos\left(\psi_b - \psi_w\right) > 0 \\ 2\lambda_{0i,TPP}x_{TPP}\dfrac{\left(1 - E\left|\left(\frac{y_{TPP}}{R}\right)^3\right|\right)}{\mu} & \text{otherwise} \end{cases} \tag{3.54}$$

Where ψ_b is the blade azimuth angle and ψ_w is the wake age.

Using such a model, it is possible to use a look-up table that stores the induced velocity over the rotor disk as a function of position, inflow, advance ratio, and angle of

attack of the tip-path plane. This is the same technique used for the Quasi-Static Acoustic Mapping method. In the following chapter, the quasi-steady wake model will be compared to the time integrated model to investigate the impact on the prediction of the aeroacoustics.

3.4 Acoustics Model

As mentioned in Chapter 1, the Ffowcs Williams-Hawking (FW-H) equation is one of the most commonly used methods to describe noise generated by surfaces in arbitrary motion. The FW-H equation is composed of three source terms: monopole, dipole, and quadrupole.

$$4\pi p'(x,t) = \begin{aligned} &\frac{\partial}{\partial t}\int_S \left[\frac{\rho_0 v_n}{r|1-M_r|}\right]_\tau dS(\eta) && \text{(monopole)} \\ &-\frac{\partial}{\partial x_i}\int_S \left[\frac{P_{ij}n_j}{r|1-M_r|}\right]_\tau dS(\eta) && \text{(dipole)} \\ &+\frac{\partial^2}{\partial x_i \partial x_j}\int_S \left[\frac{T_{ij}}{r|1-M_r|}\right]_\tau dS(\eta) && \text{(quadrupole)} \end{aligned} \tag{3.55}$$

The monopole term models the thickness noise of the rotor blade by treating the blade as a set of mass sources and sinks that displaces the medium. Blade geometry governs the distribution of the monopoles. The dipole term models the aerodynamic forces of the blade on the medium. Aerodynamic loads found using the refined aerodynamic model govern the dipoles. The quadrupole term models the aerodynamic stresses produced in the flow field around the blade. Aerodynamic stresses are important when modeling complex noise sources like high-speed impulsive noise [47]. Since the tested aircraft did not exhibit HSI during the flight test, only the monopole and dipole terms are featured in the acoustic model.

From the Farassat Formulation 1A form of the FW-H equation [48]:

$$4\pi p'(x,t) = \int \left[\underbrace{\frac{\rho_0 \frac{\partial (v_n)}{\partial \tau}}{r(1-M_r)^2} + \frac{\rho_0 v_n \left(\hat{r} \bullet \frac{\partial \vec{M}}{\partial \tau} \right)}{r(1-M_r)^3}}_{\text{Far Field Term}} + \underbrace{\frac{\rho_0 c v_n \left(M_r - M^2 \right)}{r^2 (1-M_r)^3}}_{\text{Near Field Term}} \right]_\tau dS \quad \text{(monopole)}$$
$$\int \left[\underbrace{\frac{\frac{\partial p}{\partial \tau}\cos\theta}{cr(1-M_r)^2} + \frac{\hat{r} \bullet \frac{\partial \vec{M}}{\partial \tau} p \cos\theta}{cr(1-M_r)^3}}_{\text{Far Field Term}} + \underbrace{\frac{p\left(\cos\theta - \vec{M} \bullet \hat{n}\right)}{r^2(1-M_r)^2} + \frac{\left(M_r - M^2\right) p \cos\theta}{r^2 (1-M_r)^3}}_{\text{Near Field Term}} \right]_\tau dS \quad \text{(dipole)} \tag{3.56}$$

Where p' is the acoustic pressure, ρ_0 is the density of the undisturbed medium, $\hat{n}$ is a vector normal to the blade surface, v_n is the local normal velocity of the blade surface, r is the distance from the source to the observer, $\hat{r}$ is the unit vector from the source to the observer, $\vec{M}$ is the Mach number vector of the source, M is the magnitude of the Mach number vector, M_r is the Mach number of the source projected in the radiation direction, c is the speed of sound, p is the local pressure at the surface found from the aerodynamics model, θ is the local angle between the surface normal vector and the radiation direction, and dS is the elemental surface area. The τ outside each bracket is to indicate that the values are computed at the time of emission.

3.4.1 Implementation Notes for the Acoustics Model

In implementing Farassat's Formulation 1A solution to the FW-H equation, two special considerations are addressed in this acoustics model. These include the compact chord loading assumption and the treatment of reflections for tower microphones.

As mentioned in the aerodynamics loading model, strip theory is used to compute the aerodynamic loads at each blade segment. These loads are then applied at the quarter chord. This "compact chord" assumption tends to over predict far field acoustics because

the loading distribution is localized to a single point on the blade segment. To illustrate the impact of this assumption, consider a case with a hovering helicopter interacting with a single prescribed vortex on the advancing side. The prescribed vortex is aligned such that it is coincident with the elastic axis with the blade at the 90° azimuth station.

Two cases are investigated in this example. The first assumes that the entire load for the blade segment is compact and is placed at the quarter chord. The second converts the segment load to a chordwise differential pressure on the mean chord using a flat plate model [49]. This distribution is specified as:

$$\Delta C_P = \frac{2C_l}{\pi}\sqrt{\frac{1-x}{x}} \tag{3.57}$$

Where ΔC_P is the differential pressure acting on the airfoil, C_l is the local lift coefficient, and x is the non-dimensional distance from the leading edge.

A comparison of the two loading models is presented in Figure 3.16 for an observer 30° below the tip-path plane using the high frequency aerodynamic loading model. In the compact chord model, the entire load for an airfoil segment is localized at a single point. Therefore all of the acoustic sources for that segment are bundled together and are received simultaneously by the observer resulting in higher predicted acoustic pressure levels. In the non-compact chord model, the phasing of the distributed sources results in a slight reduction of the amplitude of the wave. Furthermore, the specified loading distribution for the airfoil places the majority of the aerodynamic load near the leading edge. This results in a phasing difference between the two models where the loading noise from the non-compact chord distribution is received earlier.

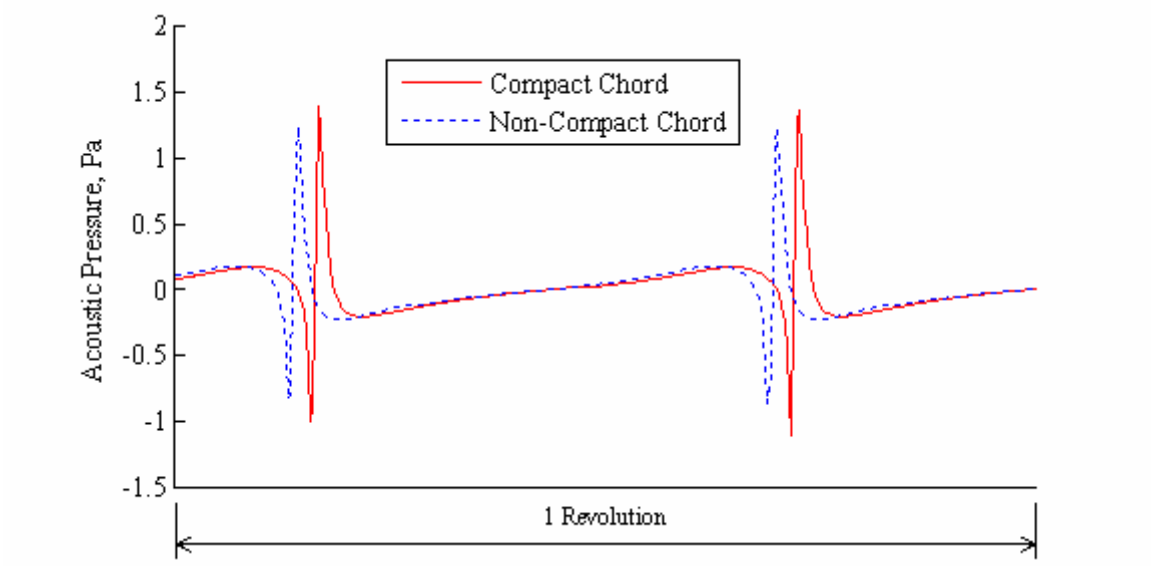

Figure 3.16. Comparison of compact and non-compact chord loadings.

The second issue addressed in the acoustic model deals with ground reflections. During the Gilroy flight test, the microphones were attached to 4' towers. As a result, source noise emitted from the aircraft was received by two paths illustrated in Figure 3.17. The direct path is represented as the solid line; the reflected path is represented as the broken line. The reflected path impacts the ground ahead of the microphone at some incidence angle θ_i and is reflected at the same incidence angle towards the microphone. The value of the incidence angle depends on the height of the microphone and the relative position of the microphone to the aircraft. Since the reflected path is longer, the reflected signal will be received by the observer later in time. In this model, the reflection is treated as an ideal specular reflection and all frequency content are reflected by the ground.

Figure 3.17. Diagram of acoustic reflection.

The effect of the reflection on the low frequency loading noise for a complete revolution is shown in Figure 3.18. The observer is positioned 30° below the tip-path plane and 4’ above the ground. Direct loading noise is plotted as a blue solid line, reflected loading noise is plotted as a blue broken line, and the total loading noise is plotted as a solid green line. The delay from the reflected signal is apparent in the phase delay between the direct and reflected signals. However, the low frequency nature of the wave causes the direct and reflected waves to combine together producing a wave nearly twice the amplitude of the direct signal.

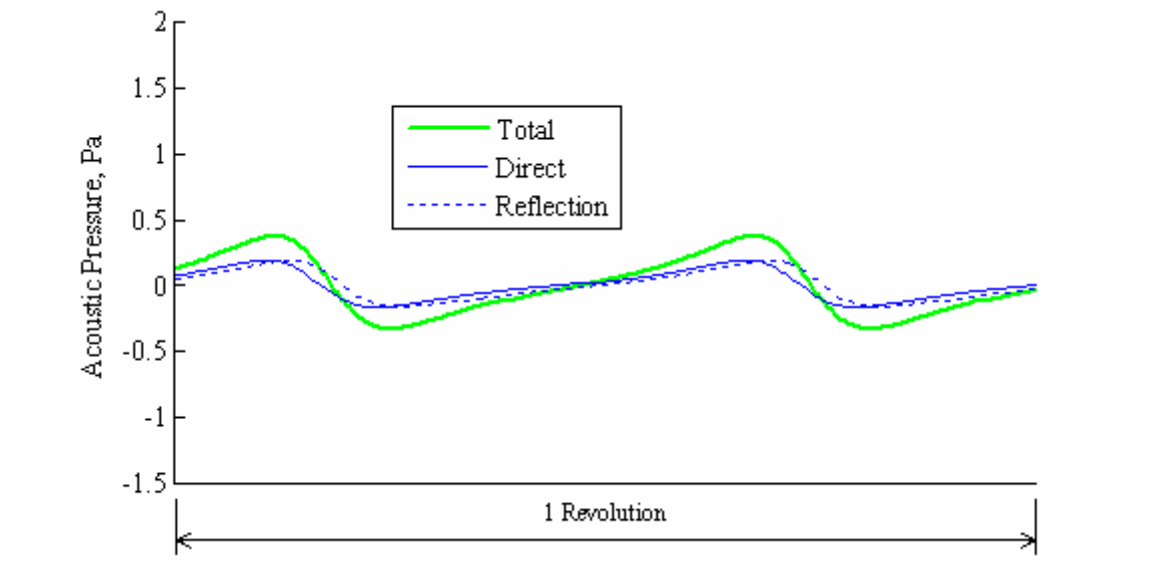

Figure 3.18. Specular reflection for the loading noise produced under the low frequency loading model.

The effect of the reflection on the high frequency loading noise for a complete revolution is shown in Figure 3.19. As in the case study for the compact chord analysis, a single prescribed vortex is placed in the tip-path plane such that it is coincident with the blade elastic axis at the 90° azimuth station. Since the vortex interaction is largely impulsive, the effects of the reflection are noticeably different. Even though the phase delay between the direct and reflected signals is identical to the low frequency case above, the impulsive nature of the signal results in the reflected signal appearing as a second vortex interaction. In the case of a single BVI, the reflected wave does not interact with the direct pulse. However, in cases with multiple BVI, the reflected signal could interact with other impulsive noise and alter the high frequency noise prediction.

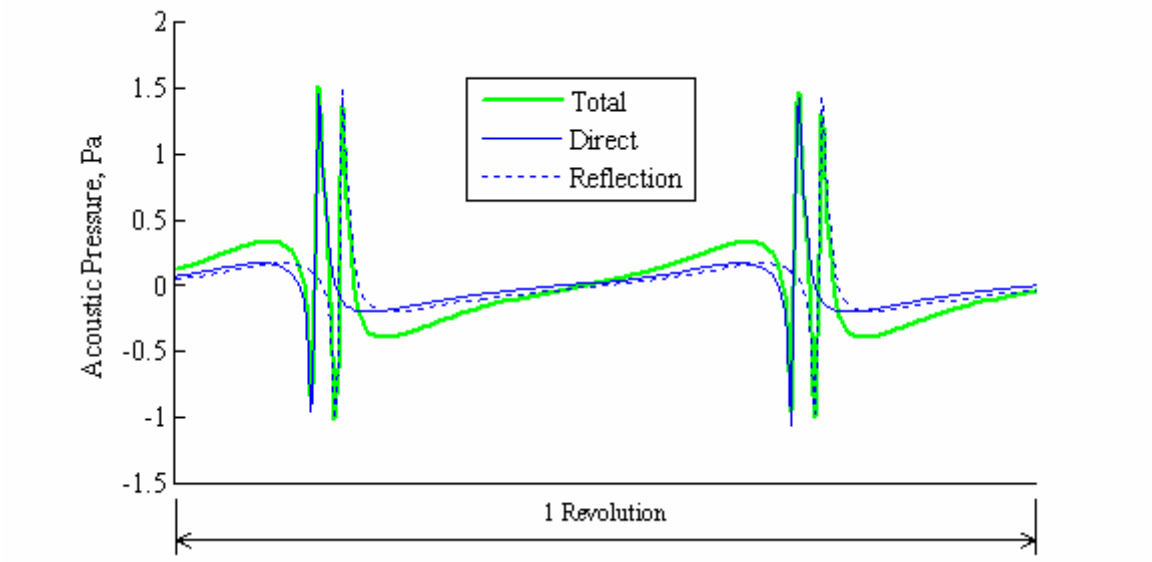

Figure 3.19. Specular reflection for the loading noise produced under the high frequency loading model.

3.5 Trim Model

During the pull-up maneuvers flown at Gilroy, the pilot first entered a steady flight corridor. This steady flight condition was maintained for several hundred feet before the pull-up maneuver was executed. To obtain the initial control settings during this steady flight corridor, a trim model is developed based on the previously described dynamics model.

Consider the free body diagram for an aircraft operating in trimmed flight as shown in Figure 3.20.

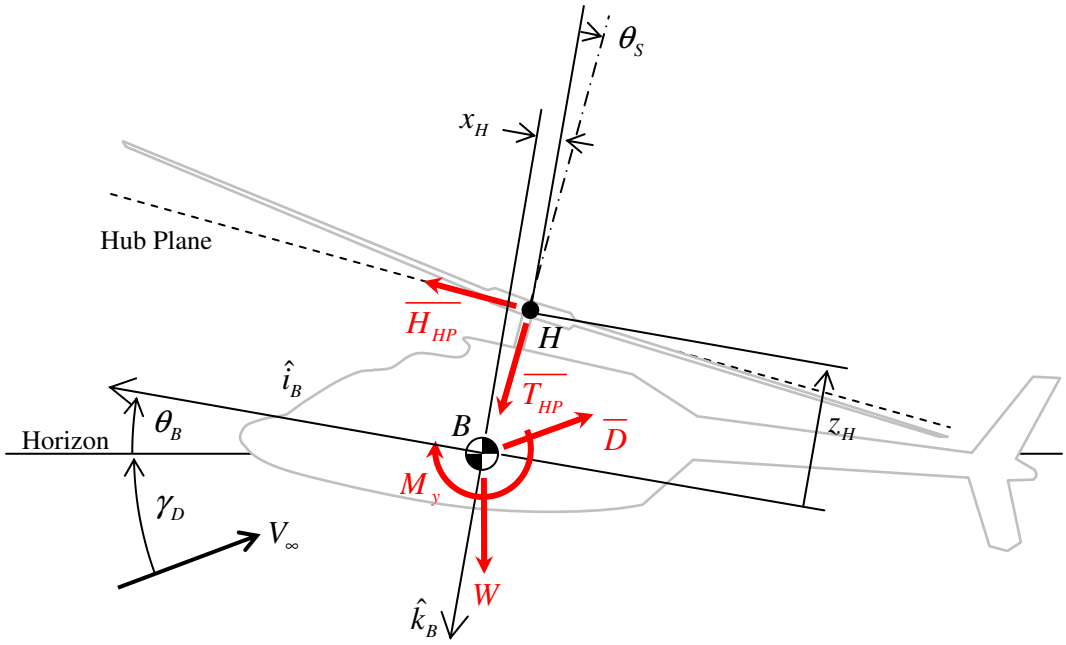

Figure 3.20. Free body diagram for trimmed flight.

The external loads have been replaced with the trimmed values that are averaged over one rotor revolution:

$$\overline{T_{HP}} = \frac{1}{2\pi}\int_0^{2\pi} T_{HP}(t)\,d\psi \tag{3.58}$$

$$\overline{H_{HP}} = \frac{1}{2\pi}\int_0^{2\pi} H_{HP}(t)\,d\psi \tag{3.59}$$

$$\overline{D} = \frac{1}{2\pi}\int_0^{2\pi} D(t)\,d\psi \tag{3.60}$$

Where the bars indicate the time-averaged value over one main rotor revolution.

From the free body diagram, the required fuselage pitch attitude and rotor loads are found by simultaneously solving the three force balance equations for θ_B, $\overline{T_{HP}}$, and $\overline{H_{HP}}$:

$$\left[\overline{D}\sin\left(\gamma_D+\theta_B\right)-W\cos\theta_B\right]x_H-\left[\overline{D}\cos\left(\gamma_D+\theta_B\right)+W\sin\theta_B\right]z_H+M_X=0 \tag{3.61}$$

$$\overline{T_{HP}}=\overline{D}\sin\left(\gamma_D+\theta_B+\theta_S\right)-W\cos\left(\theta_B+\theta_S\right) \tag{3.62}$$

$$\overline{H_{HP}}=\overline{D}\cos\left(\gamma_D+\theta_B+\theta_S\right)+W\sin\left(\theta_B+\theta_S\right) \tag{3.63}$$

Once the pitch attitude and required rotor loads for trim are known, the trim collective, $\overline{\theta_0}$, trim longitudinal cyclic, $\overline{B_1}$, and trim flapping coefficients, $\overline{a_1}$ and $\overline{b_1}$ are found by simultaneously solving the rotor load and flapping equations for steady flight.

$$\overline{T_{HP}}=\frac{1}{2}\rho cC_{L\alpha}R\left(\Omega R\right)^2\left[-\left(\frac{2}{3}+\mu_x^2\right)\overline{\theta_0}-\frac{1}{2}\left(1+\mu_x^2\right)\theta_{TW}+\mu_x\overline{B_1}+\lambda_{HP}\right] \tag{3.64}$$

$$\overline{H_{HP}}=\frac{1}{2}\rho cC_{L\alpha}R\left(\Omega R\right)^2\left[\begin{array}{l}-\left(\mu_x\lambda_{HP}+\frac{2}{3}\overline{a_1}\right)\overline{\theta_0}-\frac{1}{2}\left(\mu_x\lambda_{HP}+\overline{a_1}\right)\theta_{TW}+\frac{1}{2}\left(\lambda_{HP}+\mu_x\overline{a_1}\right)\overline{B_1}\\+\frac{3}{2}\lambda_{HP}\overline{a_1}-\frac{1}{2}\mu_x a_0^2-\frac{1}{2}\mu_x\overline{a_1^2}+\frac{1}{3}a_0\overline{b_1}-\frac{C_D}{C_{L\alpha}}\mu_x\end{array}\right] \tag{3.65}$$

$$\overline{a_1}=\frac{\frac{8}{3}\mu_x\theta_0+2\mu_x\theta_{TW}-\left(1+\frac{3}{2}\mu_x^2\right)B_1-2\mu_x\lambda_{HP}}{\left(1-\frac{1}{2}\mu_x^2\right)} \tag{3.66}$$

$$\overline{b_1}=\frac{\frac{4}{3}\mu_x a_0}{\left(1+\frac{1}{2}\mu_x^2\right)} \tag{3.67}$$

The trim solutions are shown for the Bell 206B-3 for level flight as a function of advance ratio (Figure 3.21) and as a function of flight path angle for an advance ratio of $\mu=0.20$ (Figure 3.22). In all cases, it is assumed that the lateral cyclic is 0° and the aircraft motion is purely longitudinal.

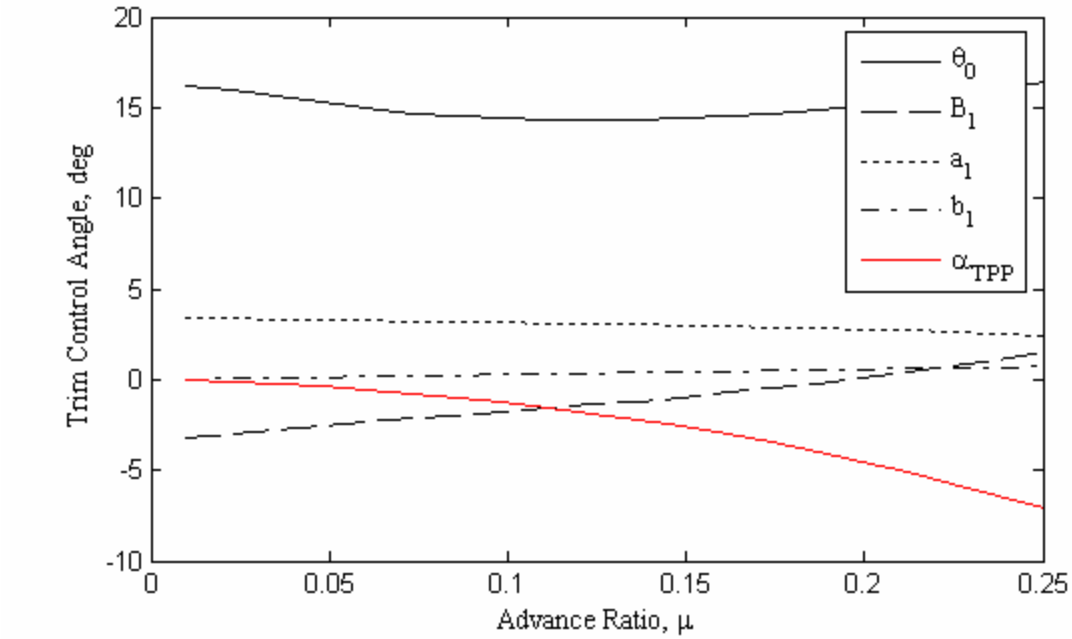

Figure 3.21. Trim control angles for level flight versus advance ratio.

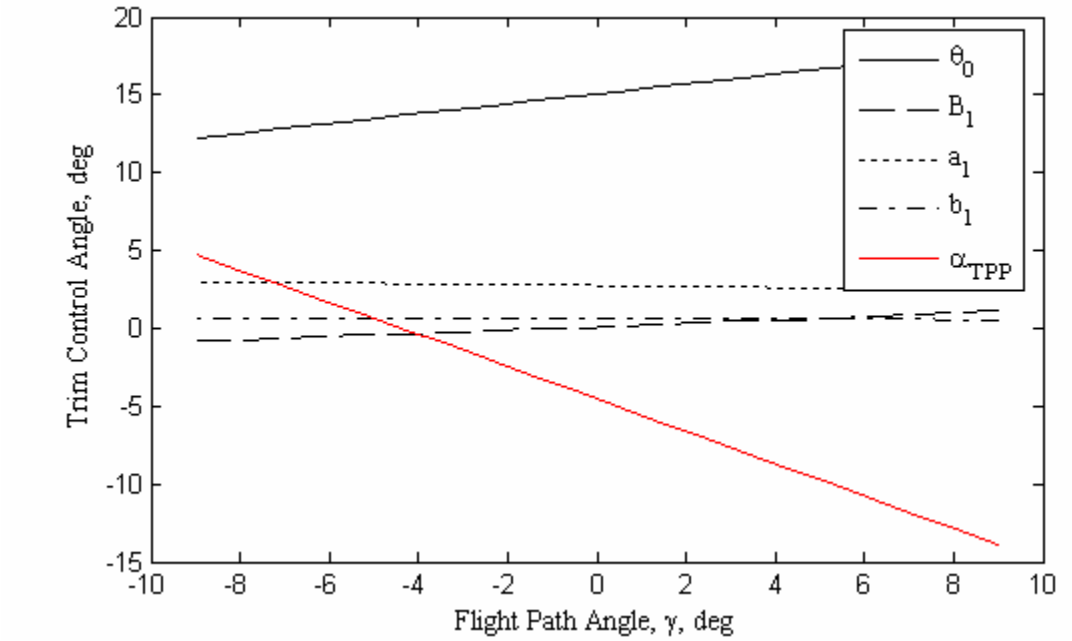

Figure 3.22. Trim control angles versus flight path angle (μ=0.2).

3.6 Summary

This chapter developed the governing equations for a first-principles dynamics, aerodynamics, and acoustics model for longitudinal flight given a prescribed set of collective and longitudinal cyclic controls. For comparing the Gilroy flight test data, these controls are set so that the response of the aircraft matches the measurements made during the flight test. However, arbitrary control inputs can be fed into the dynamics model to investigate the impact of executing alternative longitudinal maneuvers.

Once a solution to the dynamics model is found, a more advanced wake model is applied to obtain high frequency blade loading. This model incorporates a prescribed wake and uses the incompressible form of the Biot-Savart law to find the induced velocity at the blade. Unsteady aerodynamics are also included to account for the effect of the shed wake on the local aerodynamics at the blade sections.

Lastly, the blade loads and geometry are fed into an acoustics model that solves the Ffowcs-Williams Hawkings equation to predict the acoustic time histories in the far-field.

Chapter 4 Comparison with Flight Test Data

4.1 Overview

This chapter compares the predictions of the first-principles model with the in-flight measurements and ground microphone recordings taken during the Gilroy flight test. All maneuvers were flown in the early morning with low ambient winds. Wind speeds did not exceed 3 knots on the ground.

The first set of comparisons will be made for a series of steady descents. Ground microphone recordings from the three ground stations will be presented alongside the predicted acoustics. The objective of the steady descent study is to verify that the model captures general trends for the radiated acoustics.

The second set of comparisons will be made for the transient pull-up maneuvers. Measurements from the in-flight data recording system will be used to verify the predictions of the dynamics model. Measurements from the ground microphones will be used to verify the acoustics model.

Lastly, the effects of the reduced order and quasi-steady models will be studied. These include the reduced order flapping models and a quasi-steady wake positioning model. This study will be used to validate the use of quasi-steady approximations for transient pull-up maneuvers.

4.2 Steady Flight

Before applying the model derived in Chapter 3 to study the transient pull-up maneuvers, it is important to compare the model with a set of steady conditions. For this

purpose, the model predictions will be compared to a set of steady descents that were flown as part of the 2007 Gilroy flight test.

During the steady descents, the pilot, with the aid of the heads up display of the NASA PPDG system, maintained a constant flight path angle, γ_D, and airspeed. These trajectories were designed so that the pilot flew perpendicular to the microphone array at a trajectory that coincided with a point 130 m above the center microphone (see Figure 4.1).

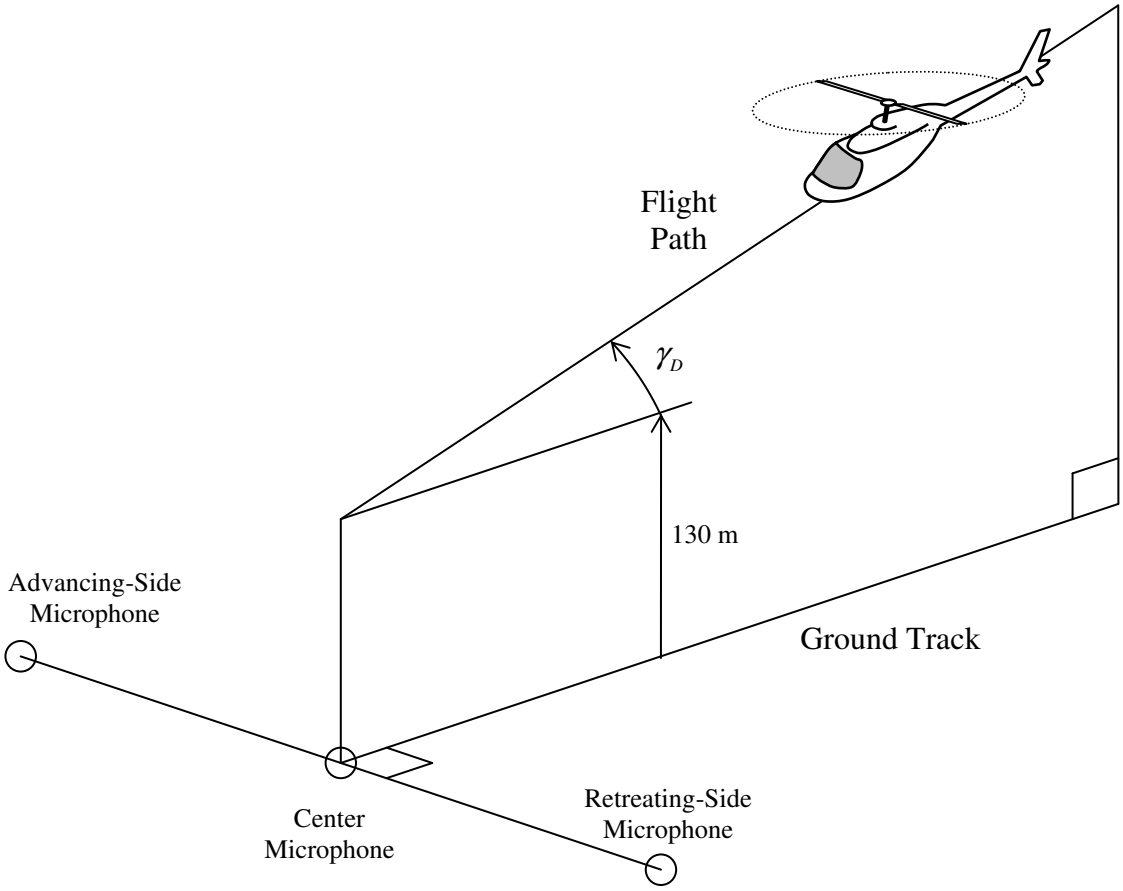

Figure 4.1. Steady descent flight trajectory.

The run log summary for the steady descents is presented in Table 4.1. Ground wind speeds measured at the ground were less than 3 knots during the steady descent maneuvers. Overall the pilot achieved a flight trajectory fairly close to the objective.

Table 4.1. Steady descent test cases.

UMD Run	Time of Day	Target		Actual	
		Airspeed	Descent Angle	Airspeed	Descent Angle
UMD329	6:16	60.0 kts	3.0 deg	62.9 kts	2.8 deg
UMD330	6:21	60.0 kts	4.5 deg	62.5 kts	4.6 deg
UMD331	6:26	60.0 kts	6.0 deg	63.1 kts	5.8 deg
UMD332	6:31	60.0 kts	7.5 deg	63.4 kts	7.0 deg
UMD336	7:38	60.0 kts	9.0 deg	64.8 kts	9.3 deg

The traces of the three ground microphones over a sphere surrounding the aircraft are illustrated in Figure 4.2. The center of the sphere is assumed coincident with the hub and the acoustics are measured in the far field. The concentric circles in the plot indicate the elevation of the microphone relative to the tip-path plane with -90° directly beneath the tip-path plane of the rotor; the radial arms in the plot indicate the bearing of the microphone relative to the tip-path plane with 180° directly ahead of the aircraft.

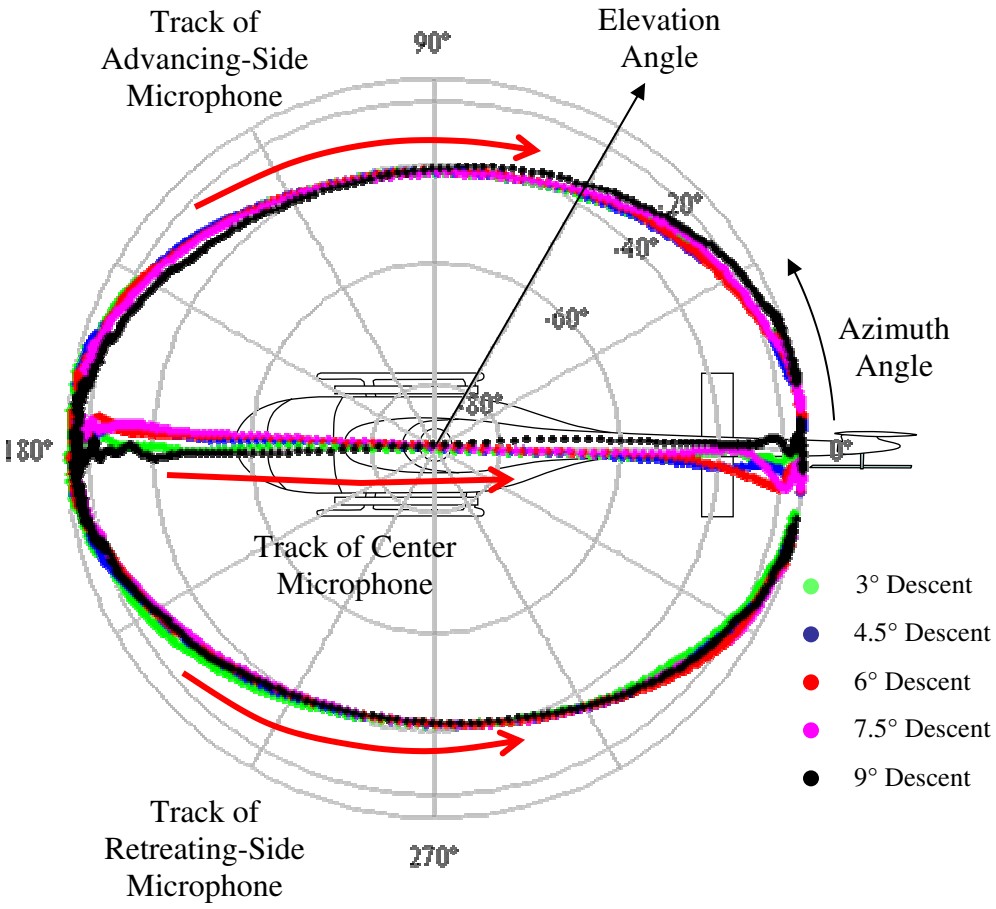

Figure 4.2. Trace of ground microphones relative to the tip-path plane for the steady descent maneuvers.

Figure 4.2 illustrates that in all of the descent maneuvers, the tracks of the microphones relative to the tip-path plane followed similar paths. This ensures that the directivity characteristics captured by the microphones should also be similar for all of the test cases.

Based on these tracks, the location of acoustic "hotspots" for each microphone can be found by referring to acoustic spheres generated for the Bell 206B-3 from previous flight tests. These regions are a result of the directivity of the various acoustic

sources; in particular BVI noise. A summary of the target microphone positions and that achieved during the steady descent is provided in Table 4.2. The acoustics captured by the microphones at these locations are compared to the theoretical signals in the following subsections.

Table 4.2.Acoustic hotspots.

Run	Microphone Azimuth*	Microphone Elevation*	Distance
Advancing-Side Microphone			
Target	**140.0 deg**	**-30.0 deg**	**280.0 m**
UMD329	139.8 deg	-30.0 deg	269.9 m
UMD330	140.2 deg	-29.2 deg	290.8 m
UMD331	139.7 deg	-30.5 deg	285.8 m
UMD332	140.1 deg	-30.6 deg	299.0 m
UMD336	140.4 deg	-33.9 deg	271.8 m
Center Microphone			
Target	**180.0 deg**	**-30.0 deg**	**300.0 m**
UMD329	179.5 deg	-29.9 deg	272.7 m
UMD330	176.1 deg	-29.9 deg	287.2 m
UMD331	176.3 deg	-29.9 deg	298.6 m
UMD332	175.9 deg	-29.9 deg	315.7 m
UMD336	180.8 deg	-30.0 deg	334.0 m
Retreating-Side Microphone			
Target	**230.0 deg**	**-35.0 deg**	**235.0 m**
UMD329	230.5 deg	-34.5 deg	237.5 m
UMD330	229.3 deg	-35.8 deg	235.5 m
UMD331	230.2 deg	-36.7 deg	233.6 m
UMD332	230.4 deg	-37.7 deg	233.7 m
UMD336	230.5 deg	-36.9 deg	246.6 m

*Relative to the Tip-Path Plane

A topographical diagram indicating all of the possible BVI interactions for the Bell 206B-3 traveling at 60 knots is shown in Figure 4.3. These locations were identified using the techniques developed in Chapter 2. Note that under these conditions, there are four possible interactions on the advancing side (#1, #2, #3, and #4) and there are three possible interactions on the retreating side (#R1, #R2, and #R3).

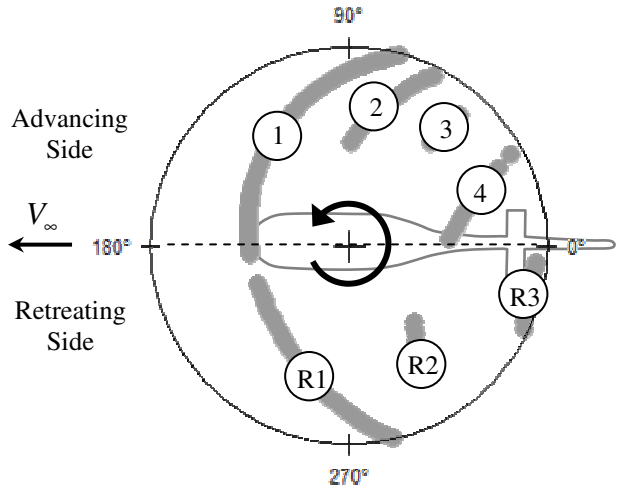

Figure 4.3. BVI Interaction Locations for a 2 bladed rotor at 60 knots (μ = 0.15)

Directivity plots of each of the possible interactions are predicted using the omni-directional disturbance model. Interactions #1, #2, and #4 on the advancing side are all oblique interactions. Interactions #1 and #2 begin at the blade tips and move inboard and tend to radiate forward and slightly towards the retreating side of the aircraft. Interaction #4 begins inboard on the blade and moves towards the tip and tends to radiate aft towards the advancing-side. Interaction #3 is a nearly parallel interaction that radiates forward and towards the advancing-side of the aircraft. Interactions #R1, #R2, and #R3 on the retreating side are all oblique interactions. Interaction #R1 propagates aft and to the retreating-side of the aircraft. Interactions #R2 and #R3 radiate slightly forward and towards the advancing-side of the aircraft.

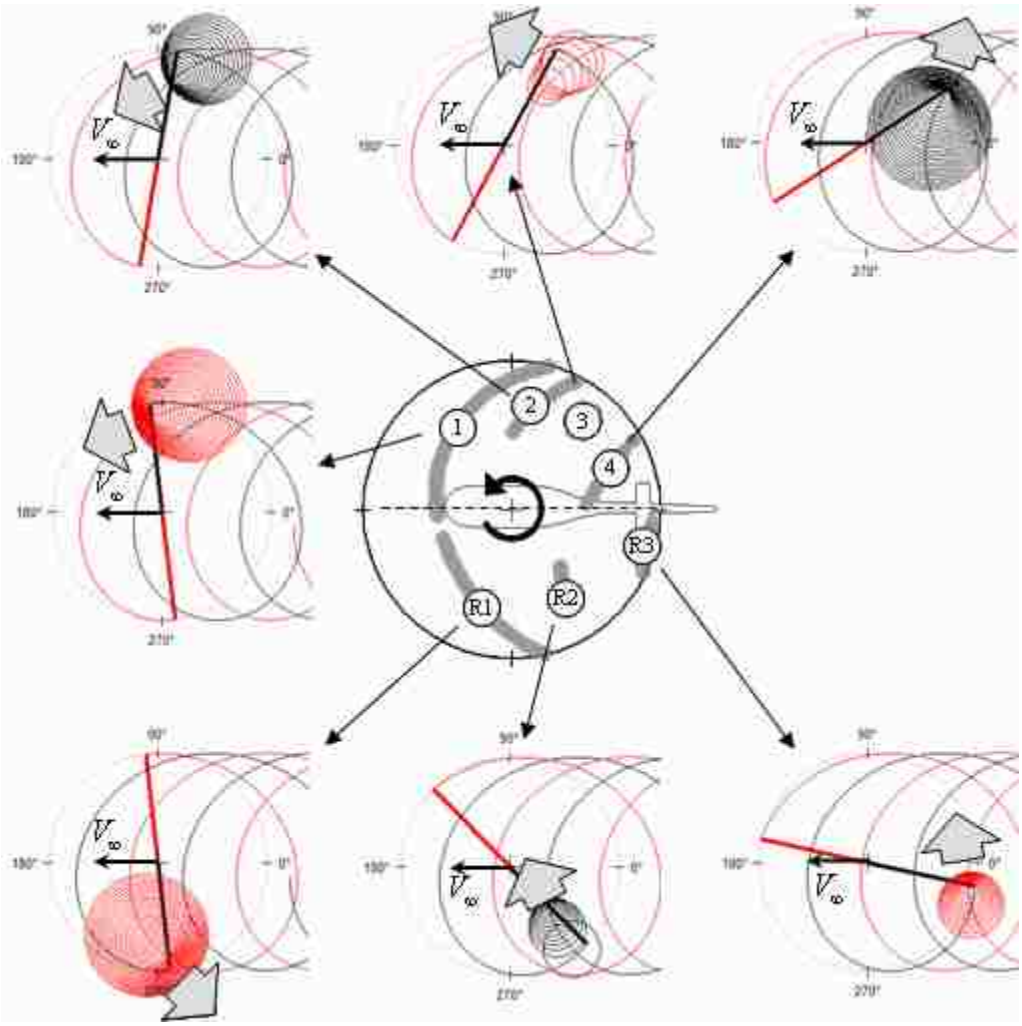

Figure 4.4. Details of BVI interactions.

Using the omni-directional disturbance model, the individual BVIs can be identified in the microphone time histories. Figure 4.5 indicates the significant BVIs for the advancing-side, center and retreating-side microphones at their target locations during a 4.5° descent. As expected from the directivity characteristics of the possible BVIs, the strongest interactions are #1, #2, and #3 on the advancing side. These three interactions are captured by the advancing-side and center microphones. While some BVI are found in the retreating-side time history, due to the directivity patterns they are not as pronounced

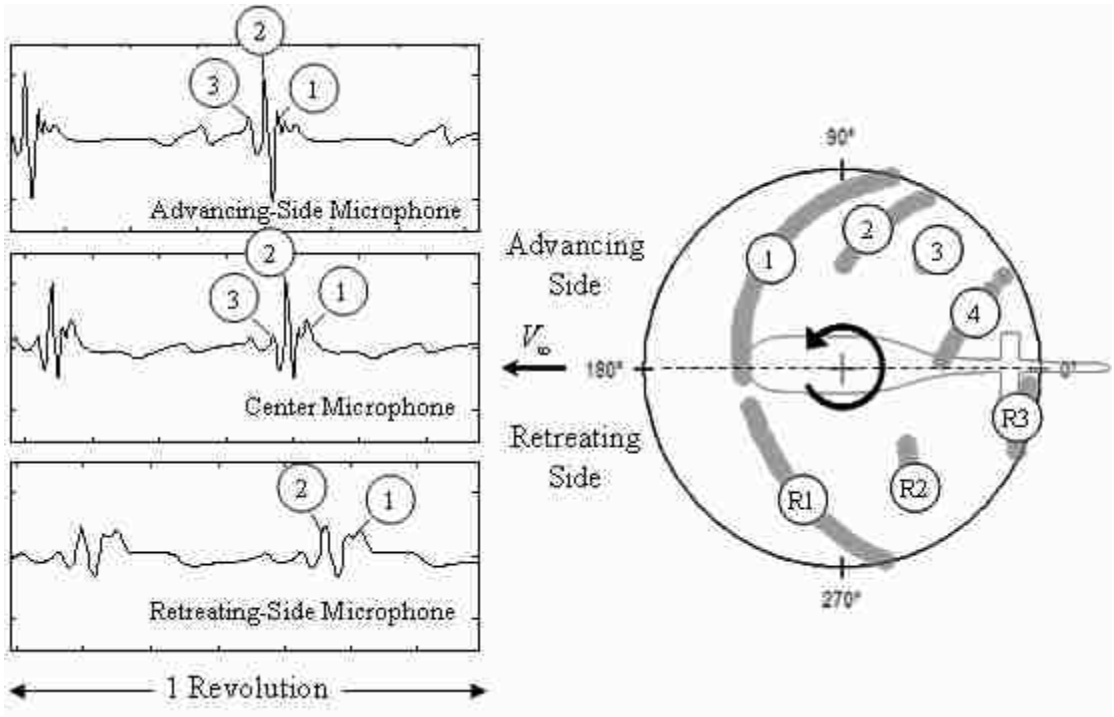

Figure 4.5. BVI details for a 4.5° descent.

4.2.1 Center Microphone

The BVI sound pressure level for the center microphone as a function of the descent angle are presented in Figure 4.6. The markers indicate the measurements made by the ground microphones and the lines indicate the predictions of the high frequency loading model. All data are for the center microphone located at an azimuth of 180° and an elevation of -30° relative to the tip-path plane.

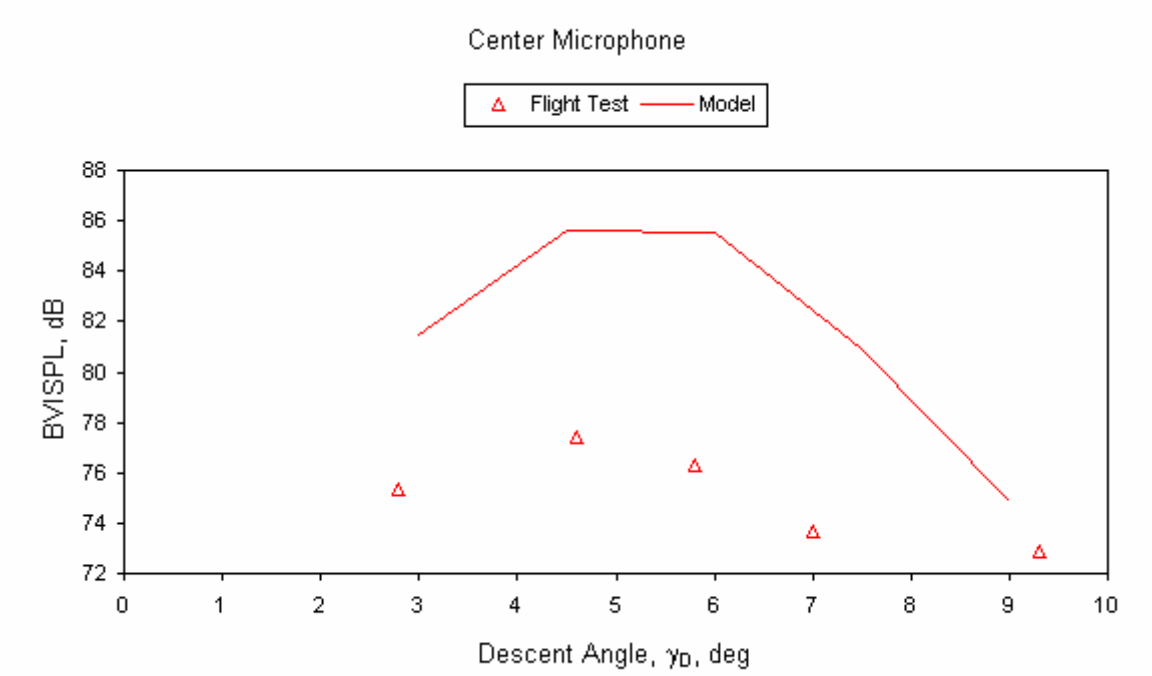

Figure 4.6. Center microphone sound pressure level trends.

At low descent angles, the wake is far enough below the main rotor, that the BVI noise is low. As the descent angle increases, the inflow through the tip-path plane is reduced and the wake remains in close proximity to the tip-path plane causing increased BVI radiation. Measurements from the ground microphones indicate that this occurs around a descent angle of 5°. Steeper descent angles result in the wake passing above the tip-path plane and the BVI levels reducing.

Overall, a similar trend is captured by the first principles model. The model does tend to over-predict the acoustic levels, but this is likely explained by the simplified prescribed structure, propagation model for the wake, and compact chord loading assumptions.

Individual time histories of the microphone recordings and those produced by the model are presented in Figure 4.7. The time histories are arranged horizontally by the

descent angle and vertically by the loading model. The first column presents the physical unfiltered ground microphone recordings over one complete revolution. The second column presents the predicted acoustics using the low-frequency loading noise model for a uniform inflow distribution. The third column presents the predicted acoustics using the low-frequency loading noise model for a Beddoes' inflow distribution. And the fourth column presents the predicted acoustics for the high-frequency loading noise model that calculates the induced velocity from the prescribed wake using the Biot-Savart law.

The low frequency content is captured well by both low frequency loading models, with a slightly better prediction of the pulse shape made by the Beddoes' inflow model. General trends in the impulsive BVI noise are also well captured with the high-frequency loading model. The model tends to over-predict the intensity of the BVIs, but the increase in BVI intensity as the descent angle approaches 5° is successfully captured by the model.

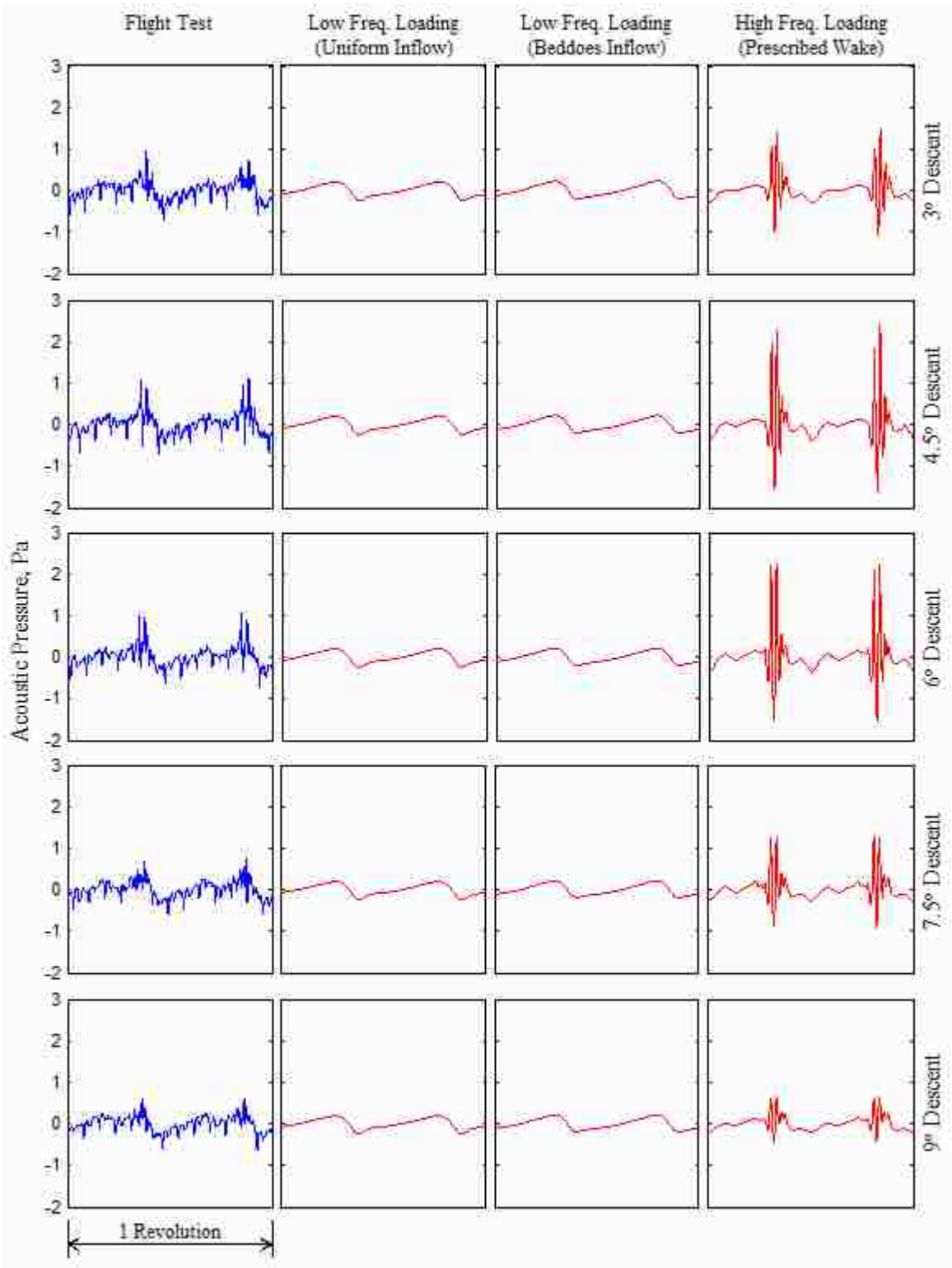

Figure 4.7. One revolution samples for center microphone.

4.2.2 Advancing-Side Microphone

The BVI sound pressure levels for the advancing-side microphone as a function of the descent angle are presented in Figure 4.8. The markers indicate the measurements made by the ground microphones and the lines indicate the predictions of the high-frequency loading model. All data are for the advancing microphone located at an azimuth of 140° and an elevation of -30° relative to the tip-path plane. As was seen for the center microphone, the model tends to over-predict the levels, but captures the general trends well.

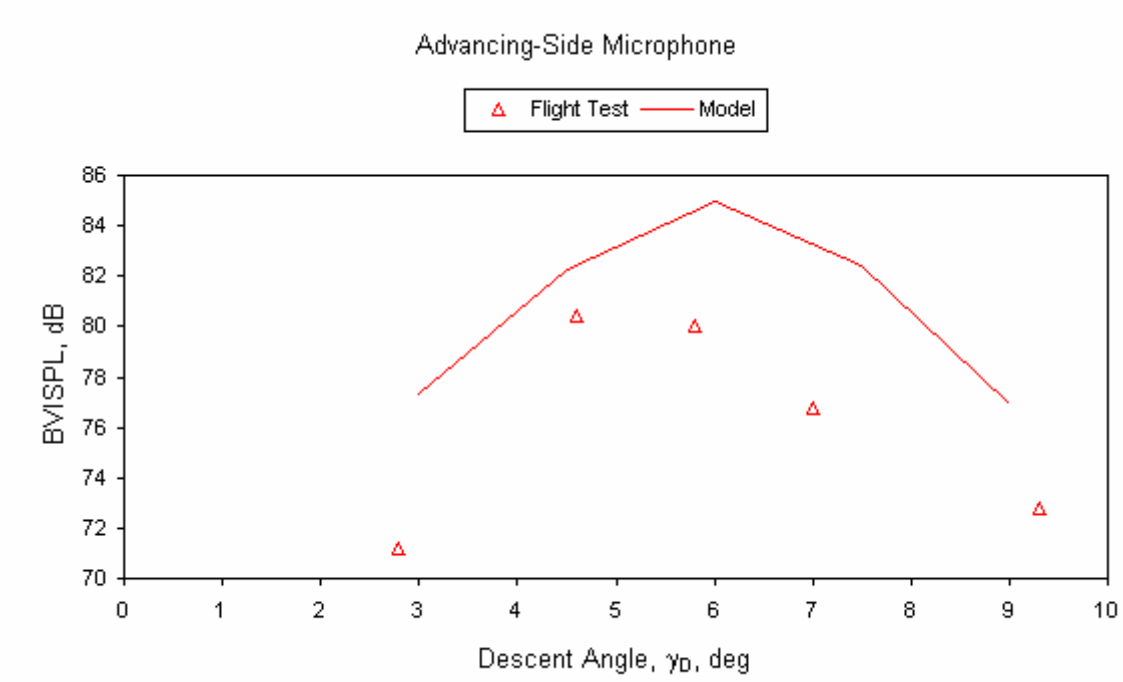

Figure 4.8. Advancing-side microphone sound pressure level trends.

Individual pulse shapes for the various loading models are provided in Figure 4.9. Both of the low-frequency loading models capture the low-frequency content visible in the ground microphones quite well, with slightly better agreement in pulse shape coming from the Beddoes' inflow model. As the wake passes closer to the tip-path plane, the high

frequency loading model captures the increase in BVI impulsive noise. In general, the initial parallel interaction is captured well by the model while the subsequent two oblique interactions tend to be over-predicted. These pulse shape discrepancies are again due to the simplified modeling of the prescribed wake and do not impeded the model's ability to capture the general trend between BVI radiation levels and wake proximity.

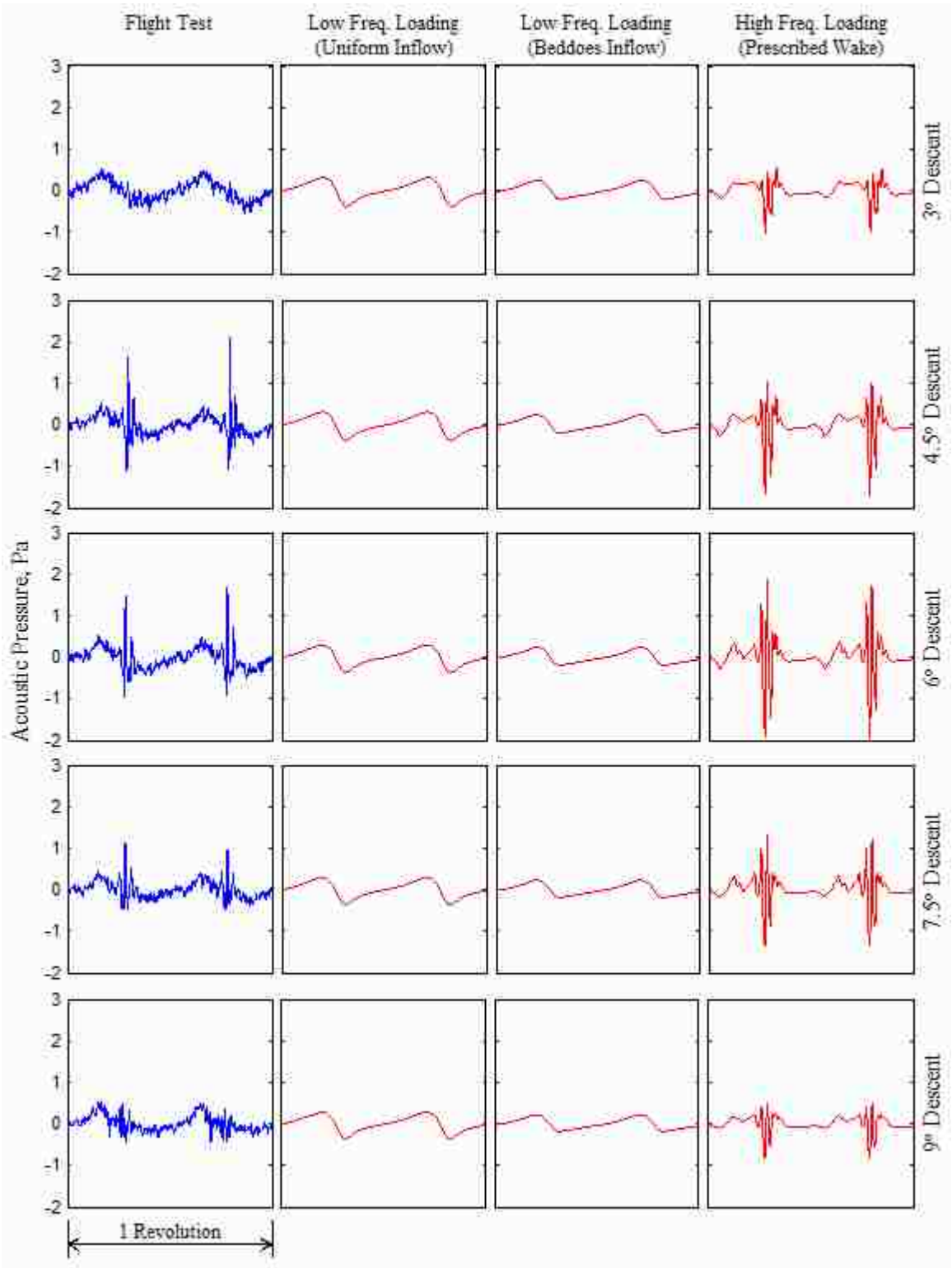

Figure 4.9. One revolution samples for advancing-side microphone.

4.2.3 Retreating-Side Microphone

The BVI sound pressure levels for the retreating-side microphone as a function of the descent angle are presented in Figure 4.10. The markers indicate the measurements made by the ground microphones and the lines indicate the predictions of the model. All data are for the advancing-side microphone located at an azimuth of 230° and an elevation of -35° relative to the tip-path plane.

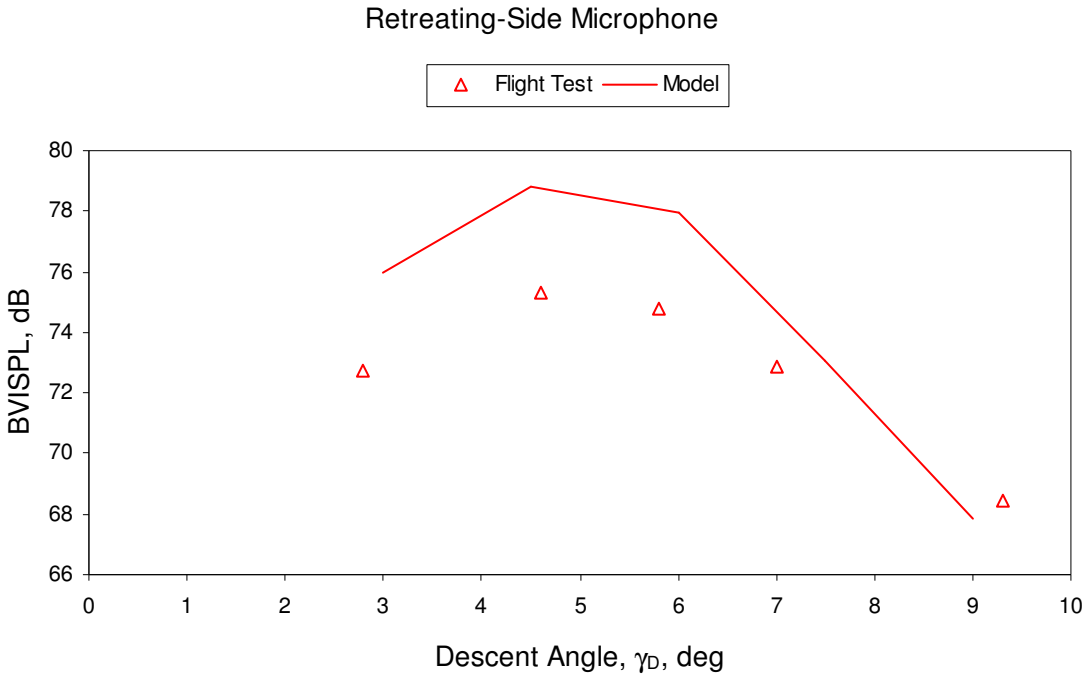

Figure 4.10. Retreating-side microphone sound pressure level trends.

As with the previous cases, the microphone recordings capture an increase in acoustic radiation as the descent angle. The model continues to over-predict the sound pressure levels, but captures the relationship between the descent angle and the level of acoustic radiation.

Individual time histories of the microphone recordings and the loading models are presented in Figure 4.11 over one complete revolution. As with the previous data sets, the low frequency content is captured well by both low frequency loading models, with a slightly better prediction of the pulse shape made by the Beddoes' inflow model. As was observed at the other microphone positions, the model tends to over-predict the high-frequency loading noise. The fuselage tends to scatter the high frequency waves radiating towards the retreating side that pass through the fuselage [50]. This scattering is not included in the mathematical model.

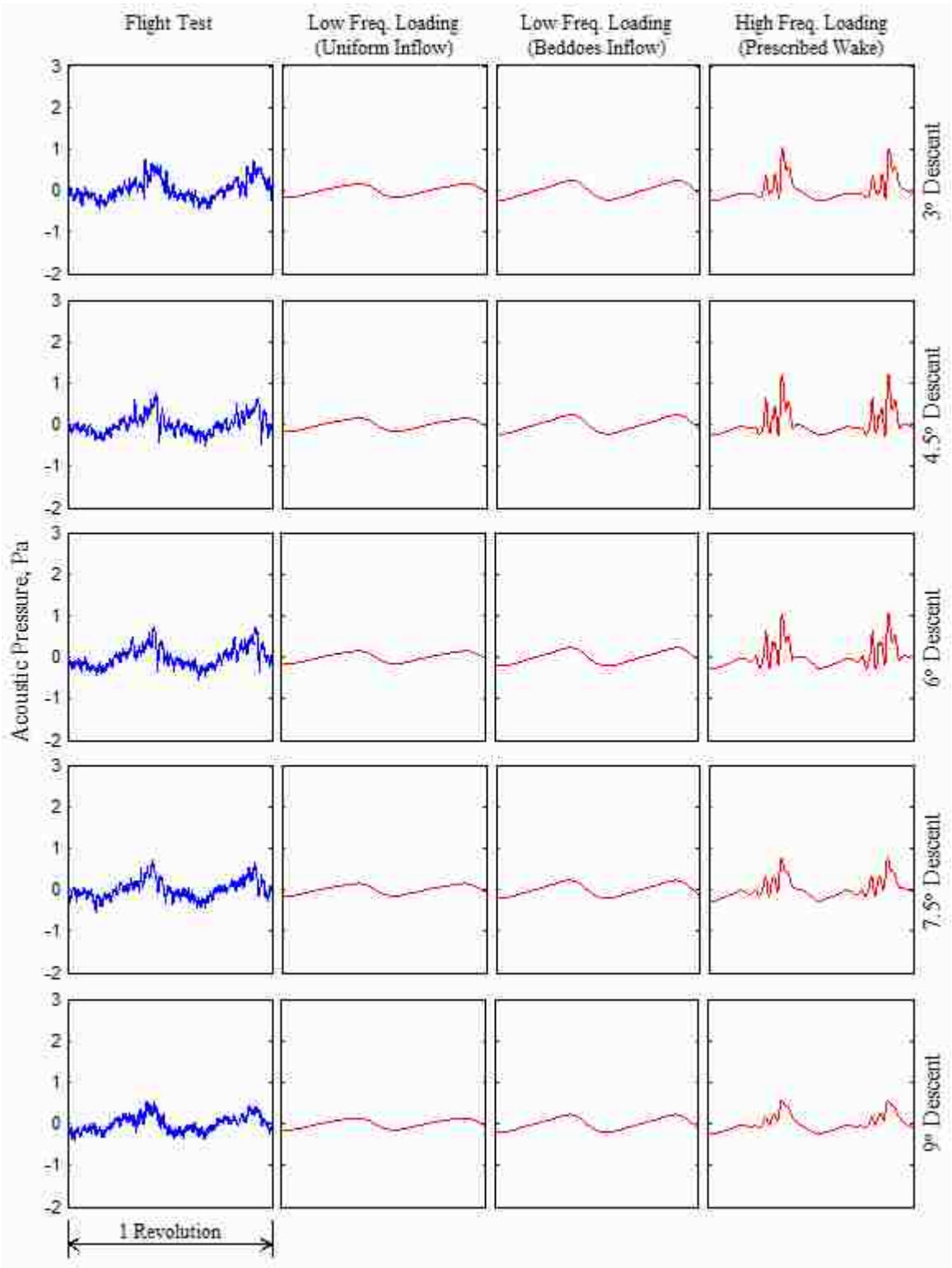

Figure 4.11. One revolution samples for retreating-side microphone.

4.3 Pull-up Maneuvers

The theoretical model will now be applied to the transient pull-up maneuvers. In addition to comparing the acoustics, the dynamics model will also be compared with the measurements made by the in-flight instrumentation. Each maneuver will be analyzed individually, starting with the moderate pull-up, then the fast pull-up, and lastly the slow pull-up. There are two reasons for studying the maneuvers in this order. First, that is the chronological order that the maneuvers were flown during the flight test. Second, during the slow pull-up maneuver, the in-flight data suggests that the aircraft was not in trimmed flight at the time of execution. This sensitivity to the trim condition is not as visible with the larger control inputs required to execute the moderate and fast pull-up maneuvers, but does result in deviations between the predictions and the measurements for the slow pull-up rate.

4.3.1 Moderate Pull-up Maneuver

The control input sequence for the pull-up maneuvers was optimized to match the fuselage pitch rate measurements made by the in-flight instrumentation. Trimmed flight is assumed 33 seconds into the data record. Thereafter, perturbations are made to the longitudinal cyclic position to match the fuselage pitch rate. Lateral cyclic and collective positions remain constant after obtaining the trim solution. The final results of this optimization procedure are displayed in Figure 4.12 for the fuselage pitching rate during the moderate pull-up maneuver. Based on this optimized control sequence, the pilot appears to have initiated the moderate pure-cyclic pull-up around 36.5 seconds into the data record.

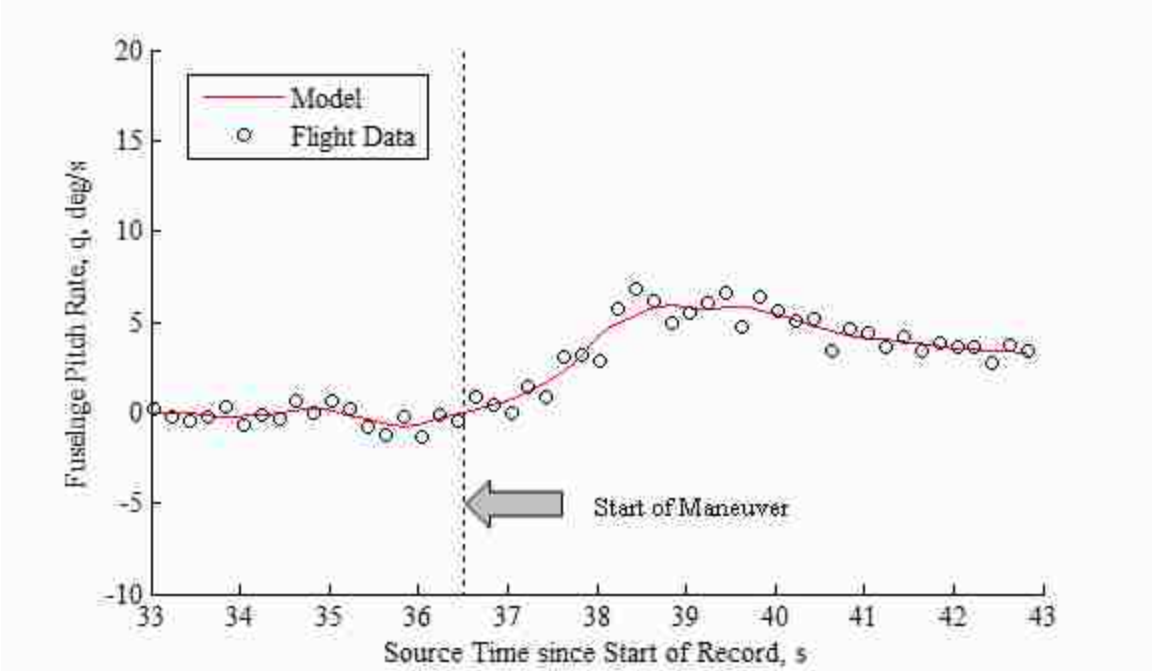

Figure 4.12. Moderate pull-up pitch rate time history.

Aircraft trajectory data are illustrated in Figure 4.13, Figure 4.14, and Figure 4.15 for the flight path angle time history, the advance radio time history, and flight trajectory of the aircraft. All three measurements agree well with the model during the region between the trim and the initiation of the pull-up. Following the pull-up perturbation, the model matches well with the in-flight measurements for several seconds before the flight path angle begins to diverge. This deviation is due to the pilot applying collective and tail rotor controls to safely exit the pull-up maneuver.

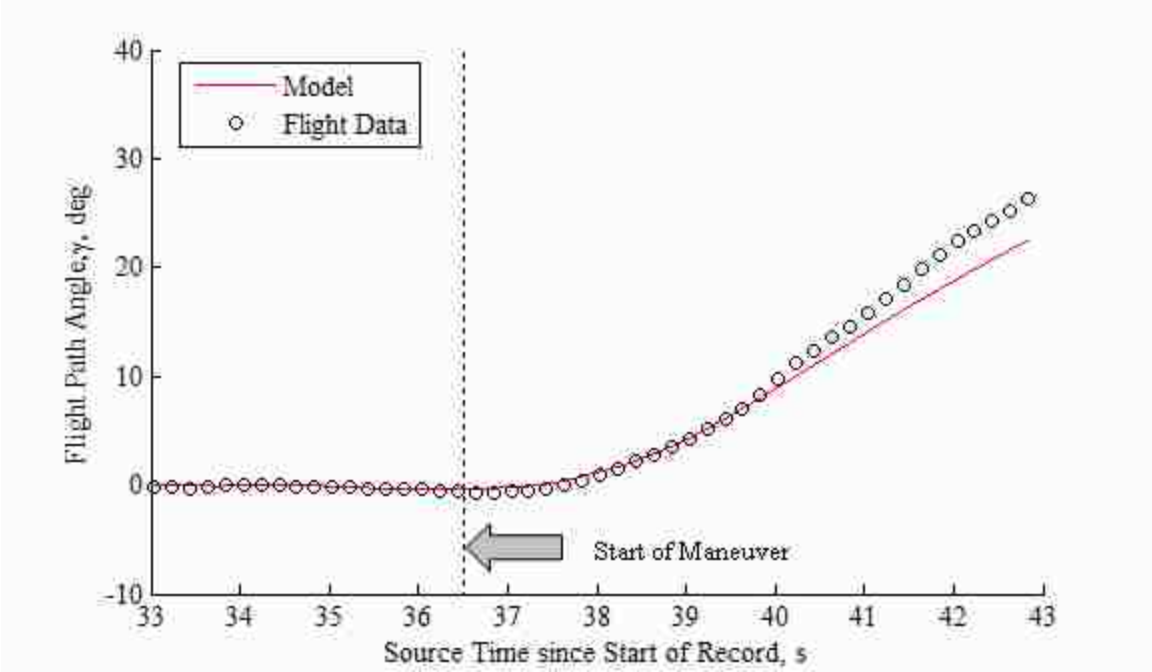

Figure 4.13. Moderate pull-up, flight path angle time history.

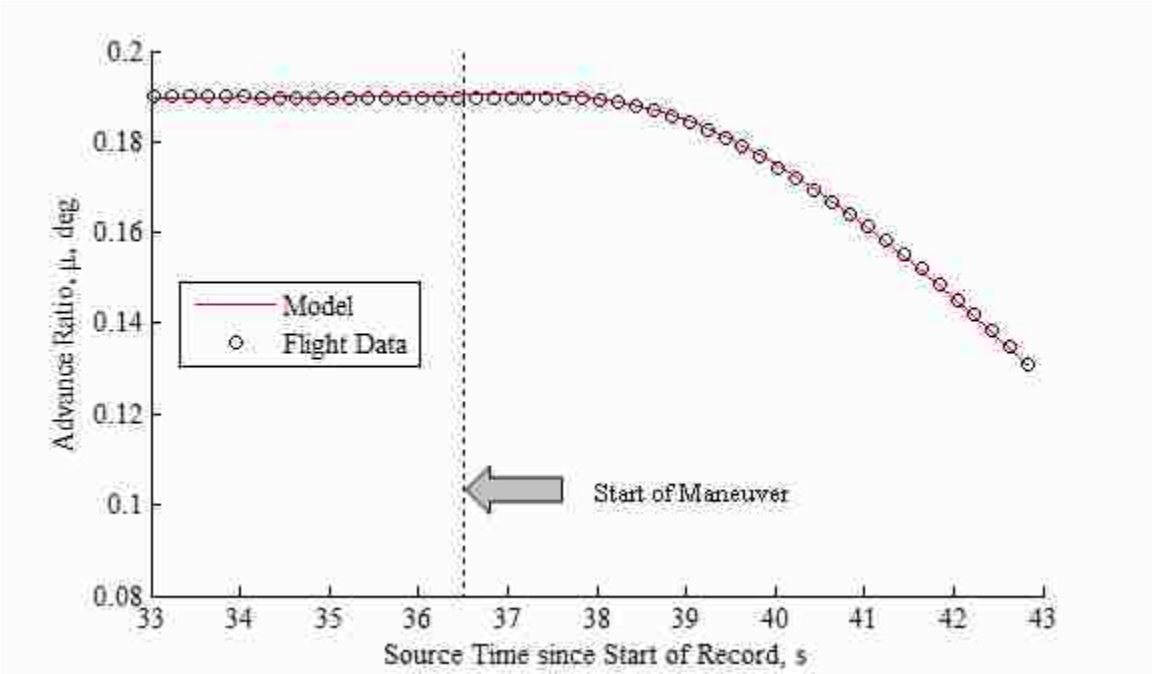

Figure 4.14. Moderate pull up advance ratio time history.

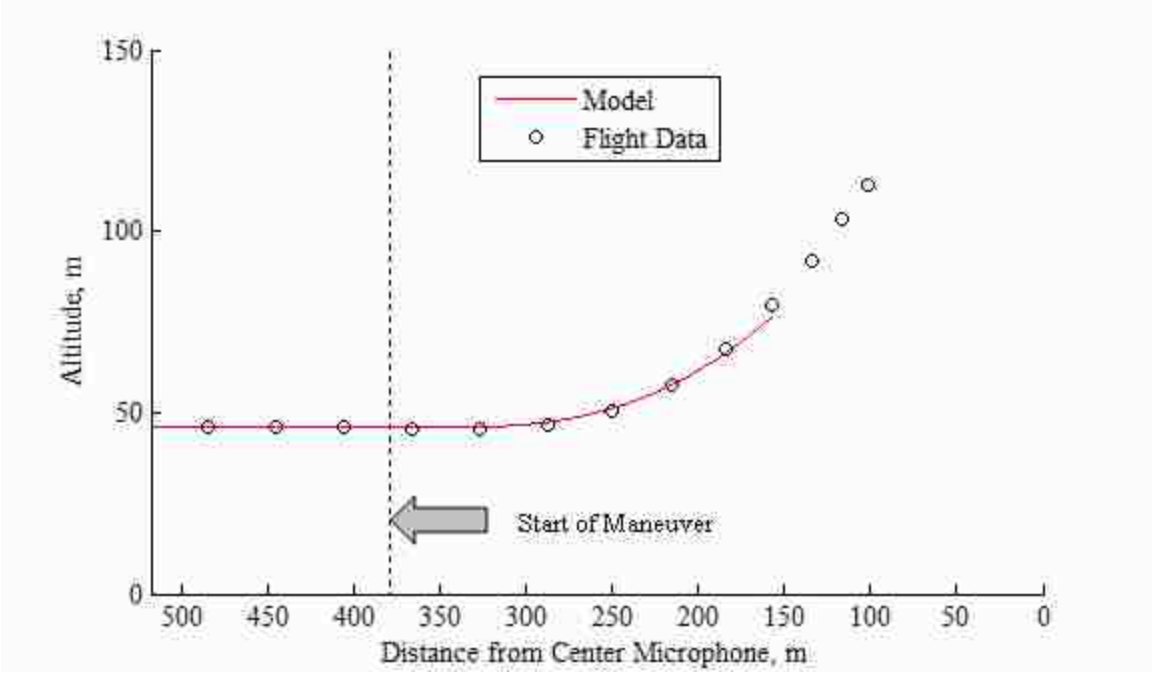

Figure 4.15. Moderate advance ratio trajectory.

The main rotor thrust time history is presented in Figure 4.16. The thrust is inferred based on longitudinal and vertical components of the fuselage acceleration. As with the flight trajectory response, the dynamics model matches well with the in-flight measurements for several seconds after the initiation of the pull-up maneuver. After a few seconds into the initial transient, the model begins to diverge from the in-flight measurements; the result of the pilot applying additional controls to safely exit the pull-up maneuver.

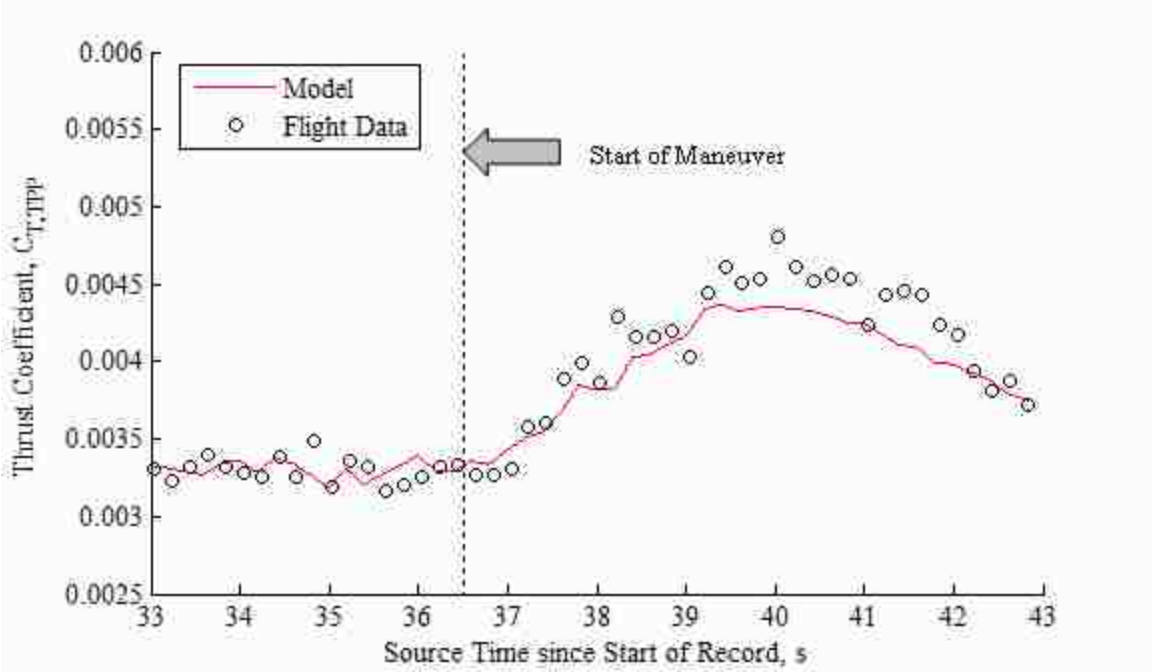

Figure 4.16. Moderate pull-up thrust coefficient.

Lastly, the angle of attack of the tip-path plane is provided in Figure 4.17. The trends of the tip-path plane angle of attack match well with the data during the level flight and for several seconds beyond the transient. The nearly constant bias between the measurements and the model are likely the result of a system misalignment on the aircraft. Recall that the tip-path plane tracking is a combination of two measurements: an inertial measurement system used to record the pitch of the fuselage, and a camera tracking system that measures the flapping of the tip-path plane relative to the fuselage. During calibration, the camera measurements are made relative to a fixed reference line on the fuselage corresponding to a null pitch attitude. However, the inertial measurement system establishes a null pitch attitude when the system is activated. Therefore the offset is likely the result of the aircraft operating from a field at Gilroy, where the local ground plane was not necessarily level.

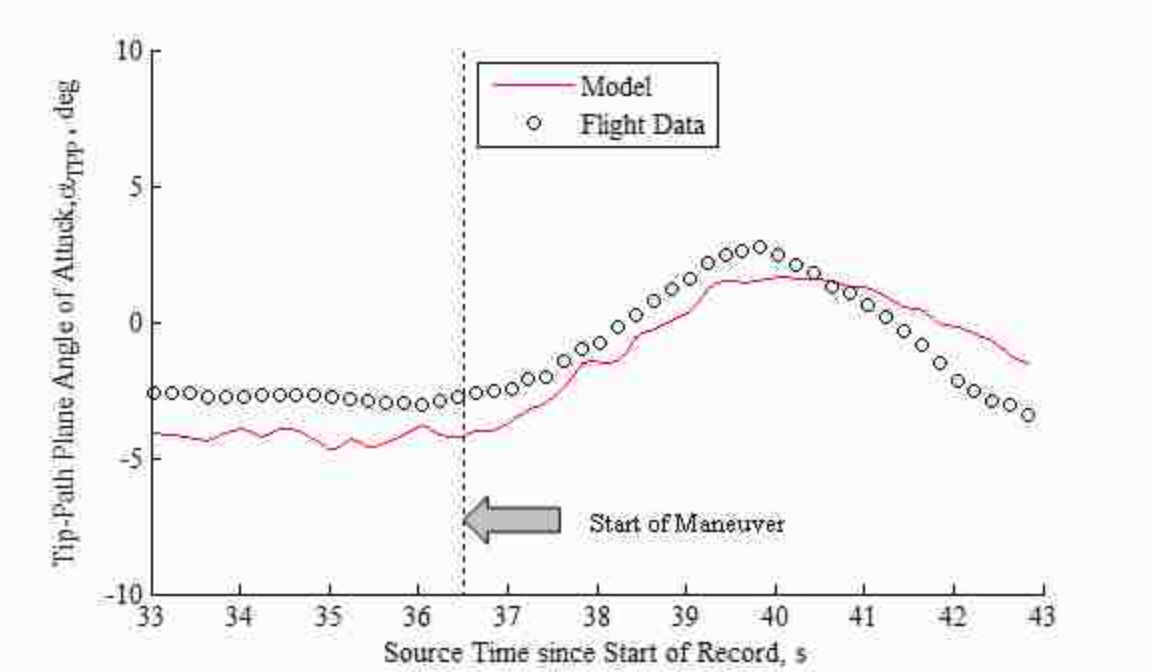

Figure 4.17. Moderate pull-up tip-path plane angle of attack.

Figure 4.18 presents the acoustic time history of the center microphone during the moderate pull-up maneuver. Actual measurements made by the center microphone are presented in the top plot while theoretical predictions using the high-frequency loading model are presented in the middle plot. The bottom plot illustrates the time histories of three metrics over the course of the maneuver. These metrics include the overall sound pressure level (OASPL) over all frequencies, the sound pressure level contained within the first 6 main rotor harmonics (1^{st}-6^{th} MR Harmonic), and the BVI sound pressure level (BVISPL) contained between the 6^{th} and 40^{th} main rotor harmonics. The acoustic model captures the general trend of the data fairly well, including the increase in BVI noise after the initiation of the maneuver.

Also plotted in Figure 4.18 are the acoustic predictions from the low-frequency loading model. Recall that this model does not incorporate BVI modeling and only

captures the low-frequency loading noise during the maneuver. The drop off in BVISPL for this model is due to the dynamic motion of the tip-path plane relative to the observer. Initially, the observer lies in the plane of the rotor and where thickness noise is most significant. Thickness noise, while largely made up of low frequency noise, does contain some frequency content in the BVISPL band. As the helicopter tip-path plane attitudes pitches up, the observer moves out of the plane of the rotor, and the acoustic levels from thickness noise decrease resulting in a reduction of levels in the BVISPL band. As the observer moves out of the plane of the rotor, additional low frequency loading noise is introduced and results in an increase in the sound pressure levels between the 1^{st} and 6^{th} main rotor harmonic. Low frequency loading noise has a negligible contribution to the BVISPL band.

Details of the acoustics over a full rotor revolution are provided in Figure 4.19 prior to initiating the pull-up (top row) and during the maneuver where BVI are present (bottom row). In both instances, the low-frequency loading noise models do an excellent job of predicting the low-frequency loading noise recorded by the center microphone. The high-frequency loading model does a fair job of capturing the occurrence and duration of the blade-vortex interaction noise event. As expected, little-to-no BVI noise is generated during the level flight region. However, during the pull-up, as the wake approaches the tip-path plane, the BVI noise increases in both the measured data and the theoretical model.

Referring to the pulse shape of the BVI at the center microphone, the model predicts the initial parallel interaction that appears as the first spike in the theoretical BVI. This interaction is absent from the ground microphone data. However, the second and

third spikes in the theoretical predictions, associated with the oblique interactions, are captured in the physical measurements. As was the case for the steady descents, these discrepancies are likely the result of the wake modeling assumptions used in the high frequency loading model and the treatment of the specular reflection. While the details of the BVI pulse shapes are not replicated perfectly, the duration and the overall trends of increased acoustic radiation during the BVI event is simulated adequately by the model.

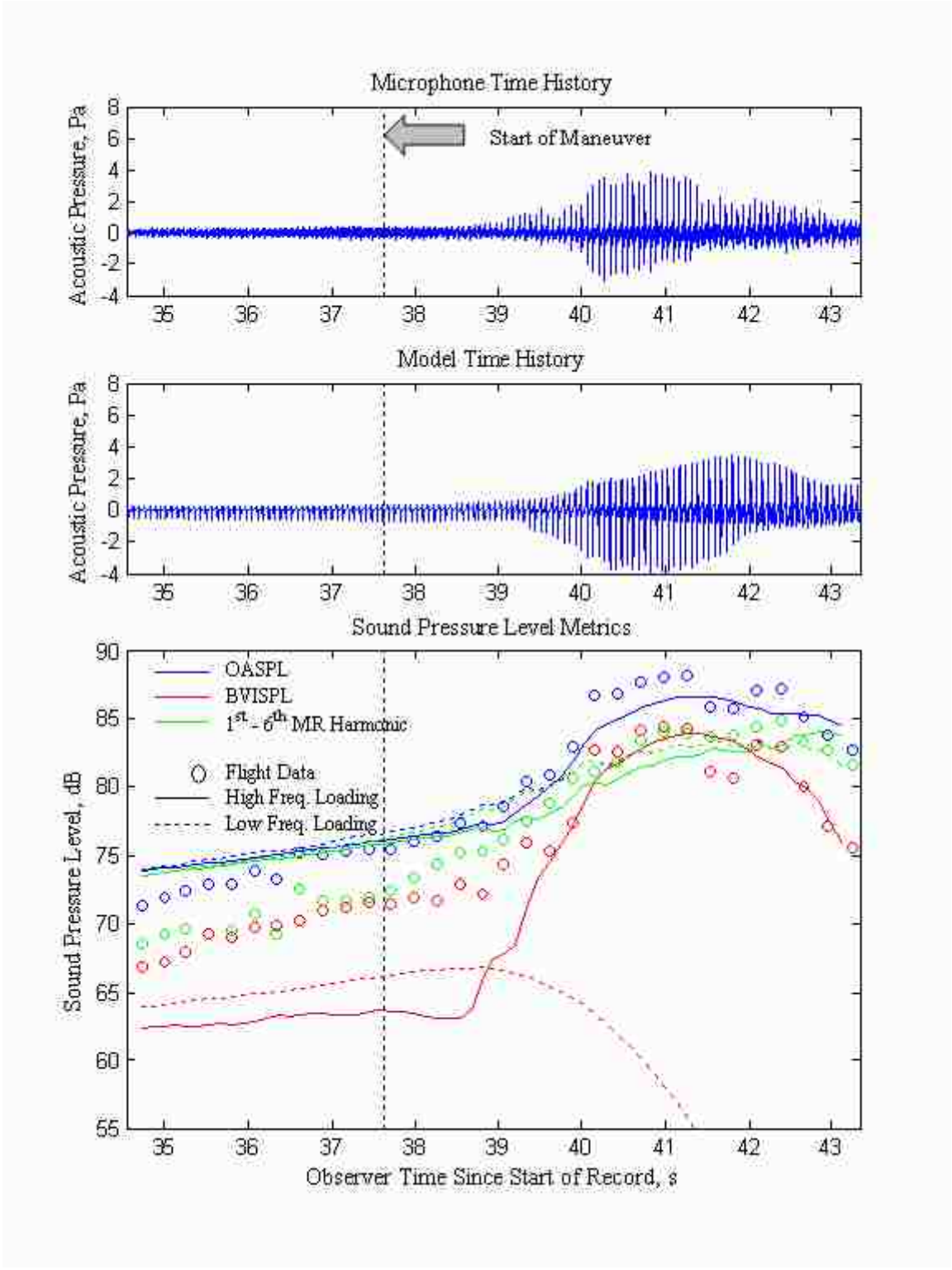

Figure 4.18. Moderate pull-up center microphone acoustics.

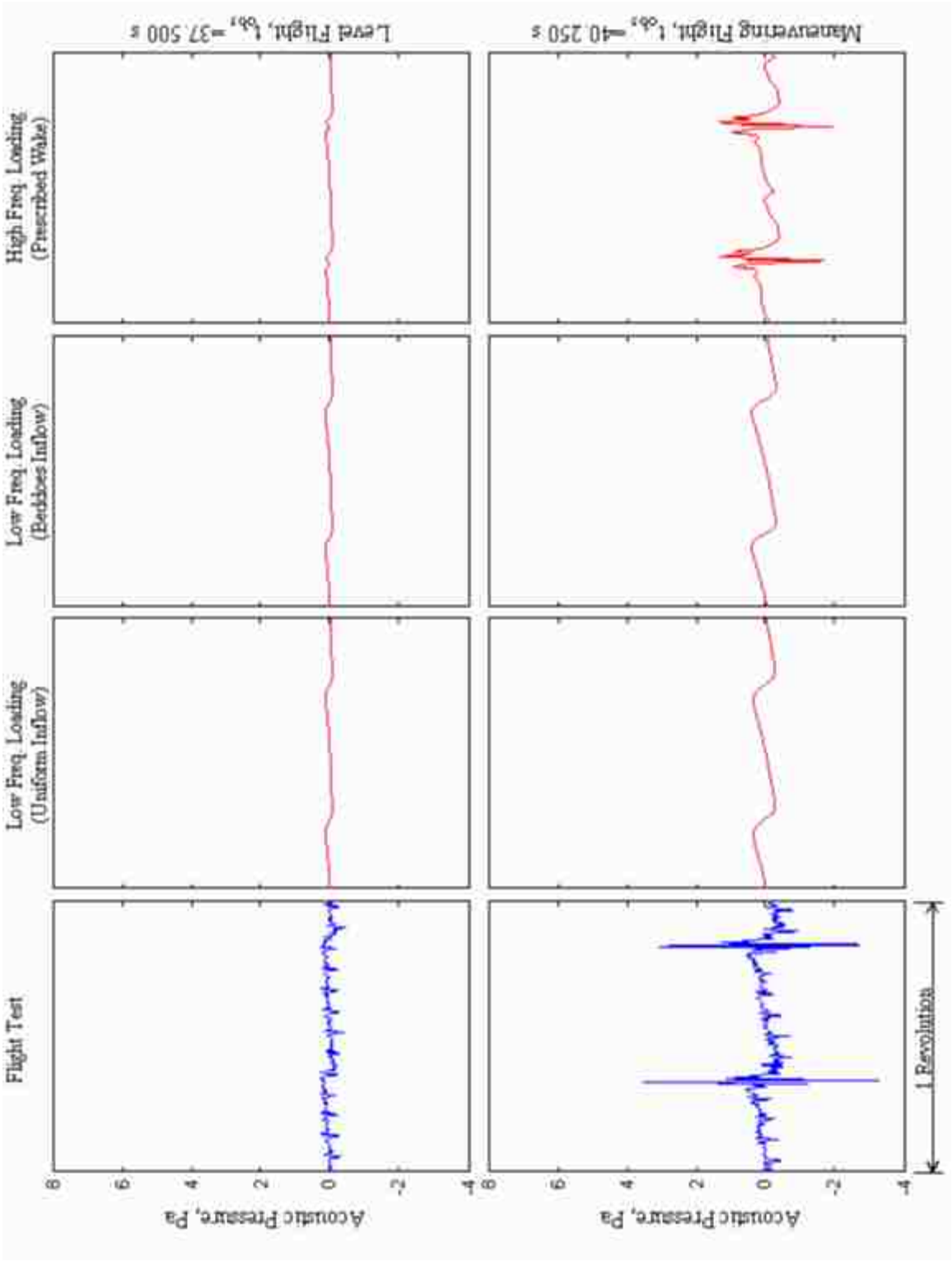

Figure 4.19. Moderate pull-up center microphone pulse shapes during level flight (top row) and during maneuvering flight (bottom row).

Acoustic measurements and predictions for the advancing side microphone are provided in Figure 4.20. As in the center microphone plots, the top plot includes the raw microphone recordings from the advancing side microphone; the center plot includes the predictions made using the high-frequency loading model; and the bottom plot illustrates the trends of the sound metrics. The theoretical model again captures the occurrence of impulsive noise over the course of the maneuver; this time over-predicting the BVI level. In the case of the low frequency loading noise model, the directivity characteristics of the thickness noise again produce a drop off in the BVISPL as the observer moves out of the plane of the rotor.

Referring to the acoustic details over a full revolution in Figure 4.21, the low frequency loading models again capture the low-frequency noise quite well while the high-frequency loading model captures the trends of the BVI event. As was evident on the center microphone, some of the details of the BVI pulse shape differ due to the wake modeling assumptions. The model tends to over-predict the levels of the parallel interaction that makes up the first BVI spike. Oblique interactions, which are expected to radiate primarily forward and to the retreating-side of the aircraft, are much less pronounced.

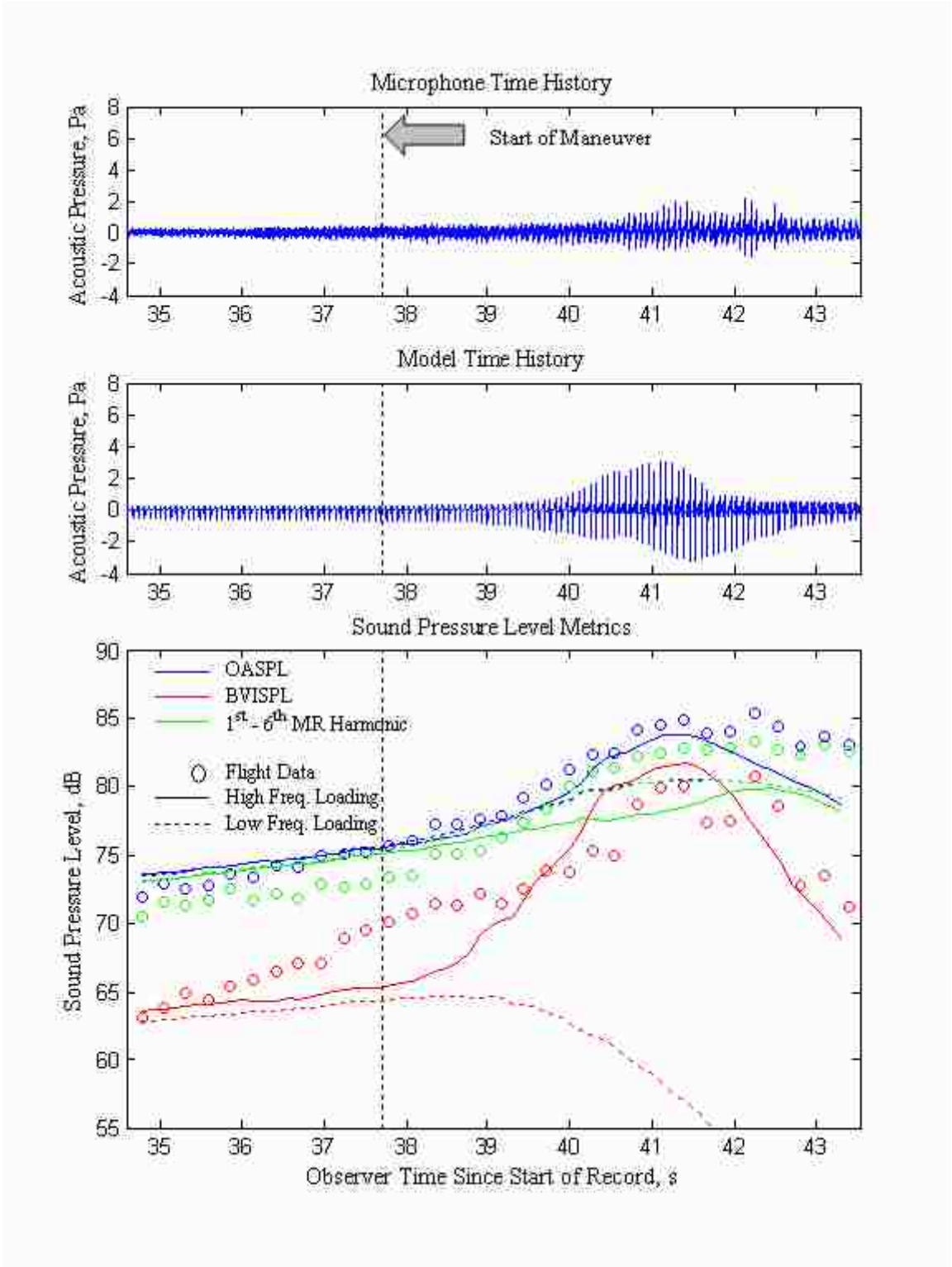

Figure 4.20. Moderate pull-up advancing side microphone acoustics.

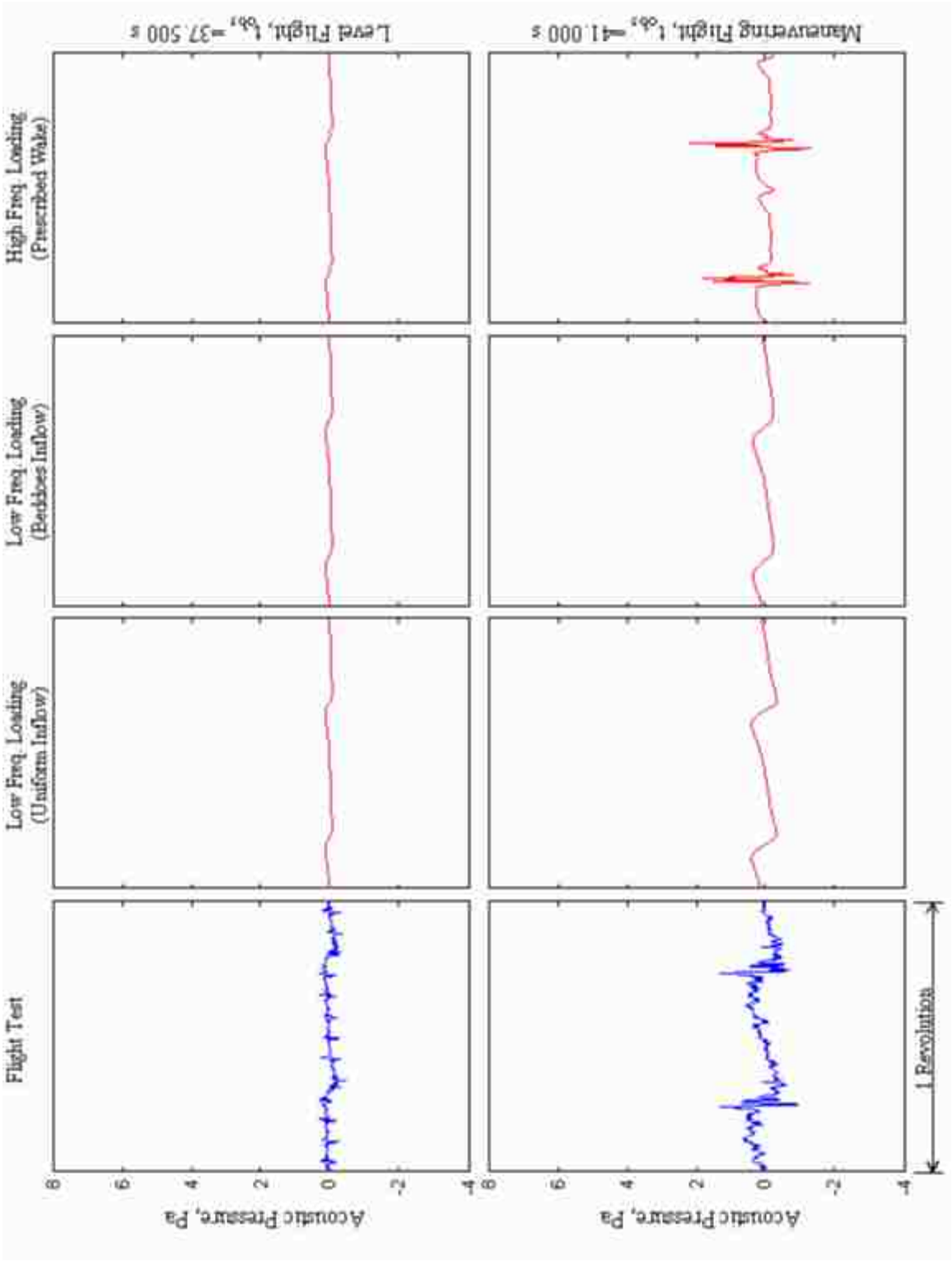

Figure 4.21. Moderate pull-up advancing side microphone details during level flight (top row) and during maneuvering flight (bottom row).

Acoustic time histories for the retreating-side microphone are provided in Figure 4.22. Again, the model does a fairly good job of capturing the build-up of BVI noise after the initiation of the pull-up maneuver. The ground microphones indicate a slightly faster build-up of BVI noise, but the sustained levels over the course of the maneuver witnessed in the data are also present in the model. In the case of the low frequency loading noise model, the directivity characteristics of the thickness noise again produce a drop off in the BVISPL as the observer moves out of the plane of the rotor.

Individual acoustic time histories over a full revolution are provided in Figure 4.23 for the retreating-side microphone. Low frequency noise levels are accurately predicted by the low frequency loading noise models and the BVI noise is picked up fairly well by the high frequency loading model. Due to the directivity patterns of the interactions, the retreating side microphone only picks up the two oblique interactions on the advancing side. While the pulse shapes are not represented perfectly, the overall levels and duration of the BVI noise match well with the ground measurements.

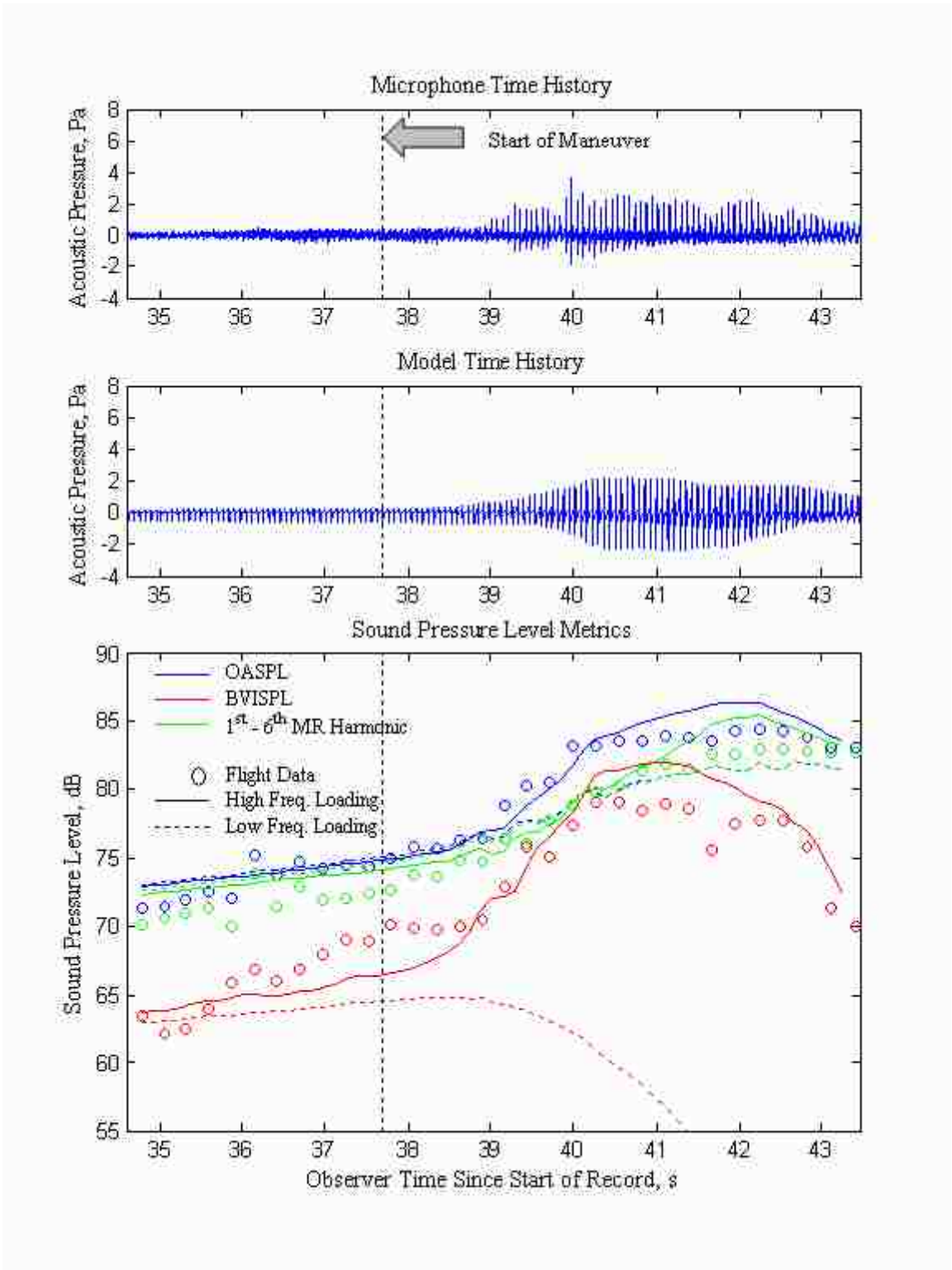

Figure 4.22. Moderate pull-up retreating microphone acoustics.

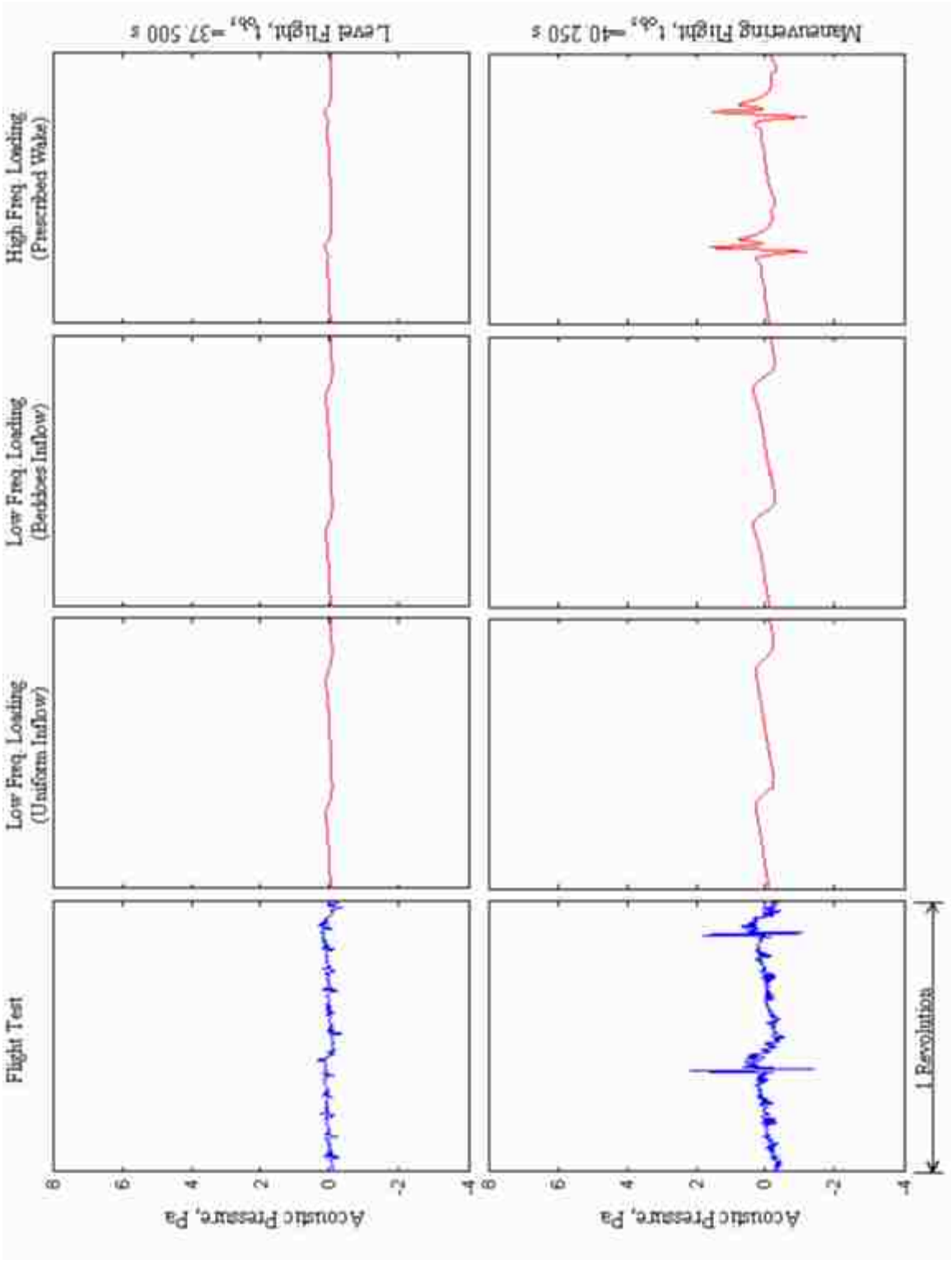

Figure 4.23. Moderate pull-up, retreating microphone detail during level flight (top row) and during maneuvering flight (bottom row).

4.3.2 Fast Pull-up Maneuver

A longitudinal cyclic perturbation sequence was optimized to match the fuselage pitch rate recorded by the in-flight measurements for the fast pull-up maneuver. Results of the optimized schedule for the fuselage pitch rate are provided in Figure 4.24. From this schedule, it appears that the pull-up maneuver was initiated around 40.75 seconds into the data record. Also note that the aircraft experienced a smaller pitching transient in the corridor between the assumed trim condition at 38 seconds and the initiation of the maneuver.

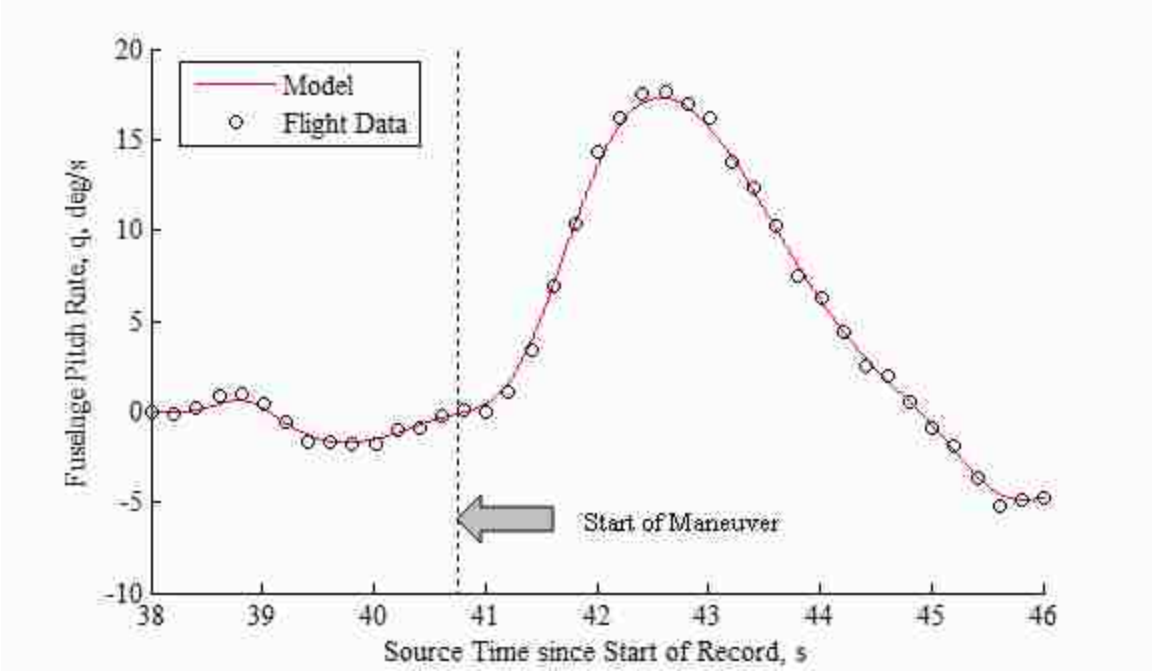

Figure 4.24. Fast pull-up fuselage pitch rate time history.

Response plots for the flight path angle, advance ratio, and aircraft trajectory are provided in Figure 4.25, Figure 4.26, and Figure 4.27 respectively. Overall, the model captures the response quite well for several seconds after initiating the pull-up transient. While the pitching transient prior to the pull-up maneuver does cause as slight deviation

between the model and the measurements, the effects are minimal. As was observed during the moderate pull-up maneuver, three seconds after the initial transient, the model begins to diverge from the measurements as the pilot applies additional controls to safely exit the pull-up maneuver.

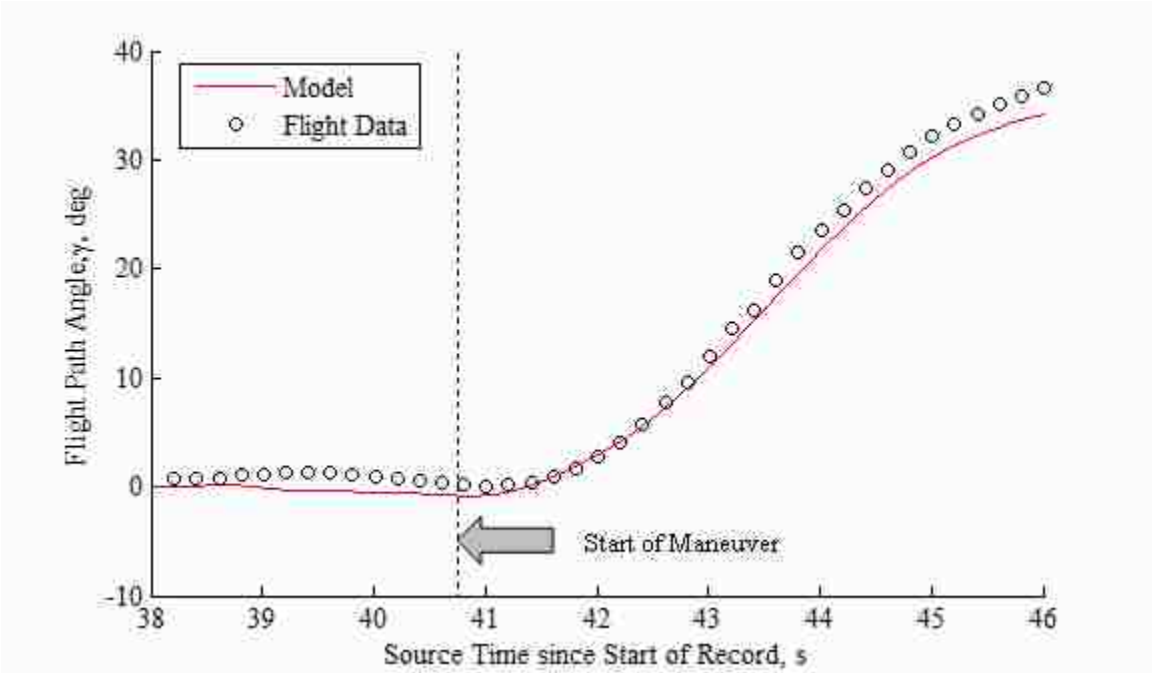

Figure 4.25. Fast pull-up fuselage flight path time history.

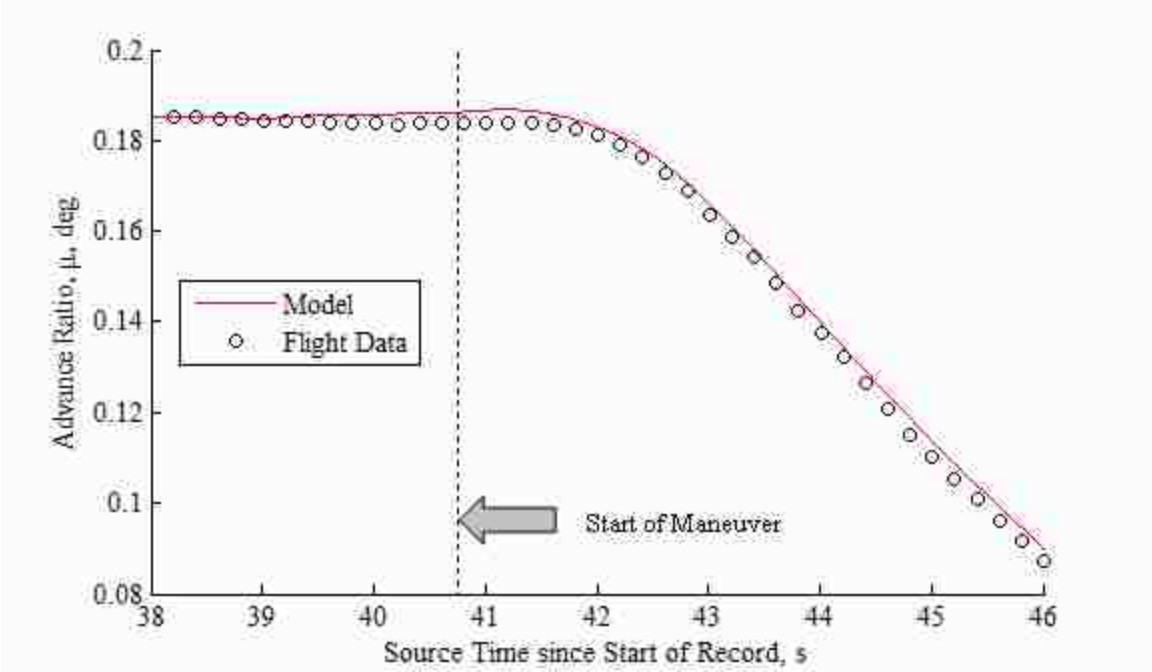

Figure 4.26. Fast pull-up advance ratio time history.

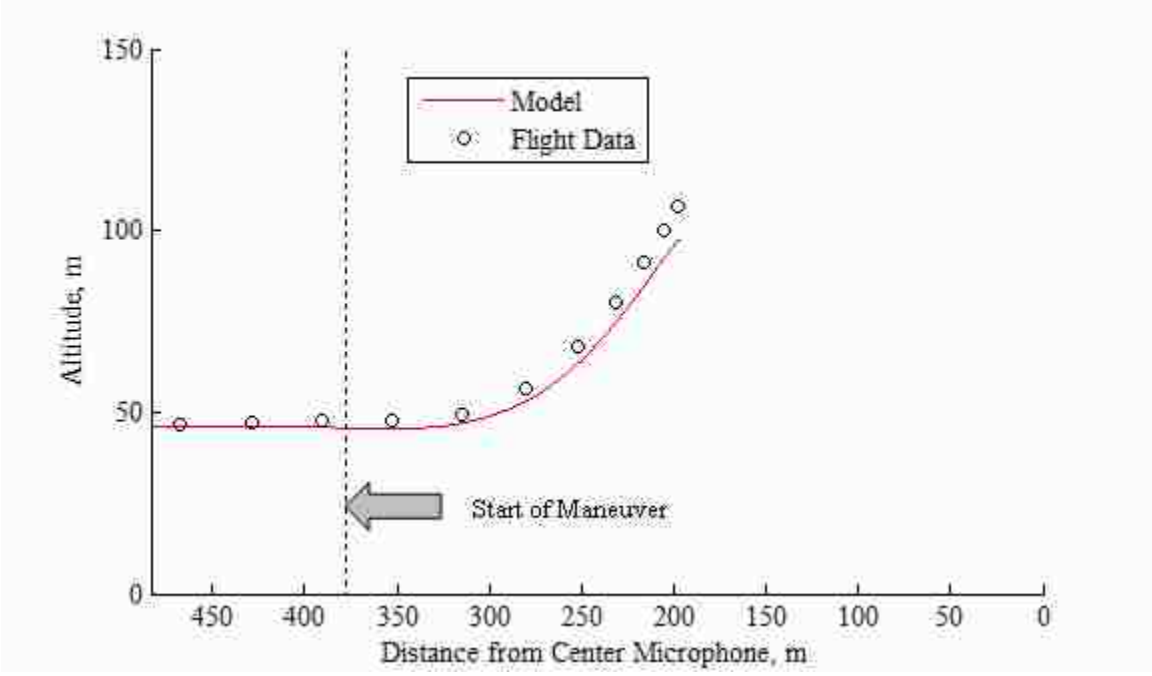

Figure 4.27. Fast pull-up flight trajectory.

The thrust coefficient time history is provided in Figure 4.28. The thrust is inferred based on the longitudinal and vertical accelerations of the body. As with the trajectory response data, the predictions of the dynamics model match well with the in-flight measurements for several seconds after the application of the longitudinal cyclic.

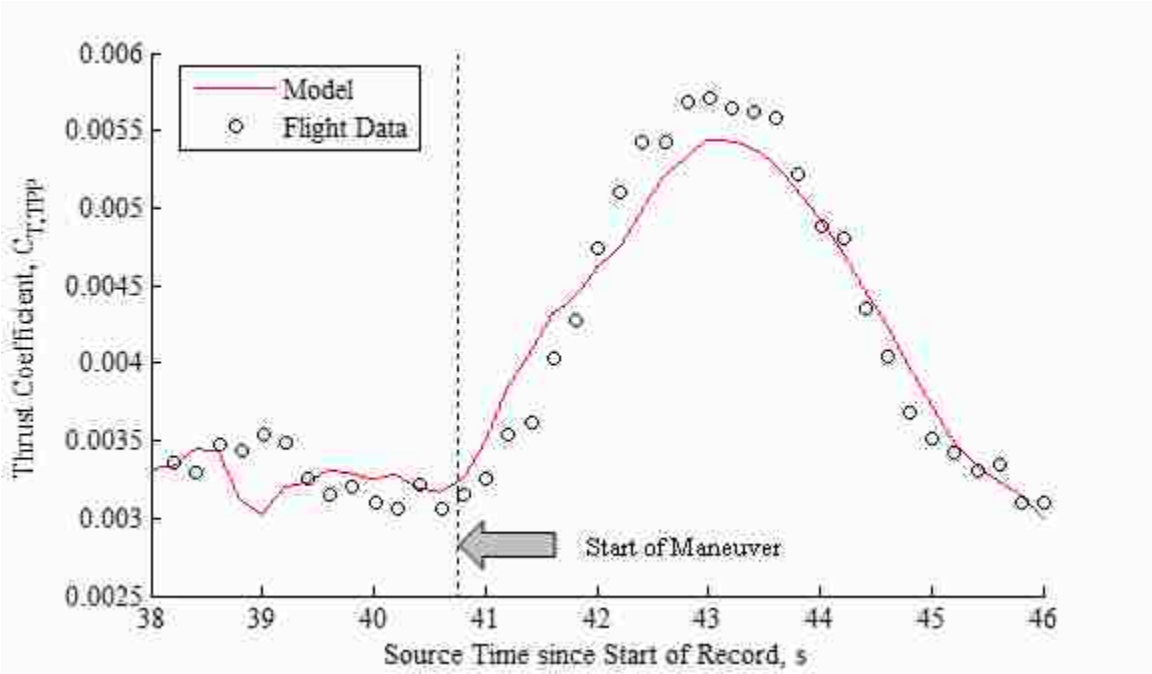

Figure 4.28. Fast pull-up thrust time history.

The tip-path plane angle of attack response is provided in Figure 4.29 for the fast pull-up maneuver. Again the model matches the trends of the data quite well. Note that the misalignment of the inertial measurement system is evident as an offset between the measurements and the predictions during the level flight region.

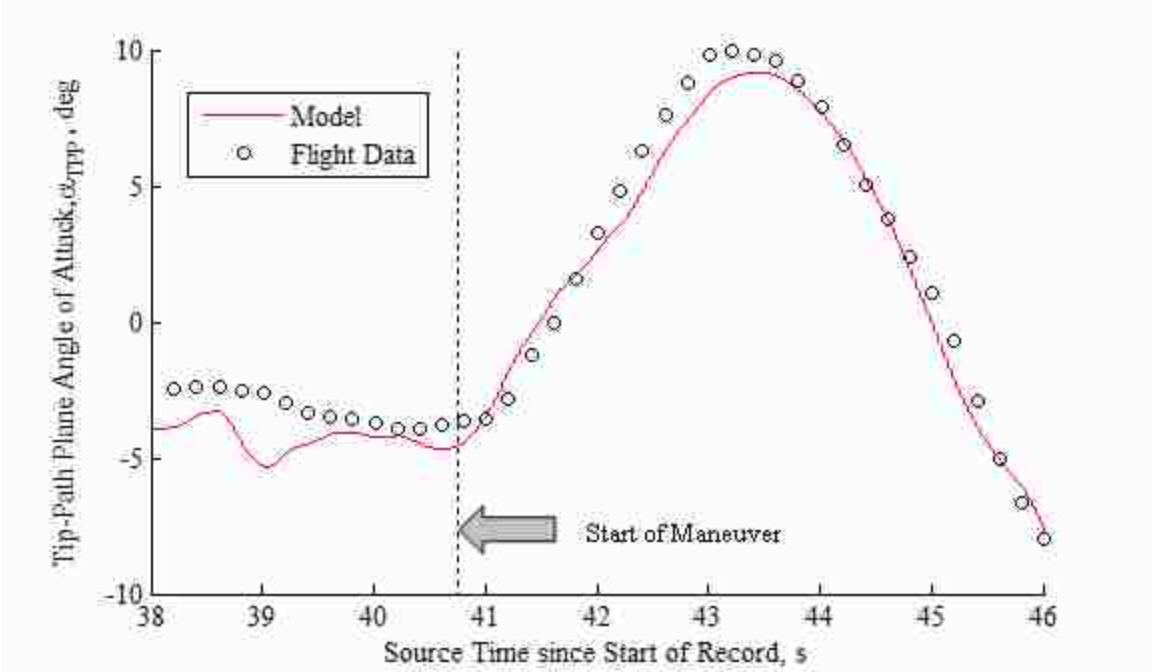

Figure 4.29. Fast pull-up tip-path plane angle of attack time history.

The acoustic time history of the center microphone over the course of the maneuver is illustrated in Figure 4.30. The top plot is the raw data from the center microphone recording; the middle plot the prediction from the high-frequency loading model; and the bottom plot the application of sound pressure level metrics.

The center microphone observed two peaks in BVI levels over the maneuver: the first around 43.5 seconds into the maneuver when the wake is believed to pass from below the tip-path plane to above the tip path plane, and the second around 44.75 seconds into the maneuver when the wake is believed to pass from above the tip-path plane to below the tip-path plane. The model also predicts two peaks in acoustic levels due to the occurrence of BVI. The initial peak is predicted by the model to occur around 43 seconds into the maneuver; the second passing is predicted to occur around 45 seconds into the maneuver. These discrepancies are likely the result of the simple wake model not fully

capturing all of the directivity characteristics. In the case of the low frequency loading noise model, the directivity characteristics of the thickness noise again produce a drop off in the BVISPL as the observer moves out of the plane of the rotor. However, the out-of-plane low frequency loading noise matches well with the measured data.

Details of the acoustics over a full revolution for the center microphone are provided in Figure 4.31. The top row features the acoustics during the level flight region prior to the execution of the pull up; the bottom row features the acoustics during the initial peak in BVI noise. In both regions, the low frequency loading models accurately predict the levels of the low-frequency loading noise generated by the main rotor while the high-frequency loading models capture the trends of the BVI noise. As was observed with the moderate pull-up maneuver, the theoretical model over predicts the parallel interaction indicated by the first BVI spike, but does a fair job of capturing the two oblique interactions indicated by the second and third BVI spikes. These discrepancies in the pulse shape details are again due to the simplified wake modeling. Overall, however, the model adequately replicates the duration and general amplitude trends of the BVI event.

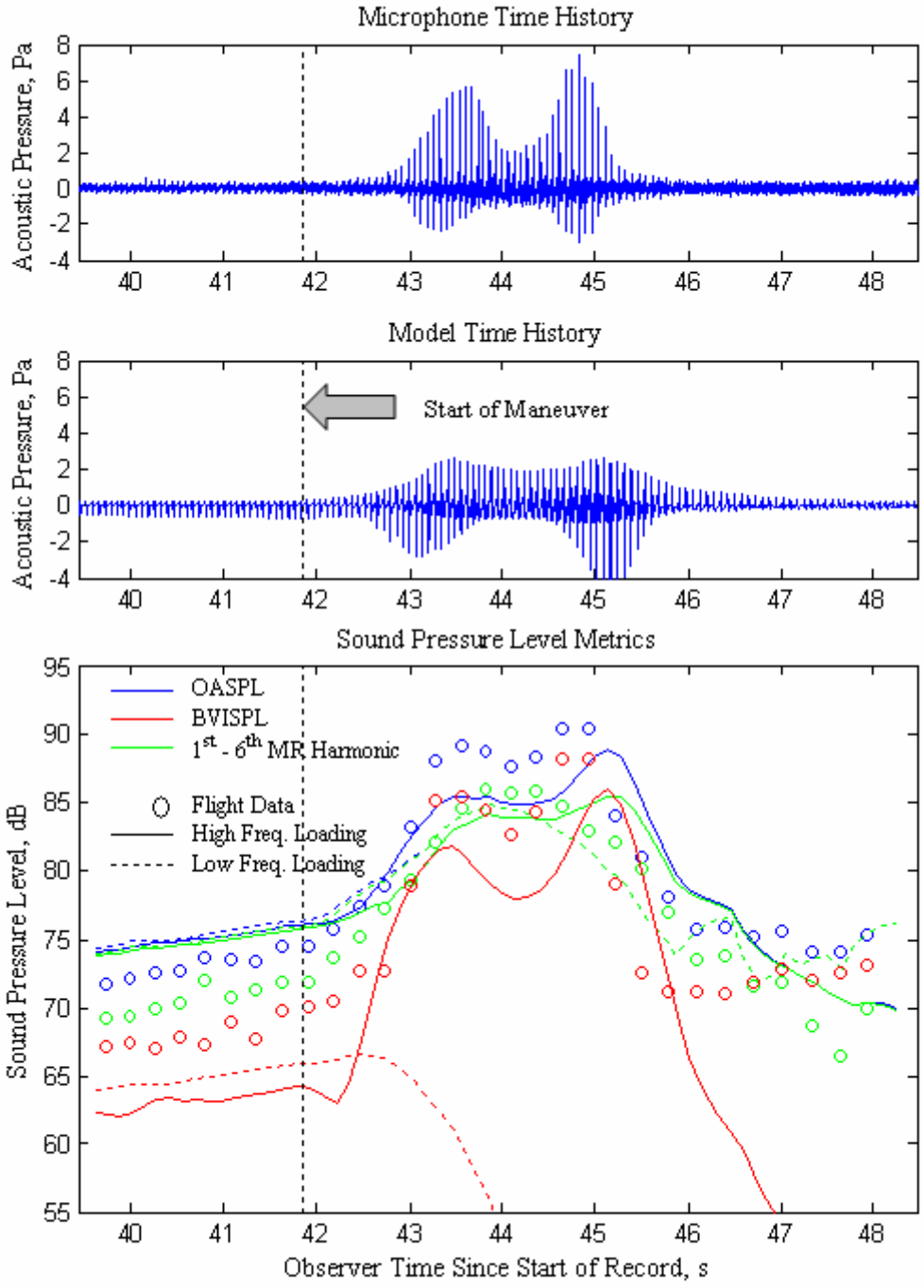

Figure 4.30. Fast pull-up center microphone acoustic trends.

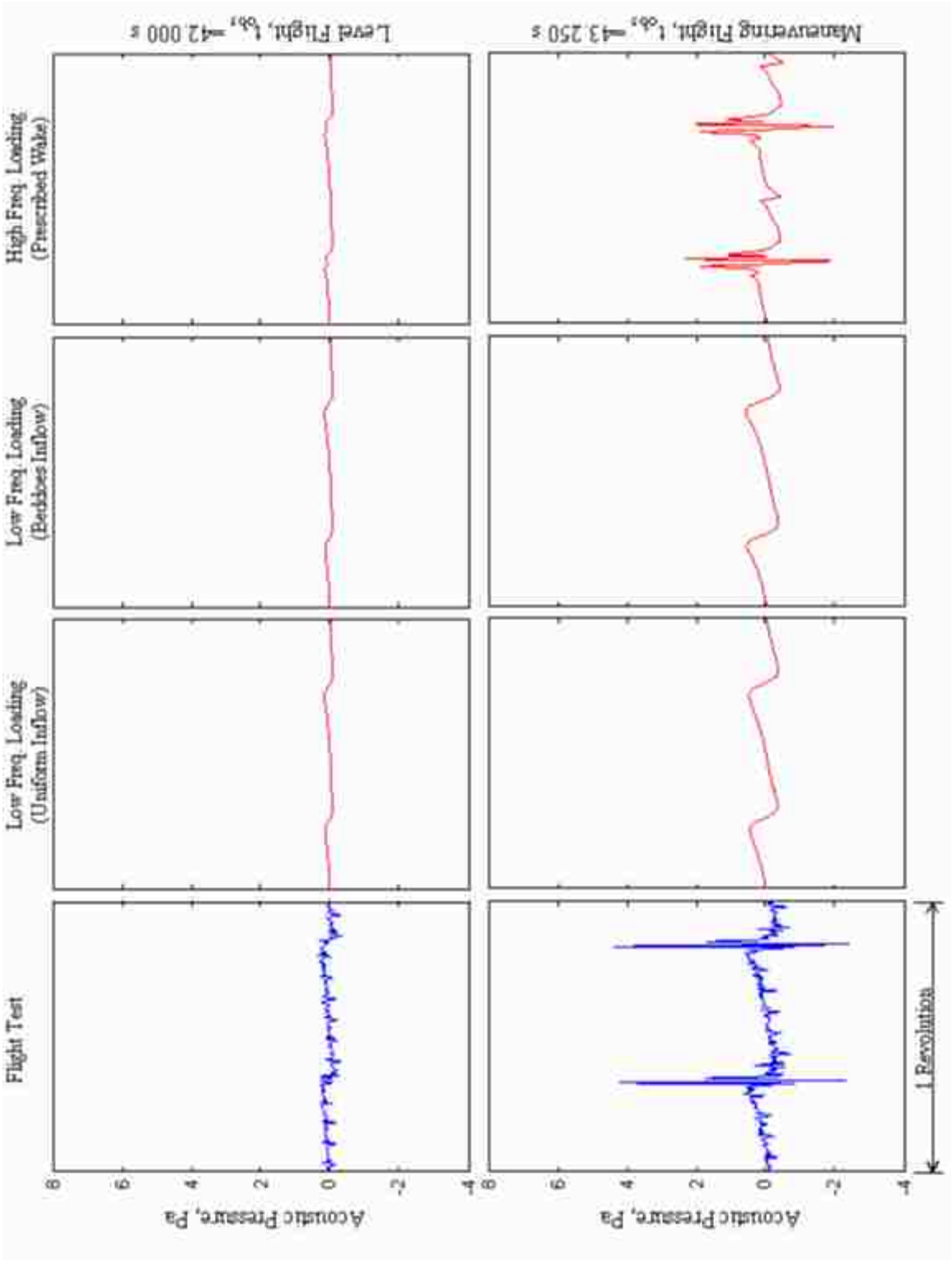

Figure 4.31. Fast pull-up center microphone acoustic details.

Acoustic trends for the advancing-side are presented in Figure 4.32. The advancing-side microphone captured a build-up of impulsive noise reaching a peak around 44.4 seconds into the flight record whereas the model predicts two separate build-ups: the first at 43.5 seconds, and the second at 45.25 seconds. This suggests that while the model captures the occurrence of BVI, the directivity characteristics of the BVI are not captured perfectly by wake model; again likely the result of the wake modeling assumptions. In the case of the low frequency loading noise model, the directivity characteristics of the thickness noise again produce a drop off in the BVISPL as the observer moves out of the plane of the rotor.

Details of the individual BVI pulses are provided in Figure 4.33. Consistent with previous observations, the low-frequency noise is captured well by the low-frequency loading models. The high-frequency loading model continues to over-predict the intensity of the parallel interaction, but the general pulse shape is similar to that recorded by the microphones.

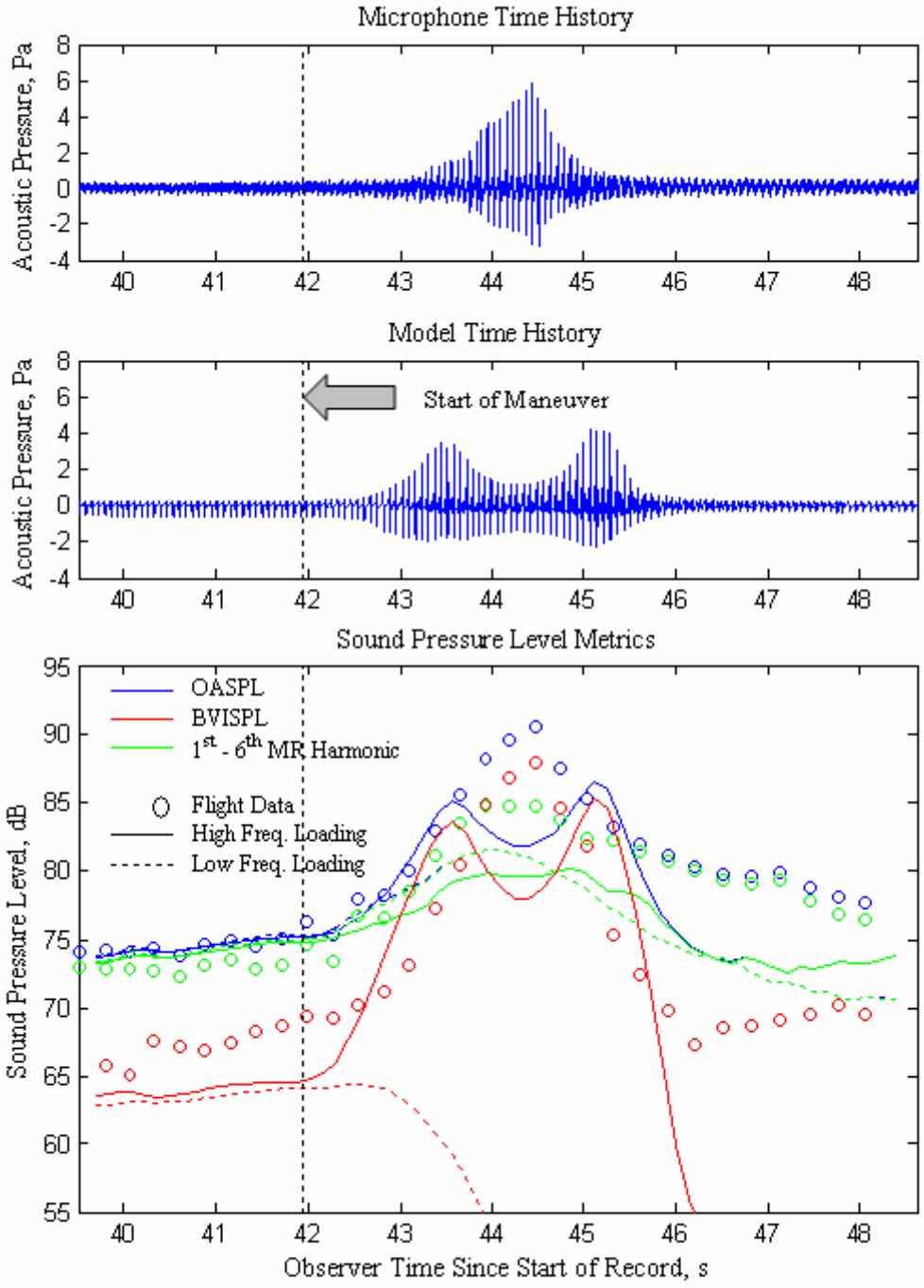

Figure 4.32. Fast pull-up advancing side microphone acoustic trends.

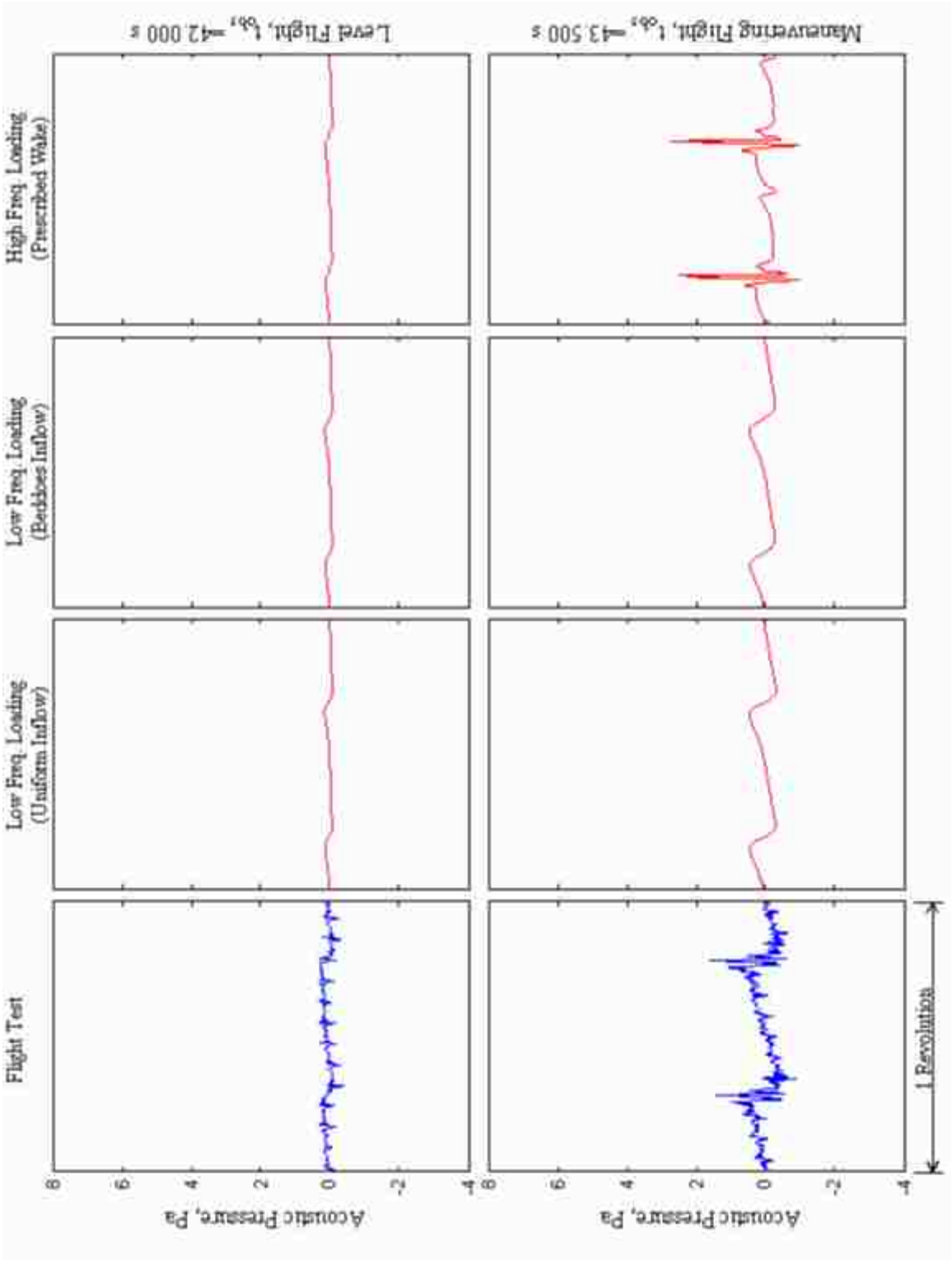

Figure 4.33. Fast pull-up advancing-side acoustic details.

Acoustic trends for the retreating-side microphone are presented in Figure 4.34. Similar to the recording from the center microphone, the retreating-side microphone captures two peaks in impulsive noise: the first at 43.7 seconds into the maneuver, the second at 45.3 seconds into the maneuver. Of the two build-ups, the microphone indicates that the former is notably louder than the later. The model also picks up two peaks, though the timings differ slightly as was observed with the center microphone. Furthermore, the model also predicts that the second build-up to be more severe than the initial build-up. However, while the specific details of the impulsive noise during the maneuver differ between the model and the recordings, the duration of impulsive noise during the maneuver is consistent between the model and the observed acoustics. Both indicate increases in impulsive noise beginning at 42.3 seconds that are maintained until 46 seconds.

Details of the pulse shapes for the retreating-side microphone are provided in Figure 4.35. Both low frequency loading models capture the low-frequency noise very well and the trends in BVI noise are captured fairly well by the high-frequency loading noise. Analysis of the theoretical BVI signature indicates an over-prediction of the parallel interaction that leads to an initial spike that does not appear in the microphone data. This interaction is followed by two oblique interactions that do appear in the microphone data, though the intensity of the first oblique interaction is under-predicted by the model.

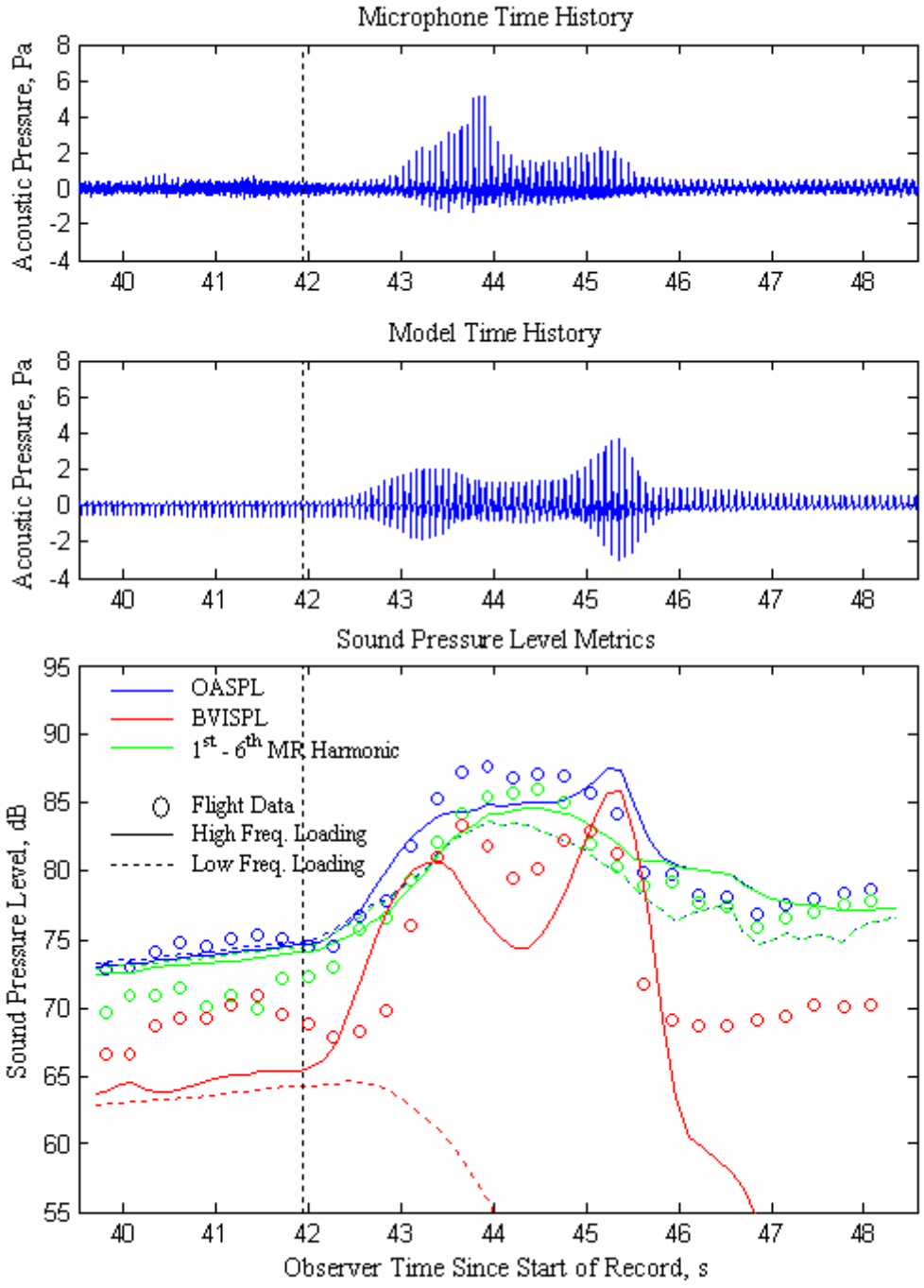

Figure 4.34. Fast pull-up retreating-side acoustic trends.

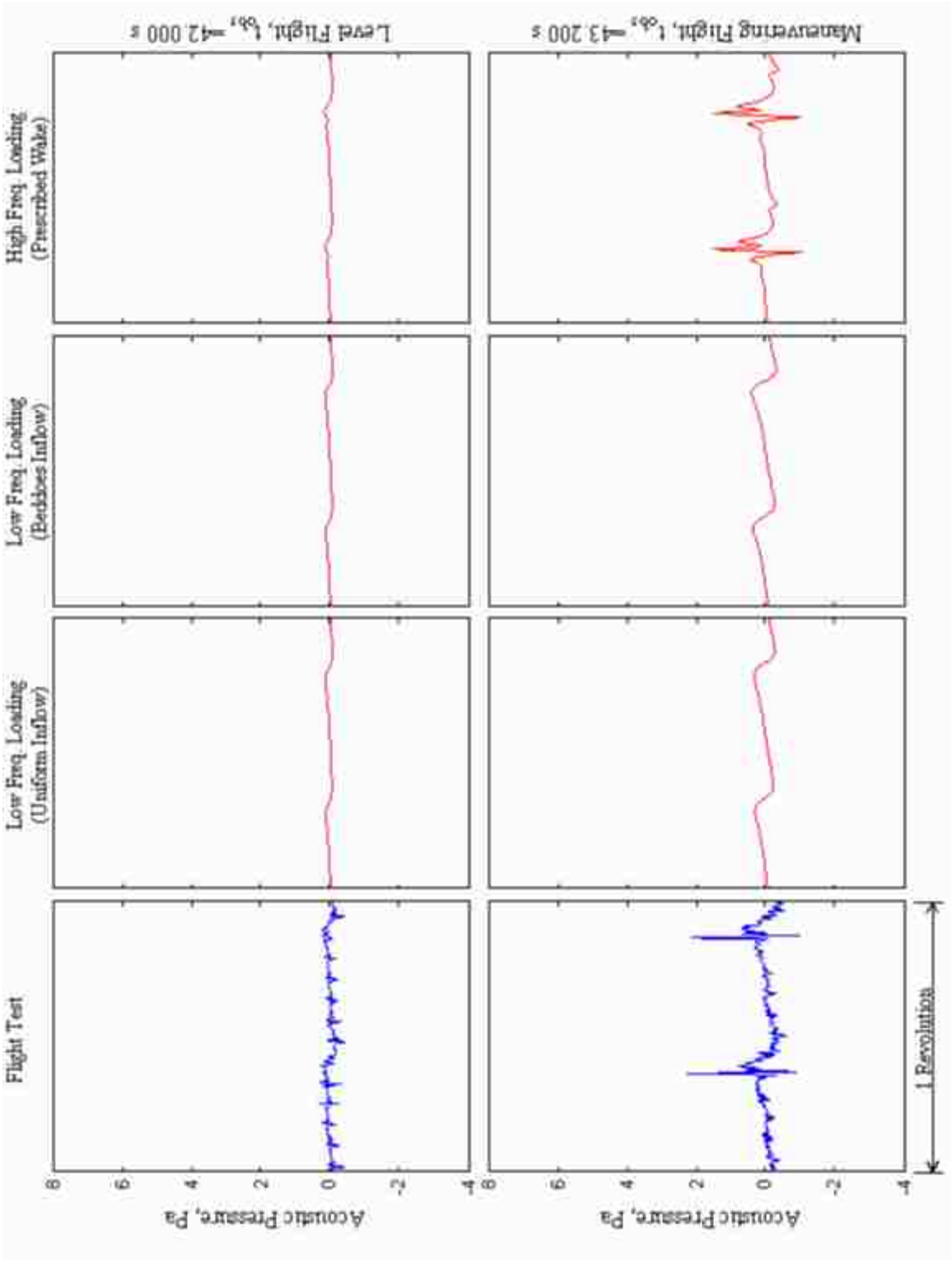

Figure 4.35. Fast pull-up retreating side acoustic details.

4.3.3 Slow Pull-up Maneuver

Controls optimized to fit the fuselage pitch rate recorded by the in-flight instruments result in the response presented in Figure 4.36 for the slow pull-up maneuver. Based on this optimization schedule, the pull-up maneuver is believed to have been initiated at 46.5 seconds into the maneuver. As witnessed in the fast pull-up maneuver, prior to applying the longitudinal cyclic, an unintended pitching transient occurred during the level flight regime. While it was possible to fit a longitudinal cyclic schedule to fit this transient, this perturbation was not fully described by a longitudinal cyclic input and does result in deviation between the model and the in-flight data.

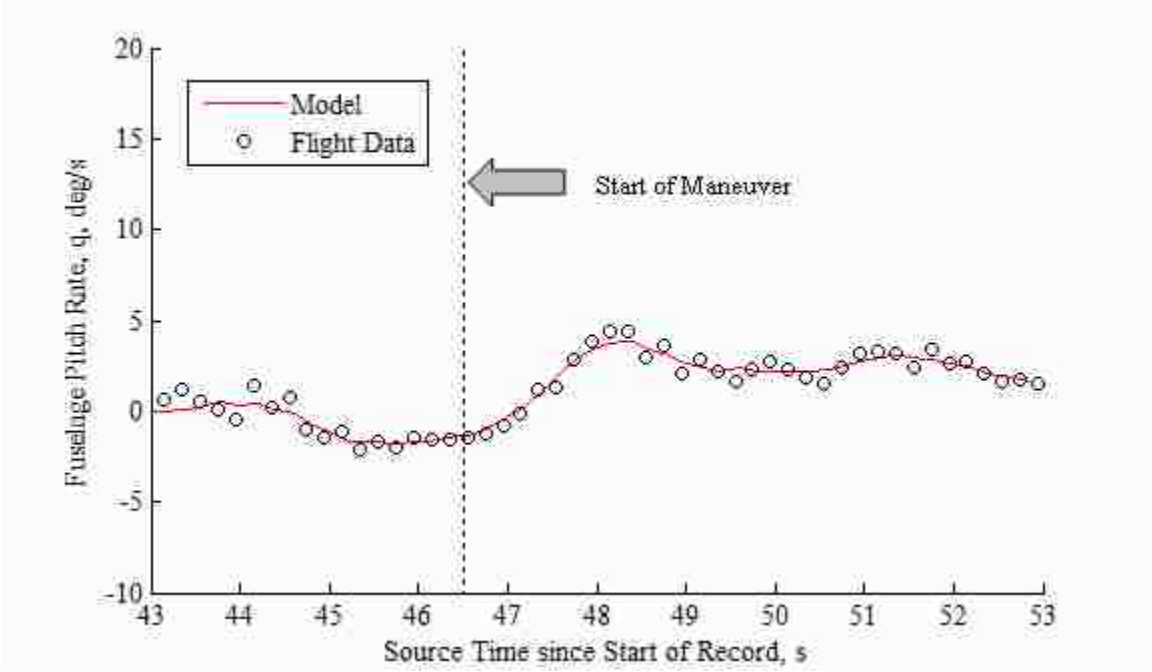

Figure 4.36. Slow pull-up fuselage pitch rate time history.

Responses of the flight path angle, advance ratio, and trajectory during the slow pull-up maneuver are provided in Figure 4.37, Figure 4.38, and Figure 4.39 respectively. Note that the observed perturbation results in an initial deviation between the model and

the in-flight measurements suggesting that the transient was not created by a purely longitudinal cyclic input. Though the trends of the model follow those recorded by the in-flight data, the controller perturbations are so small for the slow pull-up maneuver that the model never completely recovers from the unintended transient during the level flight region.

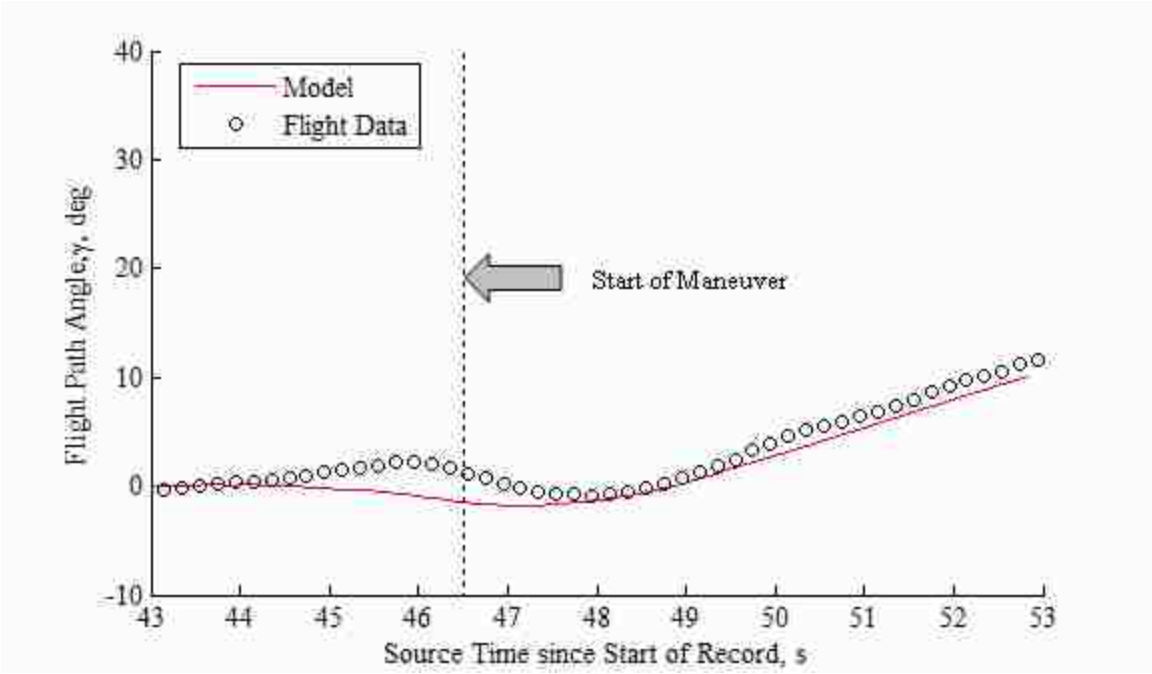

Figure 4.37. Slow pull-up flight path time history.

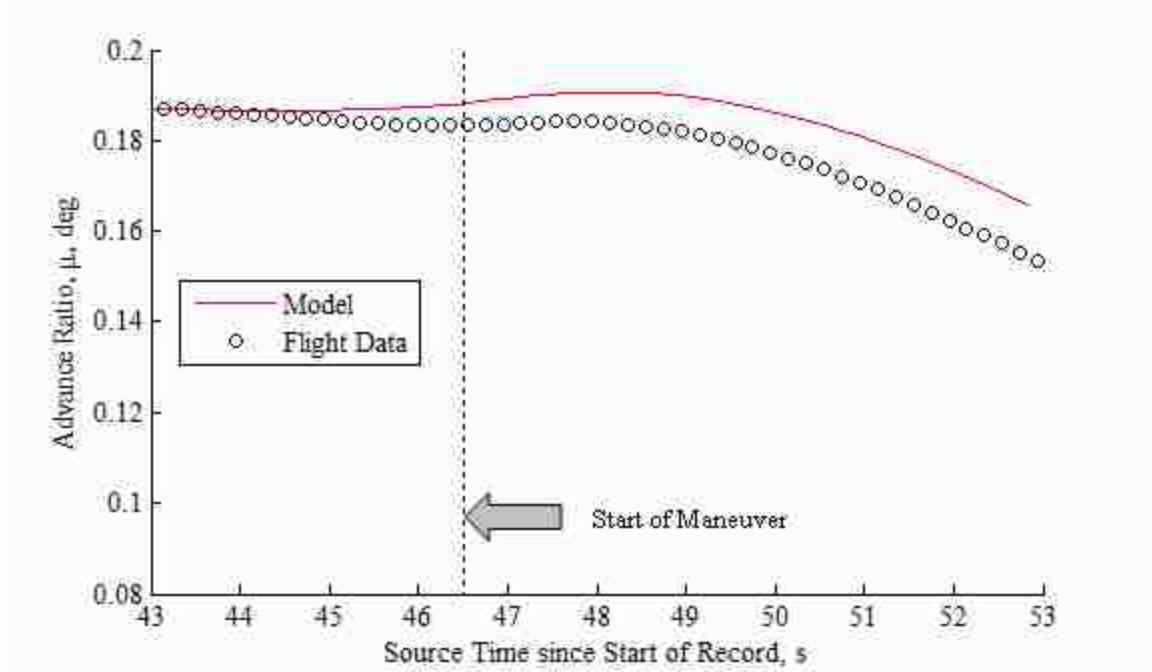

Figure 4.38. Slow pull-up advance ratio time history.

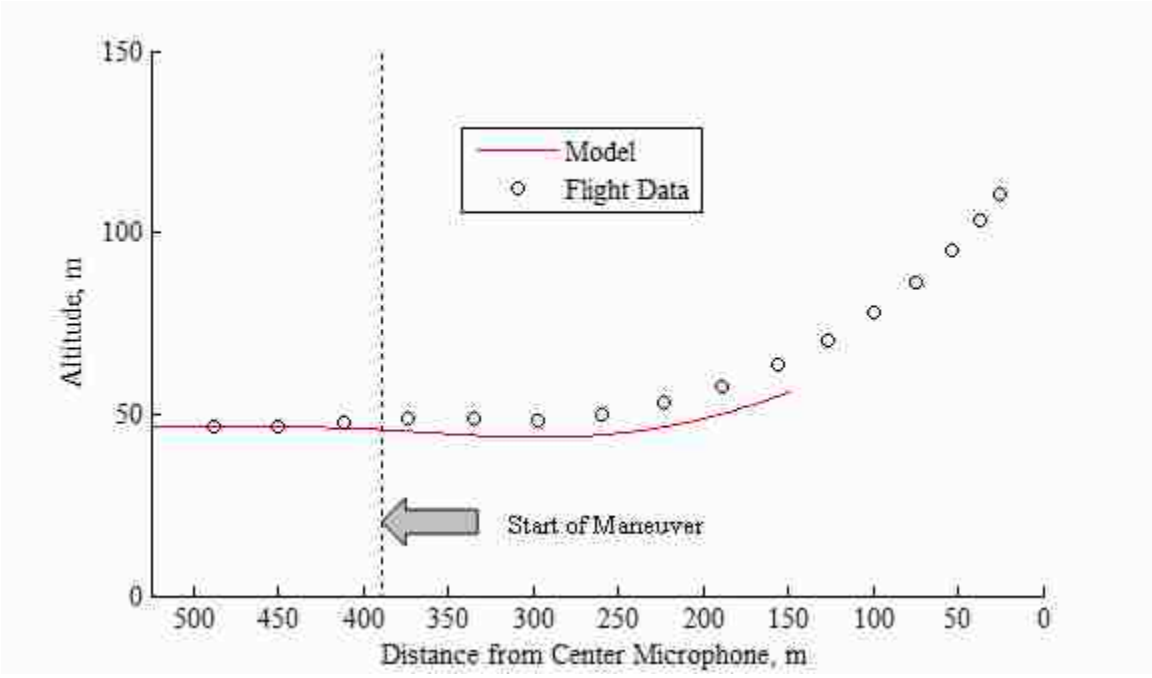

Figure 4.39. Slow pull-up flight trajectory.

Similar observations regarding the unintended transient are captured in the thrust time history (see Figure 4.40). The initial transient results in a temporary increase in main rotor thrust followed by a drop right when the maneuver is initiated. Again, the model eventually recovers, but since the controls required for the slow pull-up are so small, the effects of the unintended transient stand out more than any observed in the moderate and fast pull-up maneuvers.

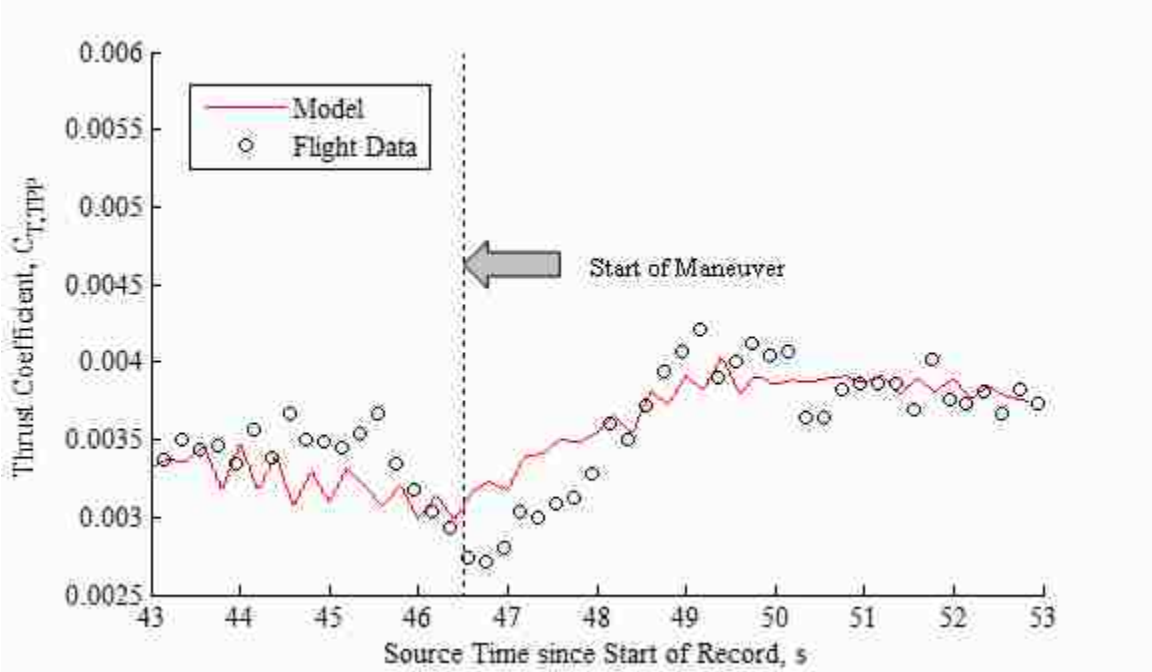

Figure 4.40. Slow pull-up thrust time history.

The transient also has an effect on the angle of attack of the tip-path plane (see Figure 4.41). The unintended transient results in an initial downward pitch of the tip-path plane that is maintained until the pull-up is initiated. Furthermore, the misalignment error in the system is evident in the offset between the model and the data.

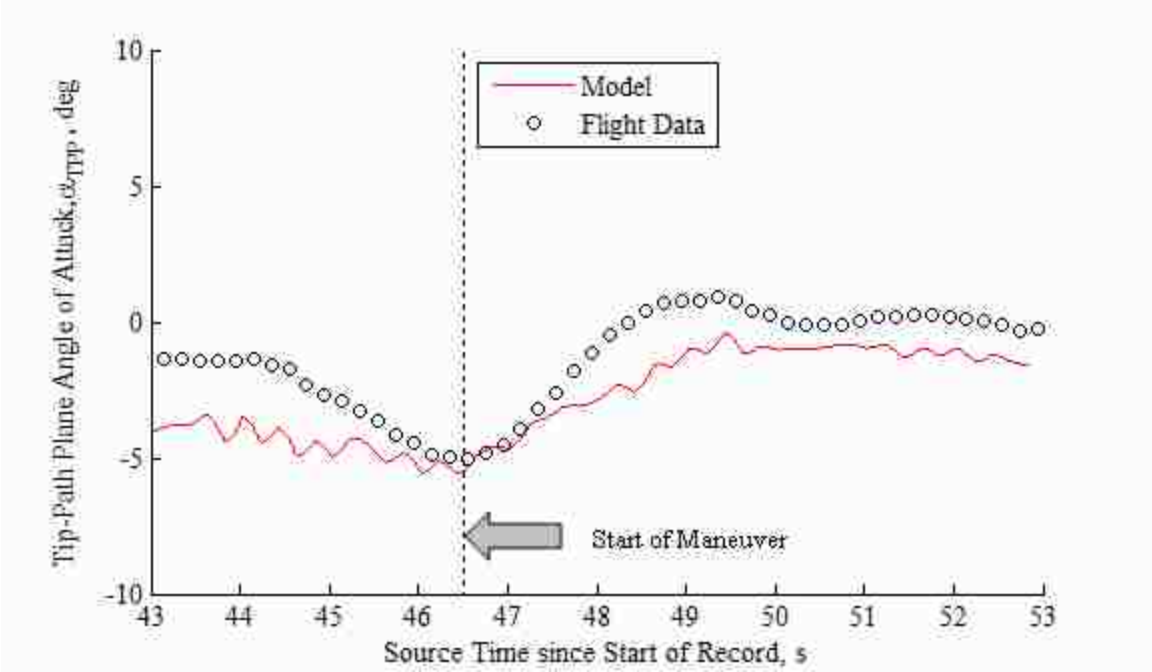

Figure 4.41. Slow pull-up tip-path plane angle of attack time history.

Acoustic trends for the center microphone during the slow pull-up maneuver are presented in Figure 4.42. The top plot illustrates the raw center microphone recordings; the center plot illustrates the predictions of the high-frequency loading mode; and the bottom plot illustrates the time histories of various acoustic metrics over the course of the maneuver.

From the data, it appears that the unintended transient results in the wake approaching the tip-path plane earlier than the model predicts. However, as the transient dissipates and the model recovers, the predicted acoustics match well with the recordings. The lack of a peak in the model suggests that the wake remains close to the tip-path plane, but does not penetrate it. In the case of the low frequency loading noise model, the directivity characteristics of the thickness noise again produce a drop off in the BVISPL

as the observer moves out of the plane of the rotor. As the tip-path plane tilt is shallower for the slow pull-up maneuver, this drop off occurs much later in the maneuver.

Details of the center microphone acoustics are provided in Figure 4.43 during the level flight region and during the maneuver when impulsive BVI noise is present. The low frequency loading models do a good job of capturing the low frequency noise in both regions while the high-frequency loading model captures the general trends of the BVI noise. As witnessed in the moderate and fast pull-up maneuvers, the initial peak in the predicted BVI pulse is an over prediction of the parallel interaction which is not found in the center microphone data. Better agreement is observed for the two oblique interactions, but the model does tend to over-predict the intensity of the negative spike of the first oblique BVI interaction.

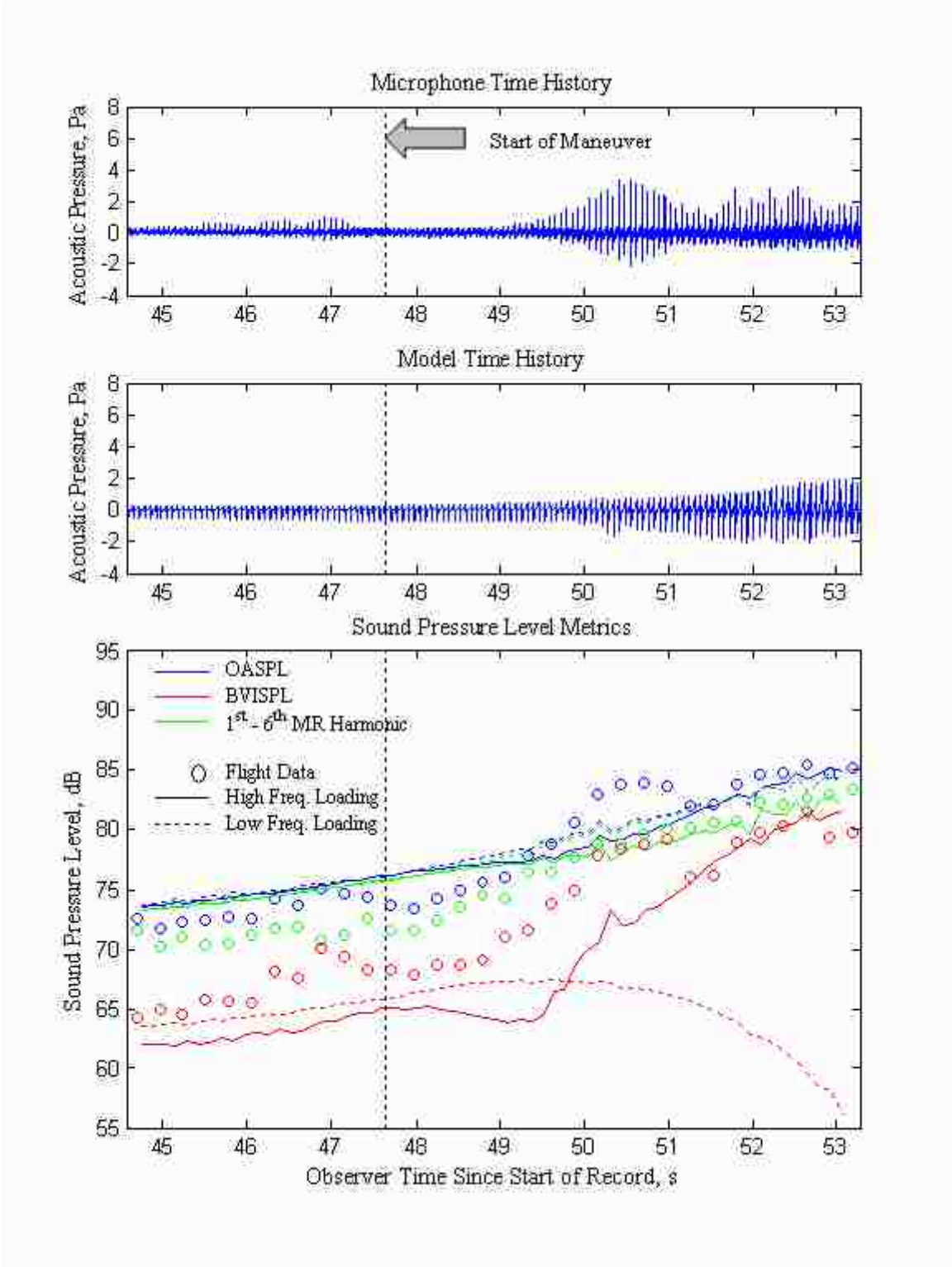

Figure 4.42. Slow pull-up center microphone acoustic trends.

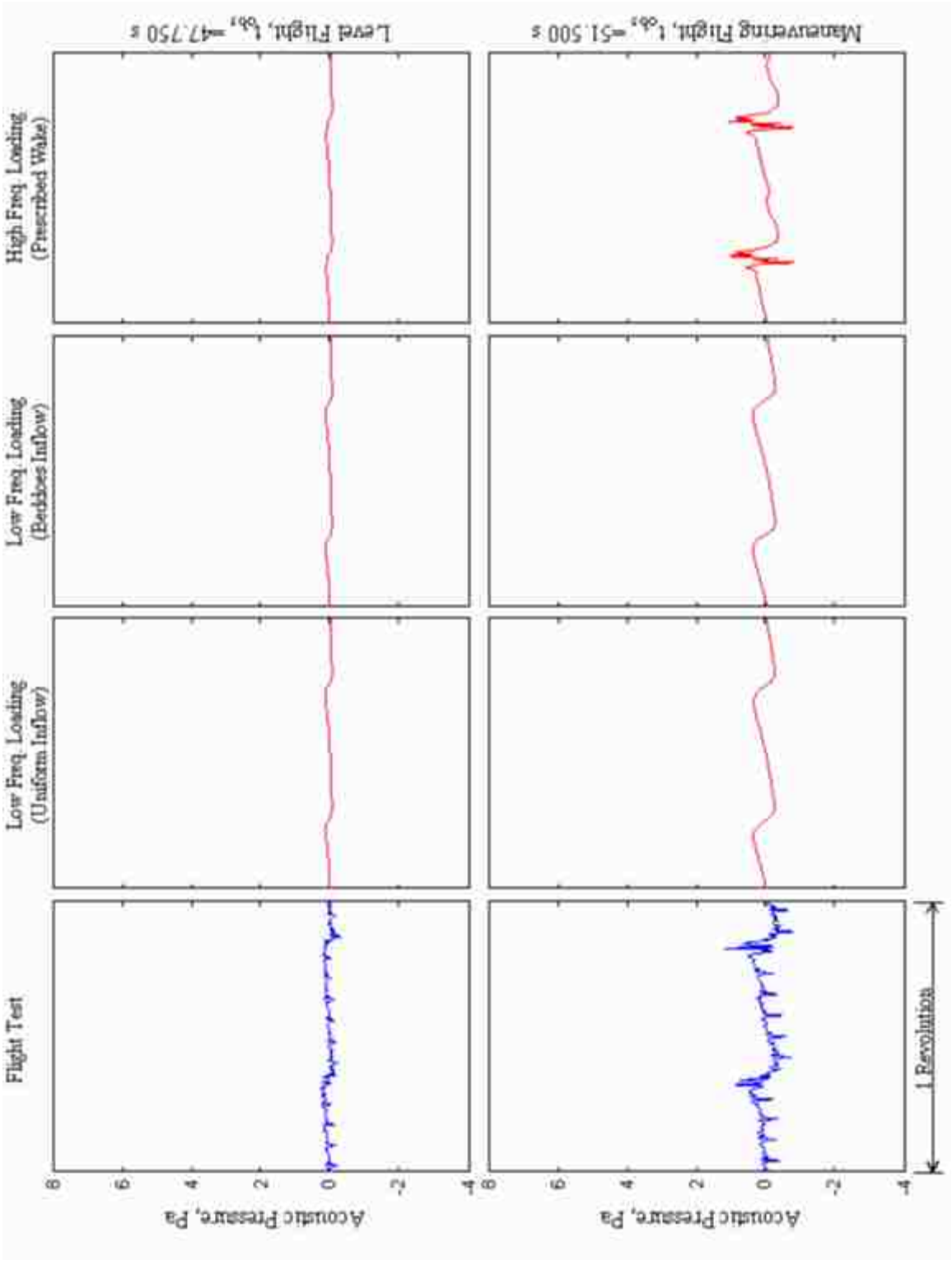

Figure 4.43. Slow pull-up center microphone acoustic details.

Acoustic trends for the advancing-side microphone are provided in Figure 4.44 for the slow pull-up maneuver. While an increase in BVI noise is predicted by the model, neither the microphone nor the model indicate significant BVI in the time history. This is due to the directivity characteristics of the parallel interaction which dominates BVI on the advancing side. During the slow pull-up maneuver, the advancing-side microphone was not in a location conducive for perceiving BVI noise.

Details of the advancing side time histories are presented in Figure 4.45. The low frequency noise is captured well by the model, but the BVI noise is insignificant at the location of the advancing-side microphone during the slow pull-up maneuver.

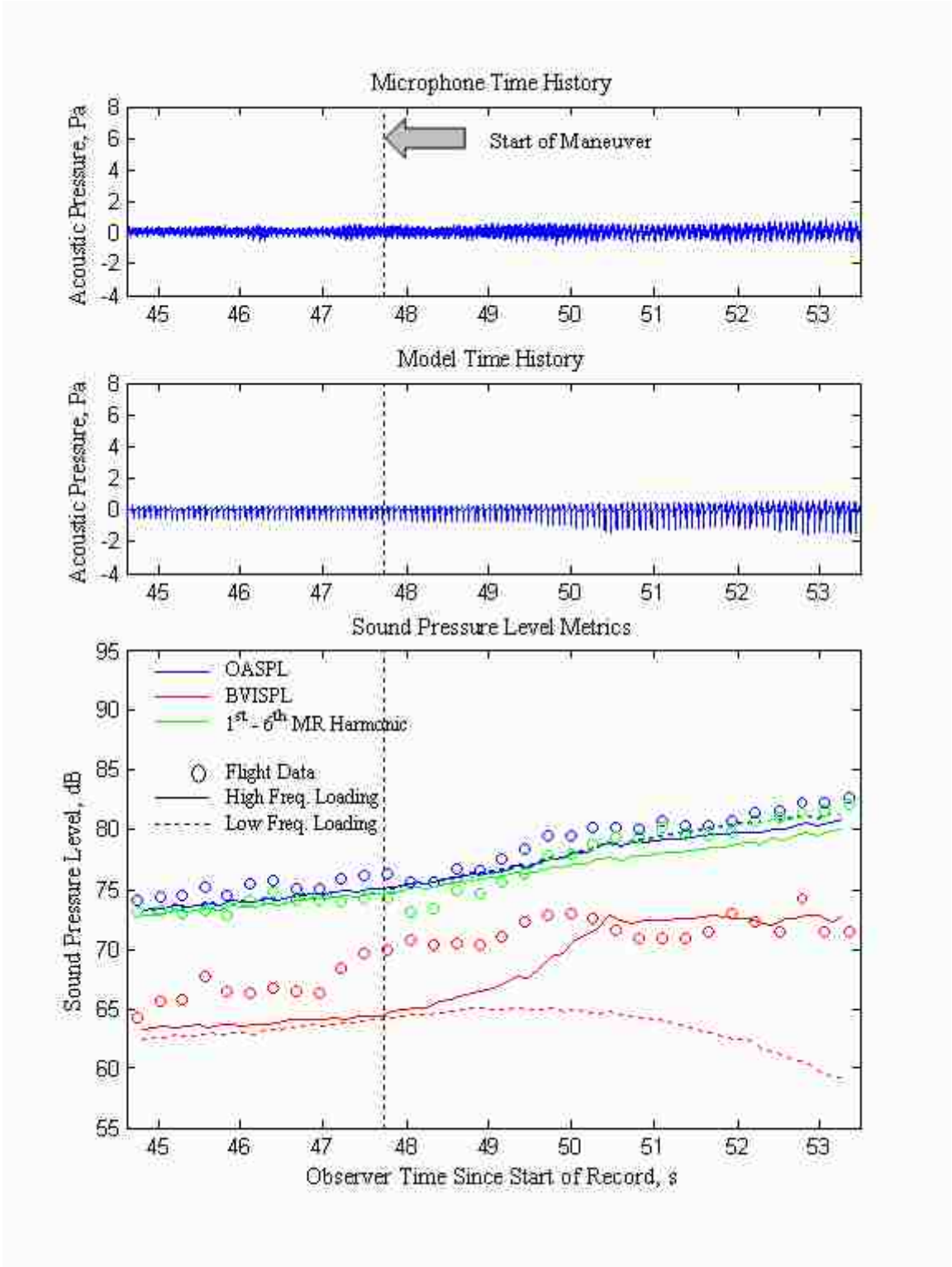

Figure 4.44. Slow pull-up advancing-side microphone acoustic trends.

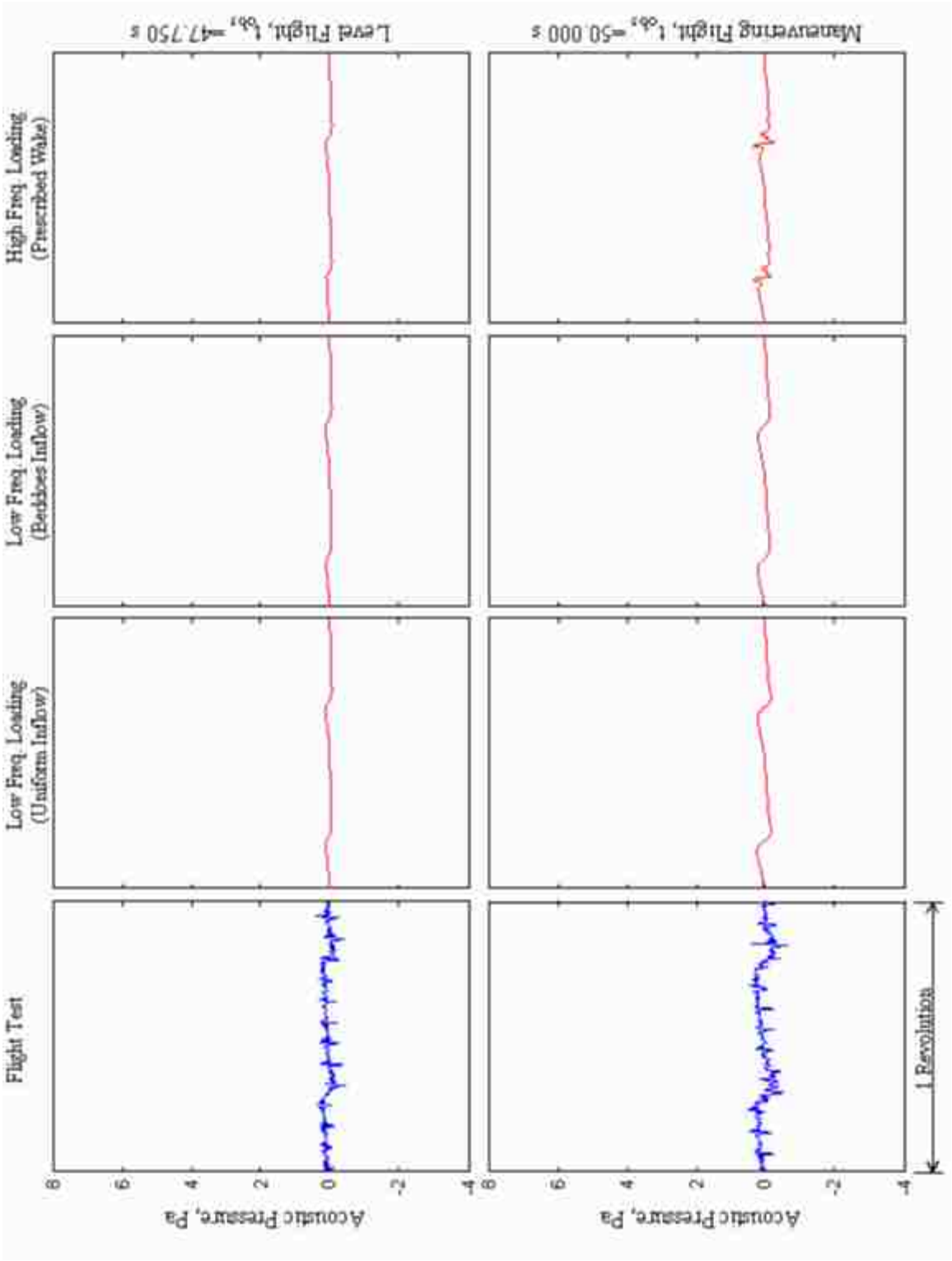

Figure 4.45. Slow pull-up advancing-side acoustic details.

Acoustics trends from the retreating-side microphone are provided in Figure 4.46. A brief peak in impulsive noise is captured by the microphones at 51 seconds into the maneuver, again likely due to the unintended transient that temporarily pushed the wake closer to the tip-path plane. However, the model does capture the gradual build-up of BVI noise as the wake approaches and settles below the tip-path plane of the main rotor.

Details of the individual pulses are provided in Figure 4.47. As observed earlier, the low frequency noise is captured well. Similarly, the characteristics of the retreating-side BVI pulses resemble those from the moderate pull-up maneuver. Both oblique interactions are captured fairly well, though the initial negative peak appears to be over-predicted by the model.

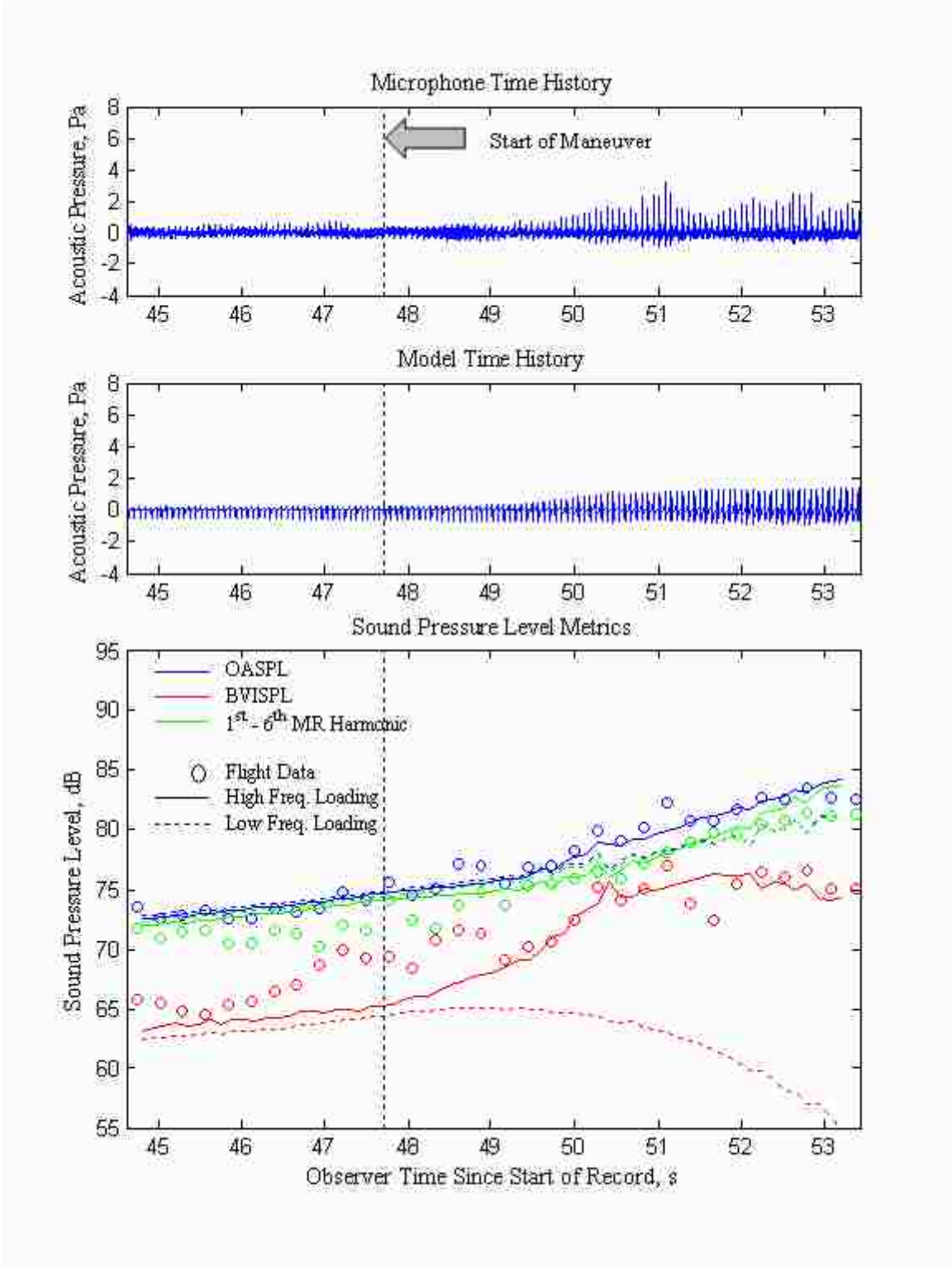

Figure 4.46. Slow pull-up retreating-side acoustic trends.

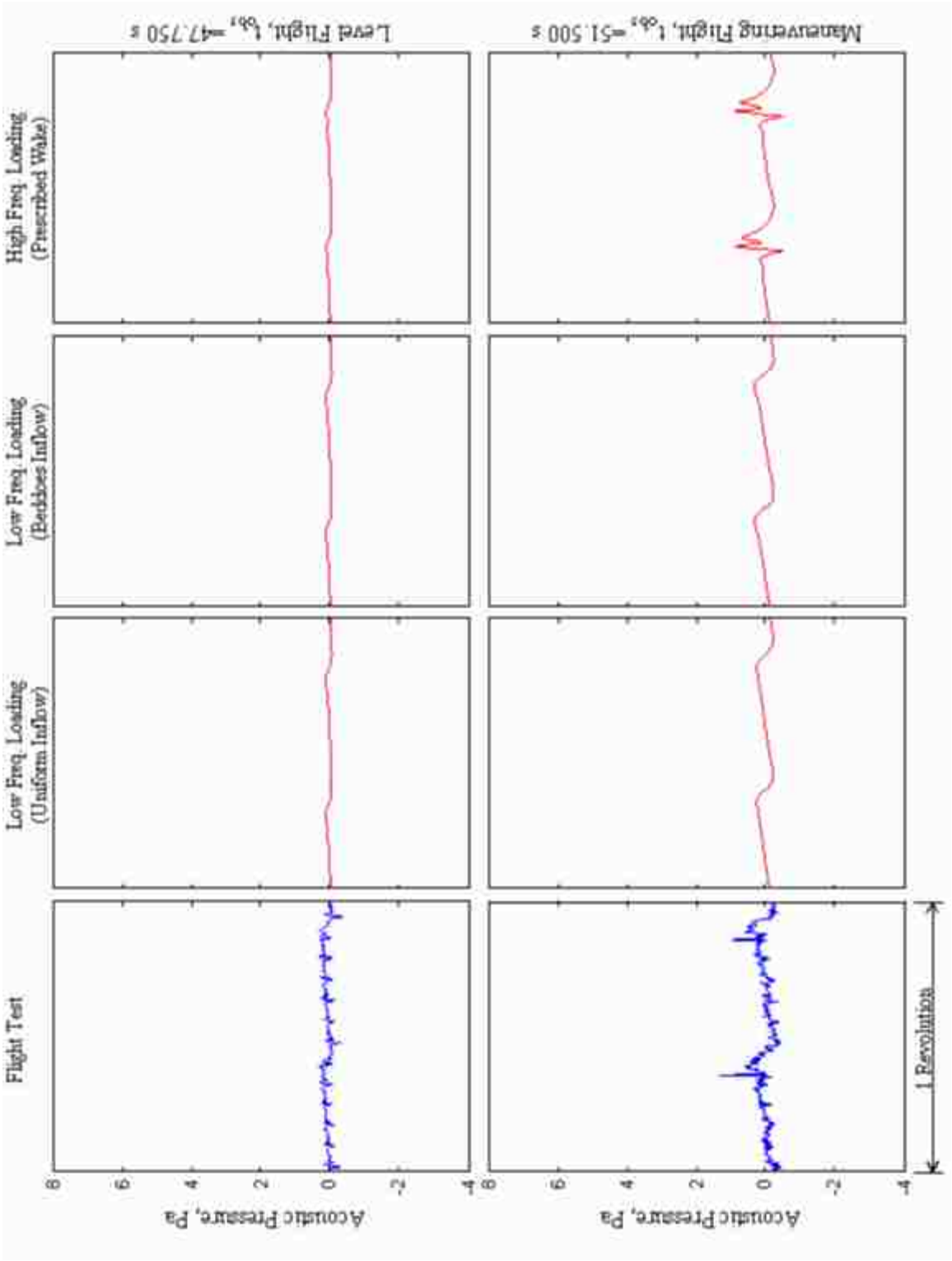

Figure 4.47. Slow pull-up retreating side acoustic details.

4.4 Reduced Order Models

The final section of this chapter investigates the impact of using reduced order and quasi-steady models. These reduced order models include simplifications made to the blade flapping model and to the prescribed wake geometry model. In the case of the blade flapping relaxations, these simplifications are made to investigate the impact of the flapping model on the dynamic response of the system and on the acoustics. In the case of the prescribed wake model, the wake will be replaced by a quasi-steady wake. These studies will be used to evaluate the validity of applying quasi-steady modeling techniques to maneuvering flight. For evaluation, the models will be applied to the fast pull-up maneuver where the effects should be the most pronounced.

4.4.1 Flapping Models

Recall that in the derivation of the flapping equation, a set of two second order differential equations was produced (see Chapter 3). This system, which will be referred to as the second order flapping model, can be represented in vector form as:

$$\begin{Bmatrix} \ddot{a}_1 \\ \ddot{b}_1 \end{Bmatrix} + \mathbf{D}\begin{Bmatrix} \dot{a}_1 \\ \dot{b}_1 \end{Bmatrix} + \mathbf{K}\begin{Bmatrix} a_0 \\ a_1 \\ b_1 \end{Bmatrix} = \vec{f} \tag{4.1}$$

In the first approximation to the flapping equation, suppose that the system can be approximated as a set of two first order differential equations. In this case, the blade inertial load due to the flapping acceleration terms, $\ddot{a}_1$ and $\ddot{b}_1$, is neglected. This system, which will be referred to as the first order flapping model, can be represented in vector form as:

$$\begin{Bmatrix} \dot{a}_1 \\ \dot{b}_1 \end{Bmatrix} + \mathbf{D}^{-1}\mathbf{K} \begin{Bmatrix} a_0 \\ a_1 \\ b_1 \end{Bmatrix} = \mathbf{D}^{-1} \vec{f} \tag{4.2}$$

In the second approximation to the flapping equation, the flapping coefficients will be found using a quasi-steady approximation. In this case, it is assumed that the aircraft is in steady flight and the centrifugal and aerodynamic flapping moments are instantaneously balanced. In this simplification, the flapping acceleration and velocity terms, $\ddot{a}_1$, $\ddot{b}_1$, $\dot{a}_1$ and $\dot{b}_1$, are omitted. This system, which will be referred to as the quasi-steady flapping model, can be represented in vector form as:

$$\begin{Bmatrix} a_0 \\ a_1 \\ b_1 \end{Bmatrix} = \mathbf{K}^{-1} \vec{f} \tag{4.3}$$

The fuselage pitch rate time histories for the three flapping models are presented in Figure 4.48 for the fast pull-up maneuver. All three cases feature the same longitudinal cyclic input schedule that was optimized to match the fuselage pitch rate using the 2nd order flapping model. The fuselage pitch response featuring the 1st and 2nd order flapping models are nearly identical. The pitch response for the quasi-steady model precedes the other models by approximately one rotor revolution, or 0.15 seconds.

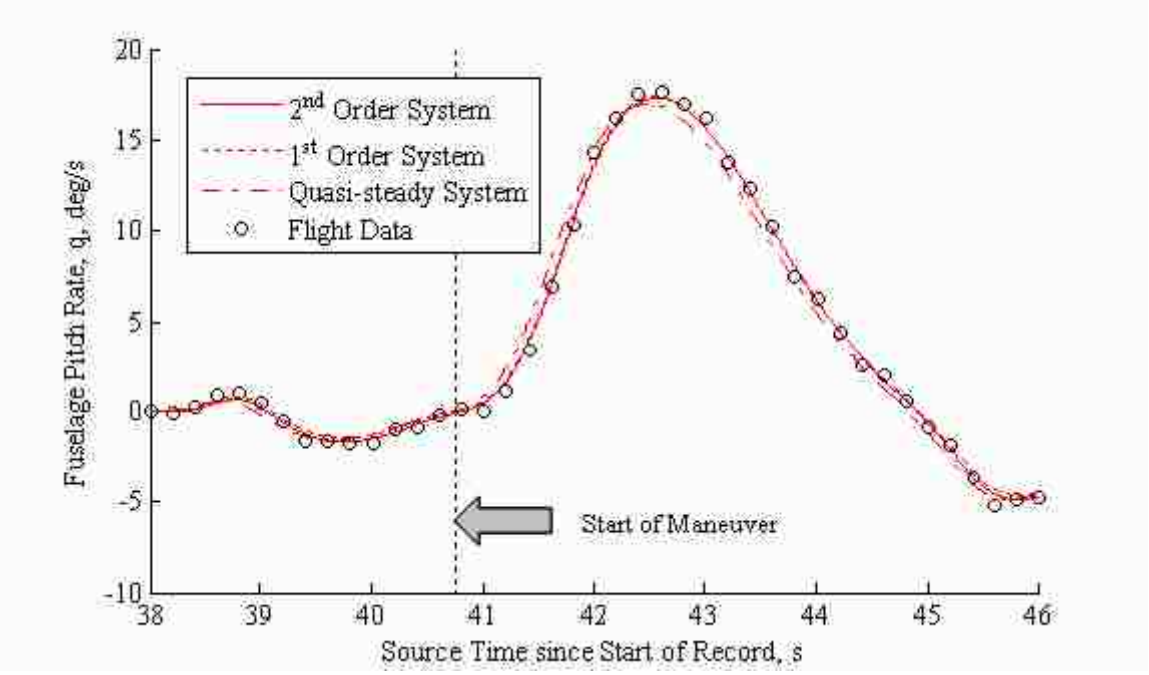

Figure 4.48. Fast pull-up fuselage pitch rate for various flapping models.

The flight path angle, advance ratio, and flight trajectories for the three flapping models are provided in Figure 4.49, Figure 4.50, and Figure 4.51 respectively. All three flapping models yield similar responses during the level flight and for several seconds after the initiation of the maneuver. The quasi-steady system again precedes the other models, but the differences are marginal.

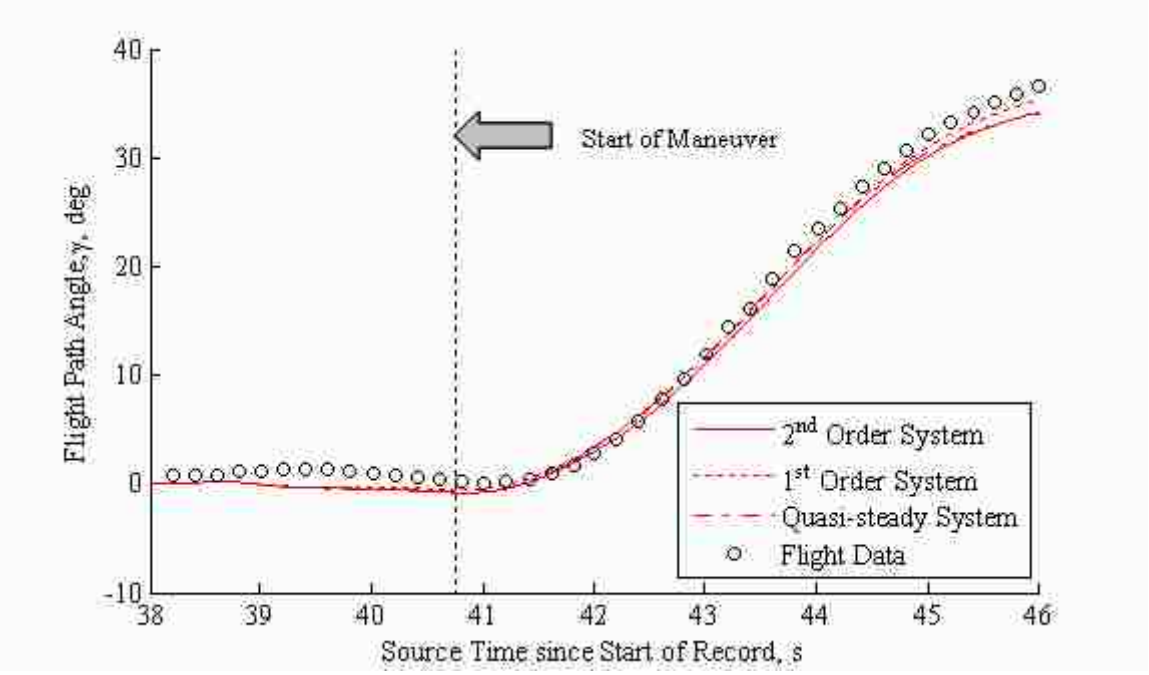

Figure 4.49. Fast pull-up flight path angle for various flapping models.

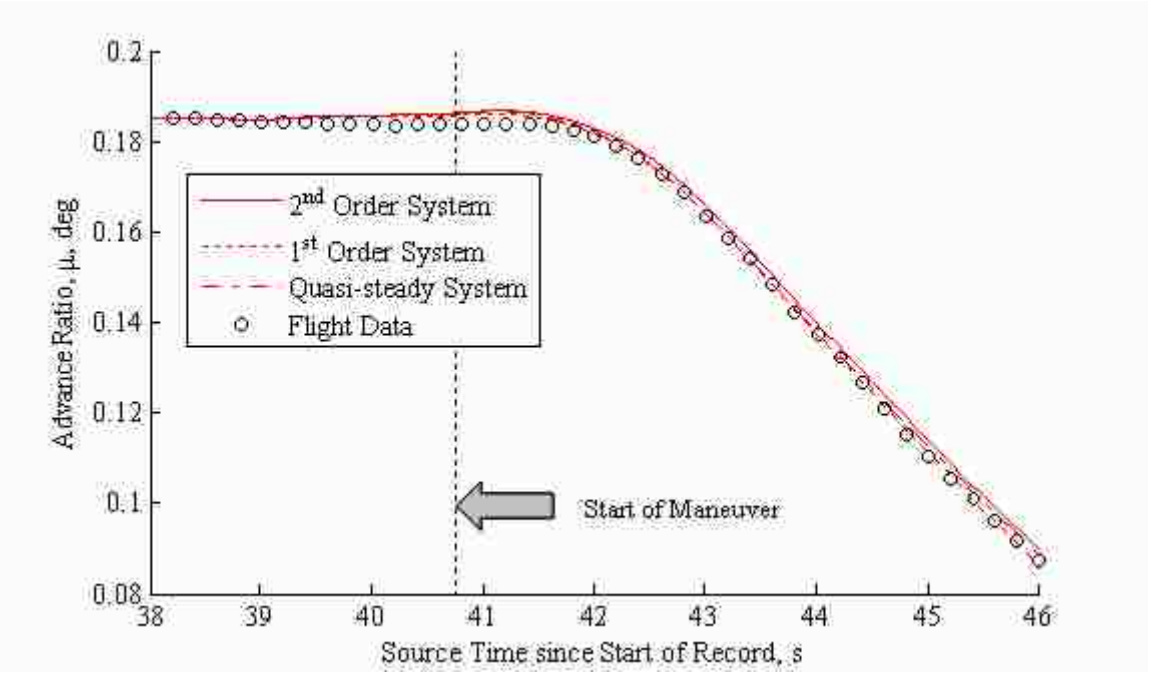

Figure 4.50. Fast pull-up advance ratio for various flapping models.

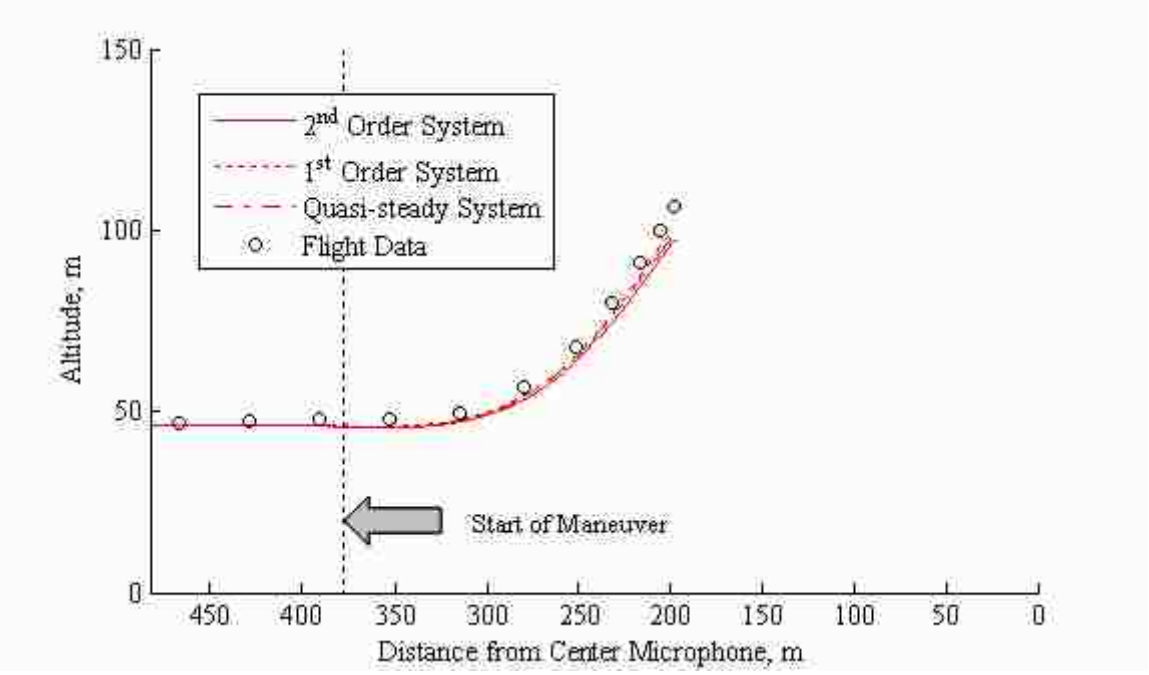

Figure 4.51. Fast pull-up flight trajectory of various flapping models.

The time history of the thrust coefficient during the fast pull-up is provided in Figure 4.52. As observed with the fuselage pitch response, the 1st and 2nd order systems behave nearly identically while the quasi-steady model precedes the others by approximately one rotor revolution (0.15 seconds).

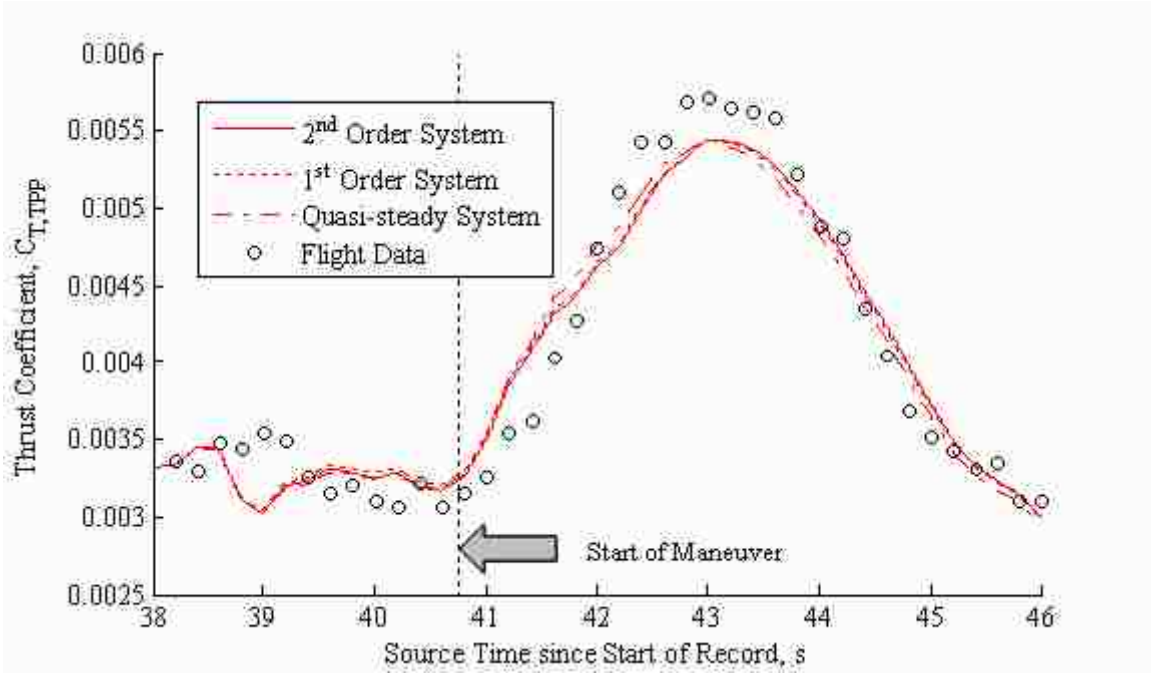

Figure 4.52. Fast pull-up thrust coefficient for various flapping models.

The angle of attack of the tip-path plane is presented in Figure 4.53 for the fast pull-up maneuver. Again, the 1st and 2nd order flapping models produce similar results while the quasi-steady flapping model precedes the others by one main rotor revolution.

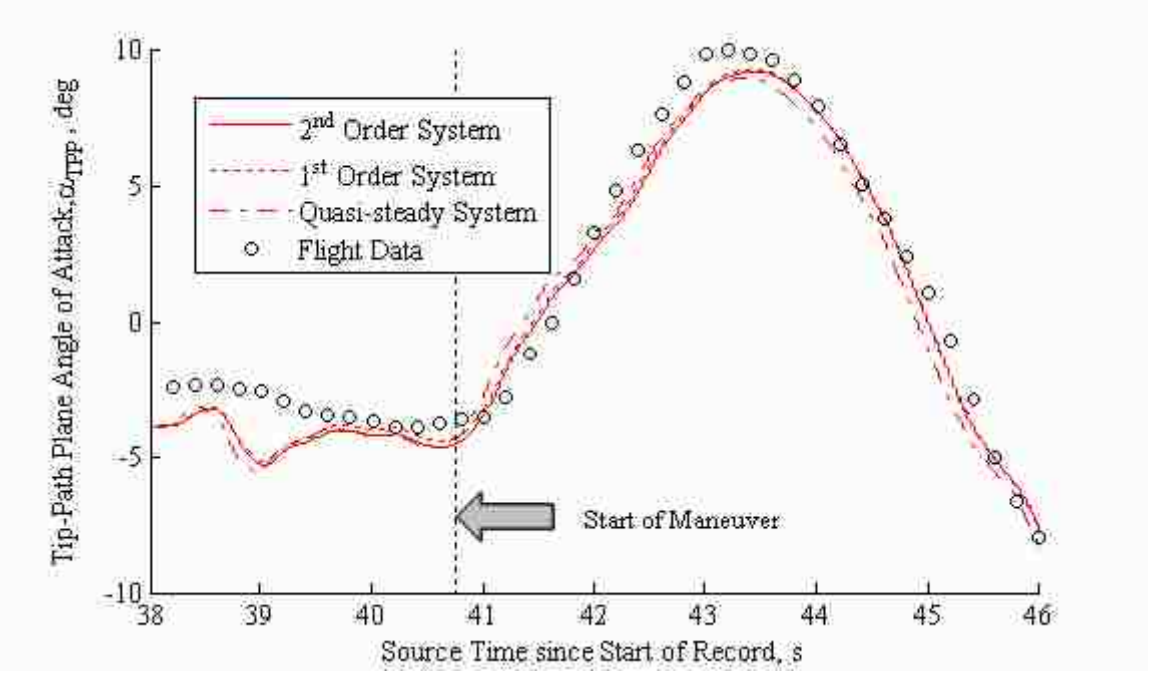

Figure 4.53. Fast pull-up tip-path plane angle of attack for various flapping models.

The time histories of several acoustic metrics are presented in Figure 4.54 for the flapping models during the fast pull-up maneuver. The overall acoustic trends between all three flapping models are extremely similar. The acoustic levels of the 1st order model are slightly ahead of the 2nd order model while the quasi-steady model continues to precede the others by one main rotor revolution. This suggests that there are slight wake geometric differences between the wakes of the flapping models. Evidence of this is illustrated in Figure 4.55 which displays the wake geometry of each of the models at different stages throughout the pull-up maneuver. While all three wakes are very similar, the 1st and quasi-steady models respond slightly faster than the 2nd order model. However, these differences are small and indicate that the reduced order flapping models do not significantly affect the acoustics radiated by the aircraft.

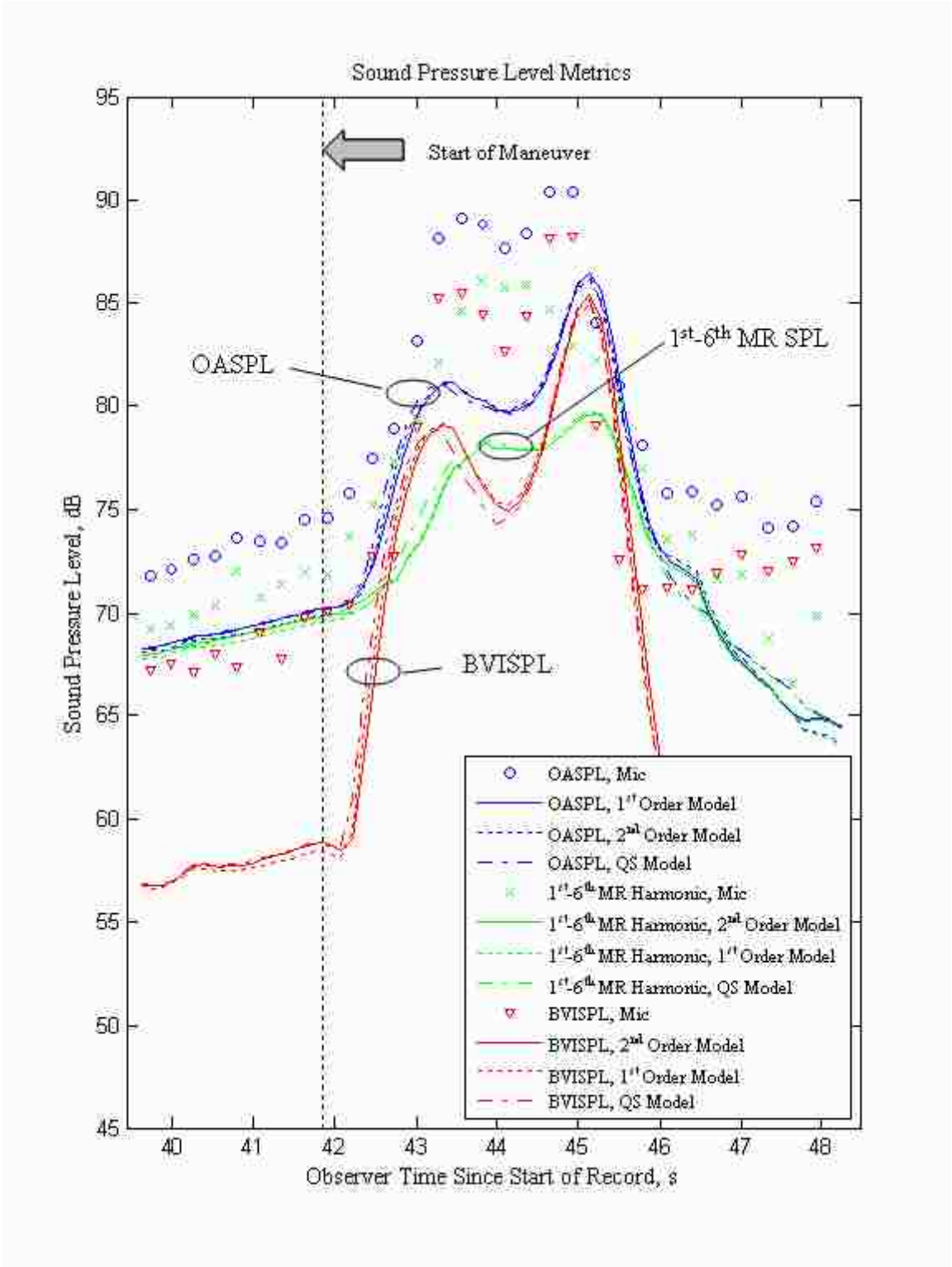

Figure 4.54. Fast pull-up acoustic trends for various flapping models.

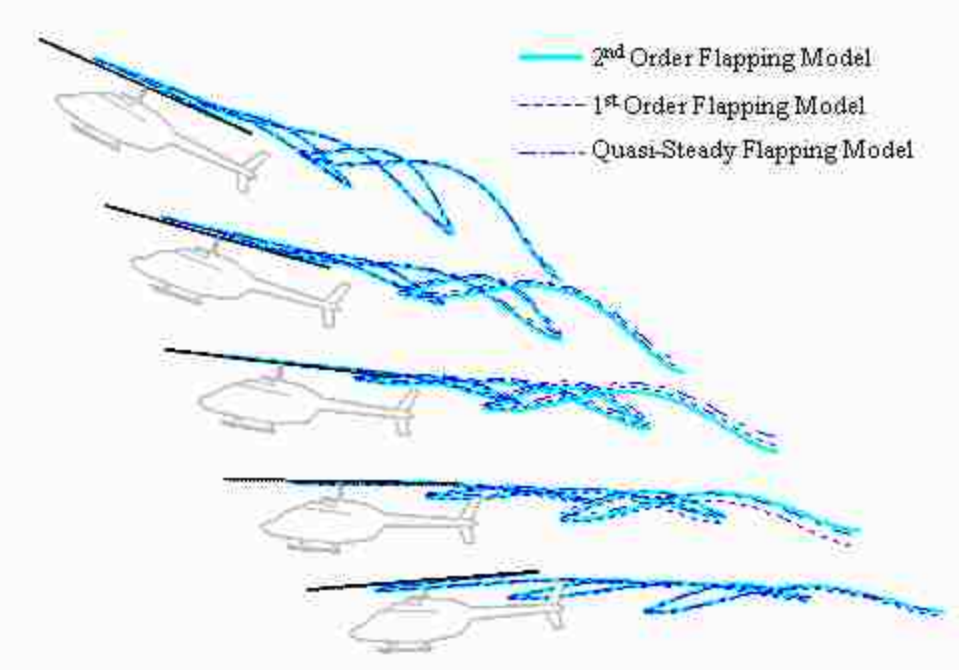

Figure 4.55. Fast pull-up wake geometry of various flapping models.

4.4.2 Wake Models

As mentioned in Chapter 3, two methods are used to obtain the geometry of the wake. In the first method, the position vectors to the wake filament nodes are found by integrating the relative velocity of each node with respect to the tip-path plane. This approach, which will be referred to as the time integrated wake model, captures the effects of the motion of the tip-plane as the aircraft maneuvers during flight. As the arbitrary motion of the tip-path plane produces unique wake geometry at each moment in time, the wake geometry and corresponding induced velocity at the blade control points must be updated at each time step.

In the second method, the position vectors to the wake filament nodes are found assuming a quasi-steady wake. This approach represents the instantaneous flight conditions using a technique similar to the Quasi-Static Acoustic Mapping (Q-SAM)

method to predict the noise shapes and levels radiated by the aircraft. This method is preferable for real time systems since the noise levels and directivity characteristics can be stored in a database in advance and referenced from look-up tables during flight for a given advance ratio, flight path angle, and main rotor thrust.

The acoustic trends from both wake modeling methods is provided in Figure 4.56 for the fast pull-up maneuver. As expected, the quasi-steady model responds slightly faster than the time integrated model, but only by approximately one main rotor revolution. This is further supported by the wake geometry plots shown during the pull-up in Figure 4.57. Initially, during the level flight region, the two models produce identical wake geometries. As the pull-up is initiated, the two models begin to separate, but most of the divergence is for wake nodes well outside of the main rotor boundary. Nodes in the vicinity of the main rotor, where the BVI noise is generated, are closer to the point of rotation and experience smaller deflections as the tip-path plane rotates. Therefore, quasi-steady approximations for the wake geometry should produce fair estimations of the acoustics during maneuvering flight.

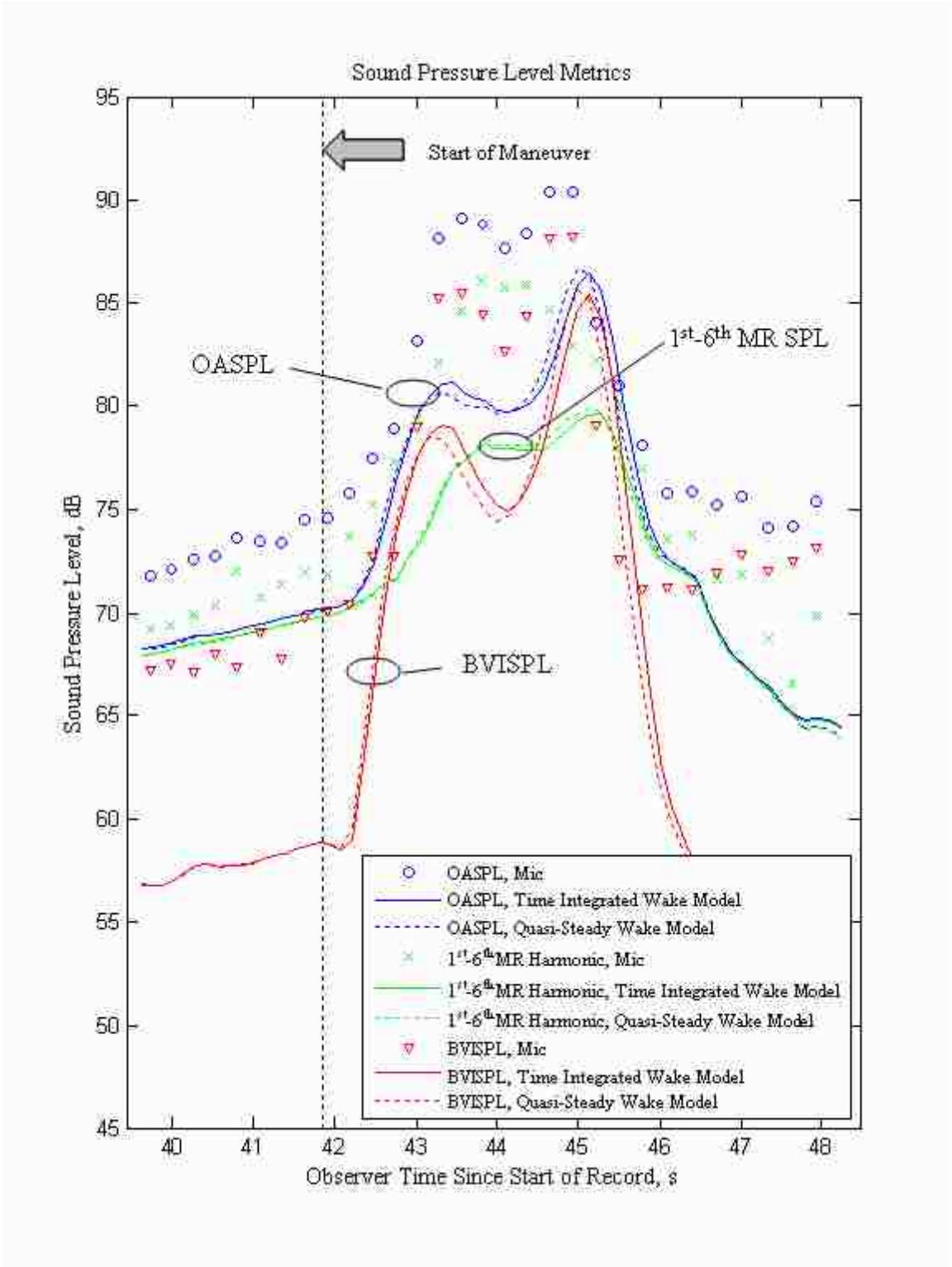

Figure 4.56. Fast pull-up acoustic trends for wake models.

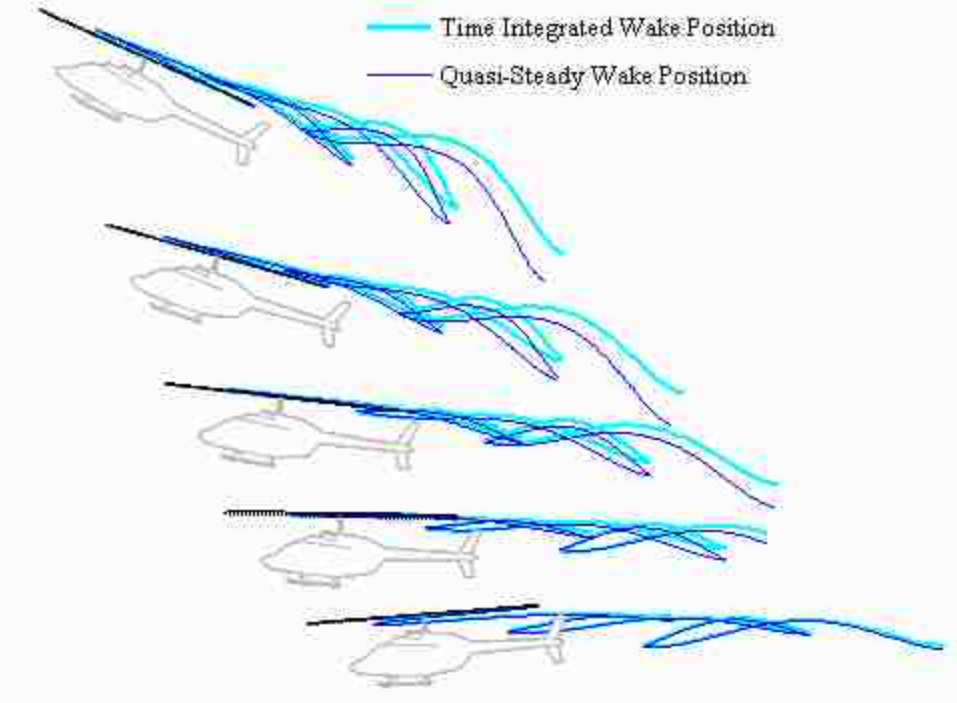

Figure 4.57. Fast pull-up wake geometry for wake models.

4.5 Summary

Overall, the first principles model captures the general trends of steady flight quite well. The low-frequency noise model accurately captures the amplitude of the low-frequency noise recorded by the microphones. Slightly better agreement is obtained using the Beddoes' inflow model, but uniform inflow produces adequate results as well. The high-frequency noise model tends to over predict the BVI intensity, but it does capture the basic pulse shape. Furthermore, the relationship between the descent angle and the intensity of the acoustic radiation of the aircraft is captured by the high-frequency loading model.

The first principles model does a fair job of capturing the acoustics radiated during the pure longitudinal cyclic pull-up maneuvers. During the moderate and fast pull-up maneuvers, the dynamics model replicated the response of the aircraft extremely well

when compared to the data recorded by the flight instruments. Slightly inferior results were obtained for the slow pull-up maneuver due to an unexpected transient experienced just prior to executing the maneuver. Since the control perturbations for the slow pull-up maneuver were quite low, the slow pull-up maneuver exhibited a high dependency on the trimmed state of the aircraft.

Overall, the acoustic model did a good job of replicating the pulse shape and amplitude of the low frequency noise generated by the main rotor during steady state and maneuvering flight. The simple wake model was also adequate for predicting the occurrence and general trends of impulsive BVI noise. The predicted levels and duration of BVI events matched reasonably well with the microphone recordings.

Some of the details of the predicted BVI pulse shapes differ from the acoustic recordings, but this is largely due to the wake modeling assumptions. Refinements to the wake model could be made by including more trailed vortex filaments and adjusting parameters to account for effects like wake contraction and vortex core growth over time. These refinements could produce more accurate pulse shapes, but little to no validation data is available for making these corrections.

Lastly, an investigation found that reasonable results can be obtained by using quasi-steady flapping and quasi-steady wake geometry models. Incorporation of quasi-steady approximations yielded acoustic responses similar to higher order models, but at significantly reduced computational cost. Typically the quasi-steady models responded approximately one rotor revolution faster, but did not dramatically differ from the higher order models. This limited impact is likely the reason for the success of studies that have

attempted to predict the acoustics of maneuvering flight by breaking the maneuver into a series of steady-state clips.

Chapter 5 Application of Model

5.1 Overview

In Chapter 3, a first principles model was developed for predicting the acoustics radiated by a two-bladed teetering rotor during longitudinal maneuvering flight. In Chapter 4, this model was successfully compared to data recorded during a flight test. Results of this analysis verified that during the pure cyclic pull-up maneuvers, BVI noise was the dominant source of the near-horizon harmonic noise radiated by the main rotor.

In this chapter, the model will be further applied to longitudinal flight. The model will first be used to study the importance of thickness and low frequency loading noise in the absence of BVI noise. Each noise source will be broken down to identify directivity characteristics and important relationships between the acoustic terms and the final wave form.

Next, the model will be used to study alternative longitudinal maneuvers. This will include evaluating other methods of initiating climbs and descents with an emphasis on reducing the levels of BVI noise generated during the maneuver and minimizing the far field acoustic radiation.

5.2 Investigation of Acoustic Sources

In the case of the Bell 206B-3 executing a pure cyclic pull-up maneuver, BVI noise was the largest contribution to noise radiated towards the horizon. While the Bell 206B-3 has a low disk loading and the wake remains in close proximity to the tip-path plane during flight, aircraft with larger disk loadings would produce wakes further below the tip-path plane and require larger pitch rates to generate substantial BVI noise.

Evidence of this was observed during a 2011 flight test with a Bell 430 where the aircraft had to descend at steep angles to produce notable BVI noise. For such aircraft, other acoustic sources generated by the main rotor could have larger contributions to the detectability of the aircraft during maneuvering flight due to the tip-path plane attitude relative to the observer. Even in the case of the Bell 206B-3, it is possible to fly maneuvers with minimal BVI where directivity characteristics from other sources including thickness noise and low frequency loading noise may have significant contributions to detection.

5.2.1 Overall Acoustic Trends

Consider Figure 5.1 which displays the predicted overall sound pressure level of thickness noise and low frequency loading noise at various observer elevation angles relative to the tip-path plane and at various advance ratios in the absence of BVI noise. In this figure, the observer is directly ahead of the helicopter at the 180° blade azimuth station. The low frequency loading noise is calculated using two inflow distributions: the uniform inflow model and the Beddoes' inflow model. At elevation angles from approximately 30° above the tip-path plane to 15° below the tip-path plane, the thickness noise is louder than the loading noise. As the advance ratio increases, the acoustic levels from thickness noise also increase. Out of the plane of the main rotor, the low frequency loading noise is exposed to the observer and the loading noise becomes louder than thickness noise. In this region, for a given airspeed, the loading noise produced by the Beddoes' inflow distribution is generally louder than the corresponding loading noise from the uniform inflow distribution.

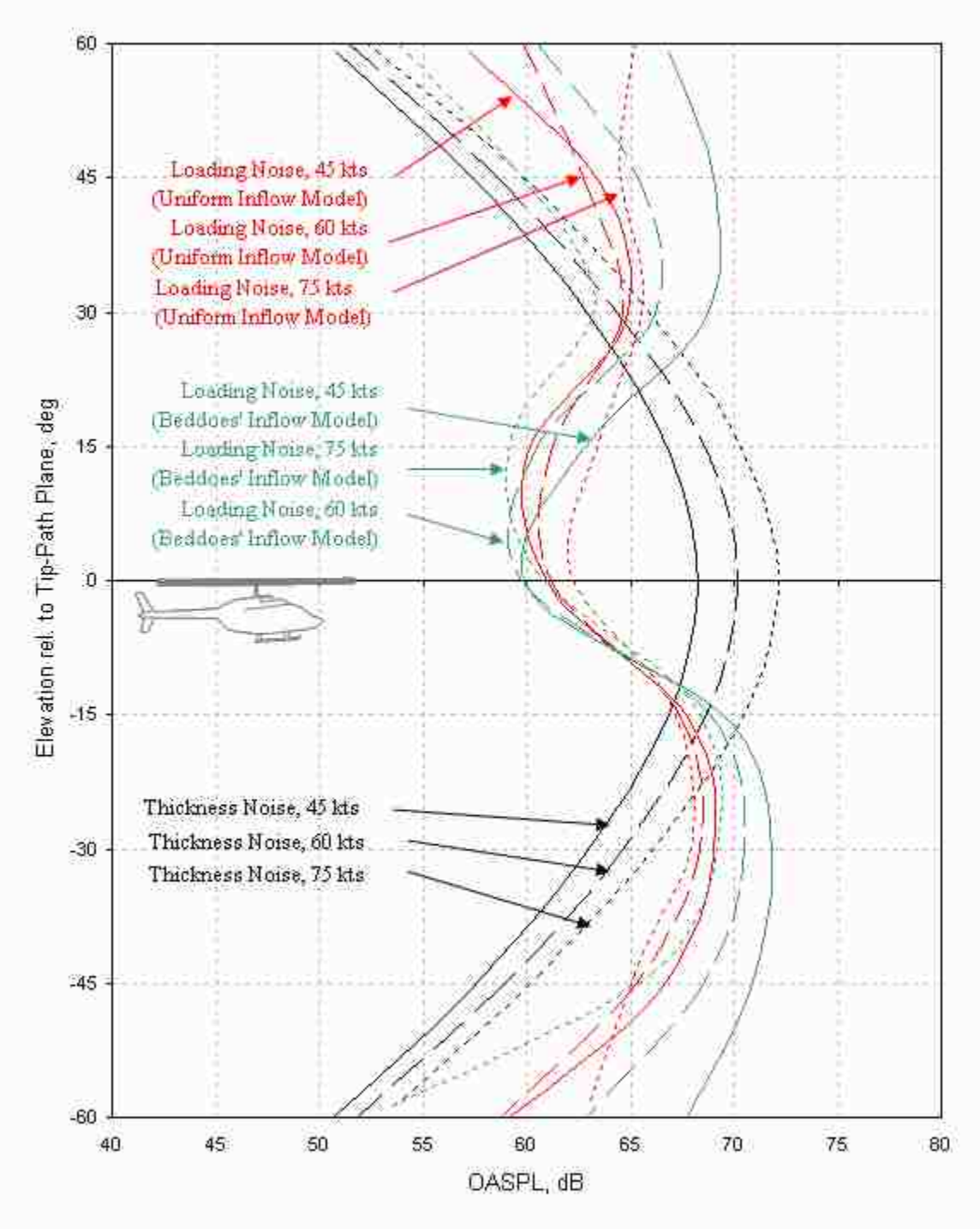

Figure 5.1. Thickness and low frequency loading noise overall sound pressure level (OASPL) at various elevation angles relative to the main rotor tip-path plane. -90° is directly below the main rotor tip-path plane.

Detailed pulse shapes of each of the noise sources are provided in Figure 5.2 over one full revolution at various observer elevations. Figure 5.2 illustrates that as the airspeed of the aircraft increases, the thickness noise becomes louder and more impulsive. Loading noise is essentially described by a saw tooth wave and the airspeed affects the sharpness of the wave. Furthermore, while the pulse shapes of the two inflow distributions are essentially the same, subtle differences are evident. The saw tooth is generally sharper for the Beddoes' inflow distributions and generates higher sound pressure levels. However, as the observer moves outside of the plane of the rotor, the relationship between the airspeed and the sharpness of the waves diverges. The model predicts sharper waves at higher airspeeds for the uniform inflow model and flatter waves at higher airspeeds for the Beddoes' inflow model. This suggests that the details of the loading distribution at certain azimuth locations may have a significant effect on the low frequency loading noise radiated towards the far field observer.

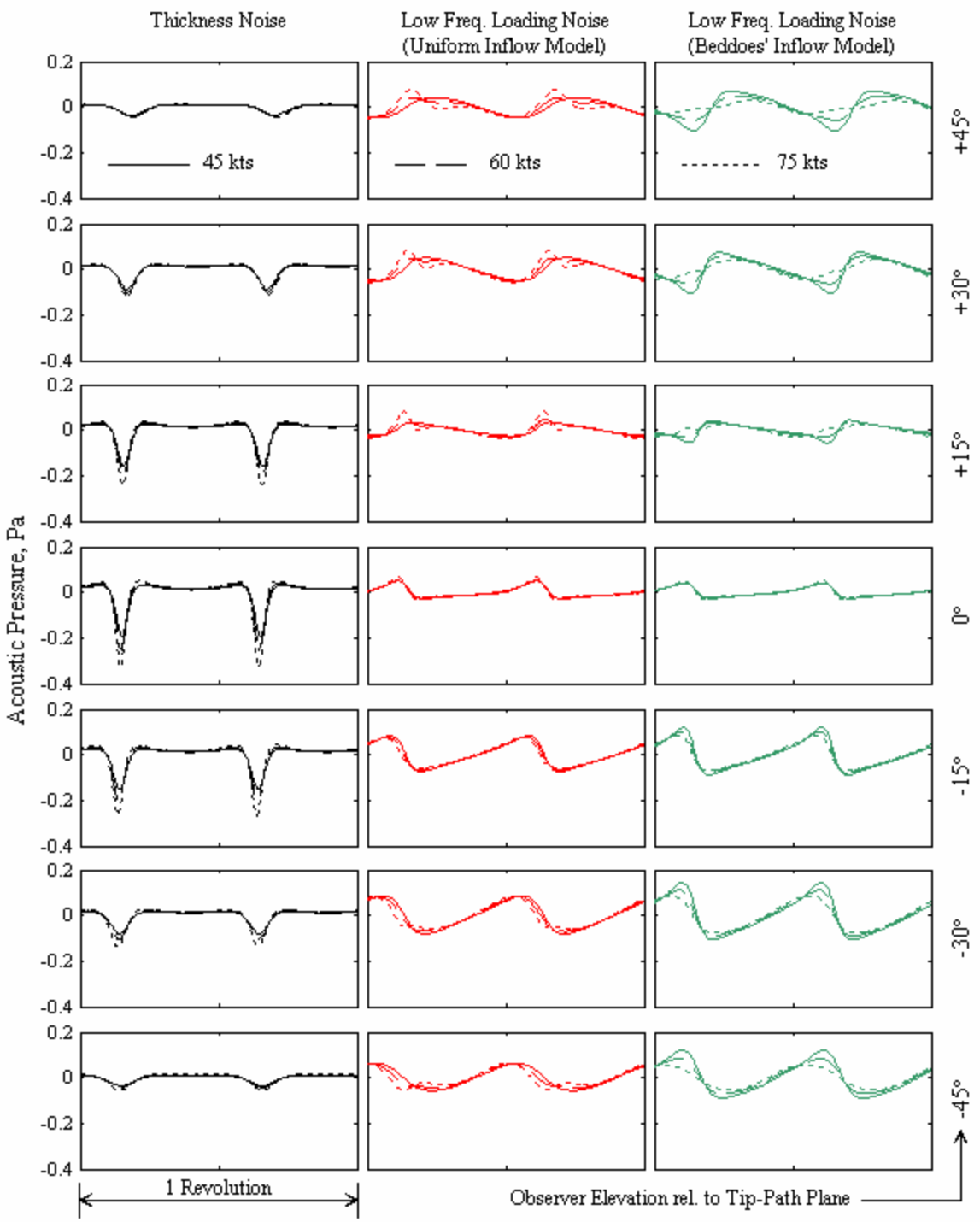

Figure 5.2. Pulse shapes of thickness and low frequency loading noise at various elevation angles relative to the tip-path plane.

Additional sound pressure metrics are provided at different observer elevation angles relative to the tip-path plane in Figure 5.3 and Figure 5.4. Figure 5.3 displays the sound pressure level between the 1st and 6th main rotor harmonics; Figure 5.4 displays the sound pressure level within the BVISPL band (between the 6th and 40th main rotor harmonic). The majority of the acoustic energy for the low frequency loading noise is captured by the first six main rotor harmonics. The impulsive nature of thickness noise does tend to produce some energy in the BVISPL band – especially as the airspeed increases – but the energy is mostly contained within the first six main rotor harmonics.

Figure 5.4 also indicates that, in the absence of BVI noise, when considering frequency content above the 6th main rotor harmonic, thickness noise is louder than loading noise over a much wider region than what was identified in Figure 5.1. If the BVISPL band is used as a metric for detection, thickness noise is louder than loading noise from around 40° below the tip-path plane to 40° above the tip-path plane. For low frequency noise between the 1st and 6th main rotor harmonics, the trends between thickness noise and low frequency loading noise are essentially identical to the OASPL trends.

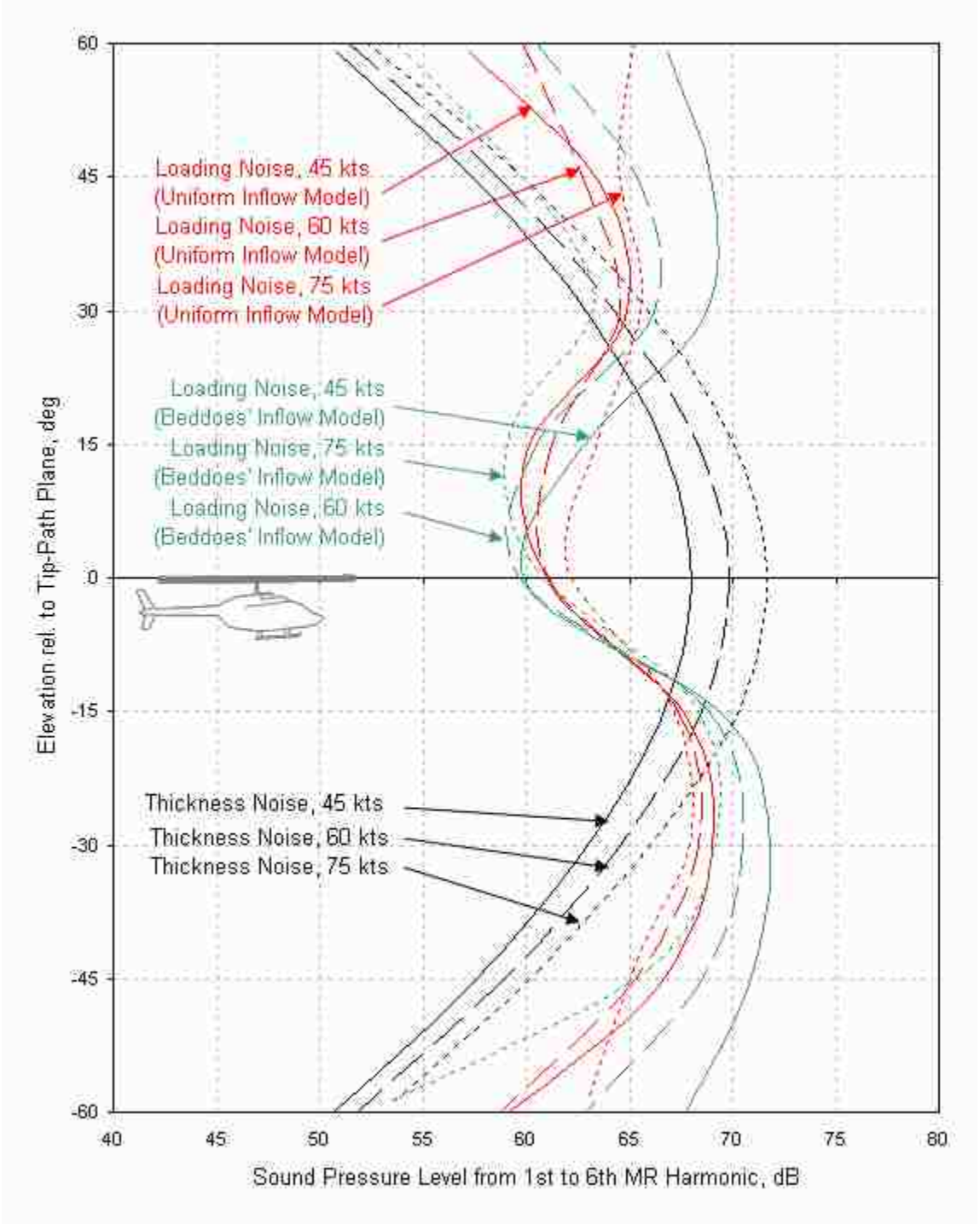

Figure 5.3. Thickness and low frequency loading noise sound pressure level below BVISPL band at various elevation angles.

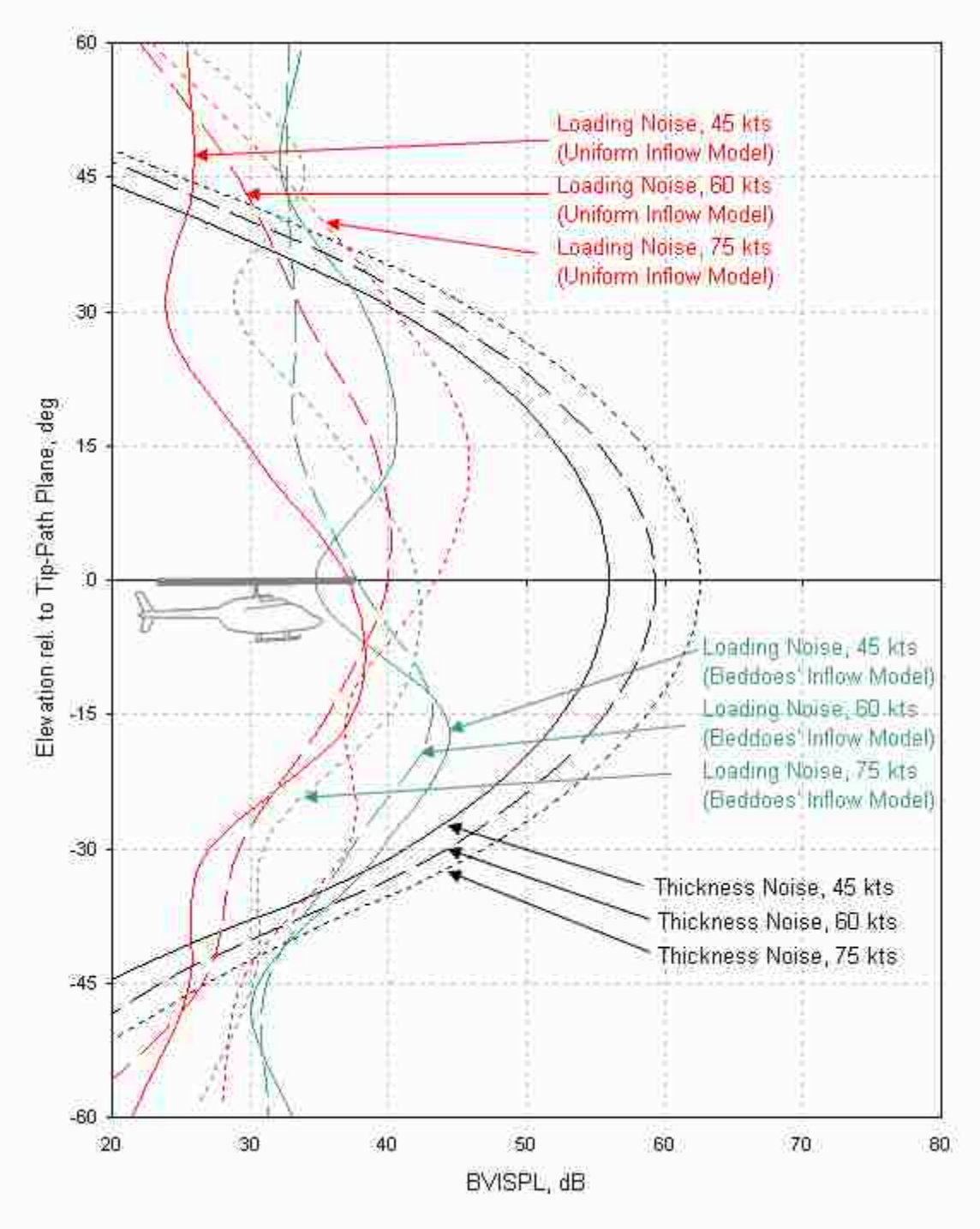

Figure 5.4. Thickness and low frequency loading noise sound pressure level in BVISPL band at various elevation angles.

Further insight to the spectral content of the thickness noise pulse is provided in Figure 5.5. The top plot in this figure displays the root-mean-squared pressure as a function of frequency. The bottom plot displays the cumulative sound pressure level as the frequency range increases. Note that the accumulated sound pressure level of the first six harmonics is 69.8 dB whereas the overall sound pressure level over all frequencies is 70.2 dB.

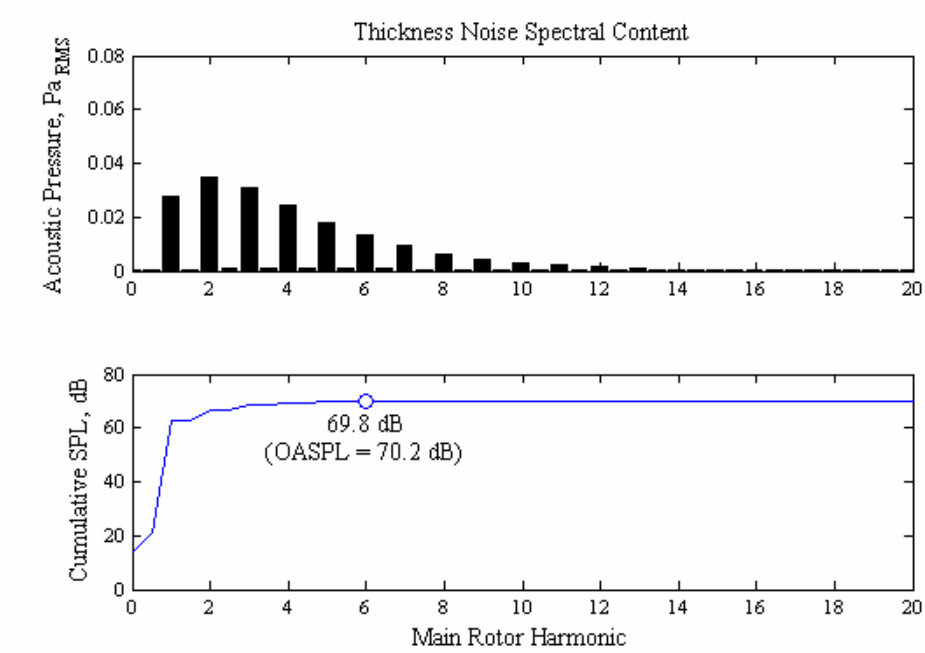

Figure 5.5. Spectral content of thickness noise. Observer in the tip-path plane for a Bell 206B-3 traveling at 60 knots.

Similar spectral plots are provided for the uniform inflow distribution in Figure 5.6 and for the Beddoes' inflow distribution in Figure 5.7. These plots show that the low frequency loading noise is even more dominated by the lower harmonics. In both cases, essentially all of the acoustic energy is captured within the first six main rotor harmonics.

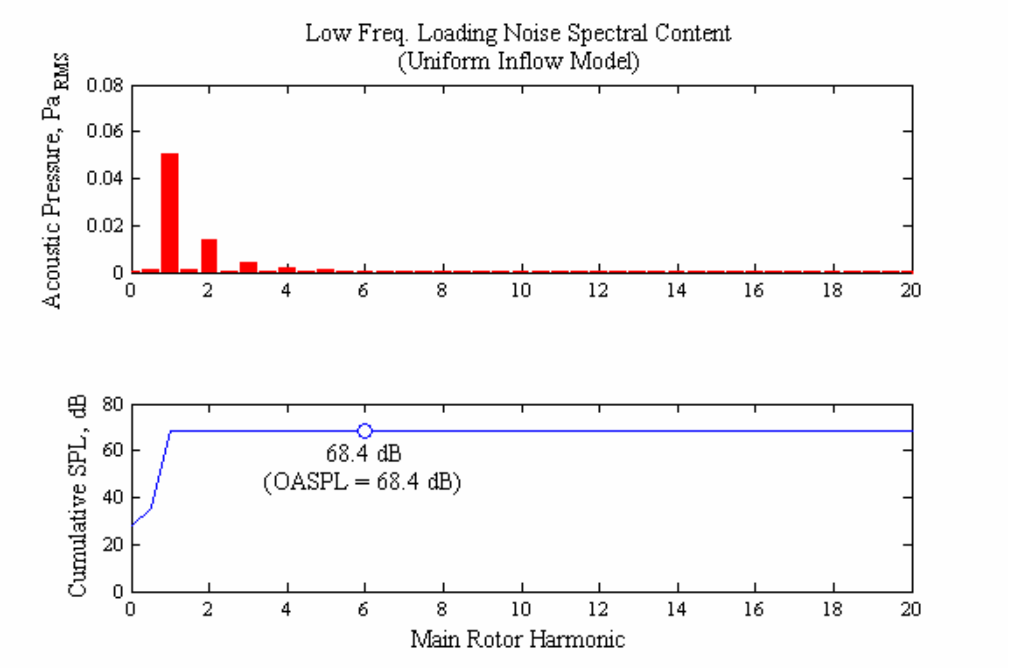

Figure 5.6. Spectral content of low frequency loading noise with a uniform inflow model. Observer is 30° below the tip-path plane for a Bell 206B-3 traveling at 60 knots.

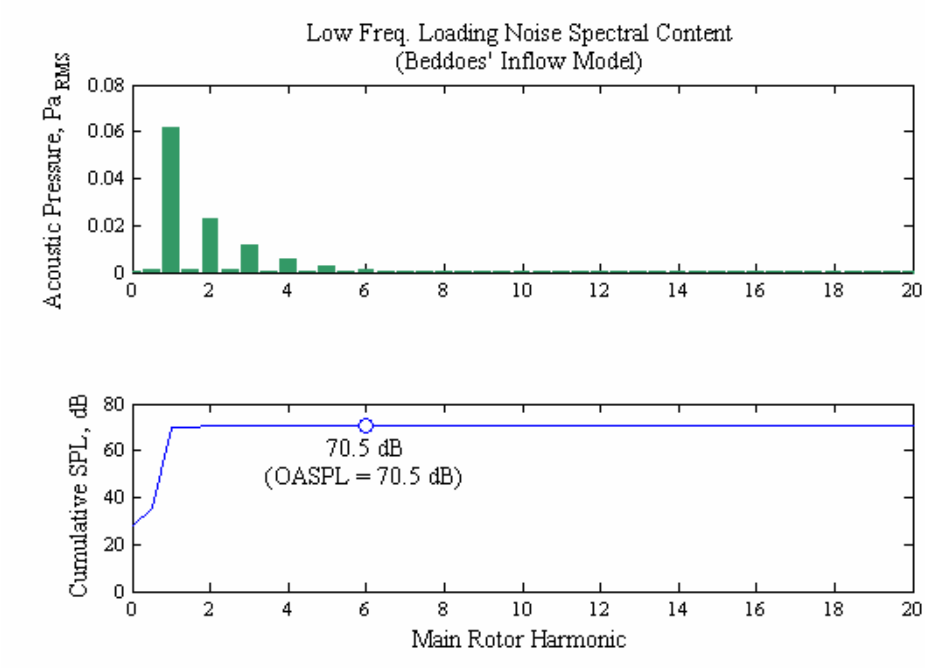

Figure 5.7. Spectral content of low frequency loading noise with a Beddoes' inflow model. Observer is 30° below the tip-path plane for a Bell 206B-3 traveling at 60 knots.

It is important to note that the low frequency loading noise for this aircraft is largely contained by the 1st and 2nd main rotor harmonic terms. In the case of the Bell 206, the 2nd main rotor harmonic occurs at 26.04 Hz. Since the threshold of human hearing is 20 Hz [51], aural detection of low frequency loading noise may not be a significant issue for this aircraft. This may not be the case for rotorcraft with main rotor systems containing additional blades or main rotor systems that operate at higher angular velocities.

5.2.2 Thickness Noise Trends

Recall that in Farassat's Formulation 1A solution to the Ffowcs Williams-Hawkings equation, the expression for far field thickness noise is a combination of two

acoustic terms. The first acoustic term is a function of the time rate of change of the velocity normal to the surface. This term tends to account for the unsteadiness in the monopole. The second acoustic term is related to the time rate of change of the source Mach number. This term effectively serves as a fading parameter applied to the monopole and is largely related to the geometry between the source and the observer. Additional details on the individual terms can be found in Appendix G. These two far field expressions are repeated below for convenience.

$$\text{Thickness Noise Term 1} = \frac{1}{4\pi}\int_S \frac{\rho_0 \frac{\partial v_n}{\partial \tau}}{r\left(1-M_r\right)^2} dS \tag{5.1}$$

$$\text{Thickness Noise Term 2} = \frac{1}{4\pi}\int_S \frac{\rho_0 v_n \left(\hat{r}\bullet\frac{\partial \vec{M}}{\partial \tau}\right)}{r\left(1-M_r\right)^3} dS \tag{5.2}$$

The contribution of both terms to the total thickness noise is presented at various elevation angles relative to the tip-path plane in Figure 5.8 for the Bell 206B-3 traveling at 60 knots. The observer is located directly ahead of the tip-path plane at the 180° azimuth station. It is evident that the fading term, equation (5.2), is the major contributor to the overall thickness noise. The term that accounts for the unsteadiness, equation (5.1), has a significantly smaller contribution.

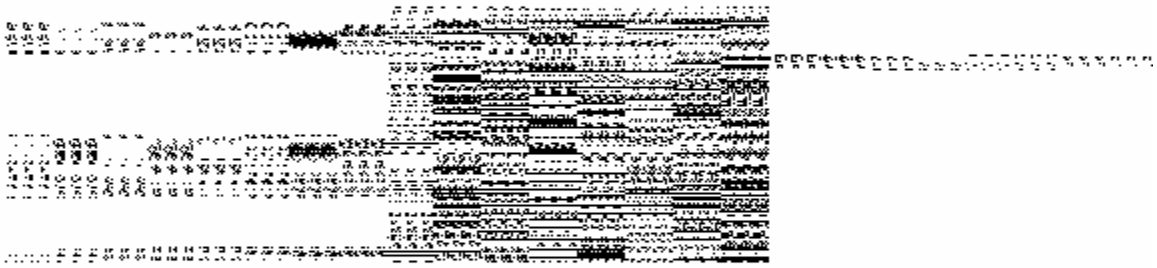

Figure 5.8. Contribution of terms in thickness noise equation at various observer angles relative to the tip-path plane. The data shown is for a Bell 206B-3 traveling at 60 knots.

5.2.3 Low Frequency Loading Noise Trends

Farassat's Formulation 1A solution to the Ffowcs Williams-Hawkings equation also contains two acoustic pressure terms for obtaining the far field loading noise. The first acoustic term is a function of the time rate of change of the pressure over the blade surface. This term is similar to the first term in the thickness noise expression and accounts for unsteadiness in the dipole. The second acoustic term is a function of the time rate of change of the source Mach number. This term behaves similar to the second term in the thickness noise expression and serves as a fading parameter to the dipole. Additional details on the individual terms can be found in Appendix G. These two far field expressions are repeated below for convenience.

$$\text{Loading Noise Term 1} = \frac{1}{4\pi c}\int_S \frac{\dfrac{\partial p}{\partial \tau}\cos\theta}{r\left(1-M_r\right)^2}\,dS \tag{5.3}$$

$$\text{Loading Noise Term 2} = \frac{1}{4\pi c}\int_S \frac{p\cos\theta\left(\hat{r}\bullet\dfrac{\partial \vec{M}}{\partial \tau}\right)}{r\left(1-M_r\right)^3}\,dS \tag{5.4}$$

The contributions of both pressure terms to the total low frequency loading noise in the absence of BVI nose is presented at various elevation angles relative to the tip-path plane in Figure 5.9 for the Bell 206B-3 traveling at 60 knots. As before, the observer is directly ahead of the rotor at the 180° azimuth station. Low frequency loading noise calculations are presented for both a uniform inflow distribution (solid red line) and the Beddoes' inflow distribution (broken green line). The overall amplitude and general shape of the low frequency loading noise is described by the fading term, equation (5.4). Both inflow distributions yield similar time histories for this term.

However, the phasing and the sharpness of the loading noise is a function of the unsteady term, equation (5.3). Under the Beddoes' inflow distribution, the time rate of change of the pressure distribution leads those predicted by the uniform inflow distribution. Furthermore, above the tip-path plane, the uniform model predicts a larger positive peak in the time rate of change of the surface pressure while below the tip-path plane, the uniform model predicts a larger negative peak. When combined with the second loading noise expression, the total low frequency loading noise from the uniform inflow model leads the prediction of the total low frequency loading noise produced under the Beddoes' inflow model. The difference in phasing becomes more pronounced as the observer moves away from the plane of the rotor.

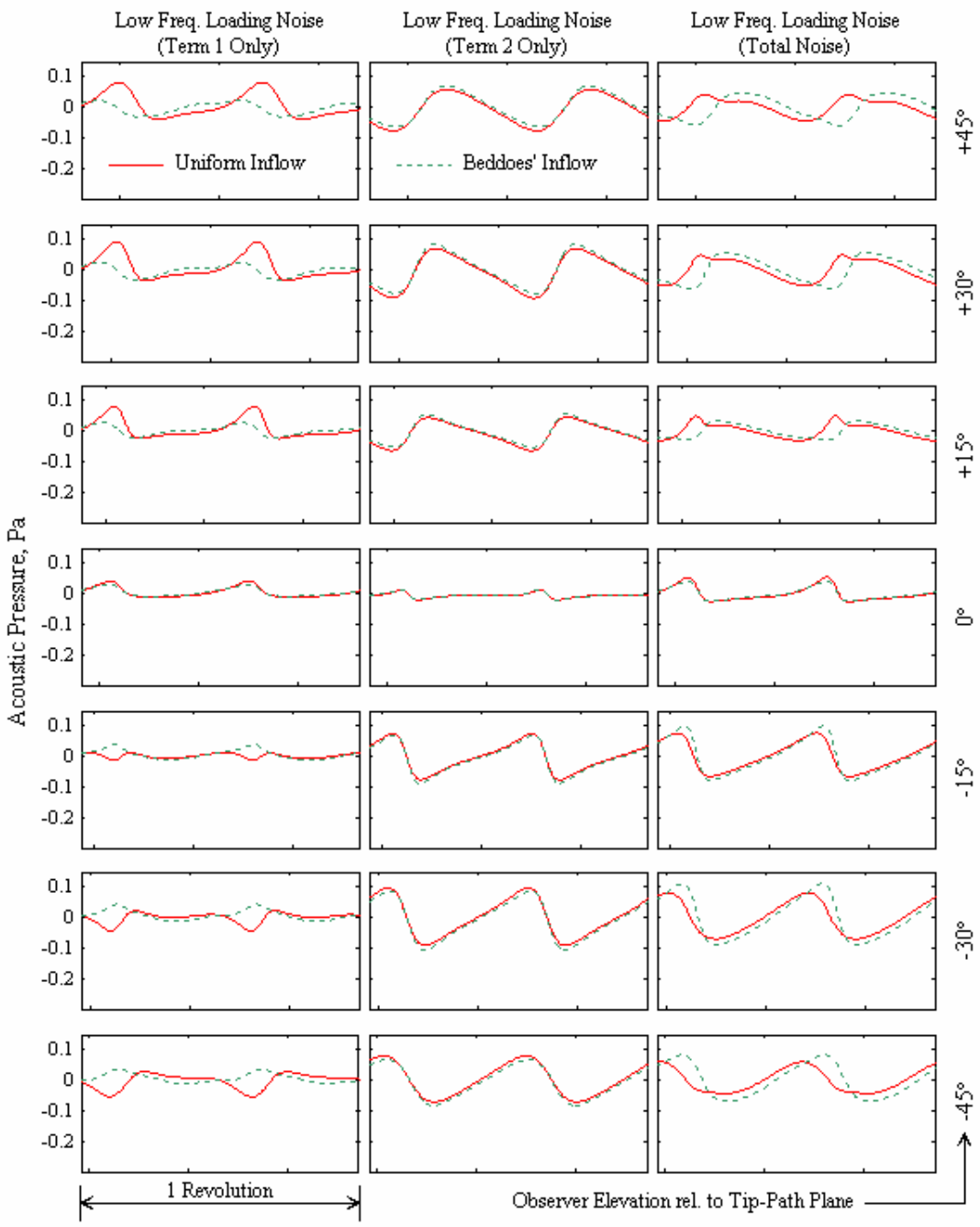

Figure 5.9. Contribution of terms in loading noise equation at various observer angles relative to the tip-path plane. The solid red curves are low frequency loading noise with a uniform inflow model; the dashed green curves are low frequency loading noise with a Beddoes' inflow model. The data shown is for a Bell 206B-3 traveling at 60 knots.

The results of the loading noise analysis indicate a significant sensitivity to the selection of a loading distribution model. Despite having similar overall pulse shapes, the Beddoes' and uniform inflow distributions produce loading noise curves with significant and consistent phasing differences. Though these discrepancies are more pronounced at observer stations out of the plane of the rotor where thrust is the largest aerodynamic source in the loading noise expression, in-plane effects are also observed due to the tilt of the local lift vector causing induced drag. These phasing discrepancies may also have significant implications on how the loading noise combines with the thickness noise. Under the right circumstances, one inflow distribution could produce little in-plane acoustics while the other produces a lot. These effects, while not observed on the Bell 206B-3 due to the dominance of BVI noise during maneuvering flight, may have important implications in predicting the acoustics of heavier aircraft with larger disk loadings.

5.3 Longitudinal Maneuvers

During the Gilroy flight test, the execution of pure cyclic pull-up maneuvers produced large levels of BVI noise that radiated towards the horizon as the main rotor passed through the trailed wake. When flying nap-of-the-earth maneuvers, climbs and descents may be unavoidable, yet the pilot may still desire to operate the aircraft in a manner that avoids detection or ground annoyance.

For longitudinal maneuvering flight, the pilot has the option of applying two controls: the longitudinal cyclic and the collective. Movement to the longitudinal cyclic alters the tilt of the tip-path plane and redirects the thrust vector. Pushing forward on the cyclic reduces the longitudinal tilt of the tip-path plane and induces a nose-down pitching

motion as the thrust vector tilts forward; pulling back on the cyclic increases the longitudinal tilt of the tip-path plane and induces a nose-up pitching motion as the thrust vector tilts aft. If the collective control and main rotor RPM are assumed fixed, the total energy of the system will remain constant for cyclic maneuvers. Therefore the cyclic inputs will result in an exchange between kinetic and potential energies. During cyclic climbs, increases in altitude will correspond to a reduction in airspeed. Similarly, during cyclic descents, the decrease in altitude will correspond to an increase in airspeed.

Movement of the collective level alters the amount of thrust produced by the main rotor. Increasing the collective increases the mean blade angle of attack and produces more thrust; decreasing the collective decreases the mean blade angle of attack and produces less thrust. A speed governor on the engine manages the power so that the angular velocity of the main rotor remains steady. Since the governor regulates the amount of power available in the system, climbs and descents due to collective inputs are the result of the pilot increasing or decreasing the total energy available to the main rotor.

Longitudinal maneuvers due to cyclic and collective inputs are discussed in this section.

5.3.1 Review of Assumptions

The analysis of the following maneuvers uses the same dynamics and aerodynamics models derived in Chapter 3. The dynamic model for fuselage and main rotor flapping was derived for a two-bladed teetering rotor system for purely longitudinal flight. The blades are rigid and follow first harmonic flapping motion. The main rotor RPM is also assumed to remain constant during the maneuver. The dynamics model also assumes uniform and non-dynamic inflow, quasi-steady aerodynamic strip theory, and

neglects reverse flow and compressibility effects. Furthermore, fuselage drag and the pitching moments from the fuselage, empennage, and horizontal stabilizer are assumed constant and independent of the fuselage angle of attack. Airframe drag is assumed to act through the center of gravity.

Using the aircraft and tip-path plane flapping response from the dynamics model, loads on the blades are updated using a refined aerodynamics model. These refinements include the incorporation of the indicial method to account for unsteady aerodynamics and the inclusion of a prescribed trailed wake for calculating high frequency aerodynamic loads. Aerodynamic loads acting on the blade are found by integrating the Biot-Savart law along the wake to obtain the induced velocity acting on the blade. These high frequency aerodynamic load calculations are used in the following acoustic computations. It is assumed that the high frequency loading does not affect aircraft motion or blade flapping and are therefore not coupled with the dynamics model.

In the analysis of alternative maneuvers that follows, it is assumed that the sum of the pitching moments from the fuselage, the empennage, and the horizontal stabilizer remains constant during the maneuver and that the center of gravity lies forward of the main rotor mast. Two aircraft body net pitching moment values will be investigated that combine the moments from the fuselage, the empennage, and the horizontal stabilizer. The first will feature a nose-up net pitching moment of 4425 N-m; the second will have a zero net pitching moment. Both cases are illustrated in Figure 5.10. In the case of the body with a nose-up net pitching moment, the thrust vector causes a nose-down moment about the center of gravity to counter the aerodynamic moments during trimmed flight. In the case of the body with a zero net pitching moment, the aircraft must pitch forward to

orient the rotor load through the center of gravity to satisfy the static moment during trimmed flight. Note that that the tip-path plane and net rotor load vectors are, to the first order, independent of the fuselage pitching moment.

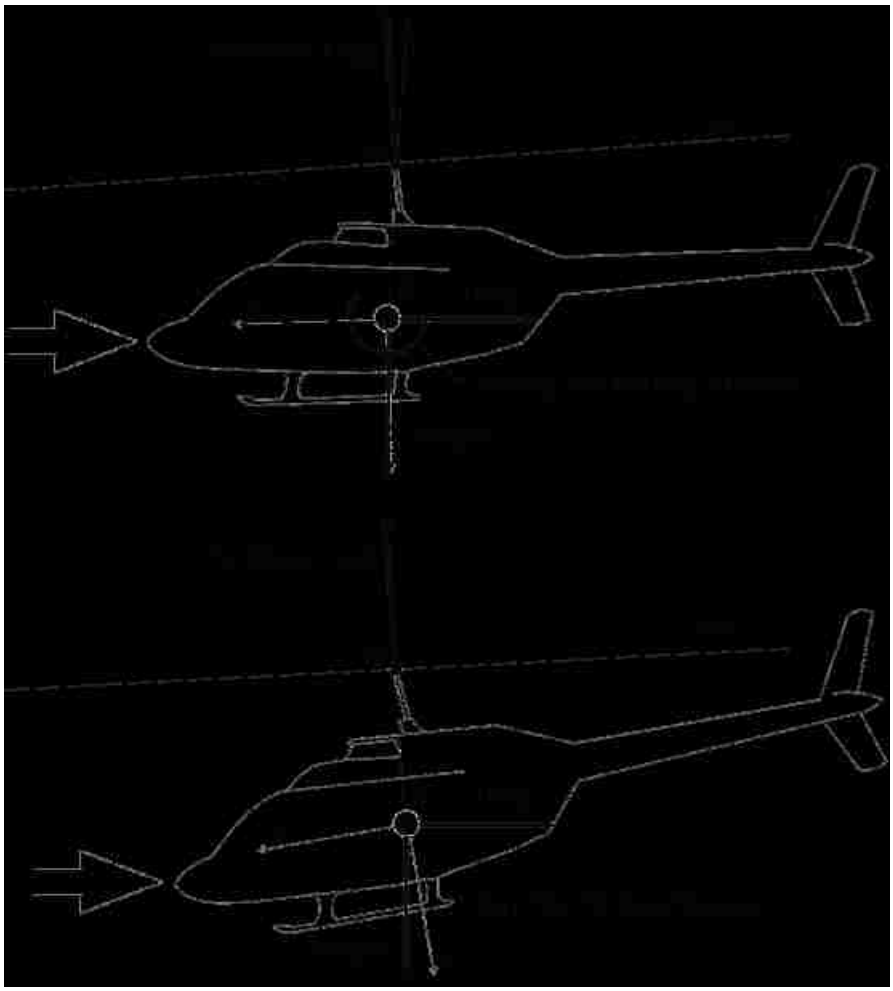

Figure 5.10. Rotor load alignment relative to center of gravity during trimmed flight. The top diagram is features a nose-up pitching moment from the sum of the fuselage, empennage, and stabilizer pitching moments. The bottom case is for an aircraft with a zero net pitching moment. All attitude and alignment angles are shown to scale for trimmed level flight at 75 knots.

Though the selection of the pitching moment will have an effect on the response of the aircraft motion, the purpose of this study is to investigate the implications of maneuvering flight to the geometry of the wake structure and the orientation of the tip-path plane.

5.3.2 Longitudinal Cyclic Climbs

To execute the longitudinal cyclic climb, a ramp input of -2°/s is applied to the longitudinal cyclic while the collective control and lateral cyclic are held at the trim position. The ramp sequence is applied to an aircraft in trimmed level flight traveling at 75 knots. The climb is initiated at an altitude of 45 m when the aircraft is 475 m away from the center microphone. Only the first few seconds of the initial transient are modeled. The time history of the control input sequence relative to the trim position is plotted in Figure 5.11.

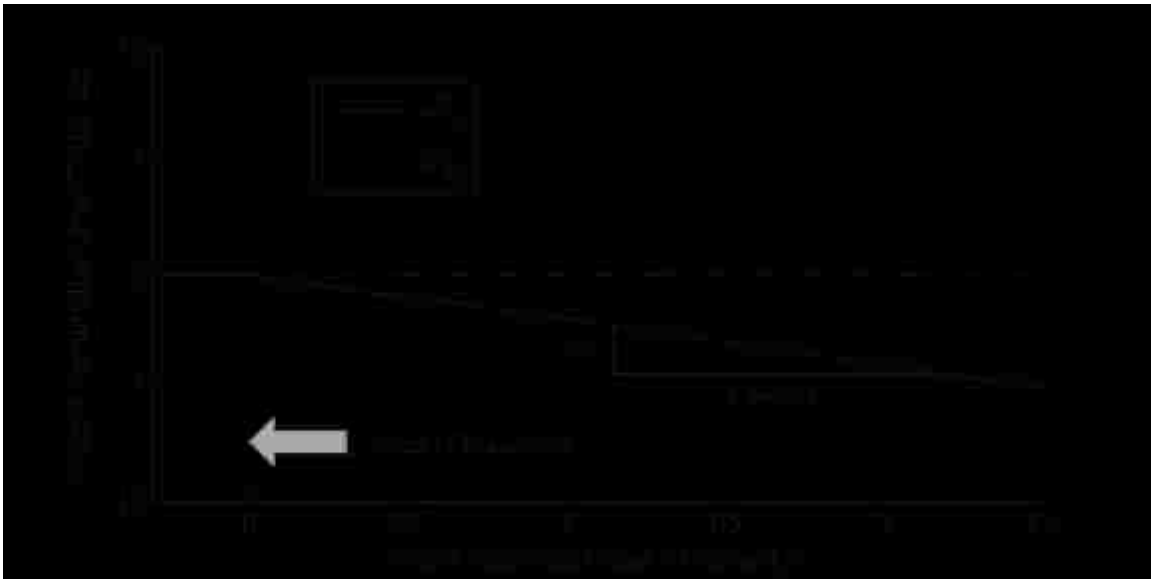

Figure 5.11. Control input time history for longitudinal cyclic climb.

The fuselage pitch response is shown in Figure 5.12. Over the course of the maneuver, the pitch rates gradually increase as the ramp input is applied. The model

indicates that the body with the zero net pitching moment has a higher angular pitching acceleration that the body with the nose-up net pitching moment.

Figure 5.12. Pitch rate response to the longitudinal cyclic climb.

The angle of attack of the tip-path plane during the course of the maneuver is presented in Figure 5.13. The tip-path plane, which is initially at a slightly negative angle of attack during forward flight, tilts back as the longitudinal cyclic is applied. During the climb, the tip-path plane angle of attack increases faster for the body with a zero net pitching moment.

Figure 5.13. Tip-path plane angle of attack response to the longitudinal cyclic climb.

A diagram showing the orientation of the thrust vector over the course of the maneuver is illustrated in Figure 5.14. For reference, the action line from the hub to the center of gravity is displayed in each image to indicate the action of the thrust vector. Note that in the case of the body with the nose-up net pitching moment, the thrust vector is initially tilted forward whereas in the case of the body with the zero net pitching moment, the thrust vector is aligned with the center of gravity. Both cyclic pull-up maneuvers result in the thrust vector tilting back with the tip-path plane, though the range of the tilt is larger for the fuselage body with the nose-up net pitching moment.

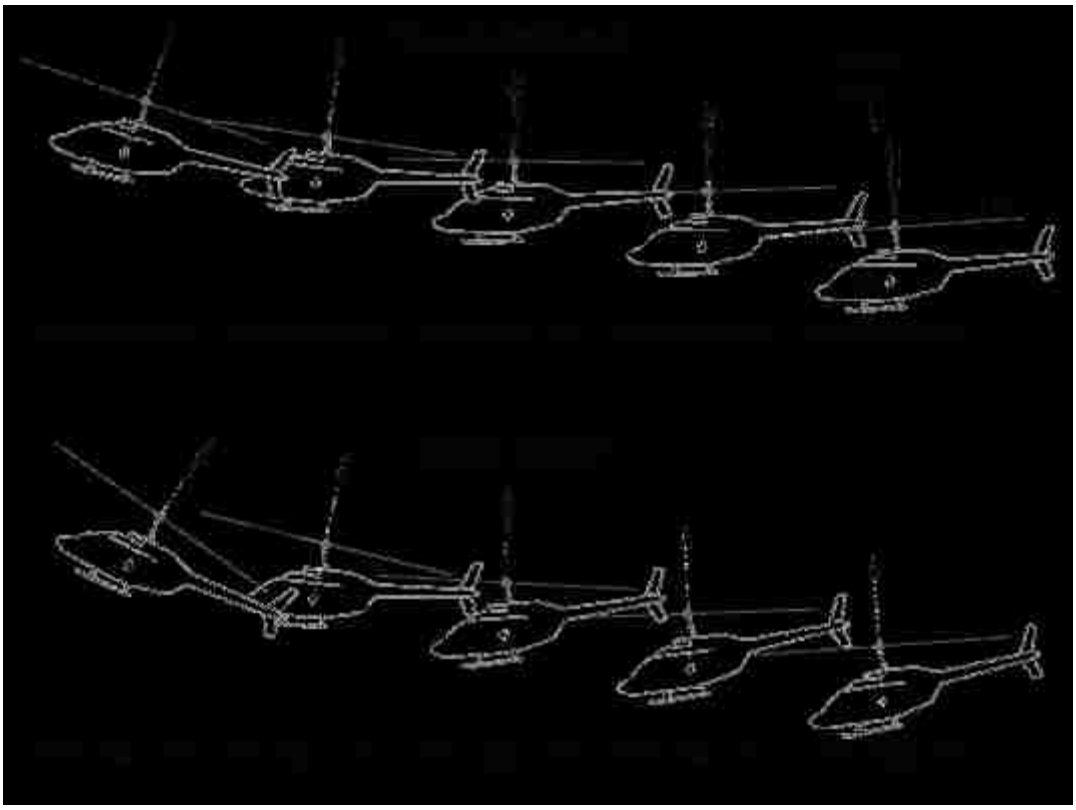

Figure 5.14. Thrust vector orientation relative to the center of gravity during longitudinal cyclic climbs. All attitudes and geometries are shown to scale.

The airspeed of the helicopter during the climbing maneuver is presented in Figure 5.15. Both aircraft experience a deceleration during the execution of the climb. This is the result of the exchange of potential and kinetic energy of the aircraft as well as the deceleration caused by the thrust vector being tilted aft. As with the previous response plots, the body with a zero net pitching moment responds faster than the body with a nose-up net pitching moment.

Figure 5.15. Free stream velocity response to the longitudinal cyclic climb.

Aircraft attitude and wake geometries over the course of the maneuver are illustrated in Figure 5.16. The control is applied at revolution #0, and the geometries and attitudes are illustrated every five main rotor revolutions. The black arrows at the nose of the aircraft indicate the angle of the free stream velocity vector. The set of attitude and wake illustrations on the top correspond to the aircraft body with a nose-up net pitching moment. The set of attitude and wake illustrations on the bottom correspond to the aircraft body with a zero net pitching moment. Note that Figure 5.16 is drawn to scale.

As was observed during the pull-up maneuvers executed during the Gilroy flight test, application of a longitudinal cyclic climb results in the tip-path plane initially tilting back into the trailed wake. Both aircraft exhibit similar results to the application of the longitudinal cyclic, though the passing of the tip-path plane through the trailed wake occurs earlier for the body with a zero net pitching moment. Because the wake passes through the tip-path plane, this maneuver is expected to produce impulsive BVI noise.

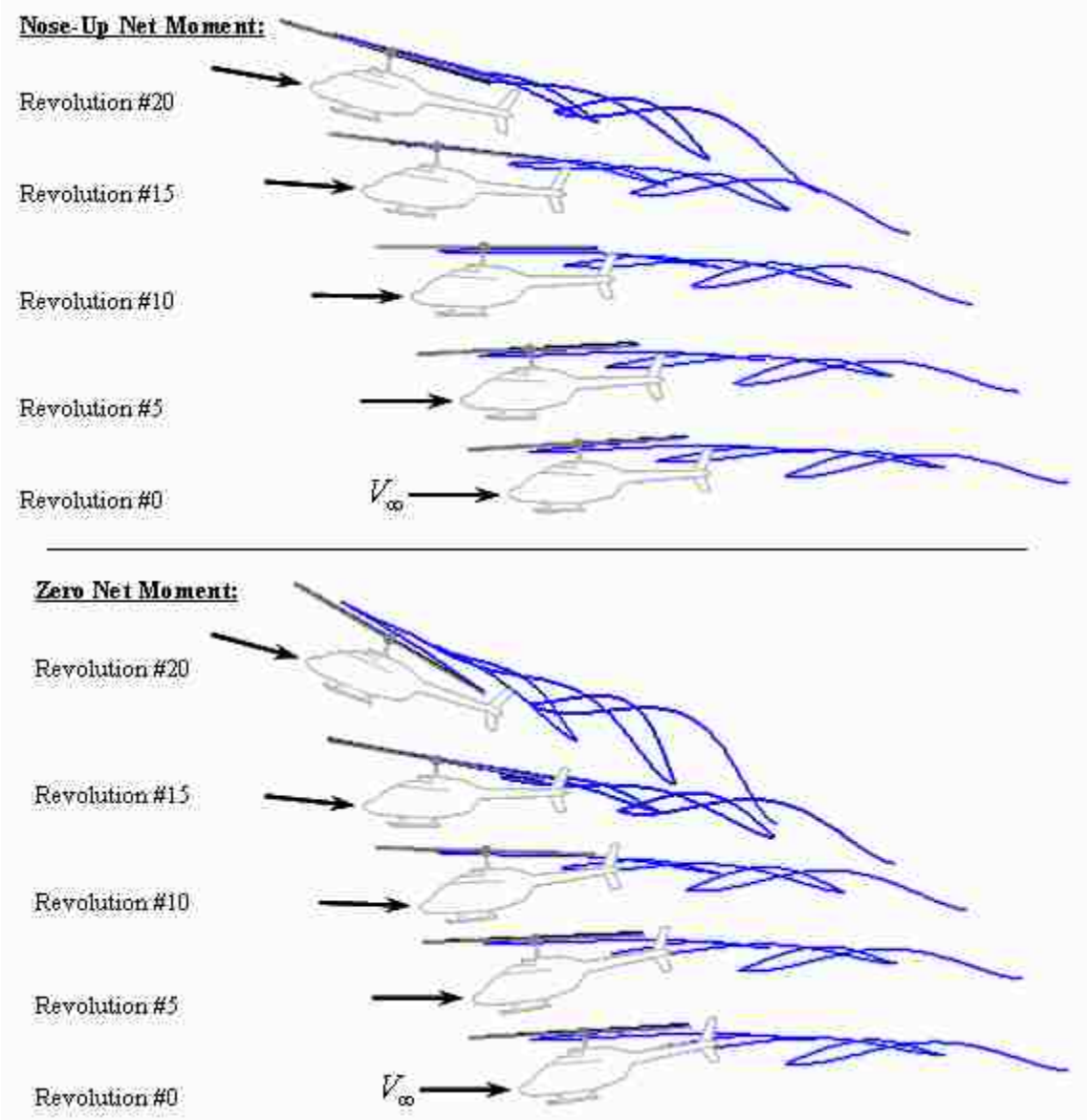

Figure 5.16. Aircraft attitude and wake geometry for the longitudinal cyclic climb. All attitudes and geometries are shown to scale.

The flight trajectory corresponding to the cyclic pitch perturbation is presented in Figure 5.17. As with the other attitude measurements, the aircraft body featuring a zero net pitching moment climbs faster than the body with the nose-up net pitching moment.

Figure 5.17. Flight trajectory for longitudinal cyclic climb.

The acoustic response to the longitudinal cyclic climb is presented in Figure 5.18. The top plot displays the acoustic time history for the fuselage body with a nose-up net pitching moment; the middle plot displays the acoustic time history for the fuselage body with a zero net pitching moment; and the bottom plot displays the time histories of sound pressure level metrics including the OASPL, the sound pressure level between the 1st and 6th main rotor harmonics, and the BVISPL. These time histories further illustrate that as the wake passes through the tip-path plane, impulsive BVI noise leads to severe increases in the levels of acoustic radiation produced by the main rotor. In the case of the body with zero net pitching moment, as the wake passes above the tip-path plane, the impulsive noise levels begin to reduce. In both cases the orientation of the tip-path plane during the climb also exposes the far field observer to the underside of the rotor and the low frequency loading noise. This is indicated by the rise in sound pressure levels between the 1st and 6th main rotor harmonics.

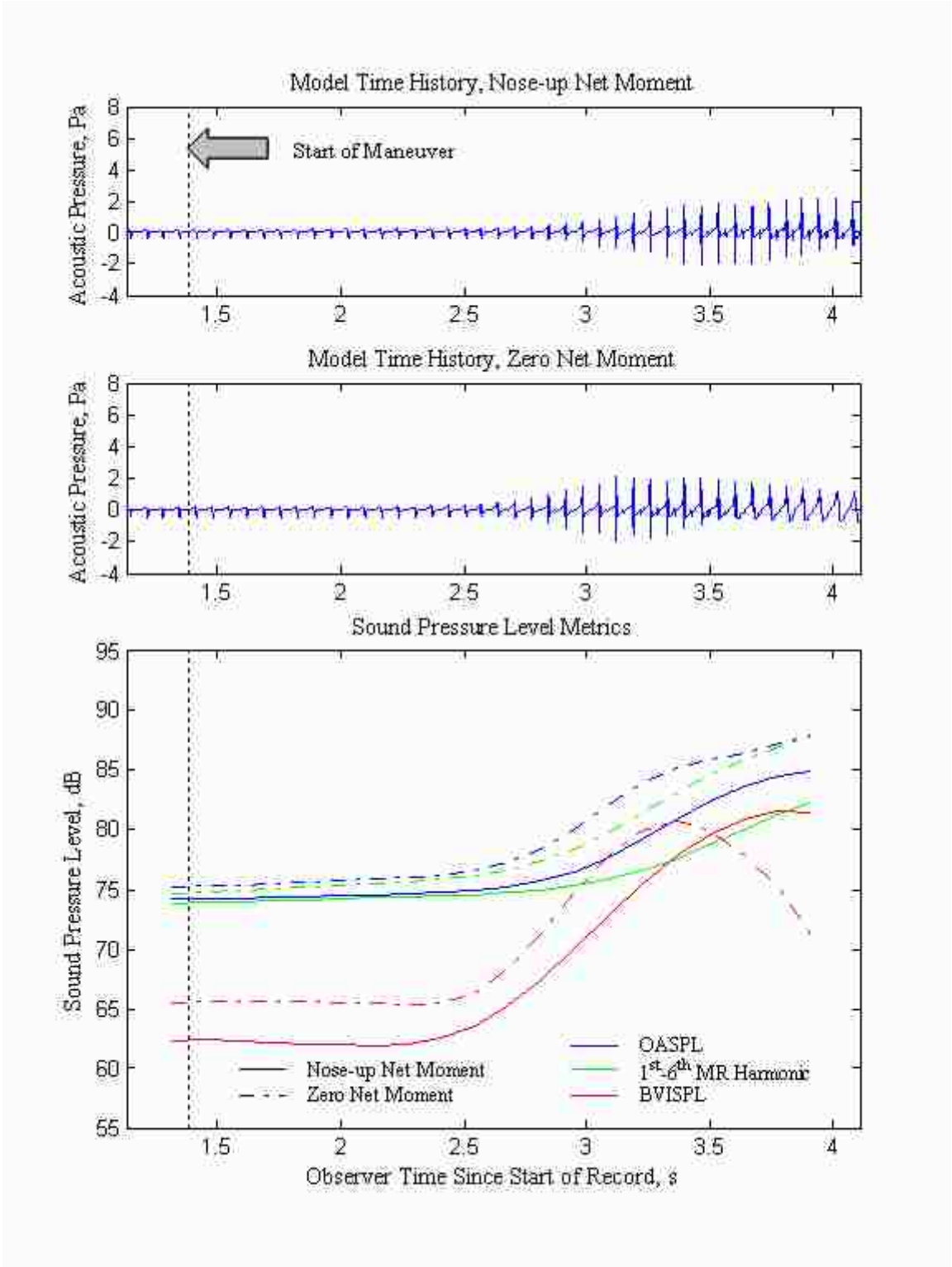

Figure 5.18. Acoustic response to the longitudinal cyclic climb.

5.3.3 Collective Climbs

To execute the collective climb, a ramp input of +2°/s is applied to the collective lever while the longitudinal cyclic control is held at the trim position. It is implicitly assumed that the power is added or subtracted by the engine governor to maintain a constant RPM. As before, the ramp sequence is applied to an aircraft in trimmed level flight traveling at 75 knots. The climb is initiated at an altitude of 45 m when the aircraft is 475 m away from the center microphone. The time history of the control input sequence relative to the trim position is plotted in Figure 5.19.

Figure 5.19. Control input time history for collective climb.

The pitch rate response to the collective climb is presented in Figure 5.20. These responses indicate slightly different behaviors between the two aircraft bodies. The aircraft body featuring the zero net pitching moment responds similar to the longitudinal cyclic climb. However, the aircraft body with a nose-up net pitching moment initially tilts forward. This is due to the angle of the thrust vector relative to the center of gravity. As was shown previously in Figure 5.10, in the case with a nose-up net pitching moment, the

thrust vector is aligned relative to the center of gravity such that it produces a nose-down pitching moment. By increasing the collective and increasing the thrust, the aircraft initially pitches forward as demonstrated in the pitch response. Over time, the thrust vector begins to tilt back and the nose-down pitching motion begins to slow down.

Figure 5.20. Pitch rate response to the collective climb.

The angle of attack of the tip-path plane during the course of the maneuver is presented in Figure 5.21. The forward tilt of the tip-path plane results in large negative magnitudes of the tip-path plane angle of attack for the aircraft body with the nose-up net pitching moment. For the case of the aircraft body with the zero net pitching moment, the rate of climb tilts the free stream velocity vector faster than the tip-path plane can rotate thereby producing increasingly negative tip-path plane angles of attack.

Figure 5.21. Tip-path plane angle of attack response to the collective climb.

A diagram showing the orientation of the thrust vector over the course of the maneuver is illustrated in Figure 5.22. For reference, the action line from the hub to the center of gravity is displayed in each image to indicate the action of the thrust vector. Note that in the case of the body with the nose-up net pitching moment, the thrust vector is initially tilted forward of the center of gravity and applying increased collective causes the tip-path plane to tilt forward. Over the course of the maneuver, the thrust vector slowly begins to tilt aft. In the case of the body with the zero net pitching moment, the thrust vector is aligned with the center of gravity, but as the tip-path plane tilts back, the thrust vector slowly tilts aft during the maneuver. Overall, the alignment of the thrust vector relative to the center of gravity remains fairly constant during the collective maneuver.

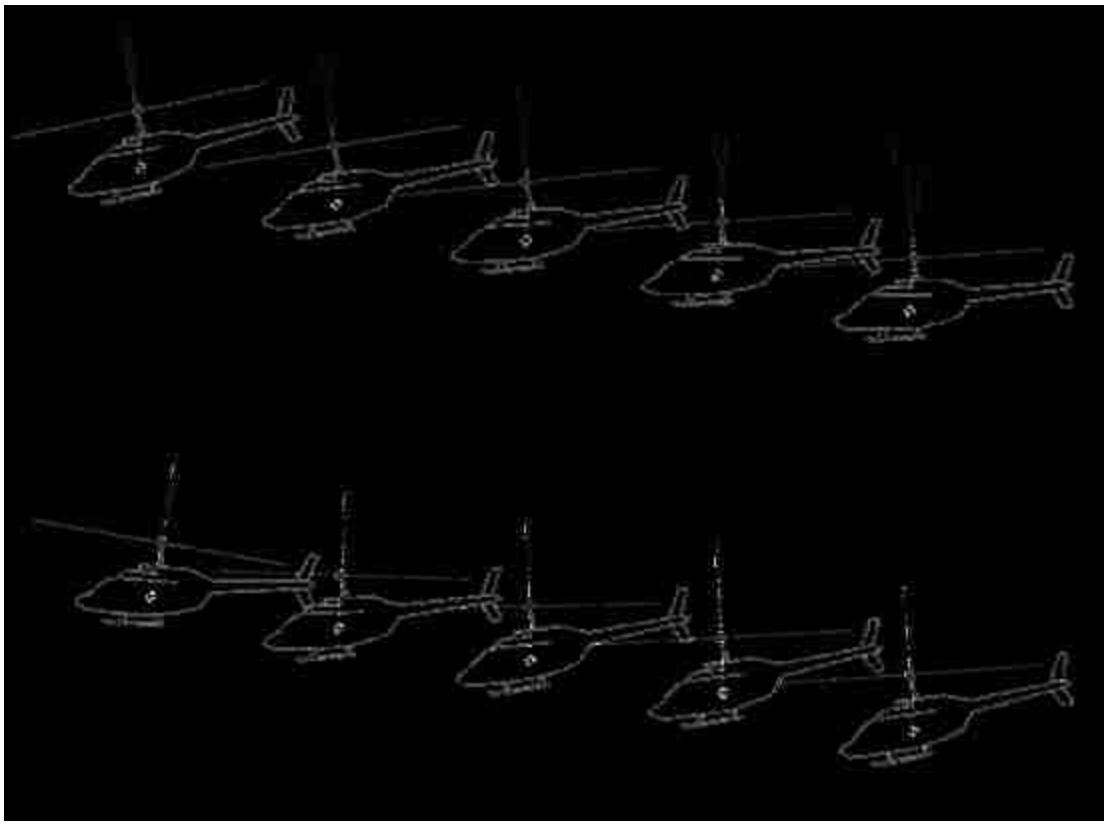

Figure 5.22. Thrust vector orientation relative to the center of gravity during collective climbs. All attitudes and geometries are shown to scale.

The airspeed of the helicopter during the climbing maneuver is presented in Figure 5.23. The forward tilt of the tip-path plane for the aircraft body with a nose-up net pitching moment results in an acceleration as additional thrust is applied. Comparatively, the airspeed for the aircraft body with a zero net pitching moment remains fairly steady over the course of the maneuver. Towards the later stages of the maneuver, as the tip-path plane begins to tilt aft, the aircraft gradually begins to slow down, but at a rate far lower than those noticed during the longitudinal cyclic climbs.

Figure 5.23. Airspeed response to the collective climb.

Aircraft attitude and wake geometries over the course of the maneuver are illustrated in Figure 5.24. The control is applied at revolution #0 and geometries and attitudes are illustrated every five main rotor revolutions. The black arrows at the nose of the aircraft indicate the angle of the free stream velocity vector. The set of attitude and wake illustrations on the top correspond to the aircraft body with a nose-up net pitching moment. The set of attitude and wake illustrations on the bottom correspond to the aircraft body with a zero net pitching moment. Note that Figure 5.24 is drawn to scale.

In the case of the aircraft body with a nose-up net pitching moment, the initial response to the collective input is for the nose of the aircraft and the tip-path plane to tilt forward. The results in an increase in the miss distance between the tip-path plane and the trailed wake. In the case of the aircraft body with a zero net pitching moment, the aircraft and the tip-path plane tilt backwards. However, the combination of the increase in thrust and the vertical climb leads to a larger inflow through the rotor and an increase in the miss distance between the trailed wake and the tip-path plane. While the miss distance is

larger for the body with a nose-up net pitching moment, neither aircraft would be expected to produce BVI when executing a collective climb.

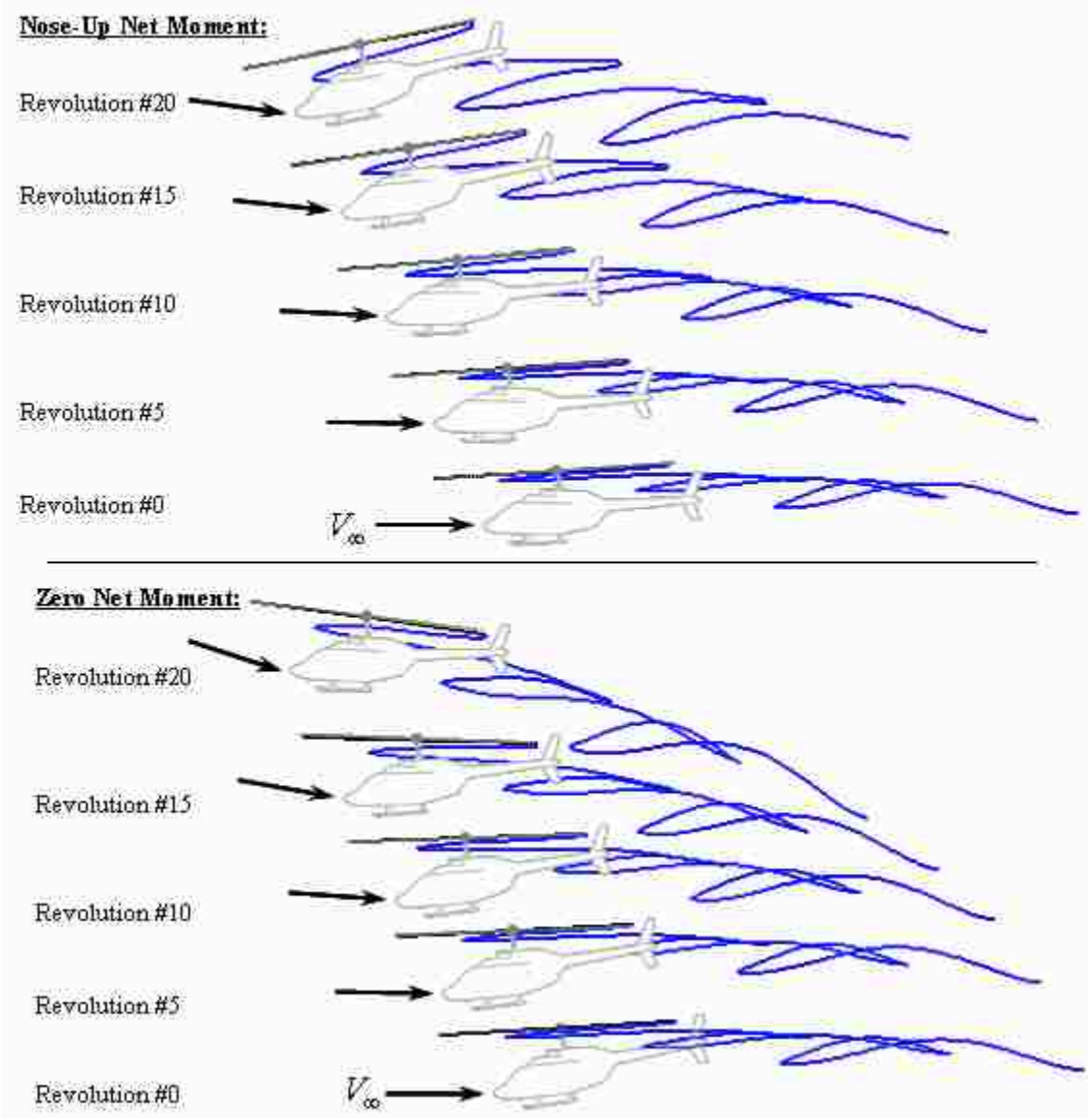

Figure 5.24. Aircraft attitude and wake geometry for the collective climb. All attitudes and geometries are shown to scale.

The flight trajectory corresponding to the collective perturbation is presented in Figure 5.25. Similar to the longitudinal cyclic model, the aircraft body featuring a zero

net pitching moment climbs faster than the aircraft body featuring a nose-up net pitching moment.

Figure 5.25. Flight trajectory for the collective climb.

The acoustic response to the collective climb is provided in Figure 5.26. The top plot presents the acoustic time history for the aircraft body with a nose-up net pitching moment; the middle plot presents the acoustic time history for the aircraft body with a zero net pitching moment; and the bottom plot presents the time histories of several sound pressure level metrics. As expected from the wake geometries relative to the tip-path plane, no significant rise in impulsive BVI noise is observed in the predicted acoustics. However, the tip-path plane tilt due to the net pitching moment does affect the levels of low frequency loading noise radiated to the horizon. The forward tilt of the tip-path plane for the fuselage body with a nose-up net pitching moment keeps the far field observer near the plane of the rotor throughout the maneuver. Comparatively, the backward tilt of the tip-path plane for the fuselage body with the zero net pitching moment exposes the far field observer to the underside of the rotor where low frequency

loading noise leads to an increase in the acoustic levels radiated towards the horizon by the main rotor.

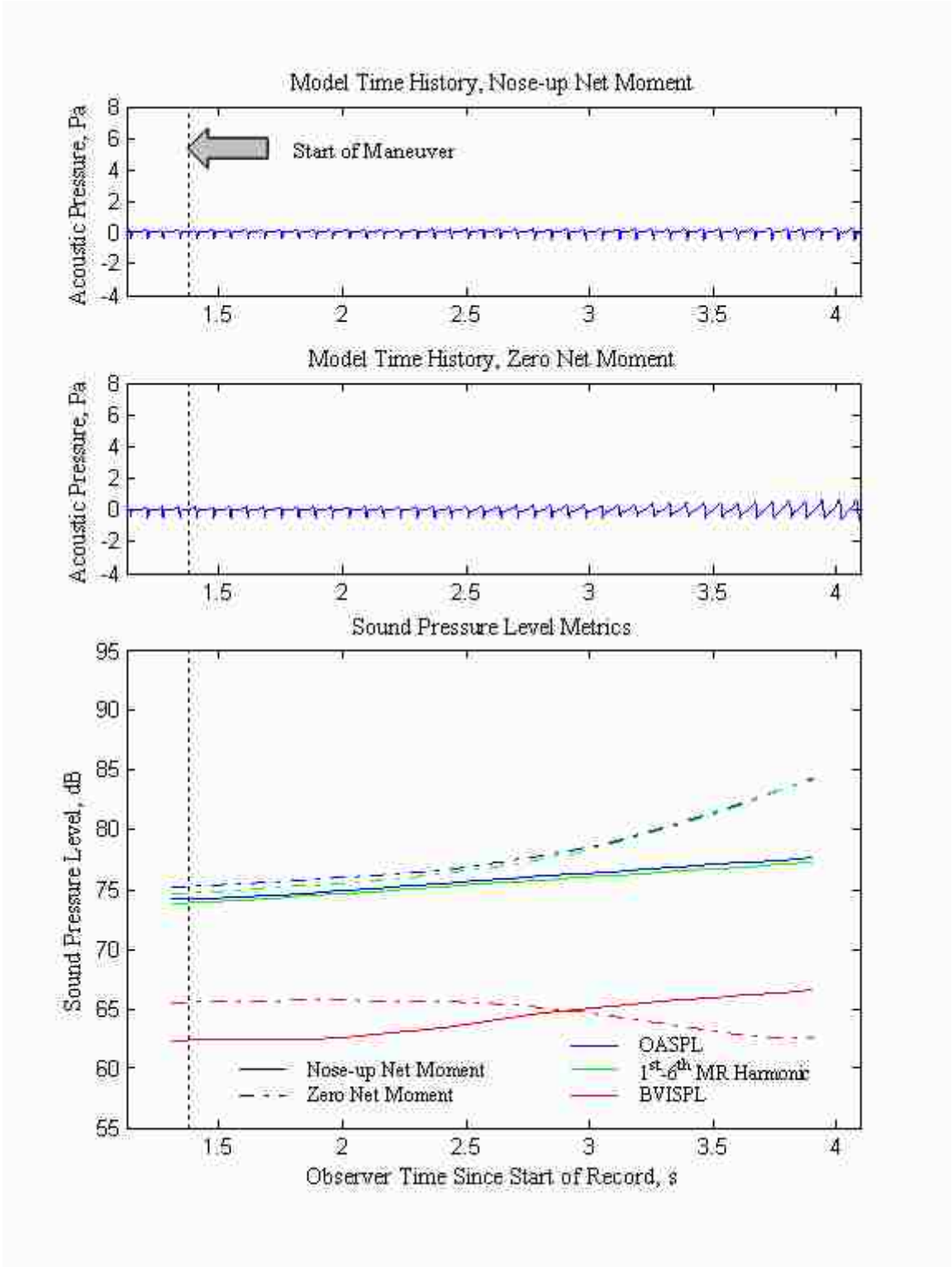

Figure 5.26. Acoustic response to the collective climb.

5.3.4 Longitudinal Cyclic Descents

To execute the longitudinal cyclic descent, a ramp input of +2°/s is applied to the longitudinal cyclic while the collective control and lateral cyclic are held at the trim position. The ramp sequence is applied to an aircraft in trimmed level flight traveling at 75 knots. The descent is initiated at an altitude of 45 m when the aircraft is 475 m away from the center microphone. The time history of the control input sequence relative to the trim position is plotted in Figure 5.27.

Figure 5.27. Control input time history for longitudinal cyclic descent.

The fuselage pitch response is shown in Figure 5.28. The nose-down pitch rates for both aircraft body models increase over the course of the maneuver with the body featuring the zero net pitching moment accelerating faster.

Figure 5.28. Pitch rate response for longitudinal cyclic descent.

The angle of attack of the tip-path plane during the course of the maneuver is presented in Figure 5.29. The cyclic descent results in increasingly negative tip-path plane angles of attack. The tip-path plane angle of attack for the fuselage body with the zero net pitching moment decreases faster than the body with a nose-up net pitching moment.

Figure 5.29. Tip-path plane angle o f attack response to the longitudinal cyclic descent.

A diagram showing the orientation of the thrust vector over the course of the maneuver is illustrated in Figure 5.30. For reference, the action line from the hub to the center of gravity is displayed in each image to indicate the action of the thrust vector. Both cyclic pull-up maneuvers result in the thrust vector tilting forward along with the tip-path plane. As was observed for the cyclic climbs, the range of the tilt is larger for the fuselage body with the nose-up net pitching moment.

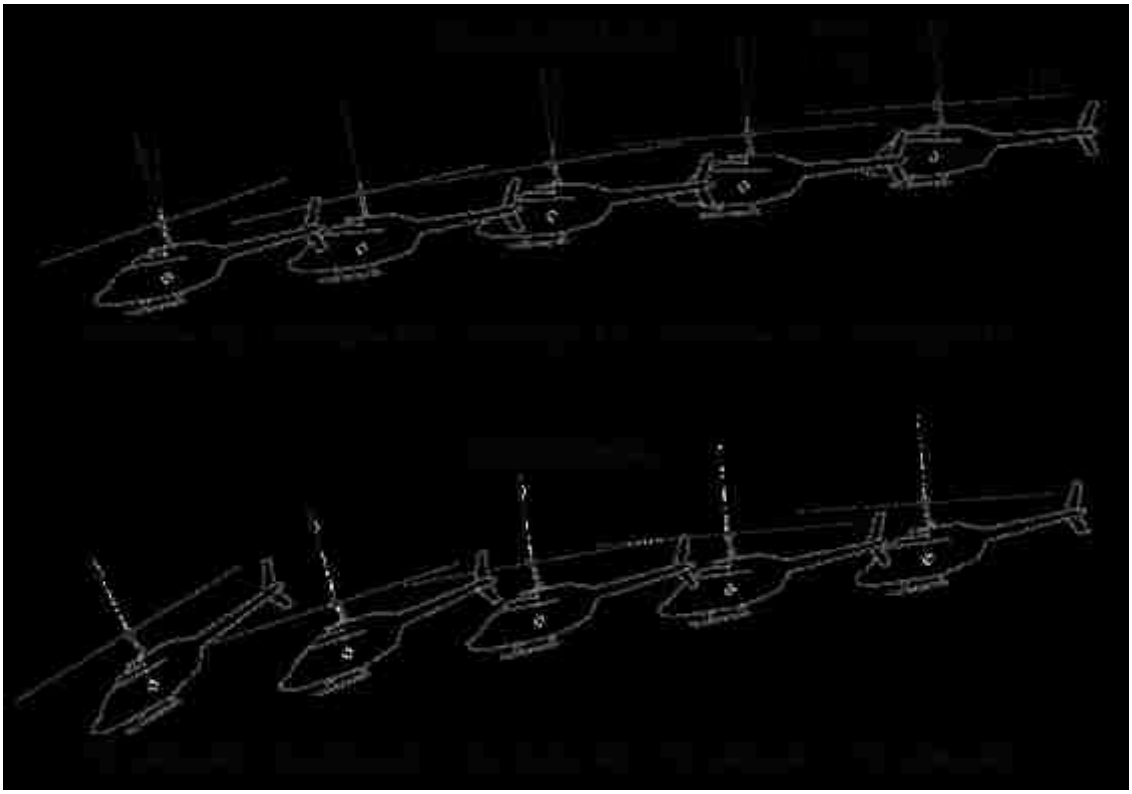

Figure 5.30. Thrust vector orientation relative to the center of gravity during longitudinal cyclic descents. All attitudes and geometries are shown to scale.

The airspeed of the helicopter during the descent is presented in Figure 5.31. During the descent, both aircraft experience acceleration. This is the result of the exchange of potential and kinetic energy of the aircraft as well as the slight acceleration from the thrust vector as it is tilted forward. The fuselage body with the zero net pitching moment increases speed slightly faster than the body with the nose-up net pitching moment.

Figure 5.31. Airspeed response to the longitudinal cyclic descent.

Aircraft attitude and wake geometries over the course of the descent maneuver are illustrated in Figure 5.32. The control is applied at revolution #0 and the geometries and attitudes are illustrated every five main rotor revolutions. The black arrows at the nose of the aircraft indicate the angle of the free stream velocity vector. The set of attitude and wake illustrations on the top correspond to the aircraft body with a nose-up net pitching moment. The set of attitude and wake illustrations on the bottom correspond to the aircraft body with a zero net pitching moment. Note that Figure 5.32 is drawn to scale.

The longitudinal cyclic descent results in the tip-path plane tilting forward thereby increasing the miss distance between the tip-path plane and the trailed wake. Both aircraft bodies exhibit similar responses to the applied control, but the body with the zero net pitching moment pitches forward at a faster rate resulting in larger miss distances. As the miss distance increases over the course of the maneuver, BVI is not expected to be produced when executing longitudinal cyclic descents.

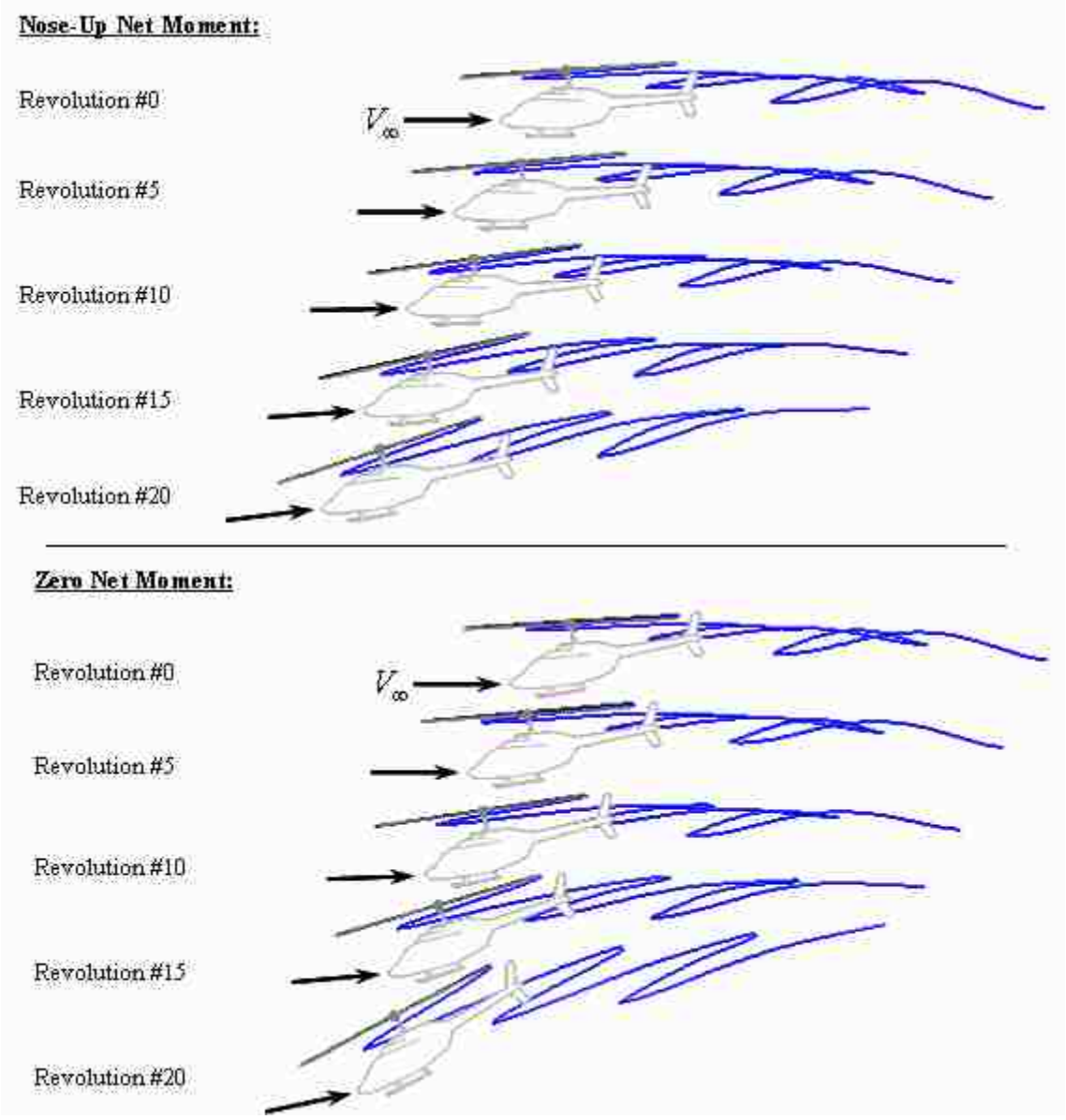

Figure 5.32. Aircraft attitude and wake geometry for the longitudinal cyclic descent. All attitudes and geometries are shown to scale.

The flight trajectory corresponding to the cyclic pitch perturbation is presented in Figure 5.33. The aircraft body featuring a zero net pitching moment descends faster than the body with the nose-up net pitching moment.

Figure 5.33. Flight trajectory for longitudinal cyclic descent.

The acoustic response to the longitudinal cyclic descent is provided in Figure 5.34. The time history for the fuselage body with a nose-up net pitching moment is plotted at the top; the time history for the fuselage body with a zero net pitching moment is plotted in the middle; and the time history of various sound pressure metrics is plotted at the bottom. The forward tilt of the tip-path plane and the increased miss distance between the wake and the rotor blades leads to no significant increase in BVI levels during the maneuver for either fuselage model. Furthermore, the forward tilt of the tip-path plane also prevents the directivity of the low frequency loading noise from being detected in the far field. The steady rise in the acoustic levels is mainly due to the aircraft approaching the observer.

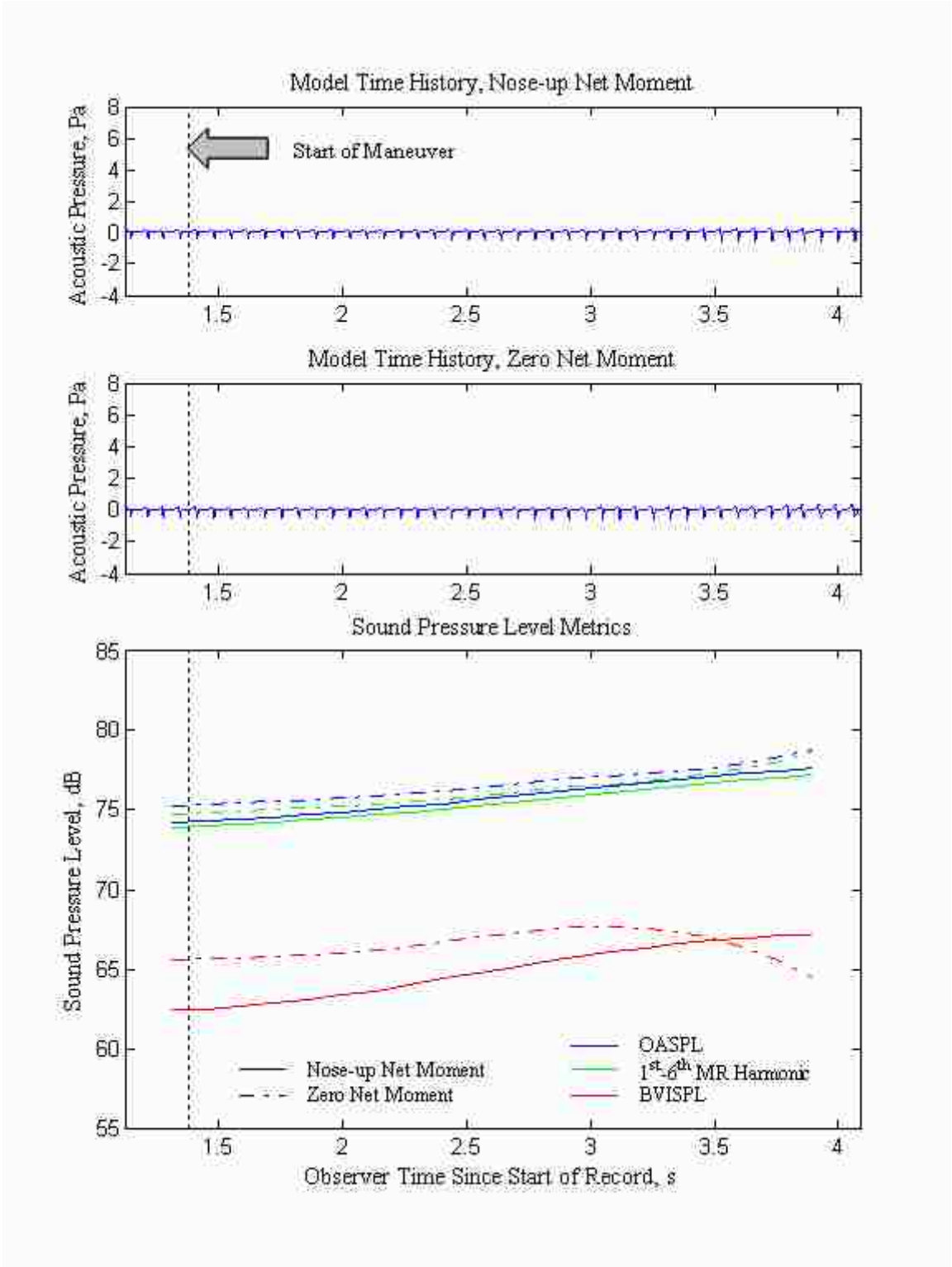

Figure 5.34. Acoustic response to the longitudinal cyclic descent.

5.3.5 Collective Descents

To execute the collective descent, a ramp input of -2°/s is applied to the collective lever while the longitudinal cyclic is held at the trim position. The ramp sequence is applied to an aircraft in trimmed level flight traveling at 75 knots. The descent is initiated at an altitude of 45 m when the aircraft is 475 m away from the center microphone. The time history of the control input sequence relative to the trim position is plotted in Figure 5.35.

Figure 5.35. Control input time history for the collective descent.

The fuselage pitch rate response to the collective descent is provided in Figure 5.36. The aircraft body with the zero net pitching moment experiences a similar pitch response to that found from the longitudinal cyclic descent. However, the body with the nose-up net pitching moment initially has a positive pitch rate. This is a similar phenomena observed during the collective climbs for the body with the nose-up net pitching moment and is the result of the action of the thrust vector relative to the center of gravity. Whereas in the climbs the increase in thrust produces a nose-down motion, here

the decrease in thrust produces a nose-up motion. Over the course of the maneuver, the pitch rate reaches a maximum and begins to decrease as the thrust vector begins to tilt forward.

Figure 5.36. Pitch rate response to the collective descent.

The angle of attack of the tip-path plane during the course of the maneuver is presented in Figure 5.37. As expected from the previous illustrations, the tip-path plane angles of attack become increasingly positive over the course of the maneuver. For the case of the aircraft body with the nose-up net pitching moment, the angle of attack increases faster due to the aft tilt of the tip-path plane. For the case of the aircraft body with the zero net pitching moment, the rate of descent tilts the free stream velocity vector faster than the tip-path plane can rotate, thereby increasing the tip-path plane angle of attack.

Figure 5.37. Tip-path plane angle of attack response to the collective descent.

A diagram showing the orientation of the thrust vector over the course of the maneuver is illustrated in Figure 5.38. For reference, the action line from the hub to the center of gravity is displayed in each image to indicate the action of the thrust vector. Note that while the alignment of the thrust vector impacts the rotation of the tip-path plane during the collective descents, the alignment of the thrust vector relative to the center of gravity remains fairly steady over the course of the maneuver. These trends are similar to those observed for the collective climbs.

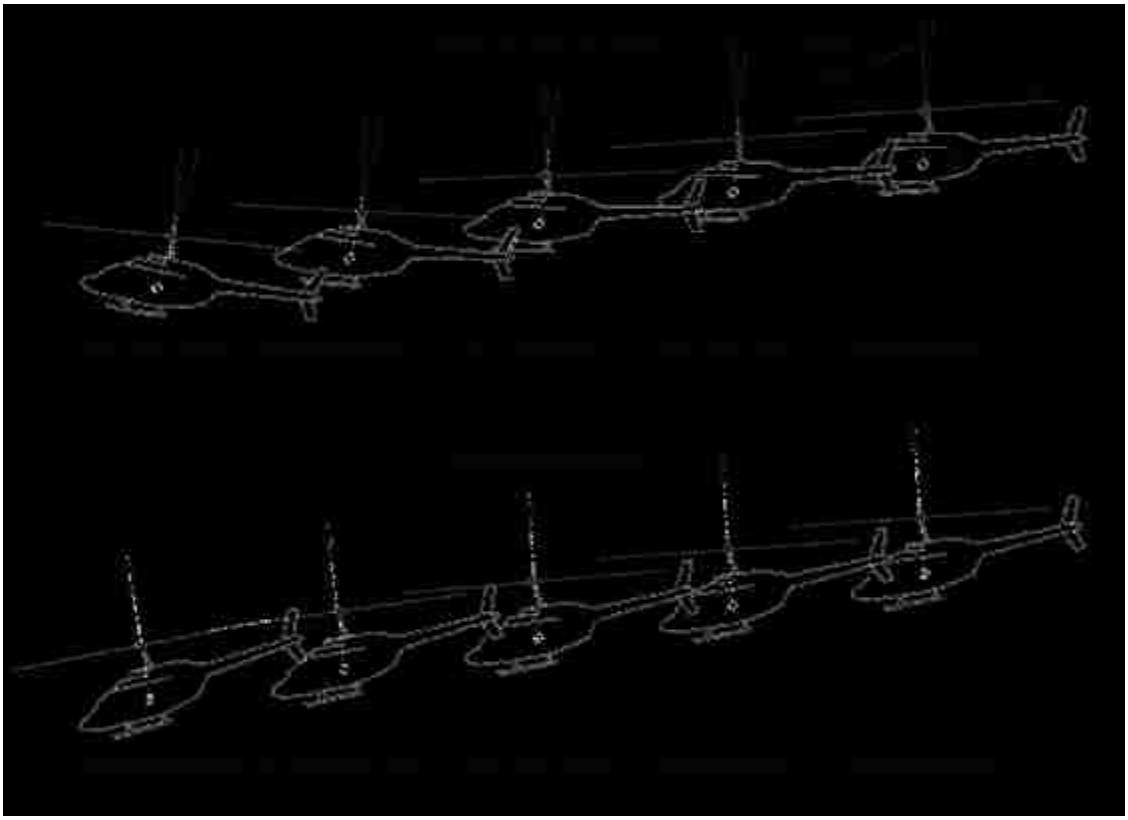

Figure 5.38. Thrust vector orientation relative to the center of gravity during collective descents. All attitudes and geometries are shown to scale.

The airspeed of the helicopter during the descent is presented in Figure 5.15. For the case of the aircraft body with a nose-up net pitching moment, the aft tilt of the tip-path plane and the thrust vector results in a slight drop in airspeed. Comparatively, the forward tilt of the tip-path plane and the thrust vector for the aircraft body with a zero net pitching moment produces a slight acceleration as the aircraft descends.

Figure 5.39. Airspeed response to the collective descent.

Aircraft attitude and wake geometries over the course of the maneuver are illustrated in Figure 5.40. The control is applied at revolution #0 and the geometries and attitudes are illustrated every five main rotor revolutions. The black arrows at the nose of the aircraft indicate the angle of the free stream velocity vector. The set of attitude and wake illustrations on the top correspond to the aircraft body with a nose-up net pitching moment. The set of attitude and wake illustrations on the bottom correspond to the aircraft body with a zero net pitching moment. Note that Figure 5.40 is drawn to scale.

In the case of the aircraft body with a nose-up net pitching moment, the initial response to the collective input is for the nose of the aircraft and the tip-path plane to tilt backward. This tilt causes the wake to pass through the tip-path plane where it eventually settles above the rotor. In the case of the aircraft body with a zero net pitching moment, the tip-path plane tilts forward. However, the combination of the decrease in thrust and the vertical descent leads to a reduction in inflow through the rotor and the wake

eventually passes through the tip-path plane. Both aircraft would be expected to produce BVI when executing a collective descent.

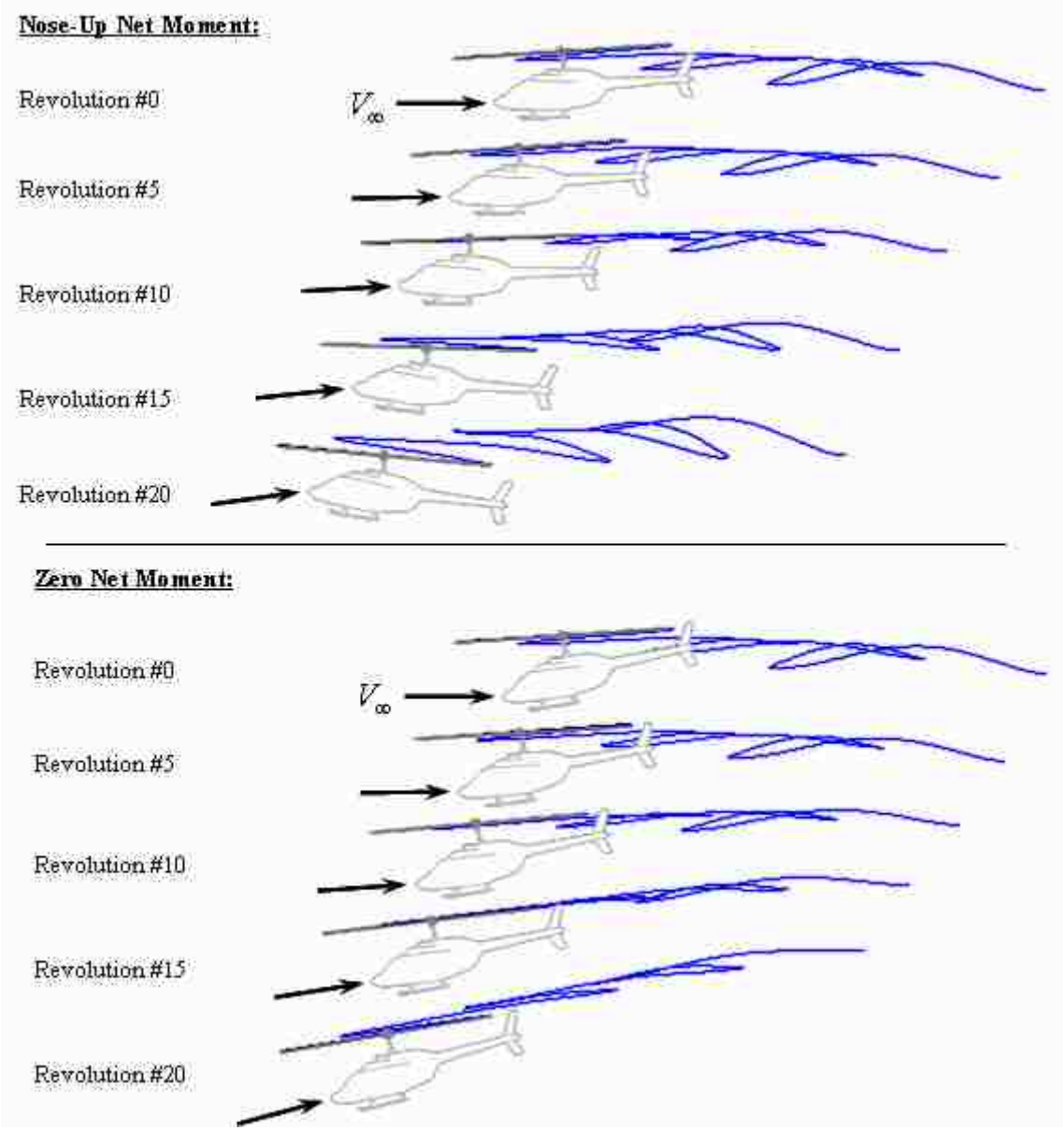

Figure 5.40. Aircraft attitude and wake geometry for the collective descent. All attitudes and geometries are shown to scale.

The flight trajectory corresponding to the collective perturbation is presented in Figure 5.41. As observed in the cyclic descents, the aircraft body with the zero net

pitching moment descends faster than the aircraft body with the nose-up net pitching moment.

Figure 5.41. Flight trajectory for the collective descent.

The acoustic response to the collective descent is provided in Figure 5.42. The top plot presents the time history for the aircraft body with a nose-up net pitching moment; the middle plot presents the time history for the aircraft body with a zero net pitching moment; and the bottom plot presents the time history of several acoustic metrics. As expected from the wake geometry illustrations, both collective descents produce impulsive BVI noise as the wake passes through the tip-path plane. However, these events are shorter in duration and less intense than those observed for the longitudinal cyclic climbs. One reason is that the wake passes through the tip-path plane much faster during the collective descents than during the cyclic climb. The second reason is due to the directivity of the BVI noise and the attitude of the helicopter during the maneuver. During the collective descents, when the wake passes through the tip-path plane, the observer generally remains in the plane of the main rotor. The slight increase of

impulsive noise observed in the time histories is due to the in-plane component of BVI noise attributed to the induced drag which generally acts in the plane of the rotor. Since the magnitude of induced drag is typically much lower than the magnitude of the lift, the in-plane BVI noise is generally much lower than the out of plane BVI noise.

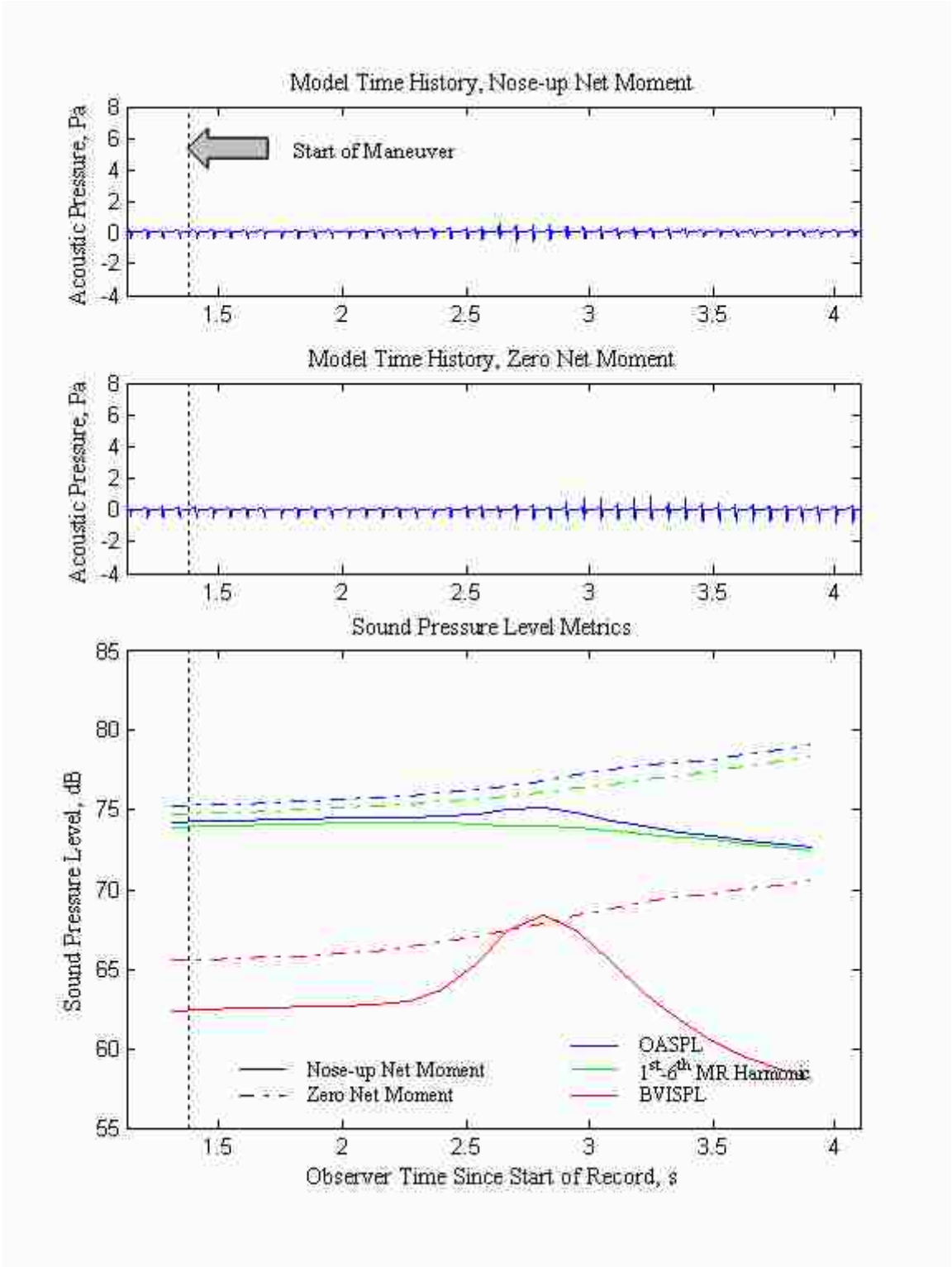

Figure 5.42. Acoustic response to collective descent.

It is important to emphasize that the discussion for the descent maneuvers applies only to the initial descent transient. As was demonstrated in the case of steady flights, the BVI noise radiated is related to the steady descent angle. Therefore, the descent angle at the end of the maneuver will have a significant impact on the BVI characteristics of the aircraft. In the case of the Bell 206B-3, peak BVI levels were observed for descent angles between 4.5° and 6°. At shallower descent angles, the trailed wake is far enough below the tip-path plane that no significant levels of BVI are radiated; at steeper descent angles, the trailed wake is far enough above the tip-path plane that no significant levels of BVI are radiated.

Therefore, selection of the appropriate control sequence will depend on the targeted exit descent angle. For shallow descent angles, the cyclic descent is preferable because the wake never passes through the tip-path plane. When the aircraft exits the transient maneuver, the wake will remain below the tip-path plane. For steeper descent angles, BVI may be unavoidable as the wake will ultimately have to pass through the tip-path plane. Therefore it will be important to consider the directivity characteristics of the tip-path plane relative to the observer when executing the descent to avoid unwanted annoyance and detection.

5.4 Summary

This chapter focused on the application of the first principles model to maneuvering flight. The first section of this chapter investigated the influence and the make-up of the thickness noise and the low frequency loading noise in the absence of BVI noise. Thickness noise is the loudest acoustic source for observers near the plane of the rotor while loading noise is the loudest acoustic source for observers outside of the

plane of the rotor. Outside of the plane of the rotor, the Beddoes' inflow distribution predicts louder sound pressure levels than those predicted from a uniform inflow model. Spectral analysis of these sources indicates that the majority of the spectral content is contained within the first six main rotor harmonics. Furthermore, loading noise tends to be largely composed of content from the first two main rotor harmonics. For the Bell 206B-3 aircraft which features a fundamental main rotor harmonic frequency of 13.02 Hz, the majority of the loading noise falls below the threshold of human detection (20 Hz) and may not be a significant factor in aural detection. Thickness noise, which is spread over a larger range, will have a larger role in detection especially at higher advance ratios. Increasing the number of blades or the angular velocity of the main rotor will lead to further contribution of thickness and low frequency loading noise to detection.

This chapter also broke apart the individual terms of Farassat's Formulation 1A solution to the Ffowcs Williams-Hawkings equation. Thickness noise was found to be largely dominated by the term featuring the time rate of change of the source Mach number relative to the observer whereas the term featuring the time rate of change of the normal velocity of the source panel had a negligible impact. When calculating loading noise, the term featuring the time rate of change of the pressure distribution effectively shifted the phase of the loading noise. In general, the uniform inflow model preceded the wave form of the Beddoes' inflow model.

This dependence between the phasing of the low frequency loading noise and the inflow distribution has the potential to have a significant impact on how the loading noise will combine with the thickness noise. While maneuvering flight for the Bell 206B-3 was largely dominated by BVI noise, the detection of heavier aircraft with larger disk

loadings may be more related to thickness noise and low frequency loading noise. Accurate prediction of far field acoustics will ultimately require accurate modeling of the time rate of change of the loading distribution.

In the second section, the model was used to investigate alternate longitudinal maneuvers for initiating climbs and descents. These maneuvers included pure longitudinal cyclic inputs and pure collective inputs. For climbing maneuvers, pure collective inputs increase the miss distance between the trailed wake and the tip-path plane and would be preferable over the pure longitudinal cyclic inputs. For descents, pure longitudinal cyclic inputs increase the miss distance between the trailed wake and the tip-path plane while pure collective inputs caused the tip-path plane to pass through the wake and projected in-plane BVI noise from the induced drag towards the horizon. However, descending maneuvers are sensitive to the exiting glide slope. The selection of the appropriate control must be made depending on the descent angle. If the pilot exits at a descent angle known to have a steady state wake above the tip-path plane, the pure collective maneuver is preferable as it minimizes the time that the trailed wake lies in the tip-path plane. If the pilot exits the descent at a descent angle known to have a steady wake below the tip-path plane, the pure longitudinal cyclic maneuver is preferable as the wake never penetrates the tip-path plane. Therefore, for flying nap-of-the-earth maneuvers, the pilot should generally ascend by executing fast collective climbs and descend by executing shallow longitudinal cyclic descents. The maximum rate of descent will be dependent on the aircraft disk loading and inflow through the main rotor.

Chapter 6 Summary and Conclusions

A first principles mathematics model has been developed to estimate the external harmonic noise radiation for a helicopter performing simple dynamic maneuvers in the longitudinal plane. The performance and noise modeling has been validated with a specifically designed and implemented full-scale flight test featuring a Bell 206B-3 helicopter for steady-state and maneuvering flight. A novel tip-path plane measurement system was used during the flight test to help in the validation of the model. The theoretical modeling has helped to improve the understanding of the origins of low frequency noise and blade-vortex interaction (BVI) noise during longitudinal maneuvering flight. The modeling has also highlighted the key parameters that control helicopter acoustic radiation directed towards the horizon.

6.1 Major Accomplishments

- **Developed and validated a new first principles helicopter dynamics and acoustics model for transient maneuvers in the longitudinal plane.**

The dynamics and flapping models agreed very well with in-flight measurements made during the flight test campaign. Even during the most aggressive longitudinal transient maneuvers, the model was successfully able to simulate the response of the fuselage, the response of the main rotor flapping, and the trajectory of the aircraft.

The acoustics model also did a good job of matching the acoustic time histories recorded by ground-based microphones during the flight test. Low frequency noise predictions for thickness noise and low frequency loading noise accurately replicated the pulse shapes and amplitudes of low frequency noise recorded during the transient

maneuvers. Additionally, the predicted levels and duration of events featuring impulsive BVI noise matched reasonably well with the microphone recordings. The success of the modeling demonstrates that relatively simple wake models are sufficient for capturing the amplitudes and shapes of low frequency harmonic noise and the overall trends of BVI noise during maneuvering flight.

- **Demonstrated that the flapping dynamics of the main rotor blades do not significantly affect the acoustics radiated by the helicopter and can be neglected.**

The main rotor blades take approximately one revolution of the main rotor (0.15 s) to respond to piloting inputs for the Bell 206B-3 aircraft. This response time produces a similar delay in the overall orientation of the tip-path plane and the acoustics radiated by the main rotor. Despite the slight time delay, the flapping dynamics did not affect the duration or the levels of low frequency or BVI noise. Furthermore, the scale of the delay due to the response time of the blade flapping tends to be small compared to the duration of the entire maneuver. As a result, the flapping dynamics of the blades can be neglected without significantly changing the acoustic predictions for a maneuvering helicopter.

- **Demonstrated that Quasi-Static Acoustic Mapping (Q-SAM) methods can be used to reliably predict noise radiated during transient maneuvers in the longitudinal plane.**

The first principles model also illustrated that even during the most aggressive transient maneuvers, the geometric distortion of the wake due to the rotation of the tip-path plane and the acceleration of the aircraft had a small impact on prediction of the acoustics. For the most aggressive transient maneuvers, BVI noise levels predicted using

a Q-SAM method led the higher order model by approximately one main rotor revolution (0.15 s). As with the flapping dynamics, this time discrepancy is small compared to the duration of the entire maneuver and has a negligible effect on the predicted levels or duration of the acoustic events.

The successful demonstration of Q-SAM methods for acoustic prediction of transient maneuvers is beneficial for the development of reduced order modeling. These models can reference databases of previously predicted or measured acoustic noise for an equivalent flight condition determined from the advance ratio, the angle of attack of the tip-path plane, and the thrust coefficient. Implementation of look up tables greatly expedites acoustic computations by several orders of magnitude and enables real time acoustic modeling.

- **Developed an expanded knowledge base of helicopter main rotor noise radiation during longitudinal transient maneuvering flight.**

The first principles model was used to investigate the individual contributions of thickness noise, low frequency loading noise, and BVI noise during maneuvering flight for the Bell 206B-3 helicopter. The model was used to correlate the radiated noise pulse shapes and directivity characteristics with each source.

Low frequency harmonic noise was shown to be attributed to thickness noise and low frequency loading noise. The model confirmed the general knowledge that thickness noise was found to dominate when the observer was in the plane of the rotor and low frequency loading noise was found to dominate when the observer was out of the plane of the rotor.

Impulsive noise during transient maneuvers was shown to be attributed to BVI noise. The BVI noise levels were verified to be related to the proximity of the wake trailed by the blade tips to the tip-path plane. Furthermore, the directivity of the BVI noise was shown to generally radiate out of the plane of the rotor. No significant wake bundling resulting in a "Super-BVI" was predicted by the model or observed in the acoustic time histories recorded during the flight test.

Overall, the contribution of the individual noise sources was found to be dependent on the orientation of the tip-path plane with respect to the far field observer. Therefore, accurate knowledge of the tip-path plane angle is essential to accurately predict low frequency and BVI noise during maneuvering flight.

- **Designed, constructed, and used a unique optics-based tip-path plane tracking system to measure the main rotor flapping of a full scale maneuvering helicopter.**

A custom tip-path plane tracking system was developed to monitor the longitudinal flapping of the main rotor blades during maneuvering flight. This system was included with the instrumentation installed on the Bell 206B-3 aircraft during the acoustic flight test campaign. Measurements from this system were used to validate the blade flapping model and to quantify the effects of the blade dynamics to the external acoustic radiation of the aircraft.

The success of this system was used to develop a second generation tip-path plane tracking system that was capable of monitoring the longitudinal and lateral flapping of the main rotor blades. This system was developed for NASA and is currently being used in Rotorcraft Noise Model (RNM) flight testing.

6.2 Research and Development Impact

The findings described in this dissertation have provided insight into the behavior of main rotor harmonic noise during longitudinal transient maneuvers. The demonstrated success of the relatively simple modeling methodology leads to several immediate applications. Two areas that are presently being explored include the development of a real time in-cabin acoustic display and the implementation for use in optimizing flight trajectories for noise mitigation. These applications are described below.

- **The operational use of Q-SAM to predict main rotor harmonic noise for transient maneuvering flight.**

Q-SAM models have the potential to greatly reduce the computational expense of modeling the external radiation of the helicopter main rotor and make real time prediction possible. Q-SAM models relate the acoustics radiated by an aircraft to the acoustics produced when operating at an equivalent steady state flight condition. This enables the implementation of a variety of existing and future Rotorcraft Noise Model (RNM) databases to be used to predict the acoustics radiated during transient maneuvers.

An immediate use of Q-SAM modeling is the development of an in-cabin display that predicts the far-field acoustics radiated by the helicopter during flight. Traditionally, the acoustic noise heard within the cabin has been used as an indicator of the far field acoustic radiation. However, due to the directivity of the main rotor noise sources and the position of the cabin relative to these sources, cabin noise is not a reliable indicator of external noise radiation. As an alternative, an in-cabin acoustic display system could monitor the operating condition of the aircraft and refer to an acoustic database for predicting the far field acoustics. While these databases are generally designed for steady

state flight, this research has shown that they can be also be used to predict the main rotor acoustics during transient maneuvers.

- **Results provide guidance for the development of techniques to fly quietly.**

The findings from this research can be used to train pilots to mitigate the levels of noise radiated by the aircraft when executing transient maneuvers and optimize flight trajectories for minimal noise production. These mitigation strategies are applicable to military and civilian missions.

When present, BVI noise is typically the loudest acoustic source of the main rotor. Since BVI intensity is related to the proximity of the blade to the trailed wake, a good practice is to avoid flying in conditions where the wake passes through the tip-path plane of the main rotor.

However, the manner in which acoustic sources radiate towards far field observers was found to be dependent on the orientation of the tip-path plane relative to those observers. In certain instances, the pilot may only be concerned with the projection of specific acoustic sources towards specified targets. A common situation arises in military missions where the observer tends to be far ahead of the helicopter towards the horizon. In this scenario, it may be more advantageous to maintain a desired tip-path plane attitude relative to the observer. Appropriate combination maneuvers can be designed such that in the event that the aircraft does produce BVI noise, the tip-path plane orientation ensures that the majority of the acoustic energy is projected below the helicopter and not towards the horizon.

6.3 Suggestions for Future Research

The findings of this research present some interesting opportunities for future research. These opportunities include extending the capabilities of the modeling and additional validation.

- **Extended capabilities and applications for the first principles model.**

The work presented in this dissertation has shown that it is possible to accurately predict the main rotor noise sources on the Bell 206B-3 helicopter for longitudinal maneuvering flight. However, several improvements could be implemented to expand the capabilities of the model.

First, the mathematical model should be expanded to study lateral flight. For these lateral maneuvers, the uniform inflow distribution used with the dynamics model should be updated to incorporate, at minimum, longitudinal inflow variations. While the longitudinal inflow variation has been shown to have small effects on longitudinal flapping, it does have a notable effect on the lateral flapping. Since wake proximity to the tip-path plane is an important consideration when predicting far field acoustics during transient maneuvers, it is essential to have an accurate model for the complete orientation of the tip-path plane during lateral maneuvers.

Second, the model should be used to perform a thorough parametric study. In particular, a study should be conducted to study the acoustic trends for aircraft of differing gross weights, operations at high elevations, and helicopters with more than two main rotor blades.

Third, the tail rotor acoustics and performance should be incorporated into the model to more accurately predict the acoustic radiation profiles of the conventional

helicopter. This requires the expansion of the dynamics and performance model to include the tail rotor in the force balance. The acoustic model would also have to be amended to compute the thickness and loading noise for the tail rotor.

Lastly, the model should be extended to support helicopters of different configurations. In particular, noise predictions should be made for counter-rotating main rotors, tandem configurations, and compound helicopters. It would be particularly beneficial to study configurations that feature high cruising speeds and the effects of the high advance ratios.

- **Additional validation for modeling improvements.**

During maneuvering flight, the pilot is likely to execute rolling maneuvers that may produce intense BVI noise. These maneuvers were also examined during the Gilroy flight test, but the tip-path plane tracking system was only capable of tracking the longitudinal flapping motion of the main rotor, so the lateral flapping motion could not be verified with onboard measurements. To validate the extension of the model to lateral maneuvers, the full scale validation efforts should be extended to lateral steady-state and maneuvering flight.

Next, the sensitivity of the low frequency loading noise indicates a necessity to identify the appropriate loading distribution on the main rotor. Measurement of the blade loads on the rotor during flight poses a significant technical challenge. However, it may be possible to study the effects of loading distributions with existing experimental data. A natural starting point would be to compare the model to available wind tunnel and flight test data for pressure instrumented blades where the loading distributions are known.

Lastly, additional aircraft should be used in the validation process. As in the parametric study, these aircraft should have a range of gross weights and feature various rotor configurations.

Appendix A Coordinate Systems

The helicopter rotor system consists of a variety of coordinate systems. Each of these systems is composed of an orthogonal basis of unit vectors that are carefully selected to measure specific properties in the first principles model. These measurements include the inertial properties of the aircraft, the aerodynamics of the blade sections, and the orientation of the tip-path plane. While no single coordinate system provides intuitive measurements for everything, transformations can be performed to convert the vector quantities expressed in one system in terms of another.

Consider, for example, two different basis sets of orthogonal unit vectors $\left\{\hat{i}_A, \hat{j}_A, \hat{k}_A\right\}$ and $\left\{\hat{i}_B, \hat{j}_B, \hat{k}_B\right\}$ as illustrated in Figure A.1. If $\overrightarrow{A^A}$ is a vector defined using the initial basis of unit vectors, then there exists a transformation matrix that allows the same vector to be described in the second basis of unit vectors, $\overrightarrow{A^B}$ [52]:

$$\begin{Bmatrix} A_{i,B} \\ A_{j,B} \\ A_{k,B} \end{Bmatrix} = \begin{bmatrix} \hat{i}_B \bullet \hat{i}_A & \hat{i}_B \bullet \hat{j}_A & \hat{i}_B \bullet \hat{k}_A \\ \hat{j}_B \bullet \hat{i}_A & \hat{j}_B \bullet \hat{j}_A & \hat{j}_B \bullet \hat{k}_A \\ \hat{k}_B \bullet \hat{i}_A & \hat{k}_B \bullet \hat{j}_A & \hat{k}_B \bullet \hat{k}_A \end{bmatrix} \begin{Bmatrix} A_{i,A} \\ A_{j,A} \\ A_{k,A} \end{Bmatrix} \tag{A.1}$$

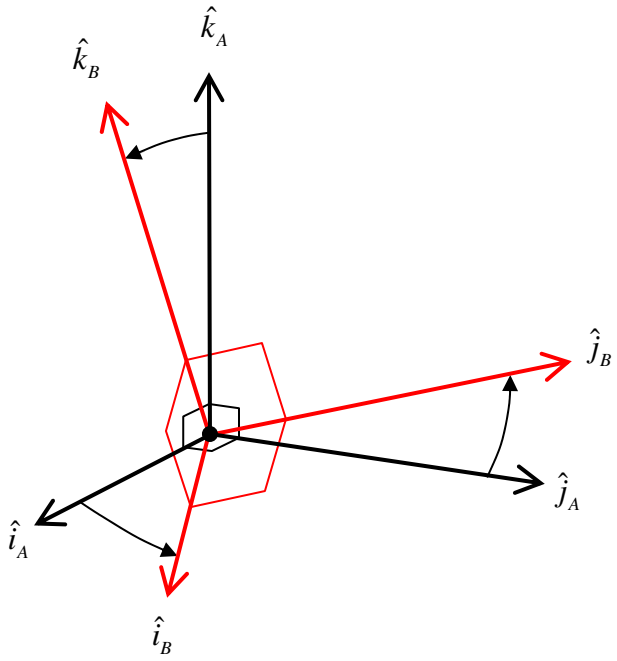

Figure A.1. General coordinate system transformation.

The following subsections describe the various coordinate systems in detail and list the transformation matrices used to convert vectors from one system to another. An overview of the various coordinate systems is shown in Figure A.2. The first letter of each coordinate system is used as shorthand when describing measurements in a particular system. Transformation matrices used to move from one coordinate system to another are shown in boxes. Therefore, the symbol $T^{X/Y}$ is to be read "the transformation matrix from coordinate system *X* to coordinate system *Y*."

As an example, a vector described in the aerodynamic system, $\overrightarrow{Y^A}$, can be expressed in the tip-path plane system, $\overrightarrow{Y^T}$, by the following transformation:

$$\overrightarrow{Y^T} = \left[T^{S/T}\right]\left[T^{R/S}\right]\left[T^{A/R}\right]\overrightarrow{Y^R} \tag{A.2}$$

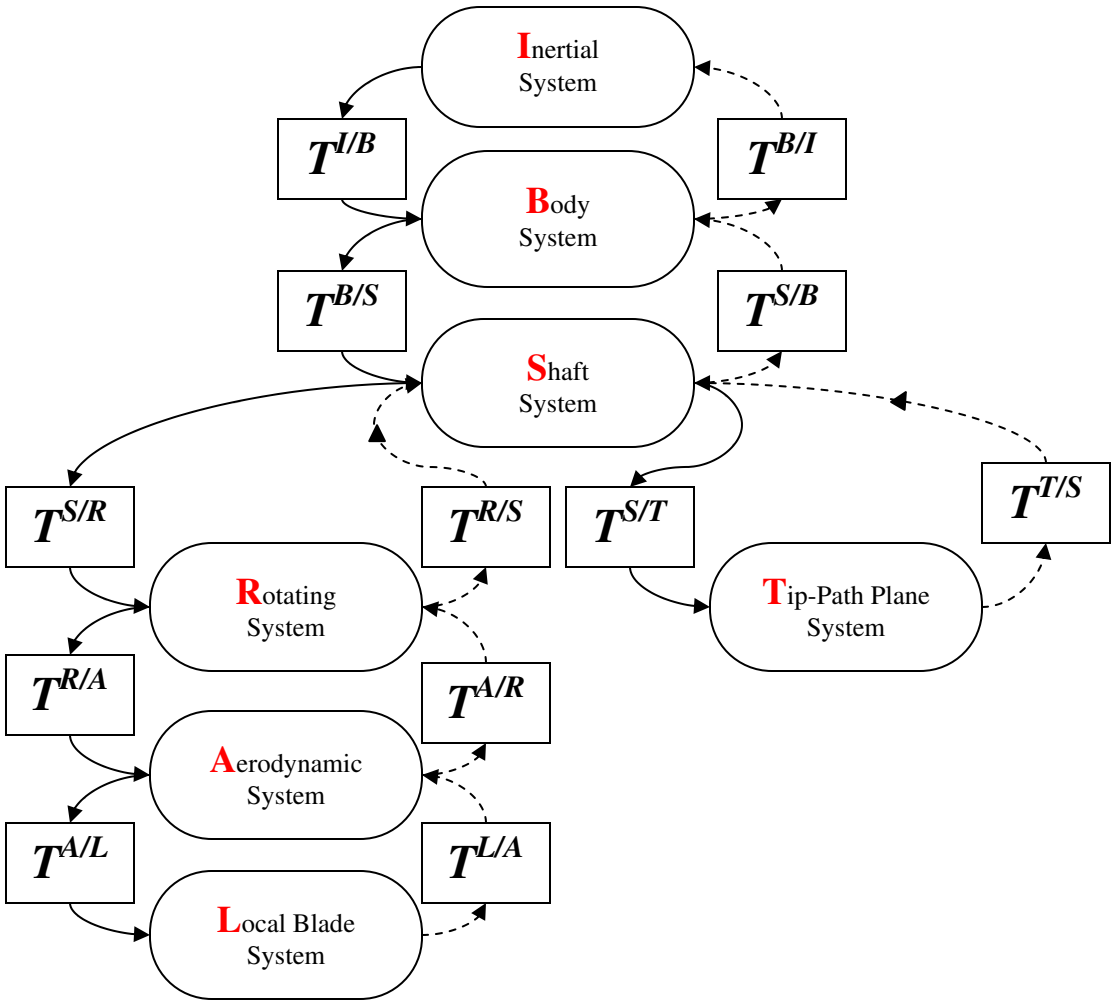

Figure A.2. Flow diagram of coordinate system transformations.

A.1 Inertial Coordinate System

The inertial coordinate system is made up of the basis of orthogonal unit vectors $\hat{i}_I$, $\hat{j}_I$, and $\hat{k}_I$. The origin of this system, point O, is collocated with the center microphone and remains fixed with respect to the earth. This system is defined such that unit vector $\hat{i}_I$ points north, unit vector $\hat{j}_I$ points east, and $\hat{k}_I$, the cross-product of $\hat{i}_I$ and $\hat{j}_I$, points down (see Figure A.3). The inertial coordinate system is used with the onboard differential GPS system to relate the position of the aircraft to the microphones.

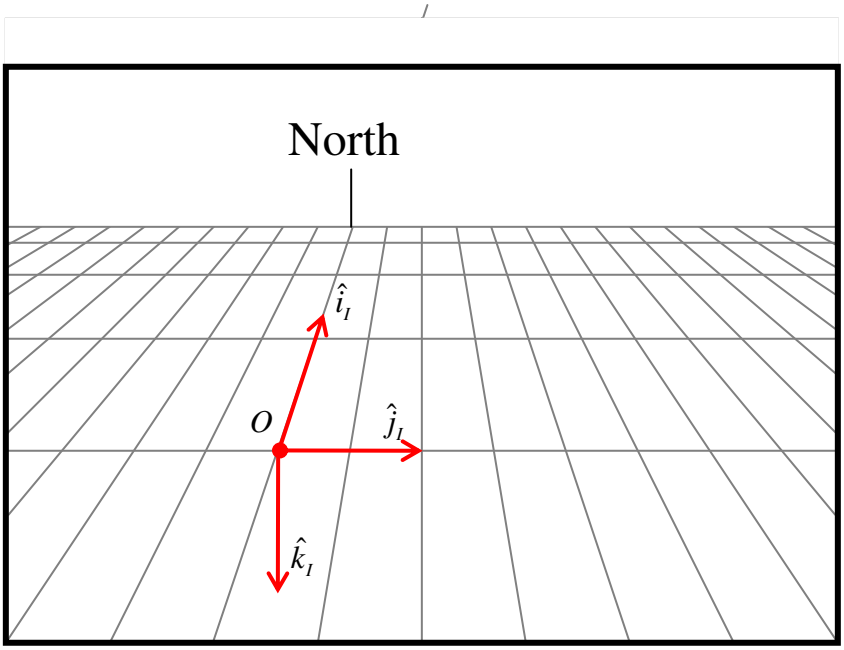

Figure A.3. Diagram of inertial coordinate system.

A.2 Body Coordinate System

The body coordinate system is made up of the basis of orthogonal unit vectors $\hat{i}_B$, $\hat{j}_B$, and $\hat{k}_B$. The origin of this system, point B, is located at the center of gravity of the aircraft. This system is defined such that unit vector $\hat{i}_B$ points towards the nose of the aircraft parallel to the fuselage waterline, unit vector $\hat{j}_B$ points to starboard parallel to the fuselage waterline, and $\hat{k}_B$, the cross product of $\hat{i}_B$ and $\hat{j}_B$, points down normal to the fuselage waterline (see Figure A.4). This reference frame rotates with the fuselage.

Inertial measurements made by the in-flight instrumentation are recorded in this reference system. Furthermore, the body coordinate system is advantageous for calculating the equations of motion for the aircraft because the moments of inertia remain constant when defined in this system.

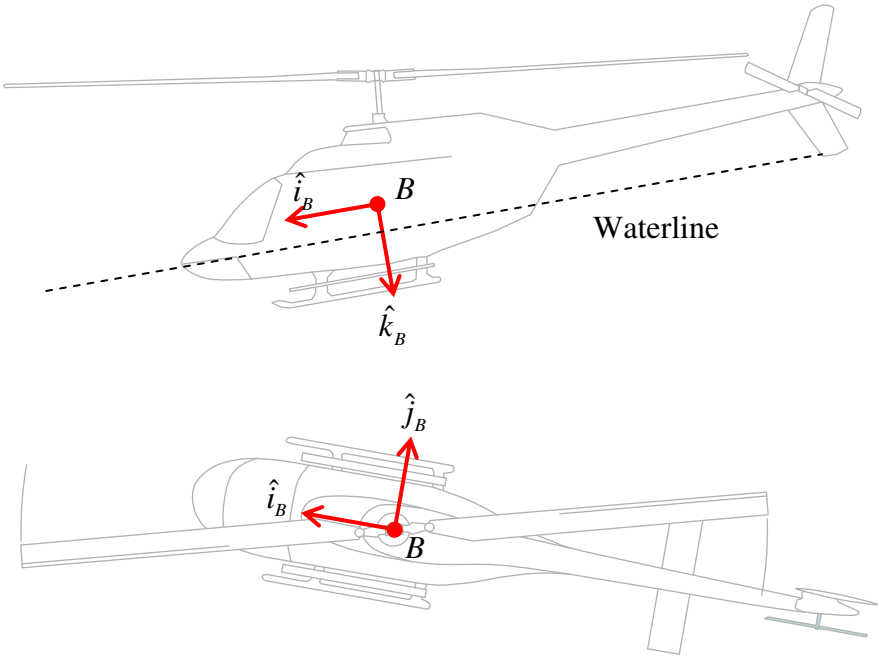

Figure A.4. Diagram of body-fixed coordinate system.

Transformation from the inertial coordinate system to the body coordinate system is performed using the standard aircraft orientation angles [53]. In this convention, first the fuselage yaw, ψ_B, is applied, then the fuselage pitch, θ_B, is applied, and lastly the fuselage roll, ϕ_B, is applied. The yaw angle is the magnetic bearing of the aircraft relative to north and is positive in the direction of increasing magnetic bearing. The pitch angle is the angle of the unit vector $\hat{i}_B$ relative to the horizon and is positive for nose up attitudes. The roll angle is the angle of the unit vector $\hat{j}_B$ relative to the horizon and is positive for starboard-wing-down attitudes. This rotation sequence is illustrated in Figure A.5.

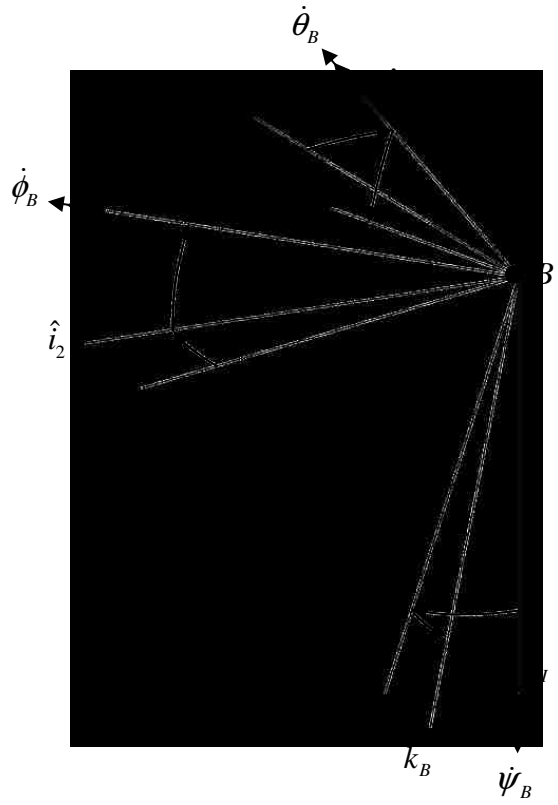

Figure A.5. Order of transformation from inertial coordinate system to the body-fixed coordinate system.

The transformation matrix from the inertial coordinate system to the body coordinate system is:

$$T^{I/B} = \begin{bmatrix} \cos\psi_B \cos\theta_B & \sin\psi_B \cos\theta_B & -\sin\theta_B \\ \begin{pmatrix}\cos\psi_B \sin\theta_B \sin\phi_B \\ -\sin\psi_B \cos\phi_B\end{pmatrix} & \begin{pmatrix}\sin\psi_B \sin\theta_B \sin\phi_B \\ +\cos\psi_B \cos\phi_B\end{pmatrix} & \cos\theta_B \sin\phi_B \\ \begin{pmatrix}\cos\psi_B \sin\theta_B \cos\phi_B \\ +\sin\psi_B \sin\phi_B\end{pmatrix} & \begin{pmatrix}\sin\psi_B \sin\theta_B \cos\phi_B \\ -\cos\psi_B \sin\phi_B\end{pmatrix} & \cos\theta_B \cos\phi_B \end{bmatrix} \quad \text{(A.3)}$$

The inverse transformation from the body coordinate system to the inertial coordinate system is:

$$T^{B/I} = \begin{bmatrix} \cos\psi_B \cos\theta_B & \begin{pmatrix} \cos\psi_B \sin\theta_B \sin\phi_B \\ -\sin\psi_B \cos\phi_B \end{pmatrix} & \begin{pmatrix} \cos\psi_B \sin\theta_B \cos\phi_B \\ +\sin\psi_B \sin\phi_B \end{pmatrix} \\ \sin\psi_B \cos\theta_B & \begin{pmatrix} \sin\psi_B \sin\theta_B \sin\phi_B \\ +\cos\psi_B \cos\phi_B \end{pmatrix} & \begin{pmatrix} \sin\psi_B \sin\theta_B \cos\phi_B \\ -\cos\psi_B \sin\phi_B \end{pmatrix} \\ -\sin\theta_B & \cos\theta_B \sin\phi_B & \cos\theta_B \cos\phi_B \end{bmatrix} \quad \text{(A.4)}$$

A.3 Shaft Coordinate System

The shaft coordinate system is made up of the basis of orthogonal unit vectors $\hat{i}_S$, $\hat{j}_S$, and $\hat{k}_S$. The origin of this system, point H, is at the main rotor hub. This system is defined such that the unit vector $\hat{k}_S$ points down parallel to the shaft, and the unit vector $\hat{i}_S$ is perpendicular to the shaft and points towards the nose (see Figure A.6). The unit vector $\hat{j}_S$ is defined as the cross product of $\hat{k}_S$ and $\hat{i}_S$ and is parallel to the unit vector $\hat{j}_B$ from the body coordinate system. Unit vectors $\hat{i}_S$ and $\hat{j}_S$ lie in the hub plane. The shaft tilt angle, θ_S, is made about the unit vector $\hat{j}_S$ and is positive when the shaft is tilted back towards the tail. Derivations of the blade flapping and shaft loads are made relative to this coordinate system.

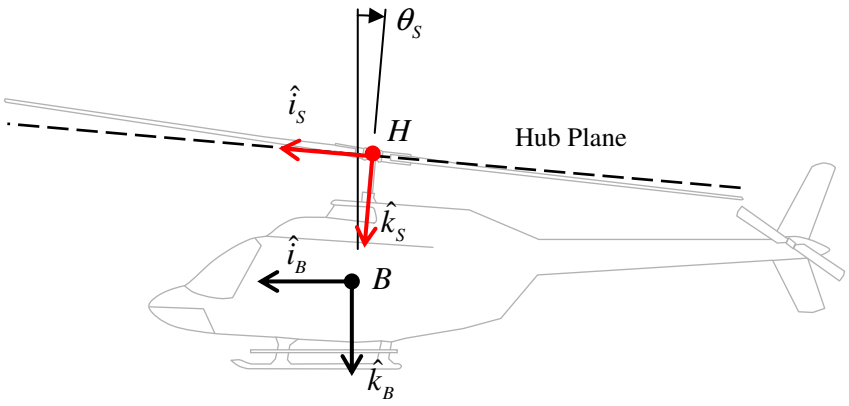

Figure A.6. Diagram of shaft-fixed coordinate system.

The transformation matrix from the body coordinate system to the shaft-fixed coordinate system is:

$$T^{B/S} = \begin{bmatrix} \cos\theta_S & 0 & -\sin\theta_S \\ 0 & 1 & 0 \\ \sin\theta_S & 0 & \cos\theta_S \end{bmatrix} \tag{A.5}$$

The inverse transformation matrix from the shaft-fixed coordinate system to the body coordinate system is:

$$T^{S/B} = \begin{bmatrix} \cos\theta_S & 0 & \sin\theta_S \\ 0 & 1 & 0 \\ -\sin\theta_S & 0 & \cos\theta_S \end{bmatrix} \tag{A.6}$$

A.4 Rotating Coordinate System

The rotating coordinate system is made up of the basis of orthogonal unit vectors $\hat{i}_R$, $\hat{j}_R$, and $\hat{k}_R$. The origin of this system, point H, is at the main rotor hub. This system rotates with the shaft and is defined such that unit vector $\hat{i}_R$ is perpendicular to the shaft and points along the projection of the blade elastic axis on the hub plane, unit vector $\hat{k}_R$ points upward parallel to the shaft, and unit vector $\hat{j}_R$ is the cross product of $\hat{k}_R$ and $\hat{i}_R$ (see Figure A.7). Unit vectors $\hat{i}_R$ and $\hat{j}_R$ both lie in the hub plane and the unit vector $\hat{k}_R$ is parallel to the unit vector $\hat{k}_S$ from the shaft coordinate system. The blade azimuth angle, ψ, is made about the unit vector $\hat{k}_R$, is positive clockwise as seen from above the plane of rotation, and is measured relative to the tail of the aircraft.

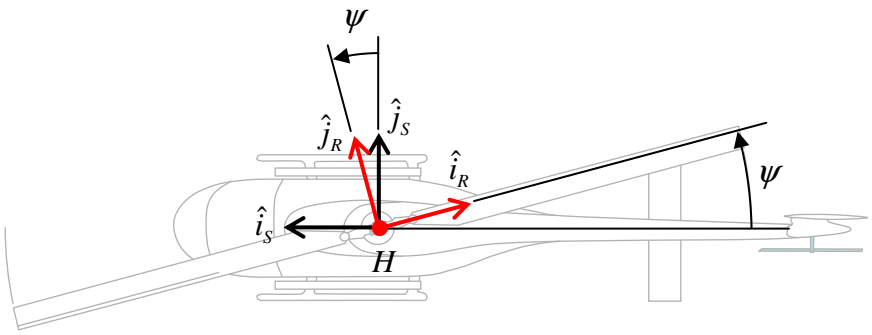

Figure A.7. Diagram of shaft-rotating coordinate system.

The transformation matrix from the shaft-fixed coordinate system to the blade rotating coordinate system is:

$$T^{S/R} = \begin{bmatrix} -\cos\psi & \sin\psi & 0 \\ \sin\psi & \cos\psi & 0 \\ 0 & 0 & -1 \end{bmatrix} \tag{A.7}$$

The inverse transformation matrix from the blade rotating coordinate system to the shaft-fixed coordinate system is:

$$T^{R/S} = \begin{bmatrix} -\cos\psi & \sin\psi & 0 \\ \sin\psi & \cos\psi & 0 \\ 0 & 0 & -1 \end{bmatrix} \tag{A.8}$$

A.5 Aerodynamic Coordinate System

The aerodynamics coordinate system is made up of the basis of orthogonal unit vectors $\hat{e}_T$, $\hat{e}_P$, and $\hat{e}_R$. The origin of this system, point H, is at the main rotor hub. This system is defined such that unit vector $\hat{e}_R$ points outward along the elastic axis of the blade, $\hat{e}_T$ is perpendicular to the shaft and lies in the hub plane, and unit vector $\hat{e}_P$ is the cross product of $\hat{e}_R$ and $\hat{e}_T$ (see Figure A.8). The unit vector $\hat{e}_T$ is parallel to the unit vector $\hat{j}_R$ from the rotating coordinate system. The blade flapping angle, β, is made about

the unit vector $\hat{e}_T$ and is positive as the blade flaps above the hub plane. This system is used to obtain the airfoil sectional aerodynamics.

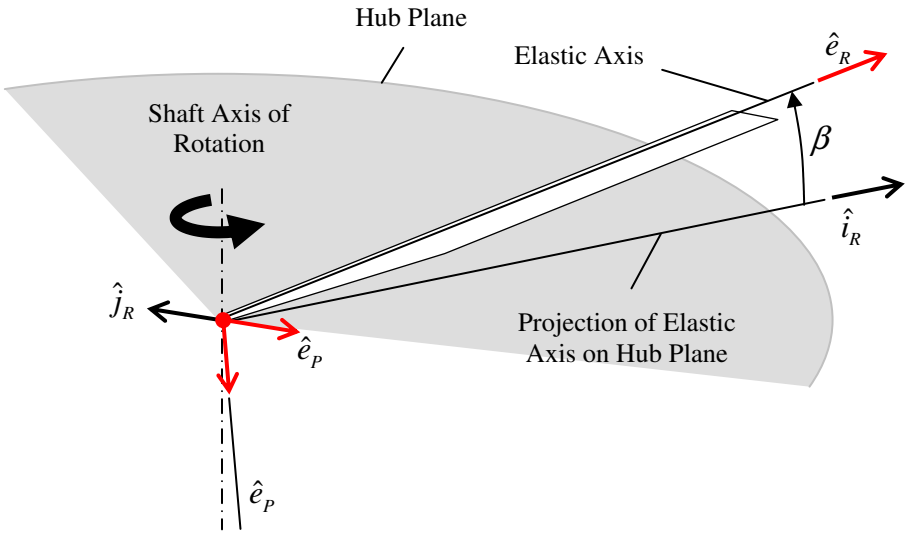

Figure A.8. Diagram of aerodynamic coordinate system.

The transformation matrix from the blade rotating coordinate system to the aerodynamic coordinate system is:

$$T^{R/A} = \begin{bmatrix} 0 & -1 & 0 \\ \sin\beta & 0 & -\cos\beta \\ \cos\beta & 0 & \sin\beta \end{bmatrix} \approx \underbrace{\begin{bmatrix} 0 & -1 & 0 \\ \beta & 0 & -1 \\ 1 & 0 & \beta \end{bmatrix}}_{\text{Small Angle Approximation}} \tag{A.9}$$

The inverse transformation matrix from the aerodynamic coordinate system to the blade rotating coordinate system is:

$$T^{A/R} = \begin{bmatrix} 0 & \sin\beta & \cos\beta \\ -1 & 0 & 0 \\ 0 & -\cos\beta & \sin\beta \end{bmatrix} \approx \underbrace{\begin{bmatrix} 0 & \beta & 1 \\ -1 & 0 & 0 \\ 0 & -1 & \beta \end{bmatrix}}_{\text{Small Angle Approximation}} \tag{A.10}$$

A.6 Local Blade Coordinate System

The local aerodynamics coordinate system is made up of the basis of orthogonal unit vectors $\hat{e}_{T,L}$, $\hat{e}_{P,L}$, and $\hat{e}_{R,L}$. The origin of this system, point P, lies on the elastic axis at the root of the blade. This system is defined such that unit vector $\hat{e}_{T,L}$ points along the chord line from the leading edge to the trailing edge of the blade at the root station, unit vector $\hat{e}_{R,L}$ points outward along the elastic axis of the blade, and unit vector $\hat{e}_{P,L}$ is the cross product of $\hat{e}_{R,L}$ and $\hat{e}_{T,L}$ (see Figure A.9). Unit vector $\hat{e}_{R,L}$ is parallel to unit vector $\hat{e}_R$ from the aerodynamic coordinate system. The root pitch angle, θ, is made about $\hat{e}_{R,L}$ and is positive as the blade pitches leading-edge-up. This coordinate system is used to conveniently describe the blade geometry.

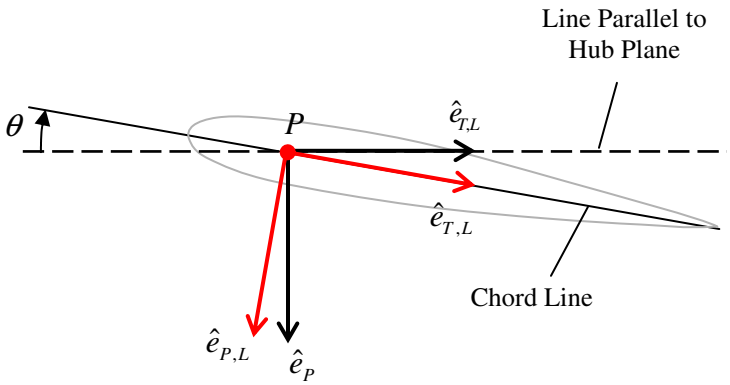

Figure A.9. Diagram of local blade coordinate system.

The transformation matrix from the aerodynamic coordinate system to the local blade coordinate system is:

$$T^{A/L} = \begin{bmatrix} \cos\theta & \sin\theta & 0 \\ -\sin\theta & \cos\theta & 0 \\ 0 & 0 & 1 \end{bmatrix} \tag{A.11}$$

The inverse transformation matrix from the local blade coordinate system to the aerodynamic coordinate system is:

$$T^{L/A} = \begin{bmatrix} \cos\theta & -\sin\theta & 0 \\ \sin\theta & \cos\theta & 0 \\ 0 & 0 & 1 \end{bmatrix} \tag{A.12}$$

A.7 Tip-Path Plane Coordinate System

The tip-path plane is defined as the plane traced by the blade tip under first harmonic flapping motion over one revolution of the main rotor:

$$\beta = a_0 - a_1 \cos\psi - b_1 \sin\psi \tag{A.13}$$

Where a_0 is the coning angle of the blade, a_1 is the longitudinal flapping angle, and b_1 is the lateral flapping angle.

The tip-path plane coordinate system is made up of the basis of orthogonal unit vectors $\hat{i}_T$, $\hat{j}_T$, and $\hat{k}_T$. This system is defined such that $\hat{k}_T$ points upward normal to the tip-path plane, unit vector $\hat{i}_T$ points along the tip-path plane towards the tail, and unit vector $\hat{j}_T$ is the cross product of $\hat{k}_T$ and $\hat{i}_T$ (see Figure A.10). The longitudinal flapping angle, a_1, is defined positive when the tip-path plane is tilted back towards the tail; the lateral flapping angle, b_1, is positive when the tip-path plane is tilted to starboard. This coordinate system is used to relate the inflow through the rotor and miss distance between the trailed wake and the blades.

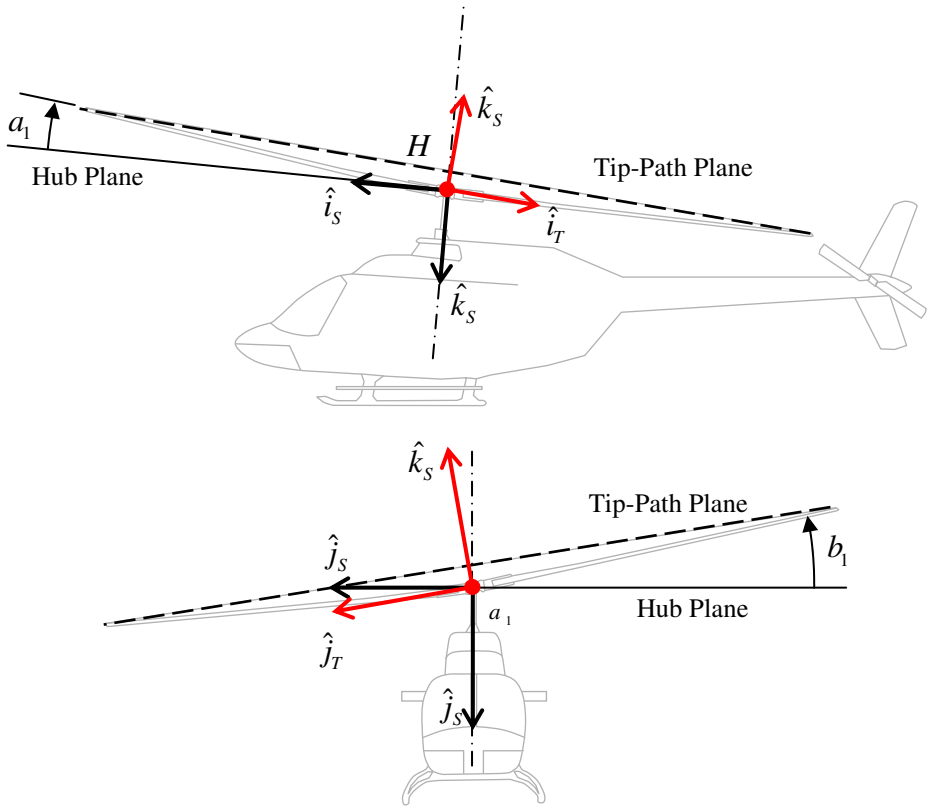

Figure A.10. Diagram of the tip-path plane coordinate system.

The transformation matrix from the shaft-fixed coordinate system to the tip-path plane coordinate system is:

$$T^{S/T} = \begin{bmatrix} -\cos a_1 & 0 & \sin a_1 \\ \sin a_1 \sin b_1 & \cos b_1 & \cos a_1 \sin b_1 \\ -\sin a_1 \cos b_1 & \sin b_1 & -\cos a_1 \cos b_1 \end{bmatrix} \tag{A.14}$$

The inverse transformation matrix from the tip-path plane coordinate system to the shaft-fixed coordinate system is:

$$T^{T/S} = \begin{bmatrix} -\cos a_1 & \sin a_1 \sin b_1 & -\sin a_1 \cos b_1 \\ 0 & \cos b_1 & \sin b_1 \\ \sin a_1 & \cos a_1 \sin b_1 & -\cos a_1 \cos b_1 \end{bmatrix} \tag{A.15}$$

Appendix B Body Equations of Motion

In this section, the Euler's equations of motion are derived for a helicopter with a symmetric fuselage shown in Figure B.1. Body velocities and accelerations, both translational and rotational, are assumed positive when acting in the same direction as the body coordinate system. The center of gravity of the entire aircraft is located at point B.

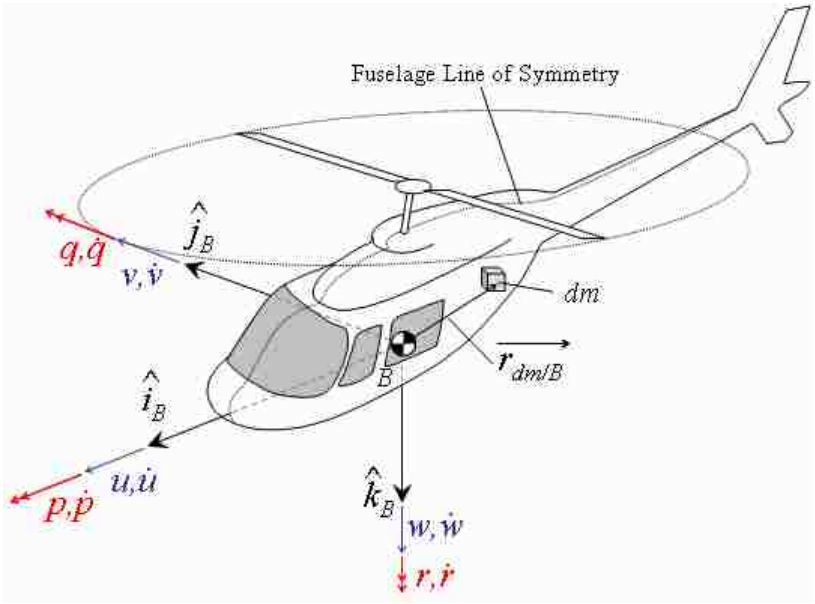

Figure B.1. Body coordinate system orientation.

Newton's second law applied to mass element dm moving with absolute velocity $\overrightarrow{{}^{I}V}$ yields:

$$\sum d\overrightarrow{{}^{I}F} = {}^{I}\left(\frac{d\overrightarrow{{}^{I}V}}{dt}\right)dm \tag{B.1}$$

Where $\sum d\overrightarrow{{}^{I}F}$ is the resultant of all forces acting on the mass element. The superscript I indicates that the term is expressed relative to the inertial frame. Integrating the above equation over the entire body yields:

$$\sum \overrightarrow{{}^{I}F} = m \, {}^{I}\left(\frac{d\overrightarrow{{}^{I}V}}{dt} \right) \tag{B.2}$$

Where $\sum \overrightarrow{{}^{I}F}$ is the resultant external force acting on the entire body at the center of mass.

Equation (B.2) can also be expressed in terms of the body coordinate system:

$$\sum \overrightarrow{{}^{I}F} = m \, {}^{I}\left(\frac{d\overrightarrow{{}^{I}V}}{dt} \right) = m\left[{}^{B}\left(\frac{d\overrightarrow{{}^{I}V}}{dt} \right) + \overrightarrow{\omega^{I/B}} \times \overrightarrow{{}^{I}V} \right] \tag{B.3}$$

Where $\overrightarrow{{}^{I}V} = u\hat{i}_B + v\hat{j}_B + w\hat{k}_B$ and $\overrightarrow{\omega^{I/B}} = p\hat{i}_B + q\hat{j}_B + r\hat{k}_B$

Expanding equation (B.3) yields:

$$\sum \overrightarrow{{}^{I}F} \bullet \hat{i}_B = X = m\dot{u} + m(qw - rv) \tag{B.4}$$

$$\sum \overrightarrow{{}^{I}F} \bullet \hat{j}_B = Y = m\dot{v} + m(ru - pw) \tag{B.5}$$

$$\sum \overrightarrow{{}^{I}F} \bullet \hat{k}_B = Z = m\dot{w} + m(pv - qu) \tag{B.6}$$

Next consider the angular momentum of a mass element. The inertial angular momentum of a mass element relative to the center of mass, B, is:

$$d\overrightarrow{{}^{I}h} = \left(\overrightarrow{r_{dm/B}} \times {}^{I}\left(\frac{d\overrightarrow{r_{dm/B}}}{dt} \right) \right) dm \tag{B.7}$$

As before, the expression can be expanded in terms of the body coordinate system:

$$d\overrightarrow{{}^{I}h} = \left(\overrightarrow{r_{dm/B}} \times \left[\underbrace{{}^{B}\left(\frac{d\overrightarrow{r_{dm/B}}}{dt} \right)}_{0 \text{ (rigid body)}} + \overrightarrow{\omega^{B/I}} \times \overrightarrow{r_{dm/B}} \right] \right) dm \tag{B.8}$$

Where $\overrightarrow{r_{dm/B}} = x\hat{i}_B + y\hat{j}_B + z\hat{k}_B$

Integrating the above expression yields the total angular momentum acting at the center of mass:

$$\overrightarrow{{}^{I}h} = \begin{bmatrix} I_{xx} & -I_{xy} & -I_{xz} \\ -I_{yx} & I_{yy} & -I_{yz} \\ -I_{zx} & -I_{zy} & I_{zz} \end{bmatrix} \begin{Bmatrix} p \\ q \\ r \end{Bmatrix} \tag{B.9}$$

Where:

$$I_{xx} = \int \left(y^2 + z^2 \right) dm; \quad I_{yy} = \int \left(x^2 + z^2 \right) dm; \quad I_{zz} = \int \left(x^2 + y^2 \right) dm$$
$$I_{xy} = I_{yx} = \int xy dm; \qquad I_{xz} = I_{zx} = \int xz dm; \qquad I_{yz} = I_{zy} = \int yz dm$$

The sum of the external moments about the center of mass, $\sum \overrightarrow{{}^{I}M}$, is the time derivative of the angular momentum relative to the inertial reference frame:

$$\sum \overrightarrow{{}^{I}M} = {}^{I}\left(\frac{d\overrightarrow{{}^{I}h}}{dt} \right) = {}^{B}\left(\frac{d\overrightarrow{{}^{I}h}}{dt} + \overrightarrow{\omega^{I/B}} \times \overrightarrow{{}^{I}h} \right) \tag{B.10}$$

Which yields:

$$\sum \overrightarrow{{}^{I}M} \bullet \hat{i}_B = L = I_{xx}\dot{p} + I_{xy}\left(pr - \dot{q} \right) - I_{xz}\left(pq + \dot{r} \right) + I_{yz}\left(r^2 - q^2 \right) + \left(I_{zz} - I_{yy} \right) qr \tag{B.11}$$

$$\sum \overrightarrow{{}^{I}M} \bullet \hat{j}_B = M = I_{yy}\dot{q} - I_{xy}\left(qr + \dot{p} \right) + I_{yz}\left(pq - \dot{r} \right) + I_{xz}\left(p^2 - r^2 \right) + \left(I_{xx} - I_{zz} \right) pr \tag{B.12}$$

$$\sum \overrightarrow{{}^{I}M} \bullet \hat{k}_B = N = I_{zz}\dot{r} + I_{xz}\left(qr - \dot{p} \right) - I_{yz}\left(pr + \dot{q} \right) + I_{xy}\left(q^2 - p^2 \right) + \left(I_{yy} - I_{xx} \right) pq \tag{B.13}$$

For a body that is symmetric about the xz plane, $I_{xy} = I_{yx} = I_{yz} = I_{zy} = 0$. Under this assumption, the moment equations reduce to:

$$L = I_{xx}\dot{p} - I_{xz}\left(pq + \dot{r}\right) + \left(I_{zz} - I_{yy}\right)qr \tag{B.14}$$

$$M = I_{yy}\dot{q} + I_{xz}\left(p^2 - r^2\right) + \left(I_{xx} - I_{zz}\right)pr \tag{B.15}$$

$$N = I_{zz}\dot{r} + I_{xz}\left(qr - \dot{p}\right) + \left(I_{yy} - I_{xx}\right)pq \tag{B.16}$$

In the case of purely longitudinal flight, $v = p = r = \dot{p} = \dot{r} = 0$. The resulting inertial force and moment equations for longitudinal flight are:

$$X = m\left(\dot{u} + qw\right) \tag{B.17}$$

$$Y = 0 \tag{B.18}$$

$$Z = m\left(\dot{w} - qu\right) \tag{B.19}$$

$$L = 0 \tag{B.20}$$

$$M = I_{yy}\dot{q} \tag{B.21}$$

$$N = 0 \tag{B.22}$$

Appendix C Blade Kinematics

This section describes the blade kinematics of the system shown in Figure C.1. Point *O* is the origin of the inertial coordinate system. Point *B* is the center of gravity of the helicopter. Point *H* is the center of the hub. Point *P* is a point along the elastic axis of the rotor blade. It is assumed in this model that the quarter-chord and elastic axis are coincident.

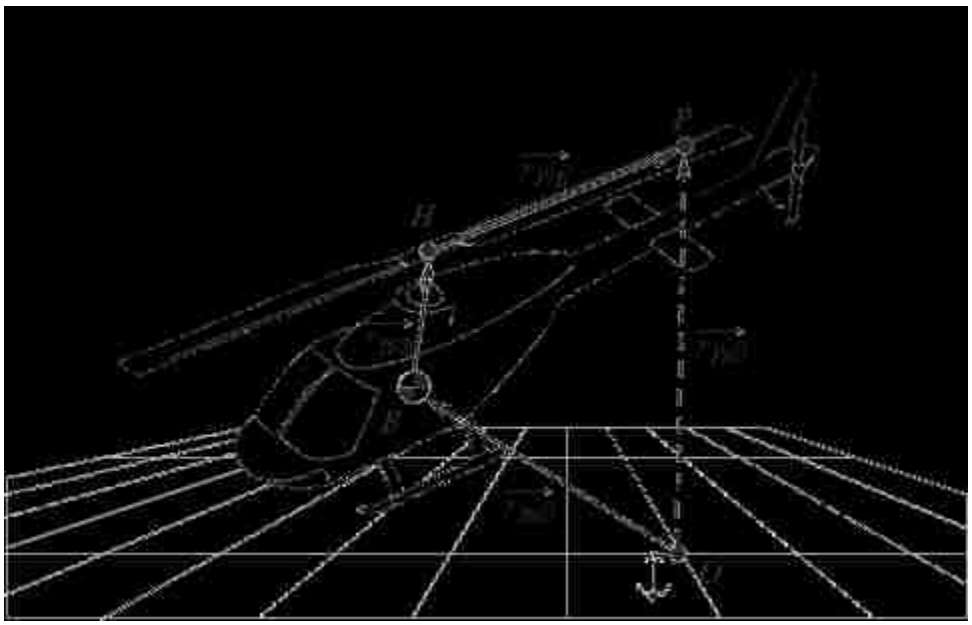

Figure C.1. Diagram of blade-related position vectors.

C.1 Position Vector to Point on the Elastic Axis

The absolute position vector from the fixed origin to the blade point, $\overrightarrow{r_{P/O}}$, read "the position vector from point *O* to point *P*" can be deconstructed into a sum of position vectors that are easily measured with respect to the appropriate coordinate system. As depicted, the absolute position vector is:

$$\overrightarrow{r_{P/O}} = \overrightarrow{r_{B/O}} + \overrightarrow{r_{H/B}} + \overrightarrow{r_{P/H}} \tag{C.1}$$

The position vector $\overrightarrow{r_{B/O}}$ is from the inertial origin to the center of gravity of the body and is represented in the inertial coordinate system:

$$\overrightarrow{r_{B/O}} = x_I \hat{i}_I + y_I \hat{j}_I + z_I \hat{k}_I \tag{C.2}$$

The position vector $\overrightarrow{r_{H/B}}$ is from the center of gravity to the hub and is represented in the body coordinate system:

$$\overrightarrow{r_{H/B}} = x_H \hat{i}_B + y_H \hat{j}_B + z_H \hat{k}_B \tag{C.3}$$

The position vector $\overrightarrow{r_{P/H}}$ is the position vector from the hub to the target point on the elastic axis of the blade and is represented in the aerodynamic coordinate system:

$$\overrightarrow{r_{P/H}} = 0\hat{e}_T + 0\hat{e}_P + r\hat{e}_R \tag{C.4}$$

C.2 Absolute Velocity of a Point on the Elastic Axis

The absolute velocity of point *P*, is found by taking the first time derivative of the absolute position vector:

$$^I\left(\frac{d\overrightarrow{r_{P/O}}}{dt}\right) = {}^I V_{P/O} = \underbrace{^I\left(\frac{d\overrightarrow{r_{B/O}}}{dt}\right)}_{1} + \underbrace{^I\left(\frac{d\overrightarrow{r_{H/B}}}{dt}\right)}_{2} + \underbrace{^I\left(\frac{d\overrightarrow{r_{P/H}}}{dt}\right)}_{3} \tag{C.5}$$

The term $^I\overrightarrow{V_{P/O}}$ is read "the velocity vector of point *P* relative to point *O*." The preceding superscript *I* indicates that the derivative was taken in the inertial reference frame. The individual terms on the right hand side of equation (C.5) can be further broken down into more appropriate forms.

The first term is simply the absolute velocity of the center of gravity. In the body coordinate system, this velocity is:

$$^{I}\left(\frac{d\overrightarrow{r_{B/O}}}{dt}\right)=\overrightarrow{{}^{I}V_{B/O}}=u\hat{i}_B+v\hat{j}_B+w\hat{k}_B \tag{C.6}$$

The second term is the inertial velocity of the hub relative to the body. The distance between the center of gravity and the hub is assumed fixed. This term can be expressed in body coordinates:

$$^{I}\left(\frac{d\overrightarrow{r_{H/B}}}{dt}\right)=\underbrace{^{B}\left(\frac{d\overrightarrow{r_{H/B}}}{dt}\right)}_{0\text{ (rigid body)}}+\overrightarrow{\omega^{B/I}}\times\overrightarrow{r_{H/B}} \tag{C.7}$$

The third term is the inertial velocity of the point on the elastic axis relative to the hub where $\overrightarrow{\omega^{B/I}}$ is the rotational velocity of the blade with respect to the inertial coordinates. It is assumed that the shaft tilt angle remains constant and that the blades are rigid. This term can be expressed in aerodynamic coordinates:

$$\begin{aligned}
^{I}\left(\frac{d\overrightarrow{r_{P/H}}}{dt}\right)&=^{B}\left(\frac{d\overrightarrow{r_{P/H}}}{dt}\right)+\overrightarrow{\omega^{B/I}}\times\overrightarrow{r_{P/B}}\\
^{I}\left(\frac{d\overrightarrow{r_{P/H}}}{dt}\right)&=^{S}\left(\frac{d\overrightarrow{r_{P/H}}}{dt}\right)+\left(\overrightarrow{\omega^{B/I}}+\underbrace{\overrightarrow{\omega^{S/B}}}_{0\text{ (rigid body)}}\right)\times\overrightarrow{r_{P/B}}\\
^{I}\left(\frac{d\overrightarrow{r_{P/H}}}{dt}\right)&=^{R}\left(\frac{d\overrightarrow{r_{P/H}}}{dt}\right)+\left(\overrightarrow{\omega^{B/I}}+\overrightarrow{\omega^{R/S}}\right)\times\overrightarrow{r_{P/B}}\\
^{I}\left(\frac{d\overrightarrow{r_{P/H}}}{dt}\right)&=\underbrace{^{A}\left(\frac{d\overrightarrow{r_{P/H}}}{dt}\right)}_{0\text{ (rigid body)}}+\left(\overrightarrow{\omega^{B/I}}+\overrightarrow{\omega^{R/S}}+\overrightarrow{\omega^{A/R}}\right)\times\overrightarrow{r_{P/B}}
\end{aligned} \tag{C.8}$$

Referring to Figure C.2, the angular velocity of the body relative to the inertial frame, $\overrightarrow{\omega^{B/I}}$, is:

$$\overrightarrow{\omega^{B/I}}=\dot{\psi}_B\hat{k}_I+\dot{\theta}_B\hat{j}_2+\dot{\phi}_B\hat{i}_B \tag{C.9}$$

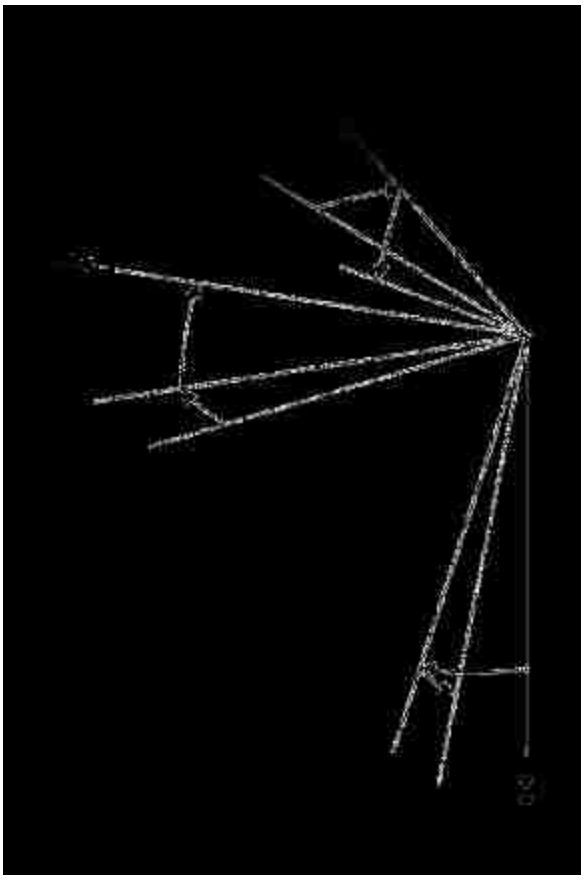

Figure C.2. Euler angle diagram.

If these rotations are transformed to the body system, equation (C.9) becomes:

$$\overrightarrow{\omega^{B/I}} = p\hat{i}_B + q\hat{j}_B + r\hat{k}_B \tag{C.10}$$

Where:

$$\begin{aligned} p &= \dot{\phi}_B - \dot{\psi}_B \sin\theta_B \\ q &= \dot{\psi}_B \cos\theta_B \sin\phi_B + \dot{\theta}_B \cos\phi_B \\ r &= \dot{\psi}_B \cos\theta_B \cos\theta_B - \dot{\theta}_B \sin\phi_B \hat{k}_B \end{aligned} \tag{C.11}$$

Similarly:

$$\begin{aligned} \dot{\theta}_B &= q\cos\phi_B - r\sin\phi_B \\ \dot{\phi}_B &= \left(r\cos\phi_B + q\sin\phi_B\right)\tan\theta_B + p \\ \dot{\psi}_B &= \left(r\cos\phi_B + q\sin\phi_B\right)\sec\theta_B \end{aligned} \tag{C.12}$$

In the following derivations, the yaw rate, *r*, is neglected.

The angular velocity of the rotating frame relative to the shaft, $\overrightarrow{\omega^{R/S}}$, is the angular velocity of the main rotor. In the rotating frame coordinates:

$$\overrightarrow{\omega^{R/S}} = 0\hat{i}_R + 0\hat{j}_R + \Omega\hat{k}_R \tag{C.13}$$

The angular velocity of the aerodynamic system relative to the blade rotating system, $\overrightarrow{\omega^{A/R}}$, is the flapping rate of the blade. Assuming no lagging or feathering, the angular velocity in the aerodynamic frame coordinates is:

$$\overrightarrow{\omega^{A/R}} = \dot{\beta}\hat{e}_T + 0\hat{e}_P + 0\hat{e}_R \tag{C.14}$$

Combining the above expressions yields the following closed form expression for the absolute velocity of a point on the elastic axis expressed in the aerodynamic coordinate system:

$$^I\overrightarrow{V_{P/O}} = V_{T,exact}\hat{e}_T + V_{P,exact}\hat{e}_P + V_{R,exact}\hat{e}_R \tag{C.15}$$

Where:

$$\begin{aligned} V_{T,exact} = & -V_{xs}\sin\psi - V_{ys}\cos\psi - qz_H\cos\theta_s\sin\psi - qx_H\sin\theta_s\sin\psi + pz_H\cos\psi \\ & -r\Omega - pr\cos\theta_s\cos\psi\beta + qr\sin\psi\beta + pr\sin\theta_s \end{aligned} \tag{C.16}$$

$$\begin{aligned} V_{P,exact} = & -V_{xs}\cos\psi\beta + V_{ys}\sin\psi\beta + V_{zs} - qz_H\cos\theta_s\cos\psi\beta - qx_H\sin\theta_s\cos\psi\beta \\ & -pz_H\sin\psi\beta + qz_H\sin\theta_s - qx_H\cos\theta_s - r\dot{\beta} + pr\cos\theta_s\sin\psi + qr\cos\psi \end{aligned} \tag{C.17}$$

$$\begin{aligned} V_{R,exact} = & -V_{xs}\cos\psi + V_{ys}\sin\psi - V_{zs}\beta - qz_H\cos\theta_s\cos\psi - qx_H\sin\theta_s\cos\psi \\ & -pz_H\sin\psi - qz_H\sin\theta_s\beta + qx_H\cos\theta_s\beta \end{aligned} \tag{C.18}$$

$$V_{xs} = u\cos\theta_s - w\sin\theta_s \tag{C.19}$$

$$V_{ys} = v \tag{C.20}$$

$$V_{zs} = u\sin\theta_s + w\cos\theta_s \tag{C.21}$$

If small magnitude terms are ignored, the absolute velocity of a point on the elastic axis can be reduced as:

$$^{I}\overrightarrow{V_{P/O}} \approx V_T \hat{e}_T + V_P \hat{e}_P + V_R \hat{e}_R \tag{C.22}$$

Where

$$V_T = -V_{xs} \sin\psi - V_{ys} \cos\psi - r\Omega \tag{C.23}$$

$$V_P = -V_{xs} \cos\psi\beta + V_{ys} \sin\psi\beta + V_{zs} + pr\cos\theta_S \sin\psi + qr\cos\psi - r\dot{\beta} \tag{C.24}$$

$$V_R = -V_{xs} \cos\psi + V_{ys} \sin\psi - V_{zs}\beta \tag{C.25}$$

To justify the elimination of the smaller terms, it is important to compare the velocity expressions. Consider the time history of the pitch-up rate, q, during the most aggressive pull-up maneuver from the Gilroy flight test is shown in Figure C.3. Note that the maximum pitch-up rate occurs at a source time of 42.61 seconds since the beginning of the data record. This point is of interest because most of the eliminated terms are related to the attitude rates of change.

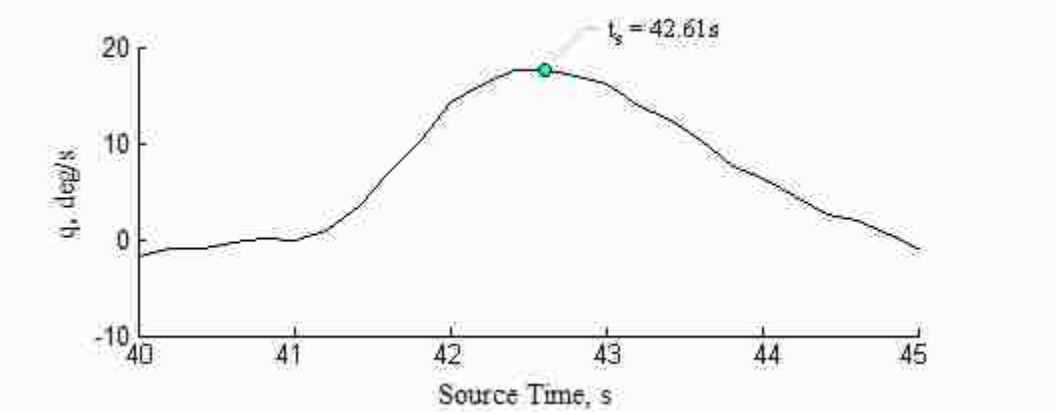

Figure C.3. Time history of pitch-up rate.

The approximate and exact forms of the absolute velocity of a point on the elastic axis are plotted together in Figure C.4. Note that the two expressions are nearly identical.

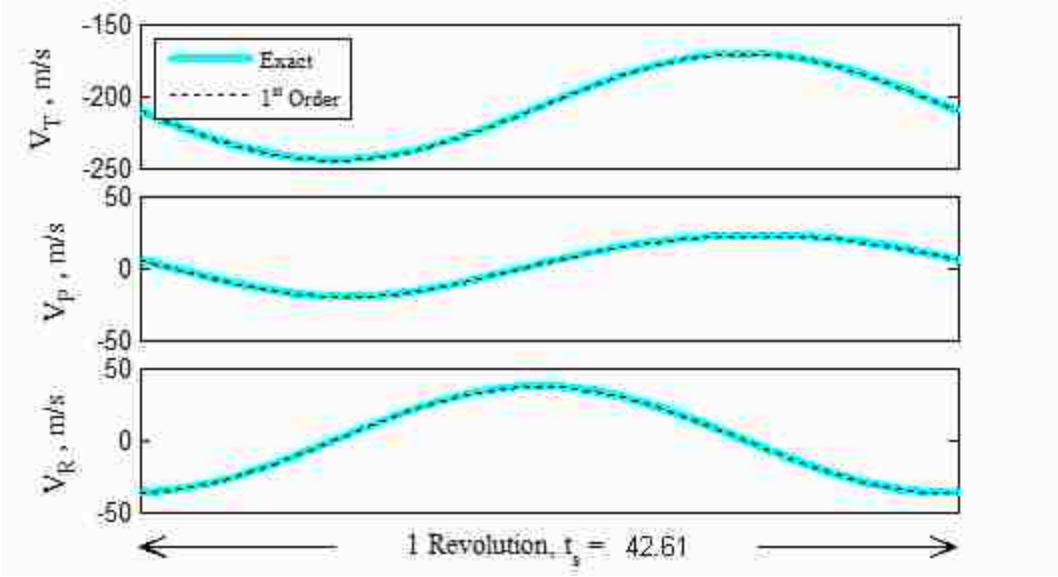

Figure C.4. Comparison of exact and approximate velocity expressions over one revolution.

For purely longitudinal flight, the absolute velocity terms further reduce to:

$$V_T = -V_{xs}\sin\psi - r\Omega \tag{C.26}$$

$$V_P = -V_{xs}\cos\psi\beta + V_{zs} + qr\cos\psi - r\dot{\beta} \tag{C.27}$$

$$V_R = -V_{xs}\cos\psi - V_{zs}\beta \tag{C.28}$$

C.3 Absolute Acceleration of a Point on the Elastic Axis

The absolute acceleration of point *P* is found by taking the second time derivative of equation (C.1) in the inertial frame.

$$^I\left(\frac{d^2\overrightarrow{r_{P/O}}}{dt^2}\right) = {}^I\overrightarrow{a_{P/O}} = {}^I\left(\frac{d^2\overrightarrow{r_{B/O}}}{dt^2}\right) + {}^I\left(\frac{d^2\overrightarrow{r_{H/B}}}{dt^2}\right) + {}^I\left(\frac{d^2\overrightarrow{r_{P/H}}}{dt^2}\right) \tag{C.29}$$

The term ${}^I\overrightarrow{a_{P/O}}$ is read "the acceleration vector of point *P* relative to point *O*." The preceding superscript *I* indicates that the derivative was taken in the inertial

reference frame. As before, the terms on the right hand side of equation (C.29) can be deconstructed into more appropriate forms:

$$\begin{aligned}{}^{I}\left(\frac{d^2\overrightarrow{r_{P/O}}}{dt^2}\right) = {}^{I}\left(\frac{d^2\overrightarrow{r_{B/O}}}{dt^2}\right) &+ \overrightarrow{\dot{\omega}^{B/I}} + \overrightarrow{\omega^{B/I}} \times \left(\overrightarrow{\omega^{B/I}} \times \overrightarrow{r_{H/B}}\right) \\ &+ \left[\overrightarrow{\dot{\omega}^{B/I}} + \overrightarrow{\omega^{B/I}} \times \overrightarrow{\omega^{R/S}} + \overrightarrow{\dot{\omega}^{A/R}} + \left(\overrightarrow{\omega^{B/I}} + \overrightarrow{\omega^{R/S}}\right) \times \overrightarrow{\omega^{A/R}}\right] \times \overrightarrow{r_{P/H}} \\ &+ \left(\overrightarrow{\omega^{B/I}} + \overrightarrow{\omega^{R/S}} + \overrightarrow{\omega^{A/R}}\right) \times \left[\left(\overrightarrow{\omega^{B/I}} + \overrightarrow{\omega^{R/S}} + \overrightarrow{\omega^{A/R}}\right) \times \overrightarrow{r_{P/H}}\right]\end{aligned} \tag{C.30}$$

The absolute acceleration of the center of gravity relative to the inertial frame can be expressed in body coordinates as:

$${}^{I}\left(\frac{d^2\overrightarrow{r_{B/O}}}{dt^2}\right) = {}^{I}\overrightarrow{a_{B/O}} = \left(\dot{u} + qw - rv\right)\hat{i}_B + \left(\dot{v} + ru - pw\right)\hat{j}_B + \left(\dot{w} + pv - qu\right)\hat{k}_B \tag{C.31}$$

The angular acceleration of the body system relative to the inertial system, $\overrightarrow{\dot{\omega}^{B/I}}$, expressed in the body coordinate system is:

$$\overrightarrow{\dot{\omega}^{B/I}} = \dot{p}\hat{i}_B + \dot{q}\hat{j}_B + \dot{r}\hat{k}_B \tag{C.32}$$

As with the velocity expression, the yaw acceleration will also be assumed negligible in the following derivations.

The angular acceleration of the aerodynamic system relative to the blade rotating system $\overrightarrow{\dot{\omega}^{A/R}}$ expressed in the aerodynamic coordinate system is:

$$\overrightarrow{\omega^{A/R}} = \ddot{\beta}\hat{e}_T \tag{C.33}$$

Combining the above expressions yields the following closed form expression for the absolute acceleration of a point on the elastic axis expressed in the aerodynamic coordinate system:

$${}^{I}\overrightarrow{a_{P/O}} = a_{T,exact}\hat{e}_T + a_{P,exact}\hat{e}_P + a_{R,exact}\hat{e}_R \tag{3.34}$$

Where

$$\begin{aligned} a_{T,exact} = & -a_{xs}\sin\psi - a_{ys}\cos\psi - \dot{q}z_H\cos\theta_s\sin\psi + 2qr\sin\psi\dot{\beta} - \dot{q}x_H\sin\theta_s\sin\psi \\ & + \dot{p}z_H\cos\psi - \dot{p}r\cos\theta_s\cos\psi\beta + \dot{q}r\sin\psi\beta + \dot{p}r\sin\theta_s - 2pr\cos\theta_s\cos\psi\dot{\beta} \\ & -2pr\sin\theta_s\beta\dot{\beta} + 2r\Omega\beta\dot{\beta} \end{aligned} \tag{C.35}$$

$$\begin{aligned} a_{P,exact} = & -a_{xs}\cos\psi\beta + a_{ys}\sin\psi\beta + a_{zs} - \dot{q}z_H\cos\theta_s\cos\psi\beta - \dot{q}x_H\sin\theta_s\cos\psi\beta \\ & -\dot{p}z_H\sin\psi\beta + \dot{q}z_H\sin\theta_s - \dot{q}x_H\cos\theta_s + \dot{p}r\cos\theta_s\sin\psi + \dot{q}r\cos\psi \\ & +2pr\Omega\cos\theta_s\cos\psi - 2qr\Omega\sin\psi - r\ddot{\beta} - r\Omega^2\beta + 2pr\Omega\sin\theta_s\beta \end{aligned} \tag{C.36}$$

$$\begin{aligned} a_{R,exact} = & -a_{xs}\cos\psi + a_{ys}\sin\psi - a_{zs}\beta - \dot{q}z_H\cos\theta_s\cos\psi - \dot{q}x_H\sin\theta_s\cos\psi \\ & -\dot{p}z_H\sin\psi - \dot{q}z_H\sin\theta_s\beta + \dot{q}x_H\cos\theta_s\beta - r\Omega^2 + 2pr\cos\theta_s\sin\psi\dot{\beta} \\ & +2qr\cos\psi\dot{\beta} - 2pr\Omega\cos\theta_s\cos\psi\beta + 2pr\Omega\sin\theta_s + 2qr\Omega\sin\psi\beta \end{aligned} \tag{C.37}$$

$$a_{xs} = (\dot{u} + qw)\cos\theta_s - (\dot{w} + pv - qu)\sin\theta_s \tag{C.38}$$

$$a_{ys} = \dot{v} - pw \tag{C.39}$$

$$a_{xs} = (\dot{u} + qw)\sin\theta_s + (\dot{w} + pv - qu)\cos\theta_s \tag{C.40}$$

If small magnitude terms are omitted, the absolute acceleration of a point on the elastic axis reduces to:

$$\overset{I}{\longrightarrow}{a}_{P/O} \approx a_T\hat{e}_T + a_P\hat{e}_P + a_R\hat{e}_R \tag{C.41}$$

Where

$$a_T = -a_{xs}\sin\psi - a_{ys}\cos\psi + 2qr\sin\psi\dot{\beta} + \dot{q}r\sin\psi\beta + 2r\Omega\beta\dot{\beta} \tag{C.42}$$

$$a_P = a_{zs} + \dot{p}r\cos\theta_s\sin\psi + \dot{q}r\cos\psi + 2pr\Omega\cos\theta_s\cos\psi - 2qr\Omega\sin\psi - r\ddot{\beta} - r\Omega^2\beta \tag{C.43}$$

$$a_R = -a_{xs}\cos\psi + a_{ys}\sin\psi - a_{zs}\beta - r\Omega^2 - 2pr\Omega\cos\theta_s\cos\psi\beta + 2qr\Omega\sin\psi\beta \tag{C.44}$$

As with the velocity expressions, it is important to compare the approximate and exact forms of the acceleration expressions. The time histories of the pitch-up rate, q, and the rate of change of the pitch-up rate, $\dot{q}$, are shown in Figure C.5. Note that the

maximum value for q occurs at 42.61 seconds since the beginning of the data record and $\dot{q}$ occurs 41.81 seconds since the beginning of the data record. As with the velocity expressions, these times are of interest because the majority of the eliminated terms from the exact acceleration expression are related to the attitude rates of change.

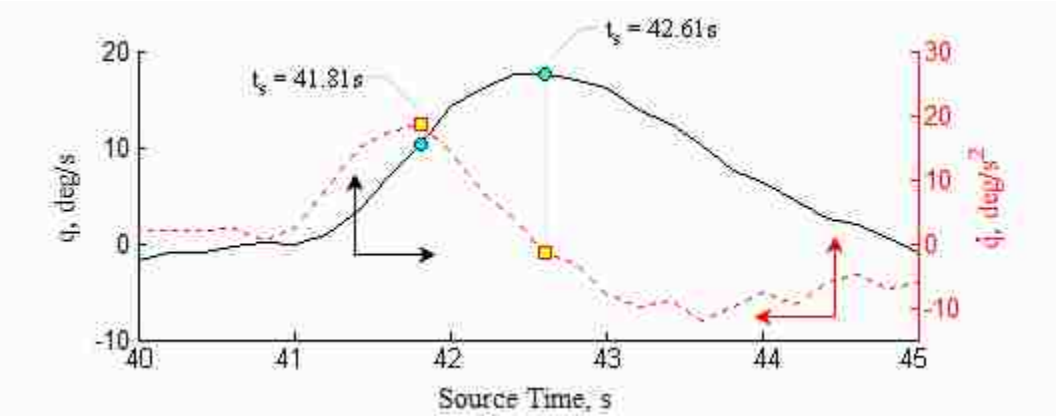

Figure C.5. Time history of pitching rate and pitching acceleration.

The approximate and exact forms of the absolute acceleration of a point on the elastic axis are plotted together in Figure C.6 at both critical times of interest. Note that at both cases the two expressions are nearly identical.

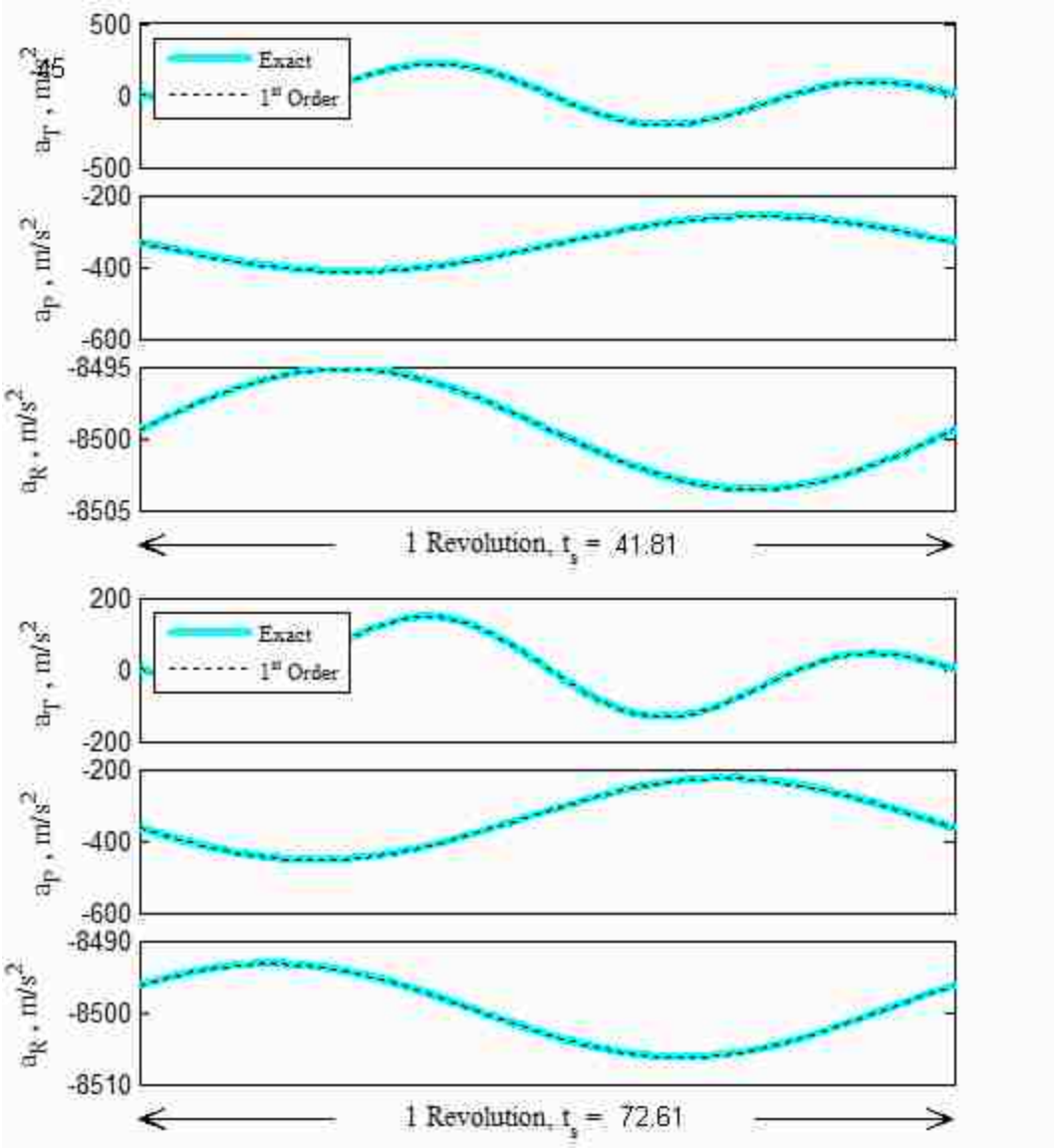

Figure C.6. Comparison of exact and approximate acceleration expressions over one revolution at maximum fuselage pitching acceleration (top set) and maximum fuselage pitch rate (bottom set).

For purely longitudinal flight, the absolute acceleration terms reduce to:

$$a_T = -a_{xs}\sin\psi + 2qr\sin\psi\dot{\beta} + \dot{q}r\sin\psi\beta + 2r\Omega\beta\dot{\beta} \tag{C.45}$$

$$a_P = a_{zs} + \dot{q}r\cos\psi - 2qr\Omega\sin\psi - r\ddot{\beta} - r\Omega^2\beta \tag{C.46}$$

$$a_R = -a_{xs}\cos\psi - a_{zs}\beta - r\Omega^2 + 2qr\Omega\sin\psi\beta \tag{C.47}$$

Appendix D Inflow Model

D.1 Review of Relevant Reference Frames

General momentum theory can be used to derive an expression for the inflow through the tip-path plane. While this procedure is commonly found in a variety of rotorcraft aerodynamics texts, it is presented here for completeness based on the sign conventions and coordinate systems defined throughout this dissertation. In the derivation of aerodynamic loads and moments, it is assumed throughout this dissertation that the result acts in the same direction as the set of basis vectors used to describe a coordinate system (see Figure D.1). In the case of the shaft coordinate system, by convention the thrust and H-force are assumed to act downwards and towards the front of the helicopter respectively. In the case of the tip-path plane coordinate system, by convention the thrust and H-force are assumed to act upwards and towards the tail of the helicopter respectively.

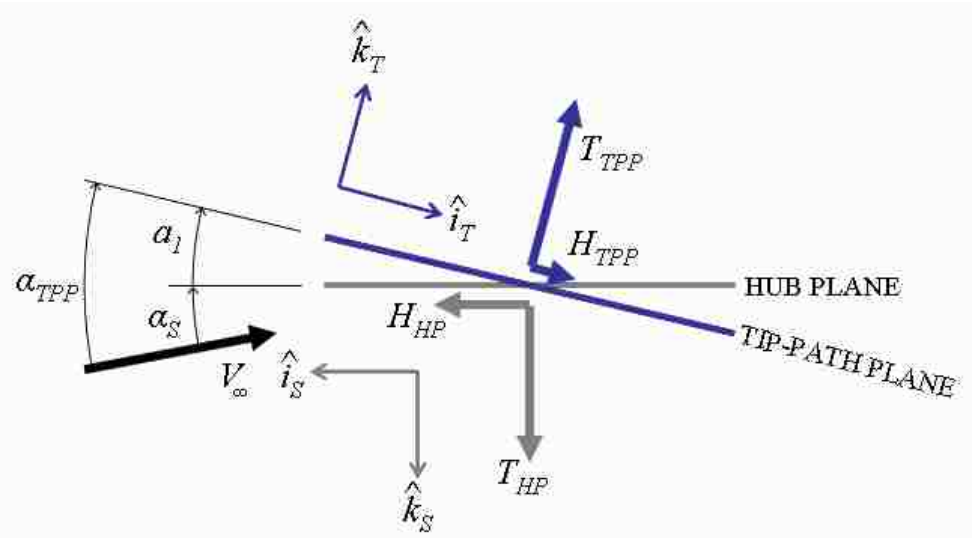

Figure D.1. Aerodynamic loads acting in their assumed positive directions.

Based on this convention, the thrust represented in the tip-path plane system, T_{TPP}, and the thrust represented in the shaft system, T_{HP}, are related as:

$$T_{TPP} = -T_{HP}\cos a_1 - H_{HP}\sin a_1 \tag{D.1}$$

Assuming $T_{HP} \gg H_{HP}\sin a_1$ and small angles for the longitudinal flapping coefficient:

$$T_{TPP} \approx -T_{HP} \tag{D.2}$$

D.2 Derivation of Inflow through the Tip-Path Plane

Consider the general inflow model of an actuator disk in forward flight shown in Figure D.2. The loads shown in this figure are the instantaneous rotor forces. Using this model and the conservation principles of mass, momentum, and energy, it is possible to obtain a relationship for the inflow through the actuator disk. Note in Figure D.2 the sign convention used in the inflow model assumes positive inflow when moving from the top of the rotor disk to the bottom.

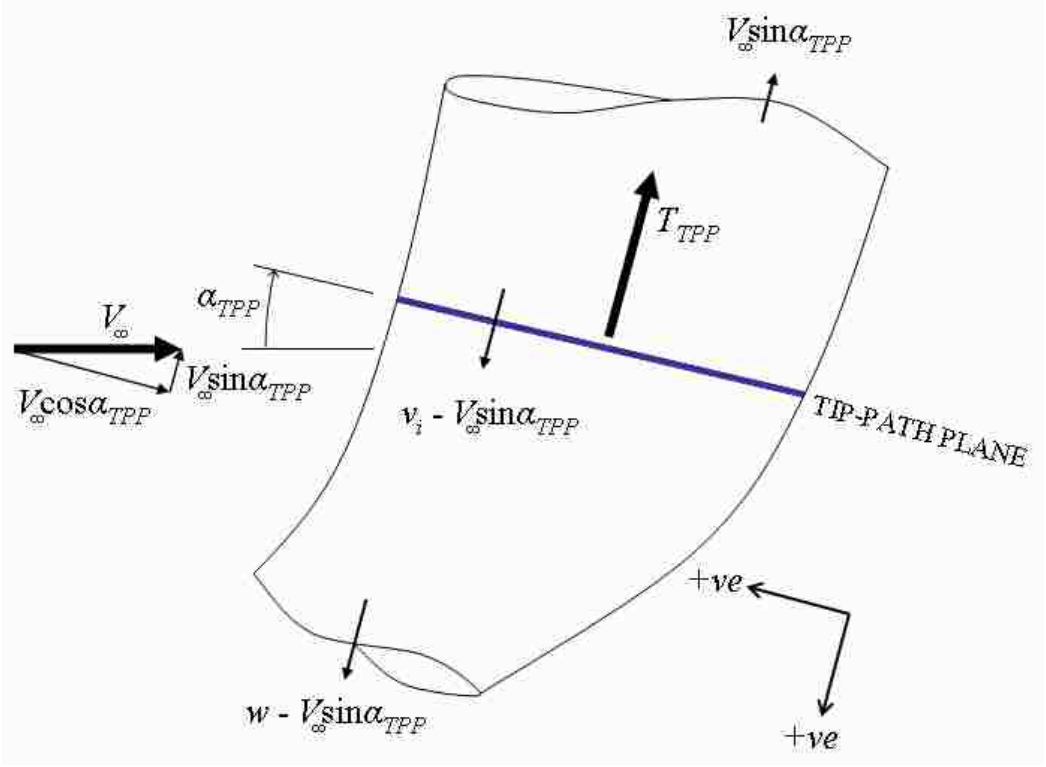

Figure D.2. Inflow model for forward flight.

From conservation of mass using Glauert's flow model

$$\dot{m} = \rho A \sqrt{\left(V_\infty \cos\alpha_{TPP}\right)^2 + \left(v_i - V_\infty \sin\alpha_{TPP}\right)^2} \tag{D.3}$$

From conservation of momentum:

$$-T_{TPP} = \dot{m}\left(w - V_\infty \sin\alpha_{TPP}\right) - \dot{m}V_\infty \sin\alpha_{TPP} \tag{D.4}$$

$$-T_{TPP} = \dot{m}w \tag{D.5}$$

From conservation of energy:

$$P_{TPP} = -T_{TPP}\left(v_i - V_\infty \sin\alpha_{TPP}\right) = \frac{1}{2}\dot{m}\left(w - V_\infty \sin\alpha_{TPP}\right)^2 - \frac{1}{2}\dot{m}\left(-V_\infty \sin\alpha_{TPP}\right)^2 \tag{D.6}$$

$$w = 2v_i \tag{D.7}$$

Combining these equations and solving for the induced velocity yields:

$$v_i = \frac{v_h^2}{\sqrt{\left(V_\infty \cos \alpha_{TPP}\right)^2 + \left(v_i - V_\infty \sin \alpha_{TPP}\right)^2}} \tag{D.8}$$

Where v_h is the induced velocity in hover:

$$v_h = \sqrt{\frac{T_{TPP}}{2\rho A}} \tag{D.9}$$

Because the induced velocity variable appears on both side of the expression, it is common to use an iterative solver to converge on the induced inflow. In the model described in this dissertation, a Newton-Raphson iteration method is applied.

The total inflow through the rotor is:

$$v_i - V_\infty \sin \alpha_{TPP} = \frac{v_h^2}{\sqrt{\left(V_\infty \cos \alpha_{TPP}\right)^2 + \left(v_i - V_\infty \sin \alpha_{TPP}\right)^2}} - V_\infty \sin \alpha_{TPP} \tag{D.10}$$

As was the case with the induced velocity, the total inflow through the disk must also be solved with an iterative solver such as the Newton-Raphson method.

The induced inflow expressions can also be expressed non-dimensionally with respect to tip-speed:

$$\frac{v_i}{\Omega R} = \lambda_i = \frac{-C_T}{2\sqrt{\mu^2 + \left(\lambda_i - \mu \tan \alpha_{TPP}\right)^2}} \tag{D.11}$$

Where

$$\mu = \frac{V_\infty \cos \alpha_{TPP}}{\Omega R} \approx \frac{V_\infty}{\Omega R} \tag{D.12}$$

$$C_T = \frac{T_{TPP}}{\rho A \left(\Omega R\right)^2} \tag{D.13}$$

Non-dimensionalizing the total inflow through the tip-path plane yields:

$$\lambda_{TPP} = \frac{-C_T}{2\sqrt{\mu^2 + \lambda_{TPP}^2}} - \mu \tan \alpha_{TPP} \tag{D.14}$$

D.3 Derivation of Inflow through the Hub Plane

Assuming small angles, the induced velocity through the tip-path plane is approximately equal to the induced velocity through the hub plane:

$$\lambda_{i,TPP} = \lambda_{i,HP} \cos a_1 \approx \lambda_{i,HP} \tag{D.15}$$

Therefore

$$\lambda_i = \lambda_{TPP} + \mu\alpha_{TPP} = \lambda_{HP} + \mu\alpha_S \tag{D.16}$$

Where α_S is the angle of attack of the hub. From Figure D.1:

$$\alpha_{TPP} = \alpha_S + a_1 \tag{D.17}$$

This yields the relationship between the total inflow through the tip-path plane and the total inflow through the hub plane:

$$\lambda_{HP} = \lambda_{TPP} + \mu a_1 \tag{D.18}$$

$$\lambda_{TPP} = \lambda_{HP} - \mu a_1 \tag{D.19}$$

D.4 Taylor Series Expansion of Inflow Model

To expedite computation of the inflow through the tip-path plane, a Taylor series expansion is presented. This approximates the inflow during a maneuver to the inflow at the nominal thrust coefficient during steady flight, $C_{T,0}$ and with the tip-path plane aligned parallel to the free-stream velocity $\left(\text{i.e. } \alpha_{TPP,0} = 0\right)$:

$$\begin{aligned}\lambda_{TPP}\left(C_T, \alpha_{TPP}\right) \approx \lambda_{TPP}\left(C_{T,0}, \alpha_{TPP,0}\right) + \frac{\partial \lambda_{TPP}\left(C_{T,0}, \alpha_{TPP,0}\right)}{\partial C_T}\left(C_T - C_{T,0}\right) \\ + \frac{\partial \lambda_{TPP}\left(C_{T,0}, \alpha_{TPP,0}\right)}{\partial \alpha_{TPP}}\left(\alpha_{TPP} - \alpha_{TPP,0}\right)\end{aligned} \tag{D.20}$$

Where

$$\lambda_{i,0} = \lambda_i\left(C_{T,0}, \alpha_{TPP,0}\right) = \sqrt{\frac{-\mu^2 + \sqrt{\mu^4 + C_{T,0}^2}}{2}} \tag{D.21}$$

$$\frac{\partial \lambda_{TPP}\left(C_{T,0}, \alpha_{TPP,0}\right)}{\partial C_T} = -\frac{1}{2\sqrt{\mu^2 + \lambda_{i,0}^2}} \tag{D.22}$$

$$\frac{\partial \lambda_{TPP}\left(C_{T,0}, \alpha_{TPP,0}\right)}{\partial \alpha_{TPP}} = -\frac{C_{T,0}\mu\lambda_{i,0}}{2\left(\mu^2 + \lambda_{i,0}^2\right)^{3/2}} - \mu \tag{D.23}$$

Comparisons between the exact inflow through the tip-path plane and the Taylor series approximations are presented in Figure D.3 for 50% nominal thrust, Figure D.4 for 100% nominal thrust, and Figure D.5 for 150% nominal thrust. Each figure plots the exact and approximate solutions versus the tip-path plane angle of attack at a variety of advance ratios in the top frame, and the relative error between the two methods versus the tip-path plane angle of attack in the bottom frame. The range of advance ratios, tip-path plane angles of attack, and thrust variations are representative of the measurements observed during the pure-cyclic pull-up maneuvers experienced during the flight test. Over this range of flight conditions, the Taylor series expansion yields inflow calculations very close to the exact solution at a substantially reduced computational cost.

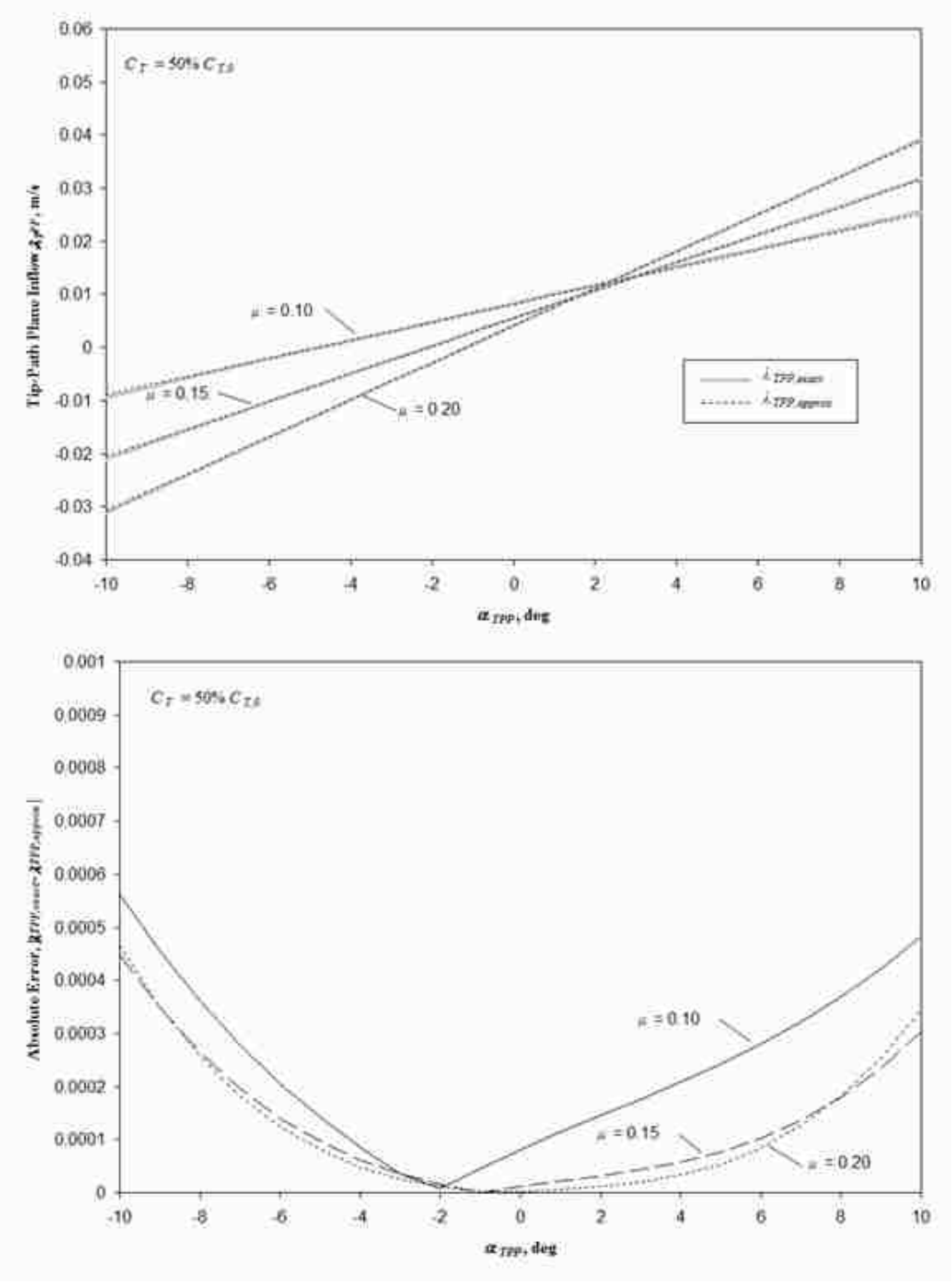

Figure D.3. Comparison of exact and approximate inflow through the tip-path plane at 50% nominal thrust. The top frame displays the computed value versus tip-path plane angle of attack; the bottom frame displays the absolute error.

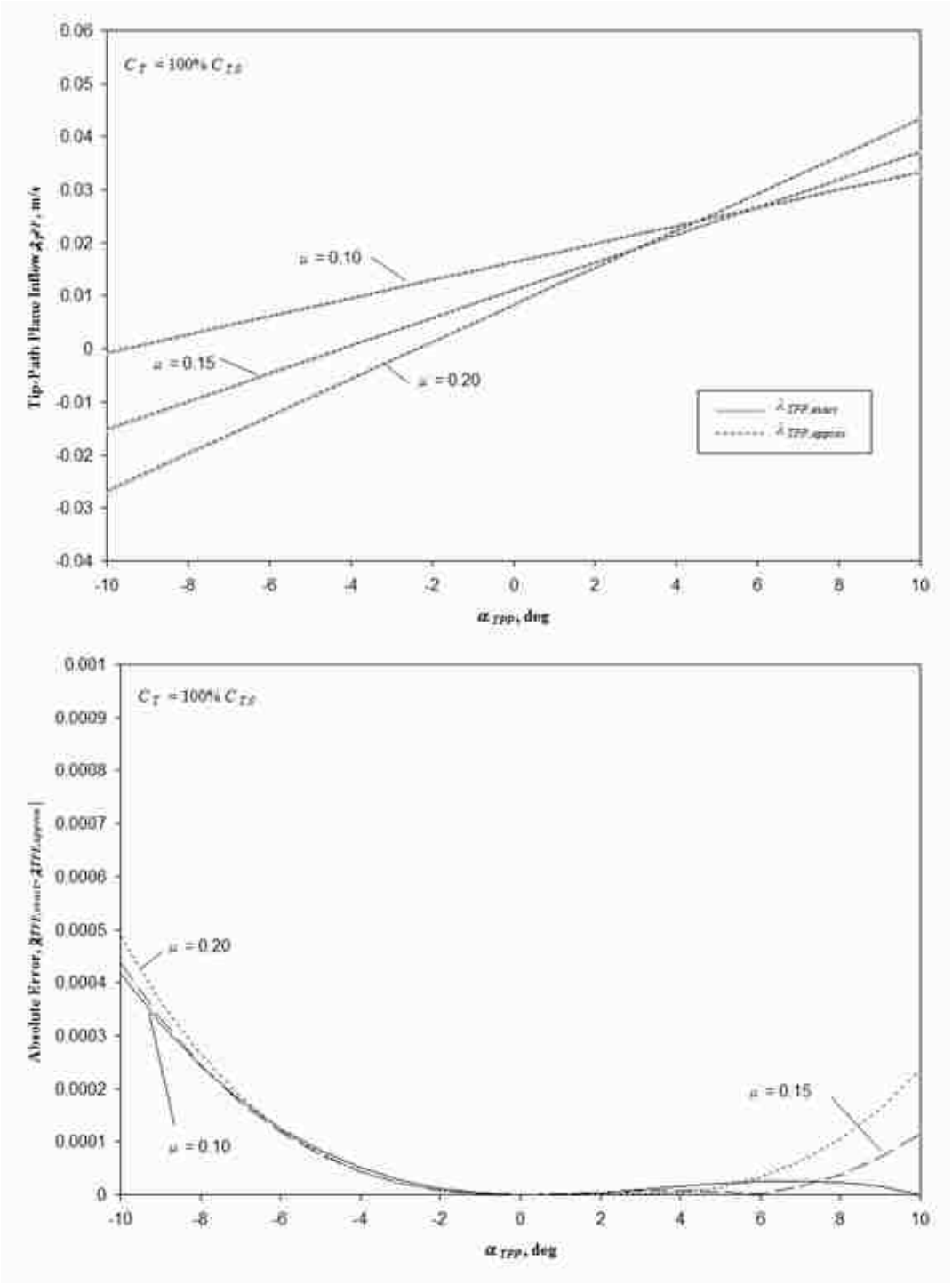

Figure D.4. Comparison of exact and approximate inflow through the tip-path plane at 100% nominal thrust. The top frame displays the computed value versus tip-path plane angle of attack; the bottom frame displays the absolute error.

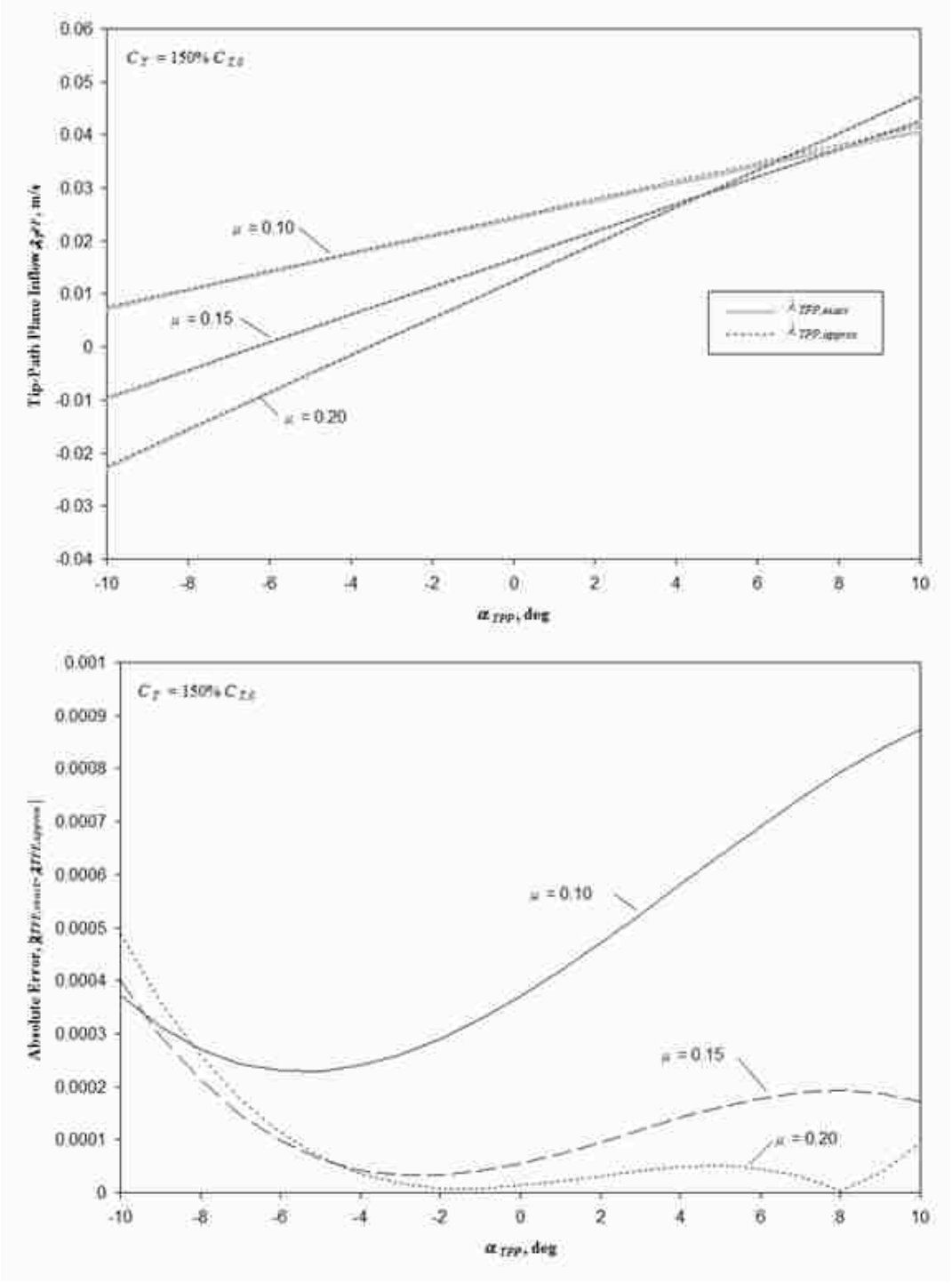

Figure D.5. Comparison of exact and approximate inflow through the tip-path plane at 150% nominal thrust. The top frame displays the computed value versus tip-path plane angle of attack; the bottom frame displays the absolute error.

Appendix E Aerodynamic Loads and Moments

In this appendix, the aerodynamic and rotor loads and moments are expanded into closed-form representation. All expressions derived in this section are instantaneous values and are functions of time.

E.1 Expansion of Main Rotor Aerodynamic Forces

Recall the non-dimensional expressions for the tangent and perpendicular fluid velocity at a given radial station:

$$u_T(t) = x + \mu_y \cos\psi + \mu_x \sin\psi \tag{E.1}$$

$$u_P(t) = \left(\lambda_{HP} - x\frac{q}{\Omega}\cos\psi - x\frac{p\cos\theta_s}{\Omega}\sin\psi\right) + \left(\mu_x \cos\psi - \mu_y \sin\psi\right)\beta + \frac{x}{\Omega}\dot{\beta} \tag{E.2}$$

Also recall from the description of the model that:

$$\beta(t) = a_0 - a_1(t)\cos\psi - b_1(t)\sin\psi \tag{E.3}$$

$$\dot{\beta}(t) = -\left(\dot{a}_1(t) + b_1(t)\Omega\right)\cos\psi - \left(\dot{b}_1(t) - a_1(t)\Omega\right)\sin\psi \tag{E.4}$$

$$\theta(t) = \theta_0(t) - A_1(t)\cos\psi - B_1(t)\sin\psi + \theta_{TW}x \tag{E.5}$$

Note that all higher harmonic terms have been omitted.

The differential aerodynamic load perpendicular to the hub plane is:

$$dF_P(t) = -\frac{1}{2}\rho c C_{L\alpha} R(\Omega R)^2 \left(u_T^2\theta - u_P u_T\right)dx \tag{E.6}$$

Integrating along the length of the blade yields:

$$\begin{aligned} F_P(t) &= \int_0^1 dF_P \\ F_P(t) &= -\frac{1}{2}\rho c C_{L\alpha} R(\Omega R)^2 \left\{\theta_0 A_{F_P} + \theta_{TW} B_{F_P} - A_1 C_{F_P} - B_1 D_{F_P} + E_{F_P}\right\} \end{aligned} \tag{E.7}$$

Where:

$$A_{F_P} = \left(\frac{1}{3} + \frac{1}{2}\mu_x^2 + \frac{1}{2}\mu_y^2\right) + \mu_y \cos\psi + \mu_x \sin\psi + \frac{1}{2}\left(\mu_y^2 - \mu_x^2\right)\cos 2\psi + \mu_x\mu_y \sin 2\psi$$

$$B_{F_P} = \left(\frac{1}{4} + \frac{1}{4}\mu_x^2 + \frac{1}{4}\mu_y^2\right) + \frac{2}{3}\mu_y \cos\psi + \frac{2}{3}\mu_x \sin\psi + \frac{1}{4}\left(\mu_y^2 - \mu_x^2\right)\cos 2\psi + \frac{1}{2}\mu_x\mu_y \sin 2\psi$$

$$C_{F_P} = \frac{1}{2}\mu_y + \left(\frac{1}{3} + \frac{1}{4}\mu_x^2 + \frac{3}{4}\mu_y^2\right)\cos\psi + \frac{1}{2}\mu_x\mu_y \sin\psi + \frac{1}{2}\mu_y \cos 2\psi + \frac{1}{2}\mu_x \sin 2\psi$$
$$+ \frac{1}{4}\left(\mu_y^2 - \mu_x^2\right)\cos 3\psi + \frac{1}{2}\mu_x\mu_y \sin 3\psi$$

$$D_{F_P} = \frac{1}{2}\mu_x + \frac{1}{2}\mu_x\mu_y \cos\psi + \left(\frac{1}{3} + \frac{3}{4}\mu_x^2 + \frac{1}{4}\mu_y^2\right)\sin\psi - \frac{1}{2}\mu_x \cos 2\psi + \frac{1}{2}\mu_y \sin 2\psi$$
$$- \frac{1}{2}\mu_x\mu_y \cos 3\psi + \frac{1}{4}\left(\mu_y^2 - \mu_x^2\right)\sin 3\psi$$

$$E_{F_P} = \left(-\frac{1}{2}\lambda_{HP} + \frac{1}{4}\mu_y\frac{q}{\Omega} + \frac{1}{4}\mu_x\frac{p\cos\theta_s}{\Omega} + \frac{1}{4}\mu_y\frac{\dot{a}_1}{\Omega} + \frac{1}{4}\mu_x\frac{\dot{b}_1}{\Omega}\right)$$
$$+ \left(-\mu_y\lambda_{HP} + \frac{1}{3}\frac{q}{\Omega} - \frac{1}{2}\mu_x a_0 + \frac{1}{2}\mu_x\mu_y a_1 + \left[\frac{1}{4}\mu_x^2 - \frac{1}{4}\mu_y^2 + \frac{1}{3}\right]b_1 + \frac{1}{3}\frac{\dot{a}_1}{\Omega}\right)\cos\psi$$
$$+ \left(-\mu_x\lambda_{HP} + \frac{1}{3}\frac{p\cos\theta_s}{\Omega} + \frac{1}{2}\mu_y a_0 + \left[\frac{1}{4}\mu_x^2 - \frac{1}{4}\mu_y^2 - \frac{1}{3}\right]a_1 - \frac{1}{2}\mu_x\mu_y b_1 + \frac{1}{3}\frac{\dot{b}_1}{\Omega}\right)\sin\psi$$
$$+ \left(-\frac{1}{4}\mu_x\frac{p\cos\theta_s}{\Omega} + \frac{1}{4}\mu_y\frac{q}{\Omega} - \mu_x\mu_y a_0 + \frac{1}{2}\mu_x a_1 + \frac{1}{2}\mu_y b_1 + \frac{1}{4}\mu_y\frac{\dot{a}_1}{\Omega} - \frac{1}{4}\mu_x\frac{\dot{b}_1}{\Omega}\right)\cos 2\psi$$
$$+ \left(\frac{1}{4}\mu_x\frac{q}{\Omega} + \frac{1}{4}\mu_y\frac{p\cos\theta_s}{\Omega} - \frac{1}{2}\left[\mu_x^2 - \mu_y^2\right]a_0 - \frac{1}{2}\mu_y a_1 + \frac{1}{2}\mu_x b_1 + \frac{1}{4}\mu_x\frac{\dot{a}_1}{\Omega} + \frac{1}{4}\mu_y\frac{\dot{b}_1}{\Omega}\right)\sin 2\psi$$
$$+ \left(\frac{1}{2}\mu_x\mu_y a_1 - \frac{1}{4}\left[\mu_x^2 - \mu_y^2\right]b_1\right)\cos 3\psi + \left(\frac{1}{4}\left[\mu_x^2 - \mu_y^2\right]a_1 + \frac{1}{2}\mu_x\mu_y b_1\right)\sin 3\psi$$

The differential aerodynamic load tangent to the hub plane is:

$$dF_T(t) = \frac{1}{2}\rho c C_{L\alpha} R\left(\Omega R\right)^2\left(u_T u_P\theta - u_P^2 + \frac{C_D}{C_{L\alpha}}u_T^2\right)dx \qquad \text{(E.8)}$$

Integrating along the length of the blade yields:

$$F_T(t) = \int_0^1 dF_T$$
$$F_T(t) = -\frac{1}{2}\rho c C_{L\alpha} R(\Omega R)^2 \left\{\theta_0 A_{F_T} + \theta_{TW} B_{F_T} - A_1 C_{F_T} - B_1 D_{F_T} + E_{F_T}\right\} \tag{E.9}$$

Where:

$$\begin{aligned}
A_{F_T} = &\left(\frac{1}{2}\lambda_{HP} - \frac{1}{4}\mu_y\frac{q}{\Omega} - \frac{1}{4}\mu_x\frac{p\cos\theta_s}{\Omega} - \frac{1}{4}\mu_y\frac{\dot{a}_1}{\Omega} - \frac{1}{4}\mu_x\frac{\dot{b}_1}{\Omega}\right)\\
&+\left(\mu_y\lambda_{HP} - \frac{1}{3}\frac{q}{\Omega} + \frac{1}{2}\mu_x a_0 - \frac{1}{2}\mu_x\mu_y a_1 - \left[\frac{1}{4}\mu_x^2 - \frac{1}{4}\mu_y^2 + \frac{1}{3}\right]b_1 - \frac{1}{3}\frac{\dot{a}_1}{\Omega}\right)\cos\psi\\
&+\left(\mu_x\lambda_{HP} - \frac{1}{3}\frac{p\cos\theta_s}{\Omega} - \frac{1}{2}\mu_y a_0 - \left[\frac{1}{4}\mu_x^2 - \frac{1}{4}\mu_y^2 - \frac{1}{3}\right]a_1 + \frac{1}{2}\mu_x\mu_y b_1 - \frac{1}{3}\frac{\dot{b}_1}{\Omega}\right)\sin\psi\\
&+\left(\frac{1}{4}\mu_x\frac{p\cos\theta_s}{\Omega} - \frac{1}{4}\mu_y\frac{q}{\Omega} + \mu_x\mu_y a_0 - \frac{1}{2}\mu_x a_1 - \frac{1}{2}\mu_y b_1 - \frac{1}{4}\mu_y\frac{\dot{a}_1}{\Omega} + \frac{1}{4}\mu_x\frac{\dot{b}_1}{\Omega}\right)\cos 2\psi\\
&+\left(-\frac{1}{4}\mu_x\frac{q}{\Omega} - \frac{1}{4}\mu_y\frac{p\cos\theta_s}{\Omega} + \frac{1}{2}\left[\mu_x^2 - \mu_y^2\right]a_0 + \frac{1}{2}\mu_y a_1 - \frac{1}{2}\mu_x b_1 - \frac{1}{4}\mu_x\frac{\dot{a}_1}{\Omega} - \frac{1}{4}\mu_y\frac{\dot{b}_1}{\Omega}\right)\sin 2\psi\\
&+\left(-\frac{1}{2}\mu_x\mu_y a_1 + \frac{1}{4}\left[\mu_x^2 - \mu_y^2\right]b_1\right)\cos 3\psi + \left(-\frac{1}{4}\left[\mu_x^2 - \mu_y^2\right]a_1 - \frac{1}{2}\mu_x\mu_y b_1\right)\sin 3\psi
\end{aligned}$$

$$\begin{aligned}
B_{F_T} = &\left(\frac{1}{3}\lambda_{HP} - \frac{1}{6}\mu_y\frac{q}{\Omega} - \frac{1}{6}\mu_x\frac{p\cos\theta_s}{\Omega} - \frac{1}{6}\mu_y\frac{\dot{a}_1}{\Omega} - \frac{1}{6}\mu_x\frac{\dot{b}_1}{\Omega}\right)\\
&+\left(\frac{1}{2}\mu_y\lambda_{HP} - \frac{1}{4}\frac{q}{\Omega} + \frac{1}{3}\mu_x a_0 - \frac{1}{4}\mu_x\mu_y a_1 - \left[\frac{1}{8}\mu_x^2 - \frac{1}{8}\mu_y^2 + \frac{1}{4}\right]b_1 - \frac{1}{4}\frac{\dot{a}_1}{\Omega}\right)\cos\psi\\
&+\left(\frac{1}{2}\mu_x\lambda_{HP} - \frac{1}{4}\frac{p\cos\theta_s}{\Omega} - \frac{1}{3}\mu_y a_0 - \left[\frac{1}{8}\mu_x^2 - \frac{1}{8}\mu_y^2 - \frac{1}{4}\right]a_1 + \frac{1}{4}\mu_x\mu_y b_1 - \frac{1}{4}\frac{\dot{b}_1}{\Omega}\right)\sin\psi\\
&+\left(\frac{1}{6}\mu_x\frac{p\cos\theta_s}{\Omega} - \frac{1}{6}\mu_y\frac{q}{\Omega} + \frac{1}{2}\mu_x\mu_y a_0 - \frac{1}{3}\mu_x a_1 - \frac{1}{3}\mu_y b_1 - \frac{1}{6}\mu_y\frac{\dot{a}_1}{\Omega} + \frac{1}{6}\mu_x\frac{\dot{b}_1}{\Omega}\right)\cos 2\psi\\
&+\left(-\frac{1}{6}\mu_x\frac{q}{\Omega} - \frac{1}{6}\mu_y\frac{p\cos\theta_s}{\Omega} + \frac{1}{4}\left[\mu_x^2 - \mu_y^2\right]a_0 + \frac{1}{3}\mu_y a_1 - \frac{1}{3}\mu_x b_1 - \frac{1}{6}\mu_x\frac{\dot{a}_1}{\Omega} - \frac{1}{6}\mu_y\frac{\dot{b}_1}{\Omega}\right)\sin 2\psi\\
&+\left(-\frac{1}{4}\mu_x\mu_y a_1 + \frac{1}{8}\left[\mu_x^2 - \mu_y^2\right]b_1\right)\cos 3\psi + \left(-\frac{1}{8}\left[\mu_x^2 - \mu_y^2\right]a_1 - \frac{1}{4}\mu_x\mu_y b_1\right)\sin 3\psi
\end{aligned}$$

$$C_{F_T} = \left(\frac{1}{2}\mu_y\lambda_{HP} - \frac{1}{6}\frac{q}{\Omega} + \frac{1}{4}\mu_x a_0 - \frac{1}{4}\mu_x\mu_y a_1 - \left[\frac{1}{8}\mu_x^2 - \frac{1}{8}\mu_y^2 + \frac{1}{6}\right]b_1 - \frac{1}{6}\frac{\dot{a}_1}{\Omega}\right)$$
$$+\left(\frac{1}{2}\lambda_{HP} - \frac{3}{8}\mu_y\frac{q}{\Omega} - \frac{1}{8}\mu_x\frac{p\cos\theta_s}{\Omega} + \frac{1}{2}\mu_x\mu_y a_0 - \frac{1}{4}\mu_x a_1 - \frac{1}{4}\mu_y b_1 - \frac{3}{8}\mu_y\frac{\dot{a}_1}{\Omega} - \frac{1}{8}\mu_x\frac{\dot{b}_1}{\Omega}\right)\cos\psi$$
$$+\left(-\frac{1}{8}\mu_x\frac{q}{\Omega} - \frac{1}{8}\mu_y\frac{p\cos\theta_s}{\Omega} + \frac{1}{4}\left[\mu_x^2 - \mu_y^2\right]a_0 + \frac{1}{4}\mu_y a_1 - \frac{1}{4}\mu_x b_1 - \frac{1}{8}\mu_x\frac{\dot{a}_1}{\Omega} - \frac{1}{8}\mu_y\frac{\dot{b}_1}{\Omega}\right)\sin\psi$$
$$+\left(\frac{1}{2}\mu_y\lambda_{HP} - \frac{1}{6}\frac{q}{\Omega} + \frac{1}{4}\mu_x a_0 - \frac{1}{2}\mu_x\mu_y a_1 - \frac{1}{6}b_1 - \frac{1}{6}\frac{\dot{a}_1}{\Omega}\right)\cos 2\psi$$
$$+\left(\frac{1}{2}\mu_x\lambda_{HP} - \frac{1}{6}\frac{p\cos\theta_s}{\Omega} - \frac{1}{4}\mu_y a_0 - \left[\frac{1}{4}\mu_x^2 - \frac{1}{4}\mu_y^2 - \frac{1}{6}\right]a_1 - \frac{1}{6}\frac{\dot{b}_1}{\Omega}\right)\sin 2\psi$$
$$+\left(\frac{1}{8}\mu_x\frac{p\cos\theta_s}{\Omega} - \frac{1}{8}\mu_y\frac{q}{\Omega} + \frac{1}{2}\mu_x\mu_y a_0 - \frac{1}{4}\mu_x a_1 - \frac{1}{4}\mu_y b_1 - \frac{1}{8}\mu_y\frac{\dot{a}_1}{\Omega} + \frac{1}{8}\mu_x\frac{\dot{b}_1}{\Omega}\right)\cos 3\psi$$
$$+\left(-\frac{1}{8}\mu_x\frac{q}{\Omega} - \frac{1}{8}\mu_y\frac{p\cos\theta_s}{\Omega} + \frac{1}{4}\left[\mu_x^2 - \mu_y^2\right]a_0 + \frac{1}{4}\mu_y a_1 - \frac{1}{4}\mu_x b_1 - \frac{1}{8}\mu_x\frac{\dot{a}_1}{\Omega} - \frac{1}{8}\mu_y\frac{\dot{b}_1}{\Omega}\right)\sin 3\psi$$
$$+\left(-\frac{1}{4}\mu_x\mu_y a_1 + \frac{1}{8}\left[\mu_x^2 - \mu_y^2\right]b_1\right)\cos 4\psi + \left(-\frac{1}{8}\left[\mu_x^2 - \mu_y^2\right]a_1 - \frac{1}{4}\mu_x\mu_y b_1\right)\sin 4\psi$$

$$D_{F_T} = \left(\frac{1}{2}\mu_x\lambda_{HP} - \frac{1}{6}\frac{p\cos\theta_s}{\Omega} - \frac{1}{4}\mu_y a_0 - \left[\frac{1}{8}\mu_x^2 - \frac{1}{8}\mu_y^2 - \frac{1}{6}\right]a_1 + \frac{1}{4}\mu_x\mu_y b_1 - \frac{1}{6}\frac{\dot{b}_1}{\Omega}\right)$$
$$+\left(-\frac{1}{8}\mu_x\frac{q}{\Omega} - \frac{1}{8}\mu_y\frac{p\cos\theta_s}{\Omega} + \frac{1}{4}\left[\mu_x^2 - \mu_y^2\right]a_0 + \frac{1}{4}\mu_y a_1 - \frac{1}{4}\mu_x b_1 - \frac{1}{8}\mu_x\frac{\dot{a}_1}{\Omega} - \frac{1}{8}\mu_y\frac{\dot{b}_1}{\Omega}\right)\cos\psi$$
$$+\left(\frac{1}{2}\lambda_{HP} - \frac{1}{8}\mu_y\frac{q}{\Omega} - \frac{3}{8}\mu_x\frac{p\cos\theta_s}{\Omega} - \frac{1}{2}\mu_x\mu_y a_0 + \frac{1}{4}\mu_x a_1 + \frac{1}{4}\mu_y b_1 - \frac{1}{8}\mu_y\frac{\dot{a}_1}{\Omega} - \frac{3}{8}\mu_x\frac{\dot{b}_1}{\Omega}\right)\sin\psi$$
$$+\left(-\frac{1}{2}\mu_x\lambda_{HP} + \frac{1}{6}\frac{p\cos\theta_s}{\Omega} + \frac{1}{4}\mu_y a_0 - \frac{1}{6}a_1 - \frac{1}{2}\mu_x\mu_y b_1 + \frac{1}{6}\frac{\dot{b}_1}{\Omega}\right)\cos 2\psi$$
$$+\left(\frac{1}{2}\mu_y\lambda_{HP} - \frac{1}{6}\frac{q}{\Omega} + \frac{1}{4}\mu_x a_0 - \left[\frac{1}{4}\mu_x^2 - \frac{1}{4}\mu_y^2 + \frac{1}{6}\right]b_1 - \frac{1}{6}\frac{\dot{a}_1}{\Omega}\right)\sin 2\psi$$
$$+\left(\frac{1}{8}\mu_x\frac{q}{\Omega} + \frac{1}{8}\mu_y\frac{p\cos\theta_s}{\Omega} - \frac{1}{4}\left[\mu_x^2 - \mu_y^2\right]a_0 - \frac{1}{4}\mu_y a_1 + \frac{1}{4}\mu_x b_1 + \frac{1}{8}\mu_x\frac{\dot{a}_1}{\Omega} + \frac{1}{8}\mu_y\frac{\dot{b}_1}{\Omega}\right)\cos 3\psi$$
$$+\left(\frac{1}{8}\mu_x\frac{p\cos\theta_s}{\Omega} - \frac{1}{8}\mu_y\frac{q}{\Omega} + \frac{1}{2}\mu_x\mu_y a_0 - \frac{1}{4}\mu_x a_1 - \frac{1}{4}\mu_y b_1 - \frac{1}{8}\mu_y\frac{\dot{a}_1}{\Omega} + \frac{1}{8}\mu_x\frac{\dot{b}_1}{\Omega}\right)\sin 3\psi$$
$$+\left(\frac{1}{8}\left[\mu_x^2 - \mu_y^2\right]a_1 + \frac{1}{4}\mu_x\mu_y b_1\right)\cos 4\psi + \left(-\frac{1}{4}\mu_x\mu_y a_1 + \frac{1}{8}\left[\mu_x^2 - \mu_y^2\right]b_1\right)\sin 4\psi$$

$$
\begin{aligned}
E_{F_z} = &\left(\begin{array}{l}
-\lambda_{HP}^2 - \frac{1}{6}\frac{q^2}{\Omega^2} - \frac{1}{6}\frac{p^2\cos^2\theta_s}{\Omega^2} - \frac{1}{2}\left[\mu_y\frac{p\cos\theta_s}{\Omega} - \mu_x\frac{q}{\Omega}\right]a_0 + \left[\lambda_{HP}\mu_x + \frac{1}{3}\frac{p\cos\theta_s}{\Omega}\right]a_1 + \left[-\lambda_{HP}\mu_y - \frac{1}{3}\frac{q}{\Omega}\right]b_1 \\
-\frac{1}{3}\frac{q}{\Omega^2}\dot{a}_1 - \frac{1}{3}\frac{p\cos\theta_s}{\Omega^2}\dot{b}_1 - \frac{1}{2}\left[\mu_x^2+\mu_y^2\right]a_0^2 + \left[-\frac{3}{8}\mu_x^2 - \frac{1}{8}\mu_y^2 - \frac{1}{6}\right]a_1^2 + \left[-\frac{1}{8}\mu_x^2 - \frac{3}{8}\mu_y^2 - \frac{1}{6}\right]b_1^2 \\
+\frac{1}{2}\mu_x\mu_y a_1 b_1 - \frac{1}{6}\left(\frac{\dot{a}_1}{\Omega}\right)^2 - \frac{1}{6}\left(\frac{\dot{b}_1}{\Omega}\right)^2 - \frac{1}{3}\frac{\dot{a}_1 b_1}{\Omega} + \frac{1}{3}\frac{\dot{b}_1 a_1}{\Omega} + \frac{1}{2}\mu_y a_0 a_1 + \frac{1}{2}\mu_x a_0 b_1 + \frac{1}{2}\mu_x\frac{\dot{a}_1 a_0}{\Omega} - \frac{1}{2}\mu_y\frac{\dot{b}_1 a_0}{\Omega} + \\
+\frac{C_D}{C_{L\alpha}}\left[\frac{1}{3}+\frac{1}{2}\mu_x^2+\frac{1}{2}\mu_y^2\right]
\end{array}\right) \\
&+\left(\begin{array}{l}
\lambda_{HP}\frac{q}{\Omega} - 2\lambda_{HP}\mu_x a_0 + \left[\frac{1}{4}\mu_y\frac{p\cos\theta_s}{\Omega} - \frac{3}{4}\mu_x\frac{q}{\Omega}\right]a_1 + \left[\frac{1}{4}\mu_y\frac{q}{\Omega} - \frac{1}{4}\mu_x\frac{p\cos\theta_s}{\Omega} + \lambda_{HP}\right]b_1 + \lambda_{HP}\frac{\dot{a}_1}{\Omega} \\
+\left[\frac{3}{2}\mu_x^2+\frac{1}{2}\mu_y^2\right]a_0 a_1 - \mu_x\mu_y a_0 b_1 - \frac{1}{4}\mu_y a_1^2 + \frac{1}{4}\mu_y b_1^2 - \frac{1}{2}\mu_x a_1 b_1 - \frac{3}{4}\mu_x\frac{\dot{a}_1 a_1}{\Omega} + \frac{1}{4}\mu_y\frac{\dot{a}_1 b_1}{\Omega} \\
+\frac{1}{4}\mu_y\frac{\dot{b}_1 a_1}{\Omega} - \frac{1}{4}\mu_x\frac{\dot{b}_1 b_1}{\Omega} + \frac{C_D}{C_{L\alpha}}\mu_y
\end{array}\right)\cos\psi \\
&+\left(\begin{array}{l}
\lambda_{HP}\frac{p\cos\theta_s}{\Omega} + 2\lambda_{HP}\mu_y a_0 + \left[\frac{1}{4}\mu_y\frac{q}{\Omega} - \frac{1}{4}\mu_x\frac{p\cos\theta_s}{\Omega} - \lambda_{HP}\right]a_1 + \left[\frac{3}{4}\mu_y\frac{p\cos\theta_s}{\Omega} - \frac{1}{4}\mu_x\frac{q}{\Omega}\right]b_1 + \lambda_{HP}\frac{\dot{b}_1}{\Omega} \\
-\mu_x\mu_y a_0 a_1 + \left[\frac{1}{2}\mu_x^2+\frac{3}{2}\mu_y^2\right]a_0 b_1 + \frac{1}{4}\mu_x a_1^2 - \frac{1}{4}\mu_x b_1^2 - \frac{1}{2}\mu_y a_1 b_1 + \frac{1}{4}\mu_y\frac{\dot{a}_1 a_1}{\Omega} - \frac{1}{4}\mu_x\frac{\dot{a}_1 b_1}{\Omega} \\
-\frac{1}{4}\mu_x\frac{\dot{b}_1 a_1}{\Omega} + \frac{3}{4}\mu_y\frac{\dot{b}_1 b_1}{\Omega} + \frac{C_D}{C_{L\alpha}}\mu_x
\end{array}\right)\sin\psi \\
&+\left(\begin{array}{l}
-\frac{1}{6}\left[\left(\frac{q}{\Omega}\right)^2 - \left(\frac{p\cos\theta_s}{\Omega}\right)^2\right] + \frac{1}{2}\left[\mu_x\frac{q}{\Omega} + \mu_y\frac{p\cos\theta_s}{\Omega}\right]a_0 + \left[\lambda_{HP}\mu_x - \frac{1}{3}\frac{p\cos\theta_s}{\Omega}\right]a_1 + \left[\lambda_{HP}\mu_y - \frac{1}{3}\frac{q}{\Omega}\right]b_1 \\
-\frac{1}{3}\frac{q}{\Omega^2}\dot{a}_1 + \frac{1}{3}\frac{p\cos\theta_s}{\Omega^2}\dot{b}_1 - \frac{1}{2}\left[\mu_x^2-\mu_y^2\right]a_0^2 + \left[-\frac{1}{2}\mu_x^2+\frac{1}{6}\right]a_1^2 + \left[\frac{1}{2}\mu_y^2-\frac{1}{6}\right]b_1^2 - \frac{1}{6}\frac{\dot{a}_1^2}{\Omega^2} + \frac{1}{6}\frac{\dot{b}_1^2}{\Omega^2} \\
-\frac{1}{3}\frac{\dot{a}_1 b_1}{\Omega} - \frac{1}{3}\frac{\dot{b}_1 a_1}{\Omega} - \frac{1}{2}\mu_y a_0 a_1 + \frac{1}{2}\mu_x a_0 b_1 + \frac{1}{2}\mu_x\frac{\dot{a}_1 a_0}{\Omega} + \frac{1}{2}\mu_y\frac{\dot{b}_1 a_0}{\Omega} + \frac{C_D}{C_{L\alpha}}\frac{1}{2}\left[\mu_y^2-\mu_x^2\right]
\end{array}\right)\cos 2\psi \\
&+\left(\begin{array}{l}
-\frac{1}{3}\frac{qp\cos\theta_s}{\Omega^2} - \frac{1}{2}\left[\mu_y\frac{q}{\Omega} - \mu_x\frac{p\cos\theta_s}{\Omega}\right]a_0 + \left(-\lambda_{HP}\mu_y + \frac{1}{3}\frac{q}{\Omega}\right)a_1 + \left(\lambda_{HP}\mu_x - \frac{1}{3}\frac{p\cos\theta_s}{\Omega}\right)b_1 \\
-\frac{1}{3}\frac{p\cos\theta_s}{\Omega^2}\dot{a}_1 - \frac{1}{3}\frac{q}{\Omega^2}\dot{b}_1 + \mu_x\mu_y a_0^2 + \frac{1}{2}\mu_x\mu_y a_1^2 + \frac{1}{2}\mu_x\mu_y b_1^2 + \left[-\frac{1}{2}\mu_x^2 - \frac{1}{2}\mu_y^2 + \frac{1}{3}\right]a_1 b_1 \\
-\frac{1}{3}\frac{\dot{a}_1\dot{b}_1}{\Omega^2} + \frac{1}{3}\frac{\dot{a}_1 a_1}{\Omega} - \frac{1}{3}\frac{\dot{b}_1 b_1}{\Omega} - \frac{1}{2}\mu_x a_0 a_1 - \frac{1}{2}\mu_y a_0 b_1 - \frac{1}{2}\mu_y\frac{\dot{a}_1 a_0}{\Omega} + \frac{1}{2}\mu_x\frac{\dot{b}_1 a_0}{\Omega} + \frac{C_D}{C_{L\alpha}}\mu_x\mu_y
\end{array}\right)\sin 2\psi \\
&+\left(\begin{array}{l}
-\frac{1}{4}\left[\mu_x\frac{q}{\Omega} + \mu_y\frac{p\cos\theta_s}{\Omega}\right]a_1 - \frac{1}{4}\left[\mu_y\frac{q}{\Omega} - \mu_x\frac{p\cos\theta_s}{\Omega}\right]b_1 + \frac{1}{2}\left[\mu_x^2-\mu_y^2\right]a_0 a_1 + \mu_x\mu_y a_0 b_1 \\
+\frac{1}{4}\mu_y a_1^2 - \frac{1}{4}\mu_y b_1^2 - \frac{1}{2}\mu_x a_1 b_1 - \frac{1}{4}\mu_x\frac{\dot{a}_1 a_1}{\Omega} - \frac{1}{4}\mu_y\frac{\dot{a}_1 b_1}{\Omega} - \frac{1}{4}\mu_y\frac{\dot{b}_1 a_1}{\Omega} + \frac{1}{4}\mu_x\frac{\dot{b}_1 b_1}{\Omega}
\end{array}\right)\cos 3\psi \\
&+\left(\begin{array}{l}
\frac{1}{4}\left[\mu_y\frac{q}{\Omega} - \mu_x\frac{p\cos\theta_s}{\Omega}\right]a_1 - \frac{1}{4}\left[\mu_x\frac{q}{\Omega} + \mu_y\frac{p\cos\theta_s}{\Omega}\right]b_1 - \mu_x\mu_y a_0 a_1 + \frac{1}{2}\left[\mu_x^2-\mu_y^2\right]a_0 b_1 \\
+\frac{1}{4}\mu_x a_1^2 - \frac{1}{4}\mu_x b_1^2 + \frac{1}{2}\mu_y a_1 b_1 + \frac{1}{4}\mu_y\frac{\dot{a}_1 a_1}{\Omega} - \frac{1}{4}\mu_x\frac{\dot{a}_1 b_1}{\Omega} - \frac{1}{4}\mu_x\frac{\dot{b}_1 a_1}{\Omega} - \frac{1}{4}\mu_y\frac{\dot{b}_1 b_1}{\Omega}
\end{array}\right)\sin 3\psi \\
&+\left(-\frac{1}{8}\left[\mu_x^2-\mu_y^2\right]a_1^2 + \frac{1}{8}\left[\mu_x^2-\mu_y^2\right]b_1^2 - \frac{1}{2}\mu_x\mu_y a_1 b_1\right)\cos 4\psi \\
&+\left(\frac{1}{4}\mu_x\mu_y a_1^2 - \frac{1}{4}\mu_x\mu_y b_1^2 - \frac{1}{4}\left[\mu_x^2-\mu_y^2\right]a_1 b_1\right)\sin 4\psi
\end{aligned}
$$

The aerodynamic loading expressions derived above are expressed in the aerodynamic coordinate system. However, since the dynamic model used in this dissertation requires the rotor loading terms to be transferred to the shaft in the fixed frame, the appropriate transformation must be applied.

$$\begin{Bmatrix} F_x \\ F_y \\ F_z \end{Bmatrix}_S = \mathbf{T}^{R/S}\mathbf{T}^{A/R}\begin{Bmatrix} F_T \\ F_P \\ 0 \end{Bmatrix}_A \tag{E.10}$$

Assuming small flapping angles this transformation yields:

$$\begin{Bmatrix} F_x(t) \\ F_y(t) \\ F_z(t) \end{Bmatrix}_S = \begin{Bmatrix} -F_P(t)\beta\cos\psi - F_T(t)\sin\psi \\ F_P(t)\beta\sin\psi - F_T(t)\cos\psi \\ F_P(t) \end{Bmatrix} \tag{E.11}$$

The total rotor load transferred to the shaft is found by summing the contributions of the individual blades. The total instantaneous in-plane H-force, H_{HP} is the sum of the rotor load in the $\hat{i}_s$ direction as a function of time; the total instantaneous in-plane Y-force, Y_{HP}, is the sum of the rotor load in the $\hat{j}_s$ direction as a function of time; and the total instantaneous thrust, T_{HP}, is the sum of the rotor load in the $\hat{k}_s$ direction as a function of time. Note that these expressions assume the force is acting in the positive direction of the basis of unit vectors. Under this model, the positive magnitude of in-plane H-force acts forwards; in-plane Y-force acts to starboard; and the thrust acts downwards.

$$\begin{Bmatrix} H_{HP}(t) \\ Y_{HP}(t) \\ T_{HP}(t) \end{Bmatrix} = \sum_{i=1}^{N_b}\begin{Bmatrix} F_x^{(i)} \\ F_y^{(i)} \\ F_z^{(i)} \end{Bmatrix} = \sum_{i=1}^{N_b}\begin{Bmatrix} -F_P^{(i)}\beta^{(i)}\cos\psi^{(i)} - F_T^{(i)}\sin\psi^{(i)} \\ F_P^{(i)}\beta^{(i)}\sin\psi^{(i)} - F_T^{(i)}\cos\psi^{(i)} \\ F_P^{(i)} \end{Bmatrix} \tag{E.12}$$

The loading and moment expressions are expanded into closed-form representation in the following subsections.

E.1.1 Main Rotor Thrust

$$T_{HP}(t) = \sum_{i=1}^{N_b} F_P^{(i)} \tag{E.13}$$

For a two-bladed teetering rotor, the thrust expression reduces to:

$$T_{HP}(t) = \frac{1}{2}\rho c C_{L\alpha} R(\Omega R)^2 \left\{ \theta_0 A_{T_{HP}} + \theta_{TW} B_{T_{HP}} - A_1 C_{T_{HP}} - B_1 D_{T_{HP}} + E_{T_{HP}} \right\} \tag{E.14}$$

Where:

$$A_{T_{HP}} = \left(-\left[\frac{2}{3} + \mu_x^2 + \mu_y^2 \right] + \left[\mu_x^2 - \mu_y^2 \right] \cos 2\psi - 2\mu_x \mu_y \sin 2\psi \right)$$

$$B_{T_{HP}} = \left(-\left[\frac{1}{2} + \frac{1}{2}\mu_x^2 + \frac{1}{2}\mu_y^2 \right] + \frac{1}{2}\left[\mu_x^2 - \mu_y^2 \right] \cos 2\psi - \mu_x \mu_y \sin 2\psi \right)$$

$$C_{T_{HP}} = \left(-\mu_y - \mu_y \cos 2\psi - \mu_x \sin 2\psi \right)$$

$$D_{T_{HP}} = \left(-\mu_x + \mu_x \cos 2\psi - \mu_y \sin 2\psi \right)$$

$$\begin{aligned} E_{T_{HP}} = {} & \left(\lambda_{HP} - \frac{1}{2}\mu_y \frac{q}{\Omega} - \frac{1}{2}\mu_x \frac{p\cos\theta_s}{\Omega} - \frac{1}{2}\mu_y \frac{\dot{a}_1}{\Omega} - \frac{1}{2}\mu_x \frac{\dot{b}_1}{\Omega} \right) \\ & + \left(\frac{1}{2}\left[\mu_x \frac{p\cos\theta_s}{\Omega} - \mu_y \frac{q}{\Omega} \right] + 2\mu_x \mu_y a_0 - \mu_x a_1 - \mu_y b_1 - \frac{1}{2}\mu_y \frac{\dot{a}_1}{\Omega} + \frac{1}{2}\mu_x \frac{\dot{b}_1}{\Omega} \right) \cos 2\psi \\ & + \left(-\frac{1}{2}\left[\mu_x \frac{q}{\Omega} + \mu_y \frac{p\cos\theta_s}{\Omega} \right] + \left[\mu_x^2 - \mu_y^2 \right] a_0 + \mu_y a_1 - \mu_x b_1 - \frac{1}{2}\mu_x \frac{\dot{a}_1}{\Omega} - \frac{1}{2}\mu_y \frac{\dot{b}_1}{\Omega} \right) \sin 2\psi \end{aligned}$$

If higher harmonics are neglected, then for longitudinal flight:

$$A_{T_{HP}} = -\left[\frac{2}{3} + \mu_x^2 \right]$$

$$B_{T_{HP}} = -\left[\frac{1}{2} + \frac{1}{2}\mu_x^2 \right]$$

$$C_{T_{HP}} = 0$$

$$D_{T_{HP}} = -\mu_x$$

$$E_{T_{HP}} = \left(\lambda_{HP} - \frac{1}{2}\mu_x \frac{\dot{b}_1}{\Omega} \right)$$

E.1.2 Main Rotor In-plane H-force

$$H_{HP}(t) = \sum_{i=1}^{N} \left[-F_P^{(i)} \beta^{(i)} \cos\psi^{(i)} - F_T^{(i)} \sin\psi^{(i)} \right] \tag{E.15}$$

For a two-bladed teetering rotor, the in-plane H-force reduces to:

$$H_{HP}(t) = \frac{1}{2}\rho c C_{L\alpha} R (\Omega R)^2 \left\{ \theta_0 A_{H_{HP}} + \theta_{TW} B_{H_{HP}} - A_1 C_{H_{HP}} - B_1 D_{H_{HP}} + E_{H_{HP}} \right\} \tag{E.16}$$

Where:

$$\begin{aligned} A_{H_{HP}} = & \left(-\mu_x \lambda_{HP} + \frac{1}{3}\frac{p\cos\theta_s}{\Omega} + \frac{3}{2}\mu_y a_0 - \left[\mu_y^2 + \frac{2}{3} \right] a_1 - \mu_x \mu_y b_1 + \frac{1}{3}\frac{\dot{b}_1}{\Omega} \right) \\ & + \left(\mu_x \lambda_{HP} - \frac{1}{3}\frac{p\cos\theta_s}{\Omega} + \frac{1}{2}\mu_y a_0 - \mu_y^2 a_1 + \mu_x \mu_y b_1 - \frac{1}{3}\frac{\dot{b}_1}{\Omega} \right) \cos 2\psi \\ & + \left(-\mu_y \lambda + \frac{1}{3}\frac{q}{\Omega} + \frac{1}{2}\mu_x a_0 - \mu_x \mu_y a_1 - \mu_y^2 b_1 + \frac{1}{3}\frac{\dot{a}_1}{\Omega} \right) \sin 2\psi \end{aligned}$$

$$\begin{aligned} B_{H_{HP}} = & \left(-\frac{1}{2}\mu_x \lambda_{HP} + \frac{1}{4}\frac{p\cos\theta_s}{\Omega} + \mu_y a_0 - \left[\frac{1}{2}\mu_y^2 + \frac{1}{2} \right] a_1 - \frac{1}{2}\mu_x \mu_y b_1 + \frac{1}{4}\frac{\dot{b}_1}{\Omega} \right) \\ & + \left(\frac{1}{2}\mu_x \lambda_{HP} - \frac{1}{4}\frac{p\cos\theta_s}{\Omega} + \frac{1}{3}\mu_y a_0 - \frac{1}{2}\mu_y^2 a_1 + \frac{1}{2}\mu_x \mu_y b_1 - \frac{1}{4}\frac{\dot{b}_1}{\Omega} \right) \cos 2\psi \\ & + \left(-\frac{1}{2}\mu_y \lambda_{HP} + \frac{1}{4}\frac{q}{\Omega} + \frac{1}{3}\mu_x a_0 - \frac{1}{2}\mu_x \mu_y a_1 - \frac{1}{2}\mu_y^2 b_1 + \frac{1}{4}\frac{\dot{a}_1}{\Omega} \right) \sin 2\psi \end{aligned}$$

$$\begin{aligned} C_{H_{HP}} = & \left(\frac{1}{8}\mu_x \frac{q}{\Omega} + \frac{1}{8}\mu_y \frac{p\cos\theta_s}{\Omega} + \left[\mu_y^2 + \frac{1}{3} \right] a_0 - \mu_y a_1 + \frac{1}{8}\mu_x \frac{\dot{a}_1}{\Omega} + \frac{1}{8}\mu_y \frac{\dot{b}_1}{\Omega} \right) \\ & + \left(\left[\frac{1}{3} + \mu_y^2 \right] a_0 - \mu_y a_1 \right) \cos 2\psi \\ & + \left(-\frac{1}{2}\lambda_{HP} + \frac{1}{4}\mu_y \frac{q}{\Omega} + \frac{1}{4}\mu_x \frac{p\cos\theta_s}{\Omega} + \mu_x \mu_y a_0 - \frac{1}{2}\mu_x a_1 - \frac{1}{2}\mu_y b_1 + \frac{1}{4}\mu_y \frac{\dot{a}_1}{\Omega} + \frac{1}{4}\mu_x \frac{\dot{b}_1}{\Omega} \right) \sin 2\psi \\ & + \left(-\frac{1}{8}\mu_x \frac{q}{\Omega} - \frac{1}{8}\mu_y \frac{p\cos\theta_s}{\Omega} - \frac{1}{8}\mu_x \frac{\dot{a}_1}{\Omega} - \frac{1}{8}\mu_y \frac{\dot{b}_1}{\Omega} \right) \cos 4\psi \\ & + \left(-\frac{1}{8}\mu_x \frac{p\cos\theta_s}{\Omega} + \frac{1}{8}\mu_y \frac{q}{\Omega} + \frac{1}{8}\mu_y \frac{\dot{a}_1}{\Omega} - \frac{1}{8}\mu_x \frac{\dot{b}_1}{\Omega} \right) \sin 4\psi \end{aligned}$$

$$D_{H_{HP}} = \left(\left[-\frac{1}{2}\lambda_{HP} + \frac{1}{8}\mu_y\frac{q}{\Omega} + \frac{3}{8}\mu_x\frac{p\cos\theta_s}{\Omega}\right] + \mu_x\mu_y a_0 - \frac{1}{2}\mu_x a_1 - \frac{1}{2}\mu_y b_1 + \frac{1}{8}\mu_y\frac{\dot{a}_1}{\Omega} + \frac{3}{8}\mu_x\frac{\dot{b}_1}{\Omega}\right)$$
$$+\left(\left[\frac{1}{2}\lambda_{HP} - \frac{1}{2}\mu_x\frac{p\cos\theta_s}{\Omega}\right] - \mu_x\mu_y a_0 + \frac{1}{2}\mu_x a_1 + \frac{1}{2}\mu_y b_1 - \frac{1}{2}\mu_x\frac{\dot{b}_1}{\Omega}\right)\cos 2\psi$$
$$+\left(\left[\frac{1}{4}\mu_x\frac{q}{\Omega} + \frac{1}{4}\mu_y\frac{p\cos\theta_s}{\Omega}\right] + \left[\mu_y^2 + \frac{1}{3}\right]a_0 - \mu_y a_1 + \frac{1}{4}\mu_x\frac{\dot{a}_1}{\Omega} + \frac{1}{4}\mu_y\frac{\dot{b}_1}{\Omega}\right)\sin 2\psi$$
$$+\left(\frac{1}{8}\mu_x\frac{p\cos\theta_s}{\Omega} - \frac{1}{8}\mu_y\frac{q}{\Omega} - \frac{1}{8}\mu_y\frac{\dot{a}_1}{\Omega} + \frac{1}{8}\mu_x\frac{\dot{b}_1}{\Omega}\right)\cos 4\psi$$
$$+\left(-\frac{1}{8}\mu_x\frac{q}{\Omega} - \frac{1}{8}\mu_y\frac{p\cos\theta_s}{\Omega} - \frac{1}{8}\mu_x\frac{\dot{a}_1}{\Omega} - \frac{1}{8}\mu_y\frac{\dot{b}_1}{\Omega}\right)\sin 4\psi$$

$$E_{H_{HP}} = \begin{pmatrix} -\lambda_{HP}\frac{p\cos\theta_s}{\Omega} - \left[3\mu_y\lambda_{HP} - \frac{1}{3}\frac{q}{\Omega}\right]a_0 - \left[\frac{5}{8}\mu_y\frac{q}{\Omega} - \frac{1}{8}\mu_x\frac{p\cos\theta_s}{\Omega} - \frac{3}{2}\lambda_{HP}\right]a_1 - \left[\frac{7}{8}\mu_y\frac{p\cos\theta_s}{\Omega} - \frac{1}{8}\mu_x\frac{q}{\Omega}\right]b_1 \\ -\frac{1}{2}\mu_x a_0^2 - \frac{1}{2}\mu_x a_1^2 + 2\mu_x\mu_y a_0 a_1 - \left[2\mu_y^2 - \frac{1}{3}\right]a_0 b_1 + \frac{1}{2}\mu_y a_1 b_1 - \lambda_{HP}\frac{\dot{b}_1}{\Omega} + \frac{1}{3}\frac{\dot{a}_1 a_0}{\Omega} - \frac{5}{8}\mu_y\frac{\dot{a}_1 a_1}{\Omega} \\ +\frac{1}{8}\mu_x\frac{\dot{a}_1 b_1}{\Omega} + \frac{1}{8}\mu_x\frac{\dot{b}_1 a_1}{\Omega} - \frac{7}{8}\mu_y\frac{\dot{b}_1 b_1}{\Omega} - \frac{C_D}{C_{L\alpha}}\mu_x \end{pmatrix}$$
$$+\begin{pmatrix} \lambda_{HP}\frac{p\cos\theta_s}{\Omega} + \left[\mu_y\lambda_{HP} + \frac{1}{3}\frac{q}{\Omega}\right]a_0 - \left[\frac{1}{2}\lambda_{HP} + \frac{1}{2}\mu_y\frac{q}{\Omega}\right]a_1 + \mu_y\frac{p\cos\theta_s}{\Omega}b_1 - \frac{1}{2}\mu_x a_0^2 - \frac{1}{2}\mu_x a_1^2 \\ +2\mu_x\mu_y a_0 a_1 + \left[2\mu_y^2 + \frac{1}{3}\right]a_0 b_1 - \frac{3}{2}\mu_y a_1 b_1 + \lambda_{HP}\frac{\dot{b}_1}{\Omega} + \frac{1}{3}\frac{\dot{a}_1 a_0}{\Omega} - \frac{1}{2}\mu_y\frac{\dot{a}_1 a_1}{\Omega} + \mu_y\frac{\dot{b}_1 b_1}{\Omega} + \frac{C_D}{C_{L\alpha}}\mu_x \end{pmatrix}\cos 2\psi$$
$$+\begin{pmatrix} -\lambda_{HP}\frac{q}{\Omega} + \left[\mu_x\lambda_{HP} + \frac{1}{3}\frac{p\cos\theta_s}{\Omega}\right]a_0 - \left[\frac{3}{4}\mu_y\frac{p\cos\theta_s}{\Omega} - \frac{1}{4}\mu_x\frac{q}{\Omega}\right]a_1 - \left[\frac{3}{4}\mu_y\frac{q}{\Omega} - \frac{1}{4}\mu_x\frac{p\cos\theta_s}{\Omega} + \frac{1}{2}\lambda_{HP}\right]b_1 \\ +\frac{1}{2}\mu_y a_0^2 + \mu_y a_1^2 - \frac{1}{2}\mu_y b_1^2 - \left[2\mu_y^2 + \frac{1}{3}\right]a_0 a_1 + 2\mu_x\mu_y a_0 b_1 - \frac{1}{2}\mu_x a_1 b_1 - \lambda_{HP}\frac{\dot{a}_1}{\Omega} + \frac{1}{4}\mu_x\frac{\dot{a}_1 a_1}{\Omega} \\ -\frac{3}{4}\mu_y\frac{\dot{a}_1 b_1}{\Omega} + \frac{1}{3}\frac{\dot{b}_1 a_0}{\Omega} - \frac{3}{4}\mu_y\frac{\dot{b}_1 a_1}{\Omega} + \frac{1}{4}\mu_x\frac{\dot{b}_1 b_1}{\Omega} - \frac{C_D}{C_{L\alpha}}\mu_y \end{pmatrix}\sin 2\psi$$
$$+\begin{pmatrix} \left[\frac{1}{8}\mu_y\frac{q}{\Omega} - \frac{1}{8}\mu_x\frac{p\cos\theta_s}{\Omega}\right]a_1 - \left[\frac{1}{8}\mu_x\frac{q}{\Omega} + \frac{1}{8}\mu_y\frac{p\cos\theta_s}{\Omega}\right]b_1 + \frac{1}{8}\mu_y\frac{\dot{a}_1 a_1}{\Omega} - \frac{1}{8}\mu_x\frac{\dot{a}_1 b_1}{\Omega} - \frac{1}{8}\mu_x\frac{\dot{b}_1 a_1}{\Omega} \\ -\frac{1}{8}\mu_y\frac{\dot{b}_1 b_1}{\Omega} \end{pmatrix}\cos 4\psi$$
$$+\begin{pmatrix} \left[\frac{1}{8}\mu_x\frac{q}{\Omega} + \frac{1}{8}\mu_y\frac{p\cos\theta_s}{\Omega}\right]a_1 + \left[\frac{1}{8}\mu_y\frac{q}{\Omega} - \frac{1}{8}\mu_x\frac{p\cos\theta_s}{\Omega}\right]b_1 + \frac{1}{8}\mu_x\frac{\dot{a}_1 a_1}{\Omega} + \frac{1}{8}\mu_y\frac{\dot{a}_1 b_1}{\Omega} + \frac{1}{8}\mu_y\frac{\dot{b}_1 a_1}{\Omega} \\ -\frac{1}{8}\mu_x\frac{\dot{b}_1 b_1}{\Omega} \end{pmatrix}\sin 4\psi$$

If higher harmonics are neglected, then for longitudinal flight:

$$A_{H_{HP}} = \left(-\mu_x\lambda_{HP} - \frac{2}{3}a_1 + \frac{1}{3}\frac{\dot{b}_1}{\Omega}\right)$$

$$B_{H_{HP}} = \left(-\frac{1}{2}\mu_x\lambda_{HP} - \frac{1}{2}a_1 + \frac{1}{4}\frac{\dot{b}_1}{\Omega}\right)$$

$$C_{H_{HP}} = \left(\frac{1}{8}\mu_x \frac{q}{\Omega} + \frac{1}{3}a_0 + \frac{1}{8}\mu_x \frac{\dot{a}_1}{\Omega} \right)$$

$$D_{H_{HP}} = \left(-\frac{1}{2}\lambda_{HP} - \frac{1}{2}\mu_x a_1 + \frac{3}{8}\mu_x \frac{\dot{b}_1}{\Omega} \right)$$

$$E_{H_{HP}} = \left(\frac{1}{3}\frac{q}{\Omega}a_0 + \frac{3}{2}\lambda_{HP}a_1 + \frac{1}{8}\mu_x \frac{q}{\Omega}b_1 - \frac{1}{2}\mu_x a_0^2 - \frac{1}{2}\mu_x a_1^2 + \frac{1}{3}a_0 b_1 - \lambda_{HP}\frac{\dot{b}_1}{\Omega} + \frac{1}{3}\frac{\dot{a}_1 a_0}{\Omega} + \frac{1}{8}\mu_x \frac{\dot{a}_1 b_1}{\Omega} + \frac{1}{8}\mu_x \frac{\dot{b}_1 a_1}{\Omega} - \frac{C_D}{C_{L\alpha}}\mu_x \right)$$

E.1.3 Main Rotor In-plane Y-force

$$Y_{HP}(t) = \sum_{i=1}^{N} \left[F_P^{(i)} \beta^{(i)} \sin\psi^{(i)} - F_T^{(i)} \cos\psi^{(i)} \right] \tag{E.17}$$

For a two-bladed teetering rotor, the in-plane Y-force reduces to:

$$Y_{HP}(t) = \frac{1}{2}\rho c C_{L\alpha} R(\Omega R)^2 \left\{ \theta_0 A_{Y_{HP}} + \theta_{TW} B_{Y_{HP}} - A_1 C_{Y_{HP}} - B_1 D_{Y_{HP}} + E_{Y_{HP}} \right\} \tag{E.18}$$

Where:

$$\begin{aligned} A_{Y_{HP}} = & \left(-\mu_y \lambda_{HP} + \frac{1}{3}\frac{q}{\Omega} - \frac{3}{2}\mu_x a_0 + \mu_x \mu_y a_1 + \left[\frac{2}{3} + \mu_x^2 \right] b_1 + \frac{1}{3}\frac{\dot{a}_1}{\Omega} \right) \\ & + \left(\left[-\mu_y \lambda_{HP} + \frac{1}{3}\frac{q}{\Omega} \right] + \frac{1}{2}\mu_x a_0 + \mu_x \mu_y a_1 - \mu_x^2 b_1 + \frac{1}{3}\frac{\dot{a}_1}{\Omega} \right) \cos 2\psi \\ & + \left(\left[-\mu_x \lambda_{HP} + \frac{1}{3}\frac{p\cos\theta_s}{\Omega} \right] - \frac{1}{2}\mu_y a_0 + \mu_x^2 a_1 + \mu_x \mu_y b_1 + \frac{1}{3}\frac{\dot{b}_1}{\Omega} \right) \sin 2\psi \end{aligned}$$

$$\begin{aligned} B_{Y_{HP}} = & \left(-\frac{1}{2}\mu_y \lambda_{HP} + \frac{1}{4}\frac{q}{\Omega} - \mu_x a_0 + \frac{1}{2}\mu_x \mu_y a_1 + \left[\frac{1}{2} + \frac{1}{2}\mu_x^2 \right] b_1 + \frac{1}{4}\frac{\dot{a}_1}{\Omega} \right) \\ & + \left(\left[-\frac{1}{2}\mu_y \lambda_{HP} + \frac{1}{4}\frac{q}{\Omega} \right] + \frac{1}{3}\mu_x a_0 + \frac{1}{2}\mu_x \mu_y a_1 - \frac{1}{2}\mu_x^2 b_1 + \frac{1}{4}\frac{\dot{a}_1}{\Omega} \right) \cos 2\psi \\ & + \left(\left[-\frac{1}{2}\mu_x \lambda_{HP} + \frac{1}{4}\frac{p\cos\theta_s}{\Omega} \right] - \frac{1}{3}\mu_y a_0 + \frac{1}{2}\mu_x^2 a_1 + \frac{1}{2}\mu_x \mu_y b_1 + \frac{1}{4}\frac{\dot{b}_1}{\Omega} \right) \sin 2\psi \end{aligned}$$

$$C_{Y_{HP}} = \left(-\frac{1}{2}\lambda_{HP} + \frac{3}{8}\mu_y \frac{q}{\Omega} + \frac{1}{8}\mu_x \frac{p\cos\theta_s}{\Omega} - \mu_x\mu_y a_0 + \frac{1}{2}\mu_x a_1 + \frac{1}{2}\mu_y b_1 + \frac{3}{8}\mu_y \frac{\dot{a}_1}{\Omega} + \frac{1}{8}\mu_x \frac{\dot{b}_1}{\Omega} \right)$$
$$+ \left(-\frac{1}{2}\lambda_{HP} + \frac{1}{2}\mu_y \frac{q}{\Omega} - \mu_x\mu_y a_0 + \frac{1}{2}\mu_x a_1 + \frac{1}{2}\mu_y b_1 + \frac{1}{2}\mu_y \frac{\dot{a}_1}{\Omega} \right)\cos 2\psi$$
$$+ \left(\frac{1}{4}\mu_x \frac{q}{\Omega} + \frac{1}{4}\mu_y \frac{p\cos\theta_s}{\Omega} - \left[\frac{1}{3} + \mu_x^2\right] a_0 + \mu_x b_1 + \frac{1}{4}\mu_x \frac{\dot{a}_1}{\Omega} + \frac{1}{4}\mu_y \frac{\dot{b}_1}{\Omega} \right)\sin 2\psi$$
$$+ \left(-\frac{1}{8}\mu_x \frac{p\cos\theta_s}{\Omega} + \frac{1}{8}\mu_y \frac{q}{\Omega} + \frac{1}{8}\mu_y \frac{\dot{a}_1}{\Omega} - \frac{1}{8}\mu_x \frac{\dot{b}_1}{\Omega} \right)\cos 4\psi$$
$$+ \left(\frac{1}{8}\mu_x \frac{q}{\Omega} + \frac{1}{8}\mu_y \frac{p\cos\theta_s}{\Omega} + \frac{1}{8}\mu_x \frac{\dot{a}_1}{\Omega} + \frac{1}{8}\mu_y \frac{\dot{b}_1}{\Omega} \right)\sin 4\psi$$

$$D_{Y_{HP}} = \left(\frac{1}{8}\mu_x \frac{q}{\Omega} + \frac{1}{8}\mu_y \frac{p\cos\theta_s}{\Omega} - \left[\frac{1}{3} + \mu_x^2\right] a_0 + \mu_x b_1 + \frac{1}{8}\mu_x \frac{\dot{a}_1}{\Omega} + \frac{1}{8}\mu_y \frac{\dot{b}_1}{\Omega} \right)$$
$$+ \left(\left[\frac{1}{3} + \mu_x^2\right] a_0 - \mu_x b_1 \right)\cos 2\psi$$
$$+ \left(-\frac{1}{2}\lambda_{HP} + \frac{1}{4}\mu_y \frac{q}{\Omega} + \frac{1}{4}\mu_x \frac{p\cos\theta_s}{\Omega} - \mu_x\mu_y a_0 + \frac{1}{2}\mu_x a_1 + \frac{1}{2}\mu_y b_1 + \frac{1}{4}\mu_y \frac{\dot{a}_1}{\Omega} + \frac{1}{4}\mu_x \frac{\dot{b}_1}{\Omega} \right)\sin 2\psi$$
$$+ \left(-\frac{1}{8}\mu_x \frac{q}{\Omega} - \frac{1}{8}\mu_y \frac{p\cos\theta_s}{\Omega} - \frac{1}{8}\mu_x \frac{\dot{a}_1}{\Omega} - \frac{1}{8}\mu_y \frac{\dot{b}_1}{\Omega} \right)\cos 4\psi$$
$$+ \left(-\frac{1}{8}\mu_x \frac{p\cos\theta_s}{\Omega} + \frac{1}{8}\mu_y \frac{q}{\Omega} + \frac{1}{8}\mu_y \frac{\dot{a}_1}{\Omega} - \frac{1}{8}\mu_x \frac{\dot{b}_1}{\Omega} \right)\sin 4\psi$$

$$
\begin{aligned}
E_{Y_{HP}} = &\begin{pmatrix}
-\lambda_{HP}\frac{q}{\Omega}+\left[3\mu_x\lambda_{HP}-\frac{1}{3}\frac{p\cos\theta_s}{\Omega}\right]a_0+\left[\frac{7}{8}\mu_x\frac{q}{\Omega}-\frac{1}{8}\mu_y\frac{p\cos\theta_s}{\Omega}\right]a_1+\left[-\frac{3}{2}\lambda_{HP}-\frac{1}{8}\mu_y\frac{q}{\Omega}+\frac{5}{8}\mu_x\frac{p\cos\theta_s}{\Omega}\right]b_1\\
-\frac{1}{2}\mu_y a_0^2-\frac{1}{2}\mu_y b_1^2+\left[-2\mu_x^2+\frac{1}{3}\right]a_0a_1+2\mu_x\mu_y a_0b_1+\frac{1}{2}\mu_x a_1b_1-\lambda_{HP}\frac{\dot{a}_1}{\Omega}+\frac{7}{8}\mu_x\frac{\dot{a}_1a_1}{\Omega}-\frac{1}{8}\mu_y\frac{\dot{a}_1b_1}{\Omega}\\
-\frac{1}{3}\frac{\dot{b}_1a_0}{\Omega}-\frac{1}{8}\mu_y\frac{\dot{b}_1a_1}{\Omega}+\frac{5}{8}\mu_x\frac{\dot{b}_1b_1}{\Omega}-\frac{C_D}{C_{L\alpha}}\mu_y
\end{pmatrix}\\
&+\begin{pmatrix}
-\lambda_{HP}\frac{q}{\Omega}+\left[\mu_x\lambda_{HP}+\frac{1}{3}\frac{p\cos\theta_s}{\Omega}\right]a_0+\mu_x\frac{q}{\Omega}a_1-\left[\frac{1}{2}\mu_x\frac{p\cos\theta_s}{\Omega}+\frac{1}{2}\lambda_{HP}\right]b_1+\frac{1}{2}\mu_y a_0^2+\frac{1}{2}\mu_y b_1^2\\
-\left[\frac{1}{3}+2\mu_x^2\right]a_0a_1-2\mu_x\mu_y a_0b_1+\frac{3}{2}\mu_x a_1b_1-\lambda_{HP}\frac{\dot{a}_1}{\Omega}+\mu_x\frac{\dot{a}_1a_1}{\Omega}+\frac{1}{3}\frac{\dot{b}_1a_0}{\Omega}-\frac{1}{2}\mu_x\frac{\dot{b}_1b_1}{\Omega}-\frac{C_D}{C_{L\alpha}}\mu_y
\end{pmatrix}\cos 2\psi\\
&+\begin{pmatrix}
-\lambda_{HP}\frac{p\cos\theta_s}{\Omega}-\left[\mu_y\lambda_{HP}+\frac{1}{3}\frac{q}{\Omega}\right]a_0+\left[\frac{1}{2}\lambda_{HP}-\frac{1}{4}\mu_y\frac{q}{\Omega}+\frac{3}{4}\mu_x\frac{p\cos\theta_s}{\Omega}\right]a_1+\left[\frac{3}{4}\mu_x\frac{q}{\Omega}-\frac{1}{4}\mu_y\frac{p\cos\theta_s}{\Omega}\right]b_1\\
+\frac{1}{2}\mu_x a_0^2-\frac{1}{2}\mu_x a_1^2+\mu_x b_1^2+2\mu_x\mu_y a_0a_1-\left[2\mu_x^2+\frac{1}{3}\right]a_0b_1-\frac{1}{2}\mu_y a_1b_1-\lambda_{HP}\frac{\dot{b}_1}{\Omega}-\frac{1}{3}\frac{\dot{a}_1a_0}{\Omega}-\frac{1}{4}\mu_y\frac{\dot{a}_1a_1}{\Omega}\\
+\frac{3}{4}\mu_x\frac{\dot{a}_1b_1}{\Omega}+\frac{3}{4}\mu_x\frac{\dot{b}_1a_1}{\Omega}-\frac{1}{4}\mu_y\frac{\dot{b}_1b_1}{\Omega}-\frac{C_D}{C_{L\alpha}}\mu_x
\end{pmatrix}\sin 2\psi\\
&+\begin{pmatrix}
\left[\frac{1}{8}\mu_x\frac{q}{\Omega}+\frac{1}{8}\mu_y\frac{p\cos\theta_s}{\Omega}\right]a_1+\left[-\frac{1}{8}\mu_x\frac{p\cos\theta_s}{\Omega}+\frac{1}{8}\mu_y\frac{q}{\Omega}\right]b_1+\frac{1}{8}\mu_x\frac{\dot{a}_1a_1}{\Omega}+\frac{1}{8}\mu_y\frac{\dot{a}_1b_1}{\Omega}+\frac{1}{8}\mu_y\frac{\dot{b}_1a_1}{\Omega}\\
-\frac{1}{8}\mu_x\frac{\dot{b}_1b_1}{\Omega}
\end{pmatrix}\cos 4\psi\\
&+\begin{pmatrix}
\left[\frac{1}{8}\mu_x\frac{p\cos\theta_s}{\Omega}-\frac{1}{8}\mu_y\frac{q}{\Omega}\right]a_1+\left[\frac{1}{8}\mu_x\frac{q}{\Omega}+\frac{1}{8}\mu_y\frac{p\cos\theta_s}{\Omega}\right]b_1-\frac{1}{8}\mu_y\frac{\dot{a}_1a_1}{\Omega}+\frac{1}{8}\mu_x\frac{\dot{a}_1b_1}{\Omega}+\frac{1}{8}\mu_x\frac{\dot{b}_1a_1}{\Omega}\\
+\frac{1}{8}\mu_y\frac{\dot{b}_1b_1}{\Omega}
\end{pmatrix}\sin 4\psi
\end{aligned}
$$

If higher harmonics are neglected, then for longitudinal flight:

$$A_{Y_{HP}} = \left(\frac{1}{3}\frac{q}{\Omega}-\frac{3}{2}\mu_x a_0+\left[\frac{2}{3}+\mu_x^2\right]b_1+\frac{1}{3}\frac{\dot{a}_1}{\Omega}\right)$$

$$B_{Y_{HP}} = \left(\frac{1}{4}\frac{q}{\Omega}-\mu_x a_0+\left[\frac{1}{2}+\frac{1}{2}\mu_x^2\right]b_1+\frac{1}{4}\frac{\dot{a}_1}{\Omega}\right)$$

$$C_{Y_{HP}} = \left(-\frac{1}{2}\lambda_{HP}+\frac{1}{2}\mu_x a_1+\frac{1}{8}\mu_x\frac{\dot{b}_1}{\Omega}\right)$$

$$D_{Y_{HP}} = \left(\frac{1}{8}\mu_x\frac{q}{\Omega}-\left[\frac{1}{3}+\mu_x^2\right]a_0+\mu_x b_1+\frac{1}{8}\mu_x\frac{\dot{a}_1}{\Omega}\right)$$

$$E_{Y_{HP}} = \left(-\lambda_{HP}\frac{q}{\Omega}+3\mu_x\lambda_{HP}a_0+\frac{7}{8}\mu_x\frac{q}{\Omega}a_1-\frac{3}{2}\lambda_{HP}b_1+\left[-2\mu_x^2+\frac{1}{3}\right]a_0a_1+\frac{1}{2}\mu_x a_1b_1-\lambda_{HP}\frac{\dot{a}_1}{\Omega}+\frac{7}{8}\mu_x\frac{\dot{a}_1a_1}{\Omega}-\frac{1}{3}\frac{\dot{b}_1a_0}{\Omega}+\frac{5}{8}\mu_x\frac{\dot{b}_1b_1}{\Omega}\right)$$

E.2 Expansion of Main Rotor Aerodynamic Moments

The differential moment resulting from the aerodynamic loads is found by taking the cross product of the position vector from the hub to a point on the elastic axis and the differential aerodynamic load acting at that point:

$$\overrightarrow{dM_A} = \begin{Bmatrix} dM_T(t) \\ dM_P(t) \\ dM_R(t) \end{Bmatrix}_R = \overrightarrow{r_{H/P}} \times \overrightarrow{dF_A} = \begin{Bmatrix} -dF_p(t)\, r \\ dF_T(t)\, r \\ 0 \end{Bmatrix}_R \tag{E.19}$$

The differential aerodynamic moment acting about the flapping axis is:

$$dM_T(t) = \frac{1}{2}\rho c C_{L\alpha} R^2 (\Omega R)^2 \left(u_T^2 \theta x - u_P u_T x\right) dx \tag{E.20}$$

Integrating along the length of the blade yields:

$$\begin{aligned} M_T(t) &= \int_0^1 dM_T(t) \\ M_T(t) &= \frac{1}{2}\rho c C_{L\alpha} R^2 (\Omega R)^2 \left\{\theta_0 A_{M_T} + \theta_{TW} B_{M_T} - A_1 C_{M_T} - B_1 D_{M_T} + E_{M_T}\right\} \end{aligned} \tag{E.21}$$

Where:

$$A_{M_T} = \left(\frac{1}{4} + \frac{1}{4}\mu_x^2 + \frac{1}{4}\mu_y^2\right) + \frac{2}{3}\mu_y \cos\psi + \frac{2}{3}\mu_x \sin\psi + \frac{1}{4}\left(\mu_y^2 - \mu_x^2\right)\cos 2\psi + \frac{1}{2}\mu_x\mu_y \sin 2\psi$$

$$B_{M_T} = \left(\frac{1}{5} + \frac{1}{6}\mu_x^2 + \frac{1}{6}\mu_y^2\right) + \frac{1}{2}\mu_y \cos\psi + \frac{1}{2}\mu_x \sin\psi + \frac{1}{6}\left(\mu_y^2 - \mu_x^2\right)\cos 2\psi + \frac{1}{3}\mu_x\mu_y \sin 2\psi$$

$$\begin{aligned} C_{M_T} = {} & \frac{1}{3}\mu_y + \left(\frac{1}{4} + \frac{1}{8}\mu_x^2 + \frac{3}{8}\mu_y^2\right)\cos\psi + \frac{1}{4}\mu_x\mu_y \sin\psi + \frac{1}{3}\mu_y \cos 2\psi + \frac{1}{3}\mu_x \sin 2\psi \\ & + \frac{1}{8}\left(\mu_y^2 - \mu_x^2\right)\cos 3\psi + \frac{1}{4}\mu_x\mu_y \sin 3\psi \end{aligned}$$

$$\begin{aligned} D_{M_T} = {} & \frac{1}{3}\mu_x + \frac{1}{4}\mu_x\mu_y \cos\psi + \left(\frac{1}{4} + \frac{3}{8}\mu_x^2 + \frac{1}{8}\mu_y^2\right)\sin\psi - \frac{1}{3}\mu_x \cos 2\psi + \frac{1}{3}\mu_y \sin 2\psi \\ & - \frac{1}{4}\mu_x\mu_y \cos 3\psi + \frac{1}{8}\left(\mu_y^2 - \mu_x^2\right)\sin 3\psi \end{aligned}$$

$$
\begin{aligned}
E_{M_T} = &\left(-\frac{1}{3}\lambda_{HP}+\frac{1}{6}\left[\mu_y\frac{q}{\Omega}+\mu_x\frac{p\cos\theta_s}{\Omega}\right]+\frac{1}{6}\mu_y\frac{\dot{a}_1}{\Omega}+\frac{1}{6}\mu_x\frac{\dot{b}_1}{\Omega}\right)\\
&+\left(-\frac{1}{2}\mu_y\lambda_{HP}+\frac{1}{4}\frac{q}{\Omega}-\frac{1}{3}\mu_x a_0+\frac{1}{4}\mu_x\mu_y a_1+\left[\frac{1}{8}\mu_x^2-\frac{1}{8}\mu_y^2+\frac{1}{4}\right]b_1+\frac{1}{4}\frac{\dot{a}_1}{\Omega}\right)\cos\psi\\
&+\left(-\frac{1}{2}\mu_x\lambda_{HP}+\frac{1}{4}\frac{p\cos\theta_s}{\Omega}+\frac{1}{3}\mu_y a_0+\left[\frac{1}{8}\mu_x^2-\frac{1}{8}\mu_y^2-\frac{1}{4}\right]a_1-\frac{1}{4}\mu_x\mu_y b_1+\frac{1}{4}\frac{\dot{b}_1}{\Omega}\right)\sin\psi\\
&+\left(-\frac{1}{6}\left[\mu_x\frac{p\cos\theta_s}{\Omega}-\mu_y\frac{q}{\Omega}\right]-\frac{1}{2}\mu_x\mu_y a_0+\frac{1}{3}\mu_x a_1+\frac{1}{3}\mu_y b_1+\frac{1}{6}\mu_y\frac{\dot{a}_1}{\Omega}-\frac{1}{6}\mu_x\frac{\dot{b}_1}{\Omega}\right)\cos 2\psi\\
&+\left(\frac{1}{6}\left[\mu_x\frac{q}{\Omega}+\mu_y\frac{p\cos\theta_s}{\Omega}\right]-\frac{1}{4}\left[\mu_x^2-\mu_y^2\right]a_0-\frac{1}{3}\mu_y a_1+\frac{1}{3}\mu_x b_1+\frac{1}{6}\mu_x\frac{\dot{a}_1}{\Omega}+\frac{1}{6}\mu_y\frac{\dot{b}_1}{\Omega}\right)\sin 2\psi\\
&+\left(\frac{1}{4}\mu_x\mu_y a_1-\frac{1}{8}\left[\mu_x^2-\mu_y^2\right]b_1\right)\cos 3\psi+\left(\frac{1}{8}\left[\mu_x^2-\mu_y^2\right]a_1+\frac{1}{4}\mu_x\mu_y b_1\right)\sin 3\psi
\end{aligned}
$$

The differential aerodynamic moment acting about the axis perpendicular to the flapping axis is:

$$
dM_P(t)=\frac{1}{2}\rho c C_{L\alpha}R^2(\Omega R)^2\left(u_T u_p\theta x-u_p^2 x+\frac{C_D}{C_{L\alpha}}u_T^2 x\right)dx \tag{E.22}
$$

Integrating along the length of the blade yields:

$$
\begin{aligned}
&M_P(t)=\int_0^1 dM_P(t)\\
&M_P(t)=\frac{1}{2}\rho c C_{L\alpha}R^2(\Omega R)^2\left\{\theta_0 A_{M_P}+\theta_{TW}B_{M_P}-A_1 C_{M_P}-B_1 D_{M_P}+E_{M_P}\right\}
\end{aligned} \tag{E.23}
$$

Where:

$$
\begin{aligned}
A_{M_P} = &\left(\frac{1}{3}\lambda_{HP}-\frac{1}{6}\mu_y\frac{q}{\Omega}-\frac{1}{6}\mu_x\frac{p\cos\theta_s}{\Omega}-\frac{1}{6}\mu_y\frac{\dot{a}_1}{\Omega}-\frac{1}{6}\mu_x\frac{\dot{b}_1}{\Omega}\right)\\
&+\left(\frac{1}{2}\mu_y\lambda_{HP}-\frac{1}{4}\frac{q}{\Omega}+\frac{1}{3}\mu_x a_0-\frac{1}{4}\mu_x\mu_y a_1-\left[\frac{1}{8}\mu_x^2-\frac{1}{8}\mu_y^2+\frac{1}{4}\right]b_1-\frac{1}{4}\frac{\dot{a}_1}{\Omega}\right)\cos\psi\\
&+\left(\frac{1}{2}\mu_x\lambda_{HP}-\frac{1}{4}\frac{p\cos\theta_s}{\Omega}-\frac{1}{3}\mu_y a_0-\left[\frac{1}{8}\mu_x^2-\frac{1}{8}\mu_y^2-\frac{1}{4}\right]a_1+\frac{1}{4}\mu_x\mu_y b_1-\frac{1}{4}\frac{\dot{b}_1}{\Omega}\right)\sin\psi\\
&+\left(\frac{1}{6}\mu_x\frac{p\cos\theta_s}{\Omega}-\frac{1}{6}\mu_y\frac{q}{\Omega}+\frac{1}{2}\mu_x\mu_y a_0-\frac{1}{3}\mu_x a_1-\frac{1}{3}\mu_y b_1-\frac{1}{6}\mu_y\frac{\dot{a}_1}{\Omega}+\frac{1}{6}\mu_x\frac{\dot{b}_1}{\Omega}\right)\cos 2\psi\\
&+\left(-\frac{1}{6}\mu_x\frac{q}{\Omega}-\frac{1}{6}\mu_y\frac{p\cos\theta_s}{\Omega}+\frac{1}{4}\left[\mu_x^2-\mu_y^2\right]a_0+\frac{1}{3}\mu_y a_1-\frac{1}{3}\mu_x b_1-\frac{1}{6}\mu_x\frac{\dot{a}_1}{\Omega}-\frac{1}{6}\mu_y\frac{\dot{b}_1}{\Omega}\right)\sin 2\psi\\
&+\left(-\frac{1}{4}\mu_x\mu_y a_1+\frac{1}{8}\left[\mu_x^2-\mu_y^2\right]b_1\right)\cos 3\psi+\left(\frac{1}{8}\left[\mu_y^2-\mu_x^2\right]a_1-\frac{1}{4}\mu_x\mu_y b_1\right)\sin 3\psi
\end{aligned}
$$

$$
\begin{aligned}
B_{M_P} = &\left(\frac{1}{4}\lambda_{HP} - \frac{1}{8}\mu_y\frac{q}{\Omega} - \frac{1}{8}\mu_x\frac{p\cos\theta_s}{\Omega} - \frac{1}{8}\mu_y\frac{\dot{a}_1}{\Omega} - \frac{1}{8}\mu_x\frac{\dot{b}_1}{\Omega}\right)\\
&+\left(\frac{1}{3}\mu_y\lambda_{HP} - \frac{1}{5}\frac{q}{\Omega} + \frac{1}{4}\mu_x a_0 - \frac{1}{6}\mu_x\mu_y a_1 - \left[\frac{1}{12}\mu_x^2 - \frac{1}{12}\mu_y^2 + \frac{1}{5}\right]b_1 - \frac{1}{5}\frac{\dot{a}_1}{\Omega}\right)\cos\psi\\
&+\left(\frac{1}{3}\mu_x\lambda_{HP} - \frac{1}{5}\frac{p\cos\theta_s}{\Omega} - \frac{1}{4}\mu_y a_0 - \left[\frac{1}{12}\mu_x^2 - \frac{1}{12}\mu_y^2 - \frac{1}{5}\right]a_1 + \frac{1}{6}\mu_x\mu_y b_1 - \frac{1}{5}\frac{\dot{b}_1}{\Omega}\right)\sin\psi\\
&+\left(\frac{1}{8}\mu_x\frac{p\cos\theta_s}{\Omega} - \frac{1}{8}\mu_y\frac{q}{\Omega} + \frac{1}{3}\mu_x\mu_y a_0 - \frac{1}{4}\mu_x a_1 - \frac{1}{4}\mu_y b_1 - \frac{1}{8}\mu_y\frac{\dot{a}_1}{\Omega} + \frac{1}{8}\mu_x\frac{\dot{b}_1}{\Omega}\right)\cos 2\psi\\
&+\left(-\frac{1}{8}\mu_x\frac{q}{\Omega} - \frac{1}{8}\mu_y\frac{p\cos\theta_s}{\Omega} + \frac{1}{6}\left[\mu_x^2 - \mu_y^2\right]a_0 + \frac{1}{4}\mu_y a_1 - \frac{1}{4}\mu_x b_1 - \frac{1}{8}\mu_x\frac{\dot{a}_1}{\Omega} - \frac{1}{8}\mu_y\frac{\dot{b}_1}{\Omega}\right)\sin 2\psi\\
&+\left(-\frac{1}{6}\mu_x\mu_y a_1 + \frac{1}{12}\left[\mu_x^2 - \mu_y^2\right]b_1\right)\cos 3\psi + \left(\frac{1}{12}\left[\mu_y^2 - \mu_x^2\right]a_1 - \frac{1}{6}\mu_x\mu_y b_1\right)\sin 3\psi
\end{aligned}
$$

$$
\begin{aligned}
C_{M_P} = &\left(\frac{1}{4}\mu_y\lambda_{HP} - \frac{1}{8}\frac{q}{\Omega} + \frac{1}{6}\mu_x a_0 - \frac{1}{8}\mu_x\mu_y a_1 - \left[\frac{1}{16}\mu_x^2 - \frac{1}{16}\mu_y^2 + \frac{1}{8}\right]b_1 - \frac{1}{8}\frac{\dot{a}_1}{\Omega}\right)\\
&+\left(\frac{1}{3}\lambda_{HP} - \frac{1}{4}\mu_y\frac{q}{\Omega} - \frac{1}{12}\mu_x\frac{p\cos\theta_s}{\Omega} + \frac{1}{4}\mu_x\mu_y a_0 - \frac{1}{6}\mu_x a_1 - \frac{1}{6}\mu_y b_1 - \frac{1}{4}\mu_y\frac{\dot{a}_1}{\Omega} - \frac{1}{12}\mu_x\frac{\dot{b}_1}{\Omega}\right)\cos\psi\\
&+\left(-\frac{1}{12}\mu_x\frac{q}{\Omega} - \frac{1}{12}\mu_y\frac{p\cos\theta_s}{\Omega} + \frac{1}{8}\left[\mu_x^2 - \mu_y^2\right]a_0 + \frac{1}{6}\mu_y a_1 - \frac{1}{6}\mu_x b_1 - \frac{1}{12}\mu_x\frac{\dot{a}_1}{\Omega} - \frac{1}{12}\mu_y\frac{\dot{b}_1}{\Omega}\right)\sin\psi\\
&+\left(\frac{1}{4}\mu_y\lambda_{HP} - \frac{1}{8}\frac{q}{\Omega} + \frac{1}{6}\mu_x a_0 - \frac{1}{4}\mu_x\mu_y a_1 - \frac{1}{8}b_1 - \frac{1}{8}\frac{\dot{a}_1}{\Omega}\right)\cos 2\psi\\
&+\left(\frac{1}{4}\mu_x\lambda_{HP} - \frac{1}{8}\frac{p\cos\theta_s}{\Omega} - \frac{1}{6}\mu_y a_0 - \left[\frac{1}{8}\mu_x^2 - \frac{1}{8}\mu_y^2 - \frac{1}{8}\right]a_1 - \frac{1}{8}\frac{\dot{b}_1}{\Omega}\right)\sin 2\psi\\
&+\left(\frac{1}{12}\mu_x\frac{p\cos\theta_s}{\Omega} - \frac{1}{12}\mu_y\frac{q}{\Omega} + \frac{1}{4}\mu_x\mu_y a_0 - \frac{1}{6}\mu_x a_1 - \frac{1}{6}\mu_y b_1 - \frac{1}{12}\mu_y\frac{\dot{a}_1}{\Omega} + \frac{1}{12}\mu_x\frac{\dot{b}_1}{\Omega}\right)\cos 3\psi\\
&+\left(-\frac{1}{12}\mu_x\frac{q}{\Omega} - \frac{1}{12}\mu_y\frac{p\cos\theta_s}{\Omega} + \frac{1}{8}\left[\mu_x^2 - \mu_y^2\right]a_0 + \frac{1}{6}\mu_y a_1 - \frac{1}{6}\mu_x b_1 - \frac{1}{12}\mu_x\frac{\dot{a}_1}{\Omega} - \frac{1}{12}\mu_y\frac{\dot{b}_1}{\Omega}\right)\sin 3\psi\\
&+\left(-\frac{1}{8}\mu_x\mu_y a_1 + \frac{1}{16}\left[\mu_x^2 - \mu_y^2\right]b_1\right)\cos 4\psi + \left(-\frac{1}{16}\left[\mu_x^2 - \mu_y^2\right]a_1 - \frac{1}{8}\mu_x\mu_y b_1\right)\sin 4\psi
\end{aligned}
$$

$$
\begin{aligned}
D_{M_P} = &\left(\frac{1}{4}\mu_x\lambda_{HP} - \frac{1}{8}\frac{p\cos\theta_s}{\Omega} - \frac{1}{6}\mu_y a_0 - \left[\frac{1}{16}\mu_x^2 - \frac{1}{16}\mu_y^2 - \frac{1}{8}\right]a_1 + \frac{1}{8}\mu_x\mu_y b_1 - \frac{1}{8}\frac{\dot{b}_1}{\Omega}\right) \\
&+\left(-\frac{1}{12}\mu_x\frac{q}{\Omega} - \frac{1}{12}\mu_y\frac{p\cos\theta_s}{\Omega} + \frac{1}{8}\left[\mu_x^2 - \mu_y^2\right]a_0 + \frac{1}{6}\mu_y a_1 - \frac{1}{6}\mu_x b_1 - \frac{1}{12}\mu_x\frac{\dot{a}_1}{\Omega} - \frac{1}{12}\mu_y\frac{\dot{b}_1}{\Omega}\right)\cos\psi \\
&+\left(\frac{1}{3}\lambda_{HP} - \frac{1}{12}\mu_y\frac{q}{\Omega} - \frac{1}{4}\mu_x\frac{p\cos\theta_s}{\Omega} - \frac{1}{4}\mu_x\mu_y a_0 + \frac{1}{6}\mu_x a_1 + \frac{1}{6}\mu_y b_1 - \frac{1}{12}\mu_y\frac{\dot{a}_1}{\Omega} - \frac{1}{4}\mu_x\frac{\dot{b}_1}{\Omega}\right)\sin\psi \\
&+\left(-\frac{1}{4}\mu_x\lambda_{HP} + \frac{1}{8}\frac{p\cos\theta_s}{\Omega} + \frac{1}{6}\mu_y a_0 - \frac{1}{8}a_1 - \frac{1}{4}\mu_x\mu_y b_1 + \frac{1}{8}\frac{\dot{b}_1}{\Omega}\right)\cos 2\psi \\
&+\left(\frac{1}{4}\mu_y\lambda_{HP} - \frac{1}{8}\frac{q}{\Omega} + \frac{1}{6}\mu_x a_0 - \left[\frac{1}{8}\mu_x^2 - \frac{1}{8}\mu_y^2 + \frac{1}{8}\right]b_1 - \frac{1}{8}\frac{\dot{a}_1}{\Omega}\right)\sin 2\psi \\
&+\left(\frac{1}{12}\mu_x\frac{q}{\Omega} + \frac{1}{12}\mu_y\frac{p\cos\theta_s}{\Omega} - \frac{1}{8}\left[\mu_x^2 - \mu_y^2\right]a_0 - \frac{1}{6}\mu_y a_1 + \frac{1}{6}\mu_x b_1 + \frac{1}{12}\mu_x\frac{\dot{a}_1}{\Omega} + \frac{1}{12}\mu_y\frac{\dot{b}_1}{\Omega}\right)\cos 3\psi \\
&+\left(\frac{1}{12}\mu_x\frac{p\cos\theta_s}{\Omega} - \frac{1}{12}\mu_y\frac{q}{\Omega} + \frac{1}{4}\mu_x\mu_y a_0 - \frac{1}{6}\mu_x a_1 - \frac{1}{6}\mu_y b_1 - \frac{1}{12}\mu_y\frac{\dot{a}_1}{\Omega} + \frac{1}{12}\mu_x\frac{\dot{b}_1}{\Omega}\right)\sin 3\psi \\
&+\left(\frac{1}{16}\left[\mu_x^2 - \mu_y^2\right]a_1 + \frac{1}{8}\mu_x\mu_y b_1\right)\cos 4\psi + \left(-\frac{1}{8}\mu_x\mu_y a_1 + \frac{1}{16}\left[\mu_x^2 - \mu_y^2\right]b_1\right)\sin 4\psi
\end{aligned}
$$

$$
\begin{aligned}
E_{M_P} = &\left(\begin{array}{l}
-\frac{1}{2}\lambda_{HP}^2-\frac{1}{8}\frac{q^2}{\Omega^2}-\frac{1}{8}\frac{p^2\cos^2\theta_s}{\Omega^2}-\frac{1}{3}\left[\mu_y\frac{p\cos\theta_s}{\Omega}-\mu_x\frac{q}{\Omega}\right]a_0+\left[\frac{1}{2}\mu_x\lambda_{HP}+\frac{1}{4}\frac{p\cos\theta_s}{\Omega}\right]a_1-\left[\frac{1}{2}\mu_y\lambda_{HP}+\frac{1}{4}\frac{q}{\Omega}\right]b_1\\
-\frac{1}{4}\left[\mu_x^2+\mu_y^2\right]a_0^2-\left[\frac{3}{16}\mu_x^2+\frac{1}{16}\mu_y^2+\frac{1}{8}\right]a_1^2-\left[\frac{1}{16}\mu_x^2+\frac{3}{16}\mu_y^2+\frac{1}{8}\right]b_1^2+\frac{1}{3}\mu_y a_0a_1+\frac{1}{3}\mu_x a_0b_1+\frac{1}{4}\mu_x\mu_y a_1b_1\\
-\frac{1}{4}\frac{q}{\Omega^2}\dot{a}_1-\frac{1}{4}\frac{p\cos\theta_s}{\Omega^2}\dot{b}_1+\frac{1}{3}\mu_x\frac{\dot{a}_1a_0}{\Omega}-\frac{1}{4}\frac{\dot{a}_1b_1}{\Omega}-\frac{1}{3}\mu_y\frac{\dot{b}_1a_0}{\Omega}+\frac{1}{4}\frac{\dot{b}_1a_1}{\Omega}-\frac{1}{8}\left(\frac{\dot{a}_1}{\Omega}\right)^2-\frac{1}{8}\left(\frac{\dot{b}_1}{\Omega}\right)^2\\
+\frac{C_D}{C_{L\alpha}}\left[\frac{1}{4}+\frac{1}{4}\mu_x^2+\frac{1}{4}\mu_y^2\right]
\end{array}\right)\\
&+\left(\begin{array}{l}
\frac{2}{3}\lambda_{HP}\frac{q}{\Omega}-\mu_x\lambda_{HP}a_0+\left[\frac{1}{6}\mu_y\frac{p\cos\theta_s}{\Omega}-\frac{1}{2}\mu_x\frac{q}{\Omega}\right]a_1+\left[\frac{1}{6}\mu_y\frac{q}{\Omega}-\frac{1}{6}\mu_x\frac{p\cos\theta_s}{\Omega}+\frac{2}{3}\lambda_{HP}\right]b_1-\frac{1}{6}\mu_y a_1^2+\frac{1}{6}\mu_y b_1^2\\
+\left[\frac{3}{4}\mu_x^2+\frac{1}{4}\mu_y^2\right]a_0a_1-\frac{1}{2}\mu_x\mu_y a_0b_1-\frac{1}{3}\mu_x a_1b_1+\frac{2}{3}\lambda_{HP}\frac{\dot{a}_1}{\Omega}-\frac{1}{2}\mu_x\frac{\dot{a}_1a_1}{\Omega}+\frac{1}{6}\mu_y\frac{\dot{a}_1b_1}{\Omega}+\frac{1}{6}\mu_y\frac{\dot{b}_1a_1}{\Omega}-\frac{1}{6}\mu_x\frac{\dot{b}_1b_1}{\Omega}\\
+\frac{C_D}{C_{L\alpha}}\frac{2}{3}\mu_y
\end{array}\right)\cos\psi\\
&+\left(\begin{array}{l}
\frac{2}{3}\lambda_{HP}\frac{p\cos\theta_s}{\Omega}+\mu_y\lambda_{HP}a_0+\left[\frac{1}{6}\mu_y\frac{q}{\Omega}-\frac{1}{6}\mu_x\frac{p\cos\theta_s}{\Omega}-\frac{2}{3}\lambda_{HP}\right]a_1+\left[\frac{1}{2}\mu_y\frac{p\cos\theta_s}{\Omega}-\frac{1}{6}\mu_x\frac{q}{\Omega}\right]b_1+\frac{1}{6}\mu_x a_1^2\\
-\frac{1}{6}\mu_x b_1^2-\frac{1}{2}\mu_x\mu_y a_0a_1+\left[\frac{1}{4}\mu_x^2+\frac{3}{4}\mu_y^2\right]a_0b_1-\frac{1}{3}\mu_y a_1b_1+\frac{2}{3}\lambda_{HP}\frac{\dot{b}_1}{\Omega}+\frac{1}{6}\mu_y\frac{\dot{a}_1a_1}{\Omega}-\frac{1}{6}\mu_x\frac{\dot{a}_1b_1}{\Omega}-\frac{1}{6}\mu_x\frac{\dot{b}_1a_1}{\Omega}\\
+\frac{1}{2}\mu_y\frac{\dot{b}_1b_1}{\Omega}+\frac{C_D}{C_{L\alpha}}\frac{2}{3}\mu_x
\end{array}\right)\sin\psi\\
&+\left(\begin{array}{l}
-\frac{1}{8}\left[\left(\frac{q}{\Omega}\right)^2-\left(\frac{p\cos\theta_s}{\Omega}\right)^2\right]+\frac{1}{3}\left[\mu_x\frac{q}{\Omega}+\mu_y\frac{p\cos\theta_s}{\Omega}\right]a_0+\left[\frac{1}{2}\mu_x\lambda_{HP}-\frac{1}{4}\frac{p\cos\theta_s}{\Omega}\right]a_1+\left[\frac{1}{2}\mu_y\lambda_{HP}-\frac{1}{4}\frac{q}{\Omega}\right]b_1\\
+\frac{1}{4}\left[\mu_y^2-\mu_x^2\right]a_0^2-\left[\frac{1}{4}\mu_x^2-\frac{1}{8}\right]a_1^2+\left[\frac{1}{4}\mu_y^2-\frac{1}{8}\right]b_1^2-\frac{1}{3}\mu_y a_0a_1+\frac{1}{3}\mu_x a_0b_1-\frac{1}{4}\frac{q}{\Omega^2}\dot{a}_1+\frac{1}{4}\frac{p\cos\theta_s}{\Omega^2}\dot{b}_1\\
+\frac{1}{3}\mu_x\frac{\dot{a}_1a_0}{\Omega}-\frac{1}{4}\frac{\dot{a}_1b_1}{\Omega}+\frac{1}{3}\mu_y\frac{\dot{b}_1a_0}{\Omega}-\frac{1}{4}\frac{\dot{b}_1a_1}{\Omega}-\frac{1}{8}\left(\frac{\dot{a}_1}{\Omega}\right)^2+\frac{1}{8}\left(\frac{\dot{b}_1}{\Omega}\right)^2+\frac{C_D}{C_{L\alpha}}\frac{1}{4}\left[\mu_y^2-\mu_x^2\right]
\end{array}\right)\cos 2\psi\\
&+\left(\begin{array}{l}
-\frac{1}{4}\frac{pq\cos\theta_s}{\Omega^2}-\frac{1}{3}\left[\mu_y\frac{q}{\Omega}-\mu_x\frac{p\cos\theta_s}{\Omega}\right]a_0-\left[\frac{1}{2}\mu_y\lambda_{HP}-\frac{1}{4}\frac{q}{\Omega}\right]a_1+\left[\frac{1}{2}\mu_x\lambda_{HP}-\frac{1}{4}\frac{p\cos\theta_s}{\Omega}\right]b_1\\
+\frac{1}{2}\mu_x\mu_y a_0^2+\frac{1}{4}\mu_x\mu_y a_1^2+\frac{1}{4}\mu_x\mu_y b_1^2-\frac{1}{3}\mu_x a_0a_1-\frac{1}{3}\mu_y a_0b_1-\left[\frac{1}{4}\mu_x^2+\frac{1}{4}\mu_y^2-\frac{1}{4}\right]a_1b_1\\
-\frac{1}{4}\frac{p\cos\theta_s}{\Omega^2}\dot{a}_1-\frac{1}{4}\frac{q}{\Omega^2}\dot{b}_1-\frac{1}{3}\mu_y\frac{\dot{a}_1a_0}{\Omega}+\frac{1}{4}\frac{\dot{a}_1a_1}{\Omega}+\frac{1}{3}\mu_x\frac{\dot{b}_1a_0}{\Omega}-\frac{1}{4}\frac{\dot{b}_1b_1}{\Omega}-\frac{1}{4}\frac{\dot{a}_1\dot{b}_1}{\Omega^2}+\frac{C_D}{C_{L\alpha}}\frac{1}{2}\mu_x\mu_y
\end{array}\right)\sin 2\psi\\
&+\left(\begin{array}{l}
-\frac{1}{6}\left[\mu_x\frac{q}{\Omega}+\mu_y\frac{p\cos\theta_s}{\Omega}\right]a_1-\frac{1}{6}\left[\mu_y\frac{q}{\Omega}-\mu_x\frac{p\cos\theta_s}{\Omega}\right]b_1+\frac{1}{6}\mu_y a_1^2-\frac{1}{6}\mu_y b_1^2+\frac{1}{4}\left[\mu_x^2-\mu_y^2\right]a_0a_1\\
+\frac{1}{2}\mu_x\mu_y a_0b_1-\frac{1}{3}\mu_x a_1b_1-\frac{1}{6}\mu_x\frac{\dot{a}_1a_1}{\Omega}-\frac{1}{6}\mu_y\frac{\dot{a}_1b_1}{\Omega}-\frac{1}{6}\mu_y\frac{\dot{b}_1a_1}{\Omega}+\frac{1}{6}\mu_x\frac{\dot{b}_1b_1}{\Omega}
\end{array}\right)\cos 3\psi\\
&+\left(\begin{array}{l}
\frac{1}{6}\left[\mu_y\frac{q}{\Omega}-\mu_x\frac{p\cos\theta_s}{\Omega}\right]a_1-\frac{1}{6}\left[\mu_x\frac{q}{\Omega}+\mu_y\frac{p\cos\theta_s}{\Omega}\right]b_1+\frac{1}{6}\mu_x a_1^2-\frac{1}{6}\mu_x b_1^2-\frac{1}{2}\mu_x\mu_y a_0a_1\\
+\frac{1}{4}\left[\mu_x^2-\mu_y^2\right]a_0b_1+\frac{1}{3}\mu_y a_1b_1+\frac{1}{6}\mu_y\frac{\dot{a}_1a_1}{\Omega}-\frac{1}{6}\mu_x\frac{\dot{a}_1b_1}{\Omega}-\frac{1}{6}\mu_x\frac{\dot{b}_1a_1}{\Omega}-\frac{1}{6}\mu_y\frac{\dot{b}_1b_1}{\Omega}
\end{array}\right)\sin 3\psi\\
&+\left(-\frac{1}{16}\left[\mu_x^2-\mu_y^2\right]a_1^2+\frac{1}{16}\left[\mu_x^2-\mu_y^2\right]b_1^2-\frac{1}{4}\mu_x\mu_y a_1b_1\right)\cos 4\psi\\
&+\left(\frac{1}{8}\mu_x\mu_y a_1^2-\frac{1}{8}\mu_x\mu_y b_1^2-\frac{1}{8}\left[\mu_x^2-\mu_y^2\right]a_1b_1\right)\sin 4\psi
\end{aligned}
$$

As with the aerodynamic loading expressions, the rotor moment terms are transferred to the shaft in the fixed frame. Assuming small flapping angles, this transformation yields:

$$\begin{Bmatrix} M_x(t) \\ M_y(t) \\ M_z(t) \end{Bmatrix}_S = \begin{Bmatrix} -M_P(t)\beta\cos\psi - M_T(t)\sin\psi \\ M_P(t)\beta\sin\psi - M_T(t)\cos\psi \\ M_P(t) \end{Bmatrix} \tag{E.24}$$

The total rotor moment transferred to the shaft is found by summing the individual contributions of the blades. This results in the total instantaneous rotor rolling moment, $M_{X_{HP}}$, about the $\hat{i}_s$ unit vector as a function of time, the total instantaneous rotor pitching moment, $M_{Y_{HP}}$, about the $\hat{j}_s$ unit vector as a function of time, and the total instantaneous rotor torque, Q_{HP}, about the $\hat{k}_s$ unit vector as a function of time. Note that these expressions assume the moment is acting in the positive direction of the basis of unit vectors.

$$\begin{Bmatrix} M_{X_{HP}}(t) \\ M_{Y_{HP}}(t) \\ Q_{HP}(t) \end{Bmatrix} = \sum_{i=1}^{N_b} \begin{Bmatrix} M_x^{(i)} \\ M_y^{(i)} \\ M_z^{(i)} \end{Bmatrix} = \sum_{i=1}^{N_b} \begin{Bmatrix} -M_P^{(i)}\beta^{(i)}\cos\psi^{(i)} - M_T^{(i)}\sin\psi^{(i)} \\ M_P^{(i)}\beta^{(i)}\sin\psi^{(i)} - M_T^{(i)}\cos\psi^{(i)} \\ M_P^{(i)} \end{Bmatrix} \tag{E.25}$$

The moment expressions are expanded into closed-form representation in the following subsections.

E.2.1 Main Rotor Pitching and Rolling Moments

$$M_{X_{HP}}(t) = \sum_{i=1}^{N_b} \left[-M_P^{(i)}\beta^{(i)}\cos\psi^{(i)} - M_T^{(i)}\sin\psi^{(i)} \right] \tag{E.26}$$

$$M_{Y_{HP}}(t) = \sum_{i=1}^{N_b} \left[M_P^{(i)}\beta^{(i)}\sin\psi^{(i)} - M_T^{(i)}\cos\psi^{(i)} \right] \tag{E.27}$$

For a two-bladed teetering rotor, and ignoring higher harmonic contributions, the above expressions both reduce to zero.

$$M_{X_{HP}} = M_{Y_{HP}} = 0 \tag{E.28}$$

E.2.2 Main Rotor Torque

$$Q_{HP}(t) = \sum_{i=1}^{N_b} M_P^{(i)} \tag{E.29}$$

For a two-bladed rotor, the main rotor torque reduces to:

$$Q_{HP}(t) = \frac{1}{2}\rho c C_{L\alpha} R^2 (\Omega R)^2 \left\{ \theta_0 A_{Q_{HP}} + \theta_{TW} B_{Q_{HP}} - A_1 C_{Q_{HP}} - B_1 D_{Q_{HP}} + E_{Q_{HP}} \right\} \tag{E.30}$$

Where:

$$\begin{aligned}
A_{Q_{HP}} &= \left(\frac{2}{3}\lambda_{HP} - \frac{1}{3}\mu_y \frac{q}{\Omega} - \frac{1}{3}\mu_x \frac{p\cos\theta_s}{\Omega} - \frac{1}{3}\mu_y \frac{\dot{a}_1}{\Omega} - \frac{1}{3}\mu_x \frac{\dot{b}_1}{\Omega} \right) \\
&+ \left(\frac{1}{3}\mu_x \frac{p\cos\theta_s}{\Omega} - \frac{1}{3}\mu_y \frac{q}{\Omega} + \mu_x\mu_y a_0 - \frac{2}{3}\mu_x a_1 - \frac{2}{3}\mu_y b_1 - \frac{1}{3}\mu_y \frac{\dot{a}_1}{\Omega} + \frac{1}{3}\mu_x \frac{\dot{b}_1}{\Omega} \right) \cos 2\psi \\
&+ \left(-\frac{1}{3}\mu_x \frac{q}{\Omega} - \frac{1}{3}\mu_y \frac{p\cos\theta_s}{\Omega} + \frac{1}{2}\left[\mu_x^2 - \mu_y^2\right] a_0 + \frac{2}{3}\mu_y a_1 - \frac{2}{3}\mu_x b_1 - \frac{1}{3}\mu_x \frac{\dot{a}_1}{\Omega} - \frac{1}{3}\mu_y \frac{\dot{b}_1}{\Omega} \right) \sin 2\psi
\end{aligned}$$

$$\begin{aligned}
B_{Q_{HP}} &= \left(\frac{1}{2}\lambda_{HP} - \frac{1}{4}\mu_y \frac{q}{\Omega} - \frac{1}{4}\mu_x \frac{p\cos\theta_s}{\Omega} - \frac{1}{4}\mu_y \frac{\dot{a}_1}{\Omega} - \frac{1}{4}\mu_x \frac{\dot{b}_1}{\Omega} \right) \\
&+ \left(\frac{1}{4}\mu_x \frac{p\cos\theta_s}{\Omega} - \frac{1}{4}\mu_y \frac{q}{\Omega} + \frac{2}{3}\mu_x\mu_y a_0 - \frac{1}{2}\mu_x a_1 - \frac{1}{2}\mu_y b_1 - \frac{1}{4}\mu_y \frac{\dot{a}_1}{\Omega} + \frac{1}{4}\mu_x \frac{\dot{b}_1}{\Omega} \right) \cos 2\psi \\
&+ \left(-\frac{1}{4}\mu_x \frac{q}{\Omega} - \frac{1}{4}\mu_y \frac{p\cos\theta_s}{\Omega} + \frac{1}{3}\left[\mu_x^2 - \mu_y^2\right] a_0 + \frac{1}{2}\mu_y a_1 - \frac{1}{2}\mu_x b_1 - \frac{1}{4}\mu_x \frac{\dot{a}_1}{\Omega} - \frac{1}{4}\mu_y \frac{\dot{b}_1}{\Omega} \right) \sin 2\psi
\end{aligned}$$

$$\begin{aligned}
C_{Q_{HP}} &= \left(\frac{1}{2}\mu_y\lambda_{HP} - \frac{1}{4}\frac{q}{\Omega} + \frac{1}{3}\mu_x a_0 - \frac{1}{4}\mu_x\mu_y a_1 - \left[\frac{1}{8}\mu_x^2 - \frac{1}{8}\mu_y^2 + \frac{1}{4} \right] b_1 - \frac{1}{4}\frac{\dot{a}_1}{\Omega} \right) \\
&+ \left(\frac{1}{2}\mu_y\lambda_{HP} - \frac{1}{4}\frac{q}{\Omega} + \frac{1}{3}\mu_x a_0 - \frac{1}{2}\mu_x\mu_y a_1 - \frac{1}{4}b_1 - \frac{1}{4}\frac{\dot{a}_1}{\Omega} \right) \cos 2\psi \\
&+ \left(\frac{1}{2}\mu_x\lambda_{HP} - \frac{1}{4}\frac{p\cos\theta_s}{\Omega} - \frac{1}{3}\mu_y a_0 - \left[\frac{1}{4}\mu_x^2 - \frac{1}{4}\mu_y^2 - \frac{1}{4} \right] a_1 - \frac{1}{4}\frac{\dot{b}_1}{\Omega} \right) \sin 2\psi \\
&+ \left(-\frac{1}{4}\mu_x\mu_y a_1 + \frac{1}{8}\left[\mu_x^2 - \mu_y^2\right] b_1 \right) \cos 4\psi + \left(-\frac{1}{8}\left[\mu_x^2 - \mu_y^2\right] a_1 - \frac{1}{4}\mu_x\mu_y b_1 \right) \sin 4\psi
\end{aligned}$$

$$
\begin{aligned}
D_{Q_{HP}} = & \left(\frac{1}{2}\mu_x\lambda_{HP} - \frac{1}{4}\frac{p\cos\theta_s}{\Omega} - \frac{1}{3}\mu_y a_0 - \left[\frac{1}{8}\mu_x^2 - \frac{1}{8}\mu_y^2 - \frac{1}{4}\right]a_1 + \frac{1}{4}\mu_x\mu_y b_1 - \frac{1}{4}\frac{\dot{b}_1}{\Omega}\right) \\
& + \left(-\frac{1}{2}\mu_x\lambda_{HP} + \frac{1}{4}\frac{p\cos\theta_s}{\Omega} + \frac{1}{3}\mu_y a_0 - \frac{1}{4}a_1 - \frac{1}{2}\mu_x\mu_y b_1 + \frac{1}{4}\frac{\dot{b}_1}{\Omega}\right)\cos 2\psi \\
& + \left(\frac{1}{2}\mu_y\lambda_{HP} - \frac{1}{4}\frac{q}{\Omega} + \frac{1}{3}\mu_x a_0 - \left[\frac{1}{4}\mu_x^2 - \frac{1}{4}\mu_y^2 + \frac{1}{4}\right]b_1 - \frac{1}{4}\frac{\dot{a}_1}{\Omega}\right)\sin 2\psi \\
& + \left(\frac{1}{8}\left[\mu_x^2 - \mu_y^2\right]a_1 + \frac{1}{4}\mu_x\mu_y b_1\right)\cos 4\psi + \left(-\frac{1}{4}\mu_x\mu_y a_1 + \frac{1}{8}\left[\mu_x^2 - \mu_y^2\right]b_1\right)\sin 4\psi
\end{aligned}
$$

$$
\begin{aligned}
E_{Q_{HP}} = & \left(\begin{array}{l}
-\lambda_{HP}^2 - \frac{1}{4}\frac{q^2}{\Omega^2} - \frac{1}{4}\frac{p^2\cos^2\theta_s}{\Omega^2} - \frac{2}{3}\left[\mu_y\frac{p\cos\theta_s}{\Omega} - \mu_x\frac{q}{\Omega}\right]a_0 + \left[\mu_x\lambda_{HP} + \frac{1}{2}\frac{p\cos\theta_s}{\Omega}\right]a_1 - \left[\mu_y\lambda_{HP} + \frac{1}{2}\frac{q}{\Omega}\right]b_1 \\
-\frac{1}{2}\left[\mu_x^2 + \mu_y^2\right]a_0^2 - \left[\frac{3}{8}\mu_x^2 + \frac{1}{8}\mu_y^2 + \frac{1}{4}\right]a_1^2 - \left[\frac{1}{8}\mu_x^2 + \frac{3}{8}\mu_y^2 + \frac{1}{4}\right]b_1^2 + \frac{2}{3}\mu_y a_0 a_1 + \frac{2}{3}\mu_x a_0 b_1 + \frac{1}{2}\mu_x\mu_y a_1 b_1 \\
-\frac{1}{2}\frac{q}{\Omega^2}\dot{a}_1 - \frac{1}{2}\frac{p\cos\theta_s}{\Omega^2}\dot{b}_1 + \frac{2}{3}\mu_x\frac{\dot{a}_1 a_0}{\Omega} - \frac{1}{2}\frac{\dot{a}_1 b_1}{\Omega} - \frac{2}{3}\mu_y\frac{\dot{b}_1 a_0}{\Omega} + \frac{1}{2}\frac{\dot{b}_1 a_1}{\Omega} - \frac{1}{4}\left(\frac{\dot{a}_1}{\Omega}\right)^2 - \frac{1}{4}\left(\frac{\dot{b}_1}{\Omega}\right)^2 \\
+\frac{C_D}{C_{L\alpha}}\left[\frac{1}{2} + \frac{1}{2}\mu_x^2 + \frac{1}{2}\mu_y^2\right]
\end{array}\right) \\
& + \left(\begin{array}{l}
-\frac{1}{4}\left[\left(\frac{q}{\Omega}\right)^2 - \left(\frac{p\cos\theta_s}{\Omega}\right)^2\right] + \frac{2}{3}\left[\mu_x\frac{q}{\Omega} + \mu_y\frac{p\cos\theta_s}{\Omega}\right]a_0 + \left[\mu_x\lambda_{HP} - \frac{1}{2}\frac{p\cos\theta_s}{\Omega}\right]a_1 + \left[\mu_y\lambda_{HP} - \frac{1}{2}\frac{q}{\Omega}\right]b_1 \\
+\frac{1}{2}\left[\mu_y^2 - \mu_x^2\right]a_0^2 - \left[\frac{1}{2}\mu_x^2 - \frac{1}{4}\right]a_1^2 + \left[\frac{1}{2}\mu_y^2 - \frac{1}{4}\right]b_1^2 - \frac{2}{3}\mu_y a_0 a_1 + \frac{2}{3}\mu_x a_0 b_1 - \frac{1}{2}\frac{q}{\Omega^2}\dot{a}_1 + \frac{1}{2}\frac{p\cos\theta_s}{\Omega^2}\dot{b}_1 \\
+\frac{2}{3}\mu_x\frac{\dot{a}_1 a_0}{\Omega} - \frac{1}{2}\frac{\dot{a}_1 b_1}{\Omega} + \frac{2}{3}\mu_y\frac{\dot{b}_1 a_0}{\Omega} - \frac{1}{2}\frac{\dot{b}_1 a_1}{\Omega} - \frac{1}{4}\left(\frac{\dot{a}_1}{\Omega}\right)^2 + \frac{1}{4}\left(\frac{\dot{b}_1}{\Omega}\right)^2 + \frac{C_D}{C_{L\alpha}}\frac{1}{2}\left[\mu_y^2 - \mu_x^2\right]
\end{array}\right)\cos 2\psi \\
& + \left(\begin{array}{l}
-\frac{1}{2}\frac{pq\cos\theta_s}{\Omega^2} - \frac{2}{3}\left[\mu_y\frac{q}{\Omega} - \mu_x\frac{p\cos\theta_s}{\Omega}\right]a_0 - \left[\mu_y\lambda_{HP} - \frac{1}{2}\frac{q}{\Omega}\right]a_1 + \left[\mu_x\lambda_{HP} - \frac{1}{2}\frac{p\cos\theta_s}{\Omega}\right]b_1 \\
+\mu_x\mu_y a_0^2 + \frac{1}{2}\mu_x\mu_y a_1^2 + \frac{1}{2}\mu_x\mu_y b_1^2 - \frac{2}{3}\mu_x a_0 a_1 - \frac{2}{3}\mu_y a_0 b_1 - \left[\frac{1}{2}\mu_x^2 + \frac{1}{2}\mu_y^2 - \frac{1}{2}\right]a_1 b_1 \\
-\frac{1}{2}\frac{p\cos\theta_s}{\Omega^2}\dot{a}_1 - \frac{1}{2}\frac{q}{\Omega^2}\dot{b}_1 - \frac{2}{3}\mu_y\frac{\dot{a}_1 a_0}{\Omega} + \frac{1}{2}\frac{\dot{a}_1 a_1}{\Omega} + \frac{2}{3}\mu_x\frac{\dot{b}_1 a_0}{\Omega} - \frac{1}{2}\frac{\dot{b}_1 b_1}{\Omega} - \frac{1}{2}\frac{\dot{a}_1\dot{b}_1}{\Omega^2} + \frac{C_D}{C_{L\alpha}}\mu_x\mu_y
\end{array}\right)\sin 2\psi \\
& + \left(-\frac{1}{8}\left[\mu_x^2 - \mu_y^2\right]a_1^2 + \frac{1}{8}\left[\mu_x^2 - \mu_y^2\right]b_1^2 - \frac{1}{2}\mu_x\mu_y a_1 b_1\right)\cos 4\psi \\
& + \left(\frac{1}{4}\mu_x\mu_y a_1^2 - \frac{1}{4}\mu_x\mu_y b_1^2 - \frac{1}{4}\left[\mu_x^2 - \mu_y^2\right]a_1 b_1\right)\sin 4\psi
\end{aligned}
$$

If higher harmonics are neglected, then for longitudinal flight:

$$
A_{Q_{HP}} = \left(\frac{2}{3}\lambda_{HP} - \frac{1}{3}\mu_x\frac{\dot{b}_1}{\Omega}\right)
$$

$$
B_{Q_{HP}} = \left(\frac{1}{2}\lambda_{HP} - \frac{1}{4}\mu_x\frac{\dot{b}_1}{\Omega}\right)
$$

$$
C_{Q_{HP}} = \left(-\frac{1}{4}\frac{q}{\Omega} + \frac{1}{3}\mu_x a_0 - \left[\frac{1}{8}\mu_x^2 + \frac{1}{4}\right]b_1 - \frac{1}{4}\frac{\dot{a}_1}{\Omega}\right)
$$

$$D_{Q_{HP}} = \left(\frac{1}{2}\mu_x \lambda_{HP} - \left[\frac{1}{8}\mu_x^2 - \frac{1}{4} \right] a_1 - \frac{1}{4}\frac{\dot{b}_1}{\Omega} \right)$$

$$E_{Q_{HP}} = \begin{pmatrix} -\lambda_{HP}^2 - \frac{1}{4}\frac{q^2}{\Omega^2} + \frac{2}{3}\mu_x \frac{q}{\Omega} a_0 + \mu_x \lambda_{HP} a_1 - \frac{1}{2}\frac{q}{\Omega} b_1 - \frac{1}{2}\mu_x^2 a_0^2 - \left[\frac{3}{8}\mu_x^2 + \frac{1}{4} \right] a_1^2 - \left[\frac{1}{8}\mu_x^2 + \frac{1}{4} \right] b_1^2 + \frac{2}{3}\mu_x a_0 b_1 \\ -\frac{1}{2}\frac{q}{\Omega^2}\dot{a}_1 + \frac{2}{3}\mu_x \frac{\dot{a}_1 a_0}{\Omega} - \frac{1}{2}\frac{\dot{a}_1 b_1}{\Omega} + \frac{1}{2}\frac{\dot{b}_1 a_1}{\Omega} - \frac{1}{4}\left(\frac{\dot{a}_1}{\Omega} \right)^2 - \frac{1}{4}\left(\frac{\dot{b}_1}{\Omega} \right)^2 + \frac{C_D}{C_{L\alpha}} \left[\frac{1}{2} + \frac{1}{2}\mu_x^2 \right] \end{pmatrix}$$

Appendix F Main Rotor Equations of Motion (Flapping Expression)

In this section the main rotor flapping equation is expanded into its closed-form representation.

The main rotor flapping expression is found by summing the flapping moment of the aerodynamic and inertial terms of all of the blades about the flapping axis of the reference blade.

$$\sum_{i=1}^{N_b}\left[\left(M_T^{(i)}-M_I^{(i)}\right)\cos\left(\frac{2\pi}{N_b}\left[i-1\right]\right)\right]=0 \tag{F.1}$$

The aerodynamic flapping moment about the flapping axis, $M_T^{(i)}$, was derived in Appendix E whereas the inertial moment is found from the acceleration expression for an element on the elastic axis derived in Appendix C.

$$M_I=-\int_0^R ma_P r dr \tag{F.2}$$

Where:

$$a_P=a_{z,s}+\left(\dot{q}r+2pr\Omega\cos\theta_s\right)\cos\psi+\left(\dot{p}r\cos\theta_s-2qr\Omega\right)\sin\psi-r\ddot{\beta}-r\Omega^2\beta \tag{F.3}$$

If the flapping expression is assumed to have the form:

$$\beta=a_0-a_1\cos\psi-b_1\sin\psi \tag{F.4}$$

With first and second time derivatives:

$$\dot{\beta}=-\left(\dot{a}_1+\Omega b_1\right)\cos\psi-\left(\dot{b}_1-\Omega a_1\right)\cos\psi \tag{F.5}$$

$$\ddot{\beta}=-\left(\ddot{a}_1+2\Omega\dot{b}_1-\Omega^2 a_1\right)\cos\psi-\left(\ddot{b}_1-2\Omega\dot{a}_1-\Omega^2 b_1\right)\cos\psi \tag{F.6}$$

Then expanding the inertial moment integral yields:

$$M_I = I_\beta \Omega^2 a_0 - S_\beta a_{z,s} - I_\beta \left(\ddot{a}_1 + 2\Omega \dot{b}_1 + \dot{q} + 2p\Omega \cos\theta_s \right) \cos\psi$$
$$- I_\beta \left(\ddot{b}_1 - 2\Omega \dot{a}_1 + \dot{p} \cos\theta_s - 2\Omega q \right) \sin\psi \tag{F.7}$$

For a two-bladed teetering rotor with rigid blades, substituting (F.7) into (F.1) generates the following expression for flapping:

$$0 = \theta_0 A_\beta + \theta_{TW} B_\beta - A_1 C_\beta - B_1 D_\beta + E_\beta \tag{F.8}$$

Where

$$A_\beta = \frac{\gamma}{3} \Omega^2 \mu_y \cos\psi + \frac{\gamma}{3} \Omega^2 \mu_x \sin\psi$$

$$B_\beta = \frac{\gamma}{4} \Omega^2 \mu_y \cos\psi + \frac{\gamma}{4} \Omega^2 \mu_x \sin\psi$$

$$C_\beta = \gamma\Omega^2 \left(\frac{1}{8} + \frac{1}{16}\mu_x^2 + \frac{3}{16}\mu_y^2 \right) \cos\psi + \frac{\gamma}{8} \Omega^2 \mu_x \mu_y \sin\psi + \frac{\gamma}{16} \Omega^2 \left(\mu_y^2 - \mu_x^2 \right) \cos 3\psi + \frac{\gamma}{8} \Omega^2 \mu_x \mu_y \sin 3\psi$$

$$D_\beta = \frac{\gamma}{8} \Omega^2 \mu_x \mu_y \cos\psi + \gamma\Omega^2 \left(\frac{1}{8} + \frac{3}{16}\mu_x^2 + \frac{1}{16}\mu_y^2 \right) \sin\psi - \frac{\gamma}{8} \Omega^2 \mu_x \mu_y \cos 3\psi + \frac{\gamma}{16} \Omega^2 \left(\mu_y^2 - \mu_x^2 \right) \sin 3\psi$$

$$E_\beta = \begin{pmatrix} -\frac{\gamma}{4} \Omega^2 \mu_y \lambda_{HP} + \frac{\gamma}{8} \Omega q + \dot{q} + 2\Omega p \cos\theta_s + \ddot{a}_1 + \frac{\gamma}{8} \Omega \dot{a}_1 + 2\Omega \dot{b}_1 - \frac{\gamma}{6} \Omega^2 \mu_x a_0 \\ + \frac{\gamma}{8} \Omega^2 \mu_x \mu_y a_1 + \gamma\Omega^2 \left[\frac{1}{16}\mu_x^2 - \frac{1}{16}\mu_y^2 + \frac{1}{8} \right] b_1 \end{pmatrix} \cos\psi$$
$$+ \begin{pmatrix} -\frac{\gamma}{4} \Omega^2 \mu_x \lambda_{HP} + \frac{\gamma}{8} \Omega p \cos\theta_s + \dot{p} \cos\theta_s - 2\Omega q + \ddot{b}_1 - 2\Omega \dot{a}_1 + \frac{\gamma}{8} \Omega \dot{b}_1 + \frac{\gamma}{6} \Omega^2 \mu_y a_0 \\ + \gamma\Omega^2 \left[\frac{1}{16}\mu_x^2 - \frac{1}{16}\mu_y^2 - \frac{1}{8} \right] a_1 - \frac{\gamma}{8} \Omega^2 \mu_x \mu_y b_1 \end{pmatrix} \sin\psi$$
$$+ \left(\frac{\gamma}{8} \Omega^2 \mu_x \mu_y a_1 - \frac{\gamma}{16} \Omega^2 \left[\mu_x^2 - \mu_y^2 \right] b_1 \right) \cos 3\psi$$
$$+ \left(\frac{\gamma}{16} \Omega^2 \left[\mu_x^2 - \mu_y^2 \right] a_1 + \frac{\gamma}{8} \Omega^2 \mu_x \mu_y b_1 \right) \sin 3\psi$$

$$\gamma = \frac{\rho C_{L\alpha} c R^4}{I_\beta}$$

The time-varying flapping coefficients, a_1 and b_1, are found by equating the sine and cosine terms from the flapping expression and solving the resulting system of second order differential equations:

$$\mathbf{M}_\beta \begin{Bmatrix} \ddot{a}_1 \\ \ddot{b}_1 \end{Bmatrix} + \mathbf{D}_\beta \begin{Bmatrix} \dot{a}_1 \\ \dot{b}_1 \end{Bmatrix} + \mathbf{K}_\beta \begin{Bmatrix} a_0 \\ a_1 \\ b_1 \end{Bmatrix} = \overrightarrow{f_\beta} \tag{F.9}$$

Where:

$$\mathbf{M}_\beta = \begin{bmatrix} 1 & 0 \\ 0 & 1 \end{bmatrix}$$

$$\mathbf{D}_\beta = \Omega \begin{bmatrix} \frac{\gamma}{8} & 2 \\ -2 & \frac{\gamma}{8} \end{bmatrix}$$

$$\mathbf{K}_\beta = \Omega^2 \begin{bmatrix} -\frac{\gamma}{6}\mu_x & \frac{\gamma}{8}\mu_x\mu_y & \gamma\left[\frac{1}{16}\mu_x^2 - \frac{1}{16}\mu_y^2 + \frac{1}{8}\right] \\ \frac{\gamma}{6}\mu_y & \gamma\left[\frac{1}{16}\mu_x^2 - \frac{1}{16}\mu_y^2 - \frac{1}{8}\right] & -\frac{\gamma}{8}\mu_x\mu_y \end{bmatrix}$$

$$\overrightarrow{f_\beta} = \Omega^2 \begin{Bmatrix} \frac{\gamma}{4}\mu_y\lambda_{HP} - \frac{\gamma}{8}\frac{q}{\Omega} - \frac{\dot{q}}{\Omega^2} - 2\frac{p\cos\theta_s}{\Omega} - \frac{\gamma}{3}\mu_y\theta_0 - \frac{\gamma}{4}\mu_y\theta_{TW} + \gamma\left[\frac{1}{8} + \frac{1}{16}\mu_x^2 + \frac{3}{16}\mu_y^2\right]A_1 + \frac{\gamma}{8}\mu_x\mu_y B_1 \\ \frac{\gamma}{4}\mu_x\lambda_{HP} - \frac{\gamma}{8}\frac{p\cos\theta_s}{\Omega} - \frac{\dot{p}\cos\theta_s}{\Omega^2} + 2\frac{q}{\Omega} - \frac{\gamma}{3}\mu_x\theta_0 - \frac{\gamma}{4}\mu_x\theta_{TW} + \frac{\gamma}{8}\mu_x\mu_y A_1 + \gamma\left[\frac{1}{8} + \frac{3}{16}\mu_x^2 + \frac{1}{16}\mu_y^2\right]B_1 \end{Bmatrix}$$

The aircraft angular acceleration terms $\dot{p}$ and $\dot{q}$ are generally small for first harmonic flapping and may be omitted [40]. In the case of purely longitudinal flight, where $\mu_y = p = 0$, the coefficient matrices in the flapping equation reduce to:

$$\mathbf{M}_\beta = \begin{bmatrix} 1 & 0 \\ 0 & 1 \end{bmatrix}$$

$$\mathbf{D}_\beta = \Omega \begin{bmatrix} \frac{\gamma}{8} & 2 \\ -2 & \frac{\gamma}{8} \end{bmatrix}$$

$$\mathbf{K}_\beta = \Omega^2 \begin{bmatrix} -\frac{\gamma}{6}\mu_x & 0 & \frac{\gamma}{8}\left[1 + \frac{1}{2}\mu_x^2\right] \\ 0 & -\frac{\gamma}{8}\left[1 - \frac{1}{2}\mu_x^2\right] & 0 \end{bmatrix}$$

$$\overrightarrow{f_\beta} = \Omega^2 \begin{Bmatrix} -\frac{\gamma}{8}\frac{q}{\Omega} + \frac{\gamma}{8}\left[1+\frac{1}{2}\mu_x^2\right]A_1 \\ \frac{\gamma}{4}\mu_x\lambda_{HP} + 2\frac{q}{\Omega} - \frac{\gamma}{3}\mu_x\theta_0 - \frac{\gamma}{4}\mu_x\theta_{TW} + \frac{\gamma}{8}\left[1+\frac{3}{2}\mu_x^2\right]B_1 \end{Bmatrix}$$

A reduced order model for flapping can be derived by ignoring the inertial forces from the blade and setting the flapping acceleration terms to zero $\left(\ddot{a}_1 = \ddot{b}_1 = 0\right)$ [40]. Solving the flapping equation for the first derivative flapping terms yields the following set of first order differential equations for flapping:

$$\dot{a}_1 = \frac{\Omega\gamma\begin{bmatrix} \frac{4\gamma}{3}\mu_x a_0 - 16\left(1-\frac{1}{2}\mu_x^2\right)a_1 - \gamma\left(1+\frac{1}{2}\mu_x^2\right)b_1 + \frac{128}{3}\mu_x\theta_0 \\ +\gamma\left(1+\frac{1}{2}\mu_x^2\right)A_1 - 16\left(1+\frac{3}{2}\mu_x^2\right)B_1 + 32\mu_x\theta_{TW} - 32\mu_x\lambda_{HP} \end{bmatrix}}{\gamma^2+256} - q \qquad \text{(F.10)}$$

$$\dot{b}_1 = \frac{\Omega\gamma\begin{bmatrix} \frac{64}{3}\mu_x a_0 + \gamma\left(1-\frac{1}{2}\mu_x^2\right)a_1 - 16\left(1+\frac{1}{2}\mu_x^2\right)b_1 - \frac{8\gamma}{3}\mu_x\theta_0 \\ +16\left(1+\frac{1}{2}\mu_x^2\right)A_1 + \gamma\left(1+\frac{3}{2}\mu_x^2\right)B_1 - 2\gamma\mu_x\theta_{TW} + 2\gamma\mu_x\lambda_{HP} \end{bmatrix}}{\gamma^2+256} \qquad \text{(F.11)}$$

A quasi-steady model for flapping can be derived by assuming an instantaneous balance of aerodynamic and centrifugal loads and setting the flapping acceleration and velocity terms to zero $\left(\ddot{a}_1 = \dot{a}_1 = \ddot{b}_1 = \dot{b}_1 = 0\right)$. Solving for the longitudinal and lateral flapping coefficients yields:

$$a_1 = \frac{\frac{8}{3}\mu_x\theta_0 + 2\mu_x\theta_{TW} - \left(1+\frac{3}{2}\mu_x^2\right)B_1 - 2\mu_x\lambda_{HP} - \frac{16}{\gamma}\frac{q}{\Omega}}{\left(1-\frac{1}{2}\mu_x^2\right)} \qquad \text{(F.12)}$$

$$b_1 = \frac{\frac{4}{3}\left(\mu_x a_0 + \frac{3}{4}\left(1+\frac{1}{2}\mu_x^2\right)A_1\right) - \frac{q}{\Omega}}{\left(1+\frac{1}{2}\mu_x^2\right)} \tag{F.13}$$

The dynamic response of the tip-path plane under a 1° step input in collective and longitudinal cyclic are shown in Figure F.1 and Figure F.2 respectively for the Bell 206B-3 traveling at $\mu = 0.20$. For reference, the responses of the reduced order model and the quasi-steady model are also provided. The longitudinal and lateral responses curves indicate the deviation of the flapping coefficients from their initial values. These plots also include reference lines for determining the settling time of the system. The settling time criteria require that the amplitudes of the oscillations be within 5% of the final quasi-steady value.

For the applied step function, the longitudinal flapping settles within 1.4 rotor revolutions; the lateral flapping settles within 2.4 revolutions. However, under both input perturbations, the overall flapping response of the tip-path plane is largely driven by the response of the longitudinal flapping coefficient.

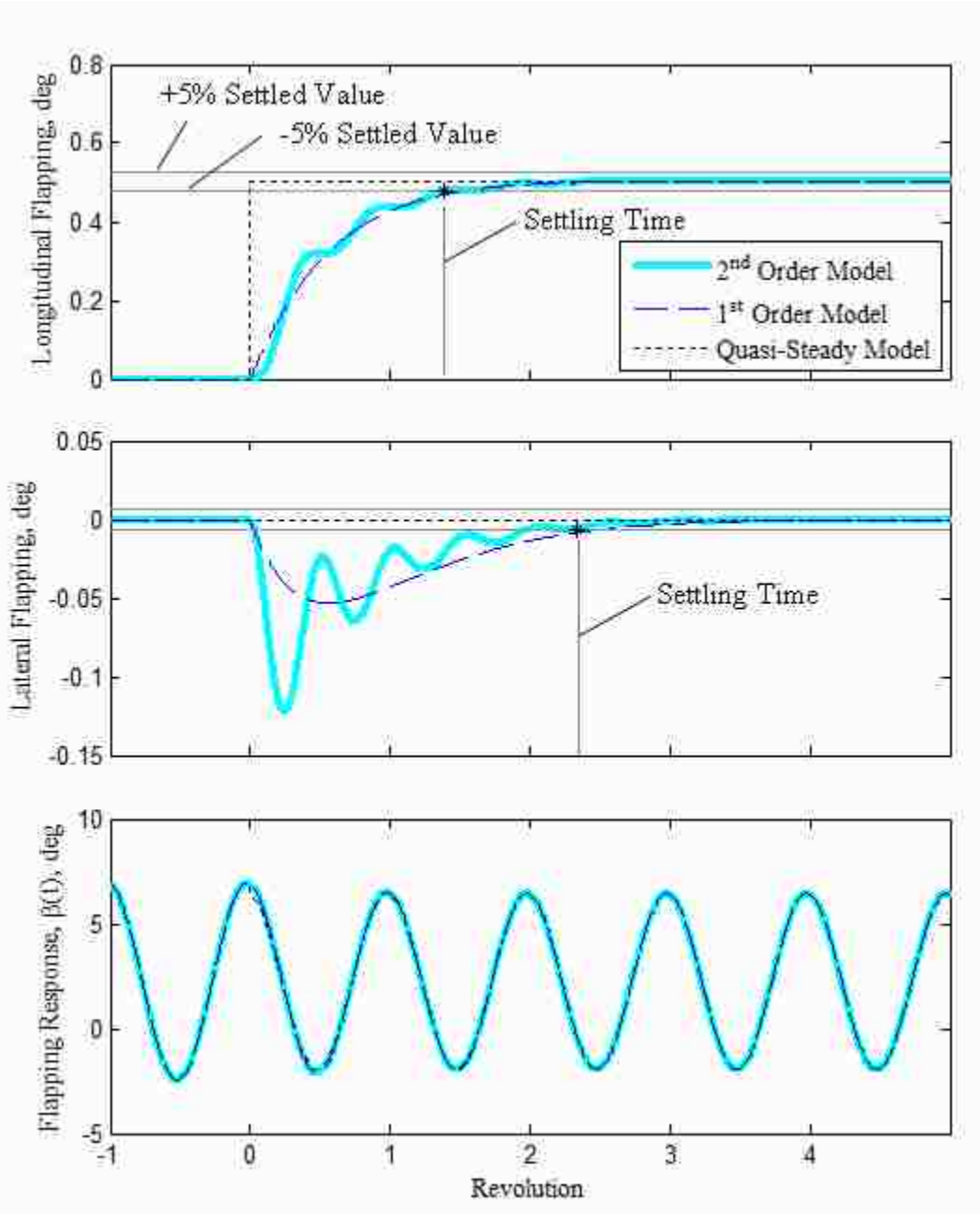

Figure F.1. Tip-path plane dynamic response to a 1° step input in collective applied at revolution #0 (Bell 206B-3 at $\mu = 0.20$). Lateral and longitudinal flapping values are measured relative to their initial conditions.

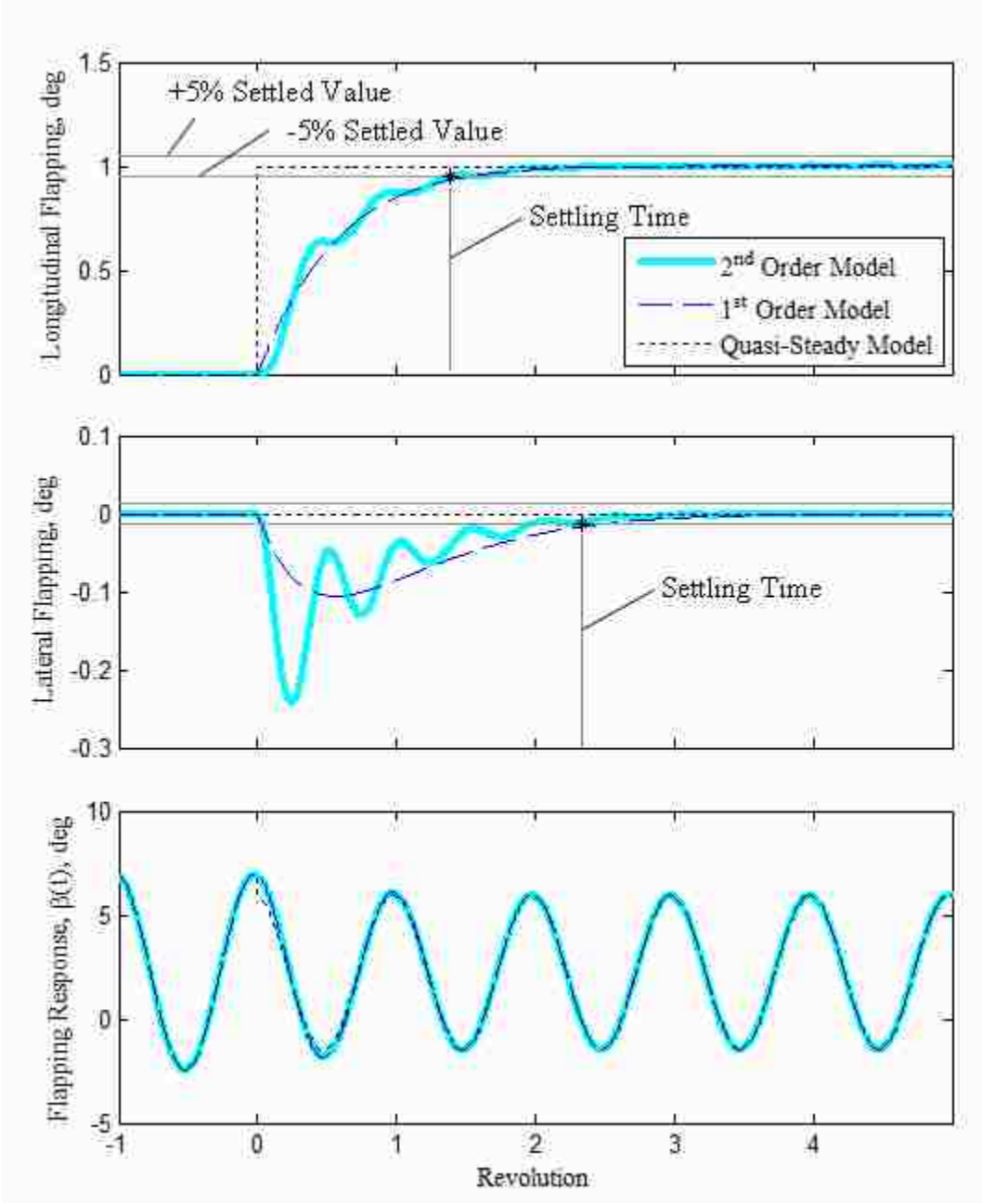

Figure F.2. Tip-path plane dynamic response to a 1° step input in longitudinal cyclic applied at revolution #0 (Bell 206B-3 at $\mu = 0.20$). Lateral and longitudinal flapping values are measured relative to their initial conditions.

Appendix G Analysis of the Acoustic Source Terms

In Chapter 5, the far field expression for thickness noise was separated into two terms. The first term features the time rate of change of the velocity normal to the blade surface; the second term features the time rate of change of the Mach number of the acoustic surface. These are repeated below as equations (G.1) and (G.2) respectively.

$$\text{Thickness Noise Term 1} = \frac{1}{4\pi}\int_{S}\frac{\rho_0\dfrac{\partial v_n}{\partial\tau}}{r\left(1-M_r\right)^2}dS \tag{G.1}$$

$$\text{Thickness Noise Term 2} = \frac{1}{4\pi}\int_{S}\frac{\rho_0 v_n\left(\hat{r}\bullet\dfrac{\partial\overrightarrow{M}}{\partial\tau}\right)}{r\left(1-M_r\right)^3}dS \tag{G.2}$$

Similarly, the far field expression for loading noise was separated into two terms. The first term features the time rate of change of the pressure on the surface; the second term features the time rate of change of the Mach number of the acoustic surface. These are repeated below as equations (G.3) and (G.4) respectively.

$$\text{Loading Noise Term 1} = \frac{1}{4\pi c}\int_{S}\frac{\dfrac{\partial p}{\partial\tau}\cos\theta}{r\left(1-M_r\right)^2}dS \tag{G.3}$$

$$\text{Loading Noise Term 2} = \frac{1}{4\pi c}\int_{S}\frac{p\cos\theta\left(\hat{r}\bullet\dfrac{\partial\overrightarrow{M}}{\partial\tau}\right)}{r\left(1-M_r\right)^3}dS \tag{G.4}$$

Separating the terms in this manner is done to show common features between the two acoustic source expressions. In both expressions, the first term deals with the time

rate of change of a property specific to the type of acoustic source being modeled. In the case of thickness noise, the first term represents unsteadiness in the monopole. In the case of loading noise, the first term represents unsteadiness in the dipole. Note also that the first terms in the thickness noise and loading noise expressions are proportional to the square of the Doppler amplification, where the Doppler amplification is defined as:

$$\text{Doppler Amplification} = \frac{1}{\left(1 - M_r\right)} \tag{G.5}$$

Similarities are also observed in the second terms for thickness and loading noise. Both expressions feature the source property multiplied by a common factor. This factor acts as a fading property applied to the acoustic source. Also note that the second terms in both expressions are proportional to the cube of the Doppler amplification.

To better understand the contributions of each term, the individual components will be analyzed independently. First, the common terms will be studied, then the source-specific quantities.

Consider first the Doppler amplification factors. The relative Mach number, M_r, is maximum when the velocity vector of the source is parallel with the radiation vector from the source to the observer. For an observer directly ahead of the rotor, the maximum relative Mach number occurs near the 90° azimuth station on the advancing side of the rotor. As the relative Mach number approaches Mach 1, the amplification becomes increasingly high. The amplification is stronger in the second term of each acoustic expression because the Doppler amplification is raised one power higher. These trends are illustrated in Figure G.1. The top contour plots show the distribution of each amplification term across the entire rotor disk. The bottom plot traces the magnitudes over one revolution at various radial stations along the blade. Note that the amplification

expression in the second term is much larger than the expression appearing in the first term.

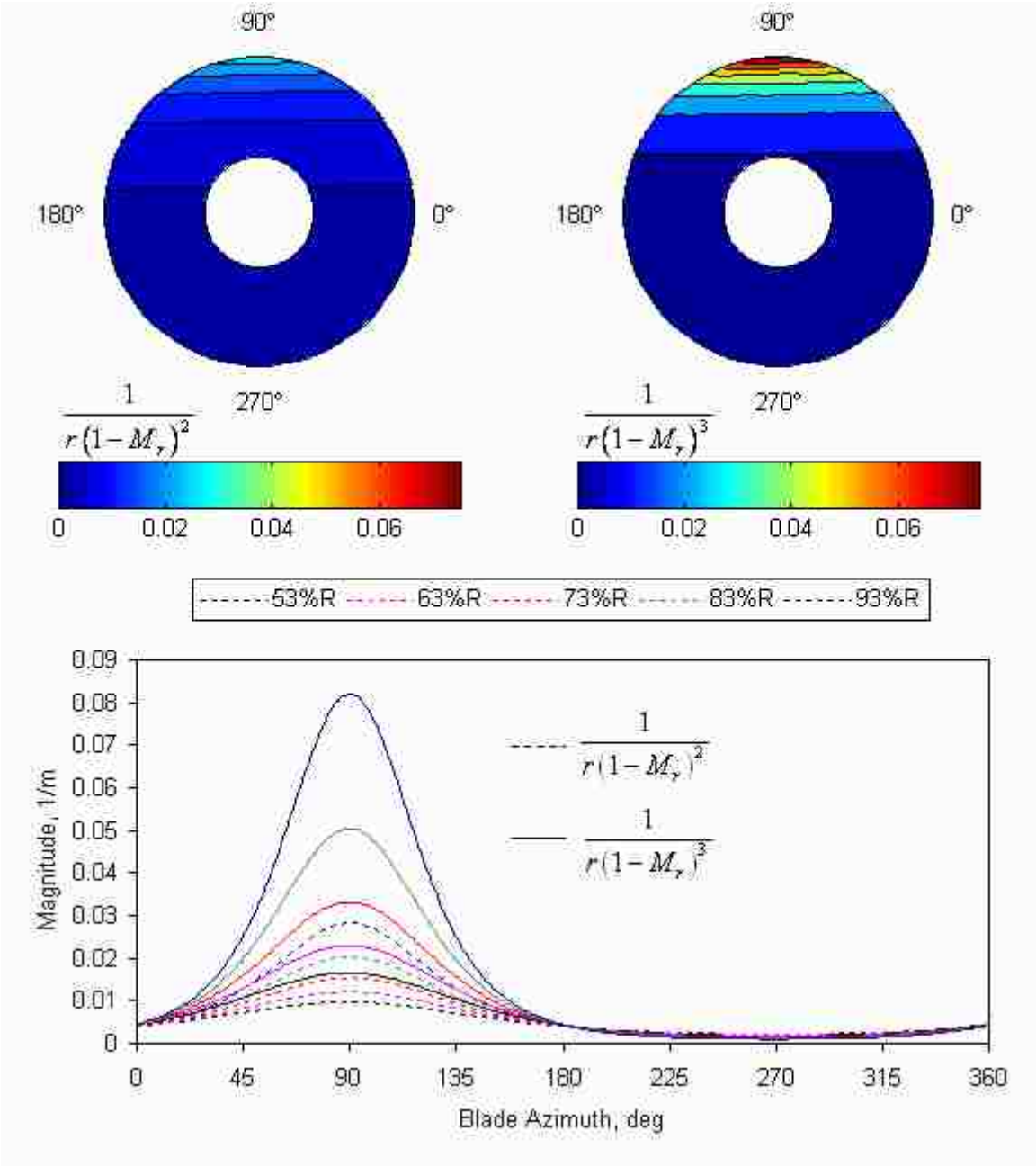

Figure G.1. Denominator magnitude.

Next consider the common numerator quantity that appears in the second terms of both noise source expressions:

$$\hat{r} \bullet \frac{\partial \vec{M}}{\partial \tau} \tag{G.6}$$

The contour and time history plots for this term are illustrated in Figure G.2 for an observer directly ahead of the main rotor. Note that the term is maximum at the 0° azimuth station, is minimum at the 180° station, and is near zero at the 90° and 270° stations. This product will effectively apply a once-per-revolution fade.

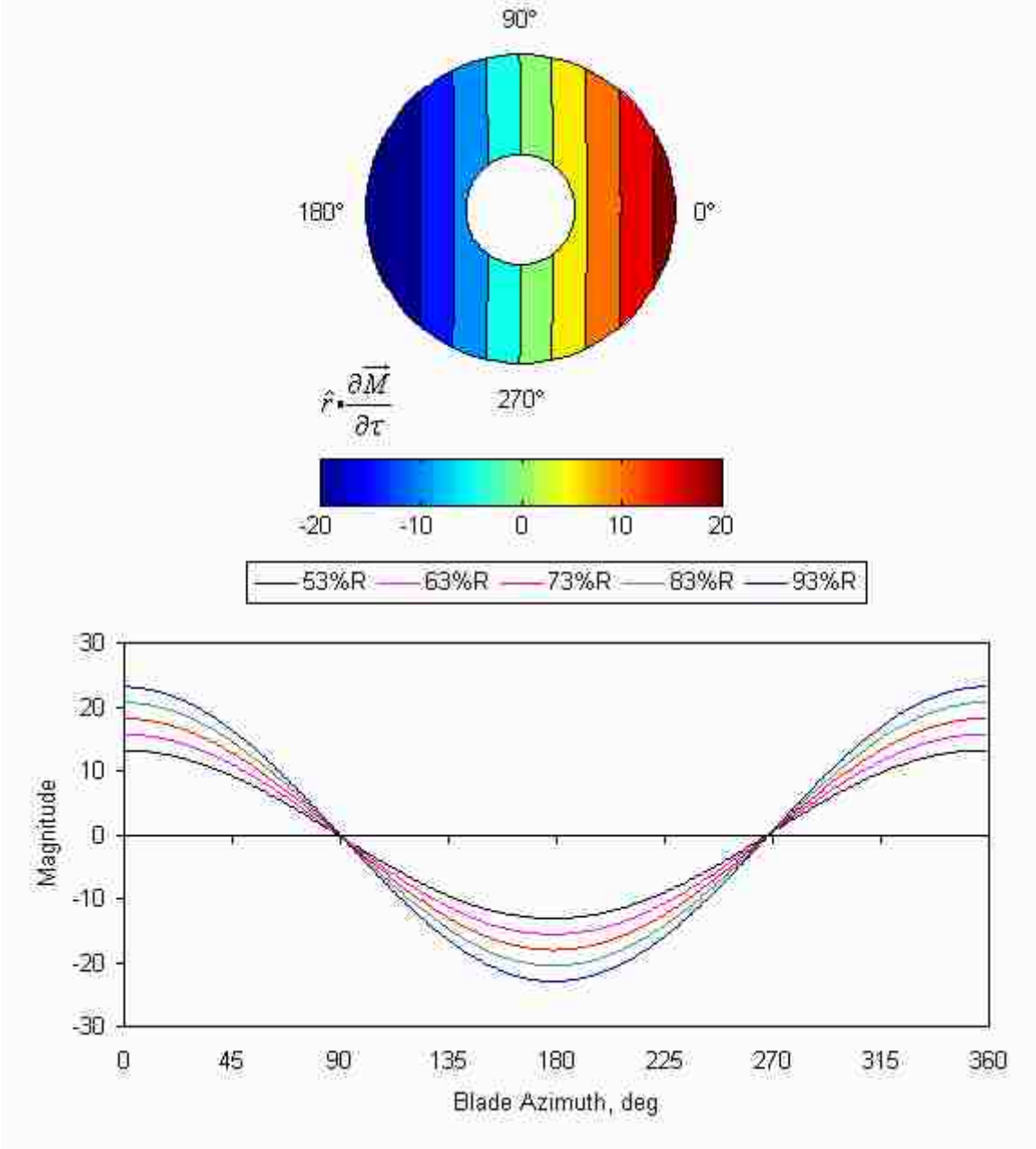

Figure G.2. Magnitude of Mach number time derivative dot product.

Lastly, Figure G.3 illustrates the combined effect of the common quantities present in both expressions of the second acoustic term:

$$\frac{\left(\hat{r} \bullet \frac{\partial \vec{M}}{\partial \tau}\right)}{r\left(1 - M_r\right)^3} \tag{G.7}$$

For observers directly ahead of the rotor, the combination of these terms serves to highlight acoustic sources that are on the advancing side of the rotor, where the relative Mach number is at a maximum, and dampens acoustic sources on the retreating side. In the case of thickness noise, the phasing of this factor will control how the monopoles combine to produce thickness noise. In the case of loading noise, the phasing of this factor illustrates what portions of the rotor disk loading will contribute the most to loading noise. In the case of an observer ahead of the rotor, the region on the advancing side of the rotor near the blade tips will be of significant influence.

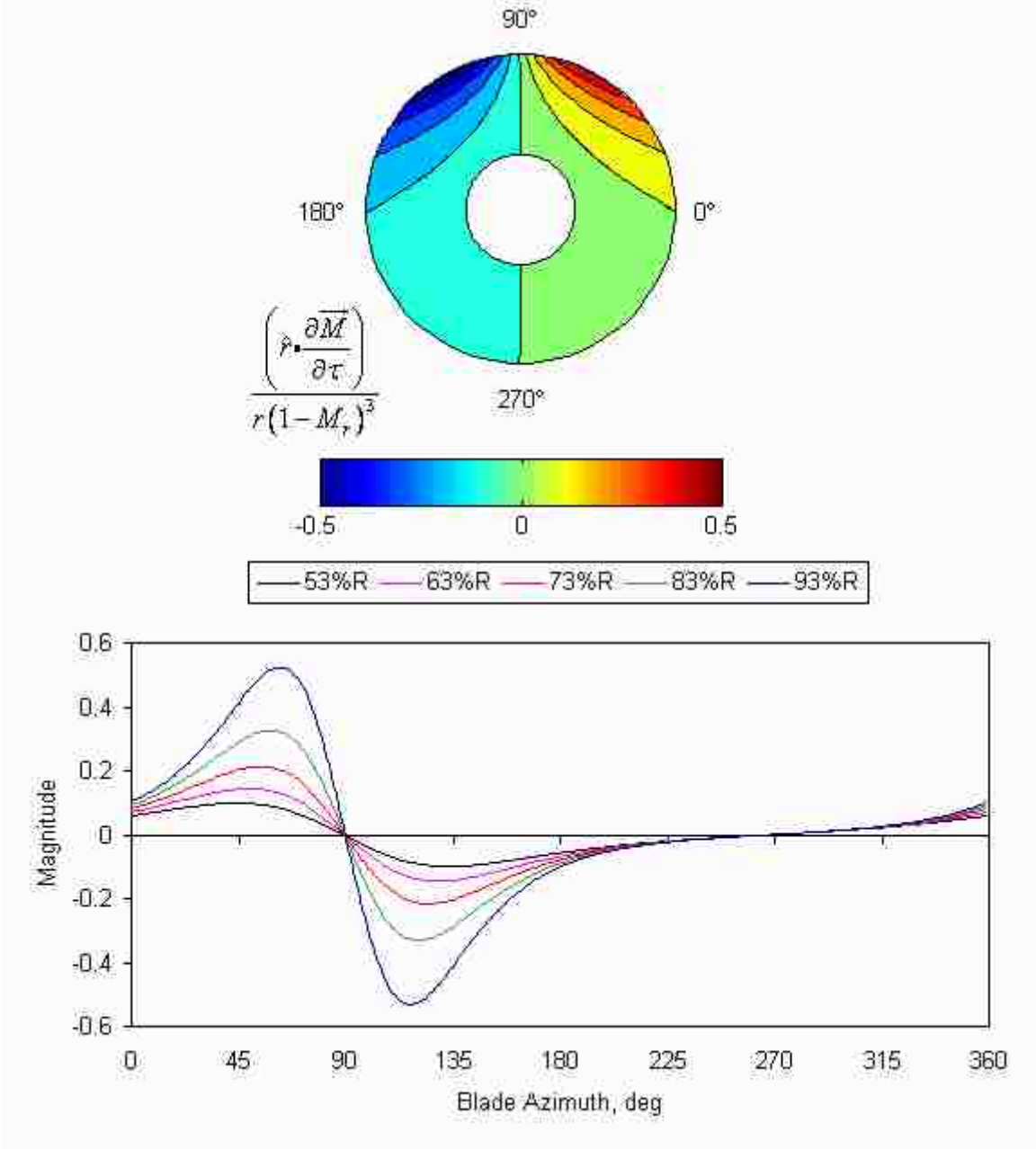

Figure G.3. Distribution of expressions common to term 2.

Next, consider the source terms specific to thickness noise. These include the velocity normal to the surface, and the time derivative of the velocity normal to the surface. Their respective distributions over the tip-path plane are illustrated in Figure G.4 for a series of sources on the leading edge of the airfoil. Notice that the normal velocity

profiles for each radial station are similar in shape, but include an offset due to the radial velocity of the main rotor. This results in nearly identical time derivatives of the velocities normal to the surface.

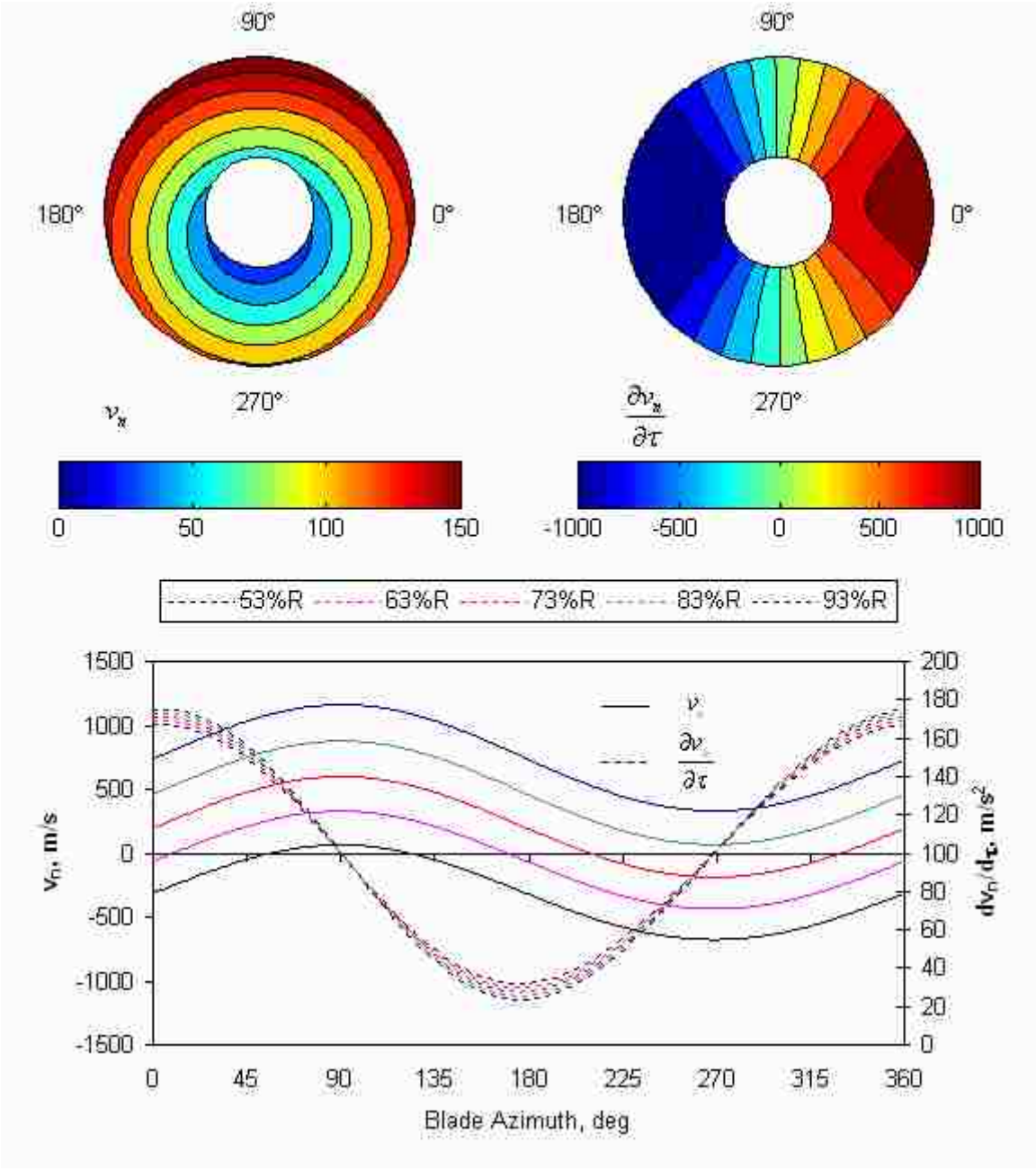

Figure G.4. Thickness noise specific distributions.

While that the magnitudes of the time derivatives are quite large, the remaining quantities in the first term of the thickness noise expression are quite small. Therefore, the thickness noise pulse shapes and amplitudes are mostly defined by the second term in the thickness noise expression.

Lastly, consider the terms specific to the loading noise expressions. These include the load distribution relative to the observer, and the time rate of change of the load distribution. The relative loading distribution is shown in Figure G.5. The surface pressures have been integrated over the blade segment to produce a compact load. This distribution plot indicates that the uniform inflow predicts lower loads over the forward half of the rotor and the load time histories tend to lag behind those associated with the Beddoes' inflow distribution. This phase difference will produce a slight phasing difference in the second term of the loading noise expression.

The time rate of change of the loading distribution is shown in Figure G.6. Note that the time derivatives of the loading distributions have noticeable differences. In the aft region of the tip-path plane, the uniform inflow distribution lags significantly behind the Beddoes' model. This lag is most notable approaching the 90° azimuth station where the relative Mach number and Doppler amplification are maximum. Therefore the loading distribution discrepancies are expected to alter the loading noise pulse shapes.

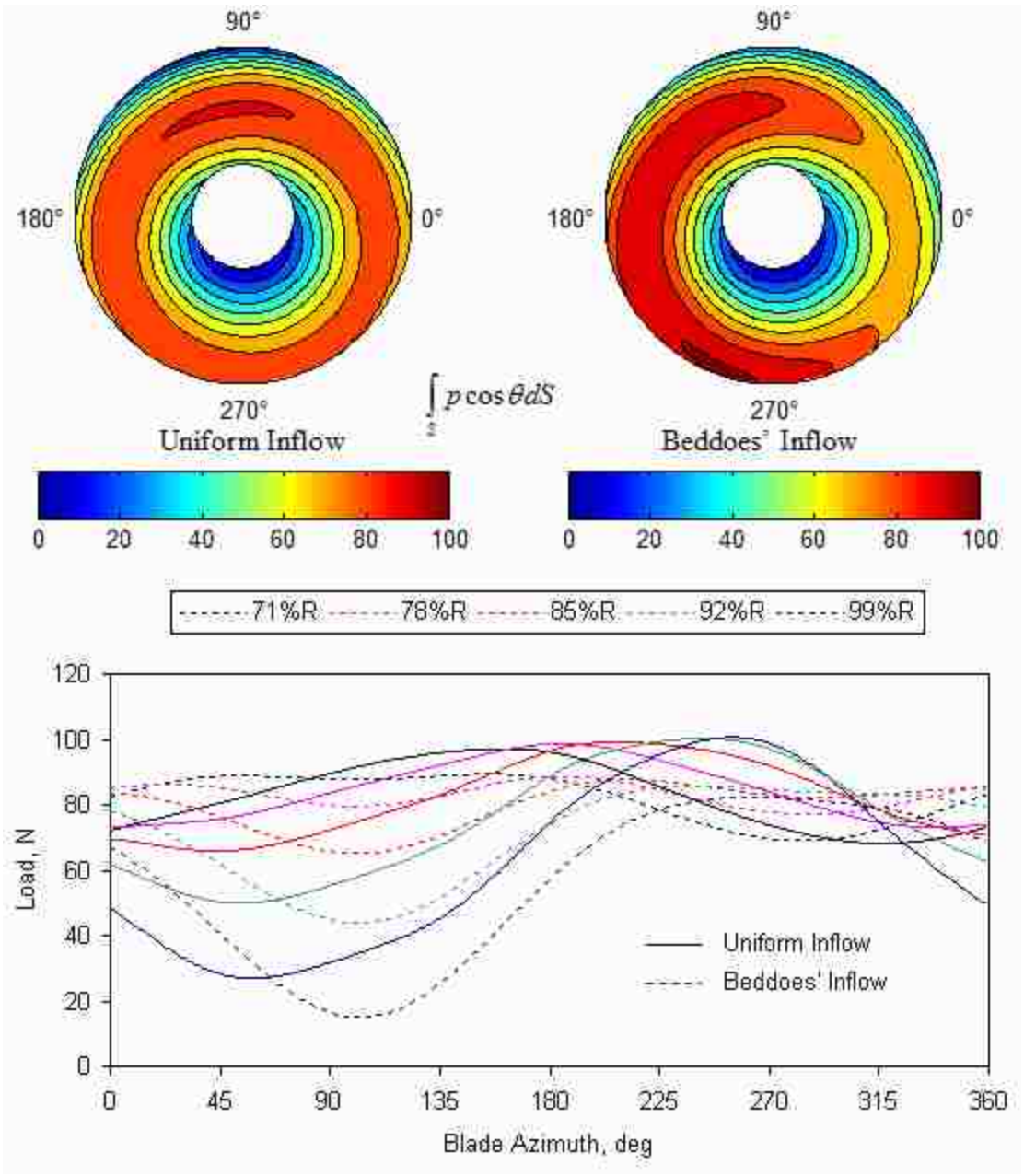

Figure G.5. Distribution of the load.

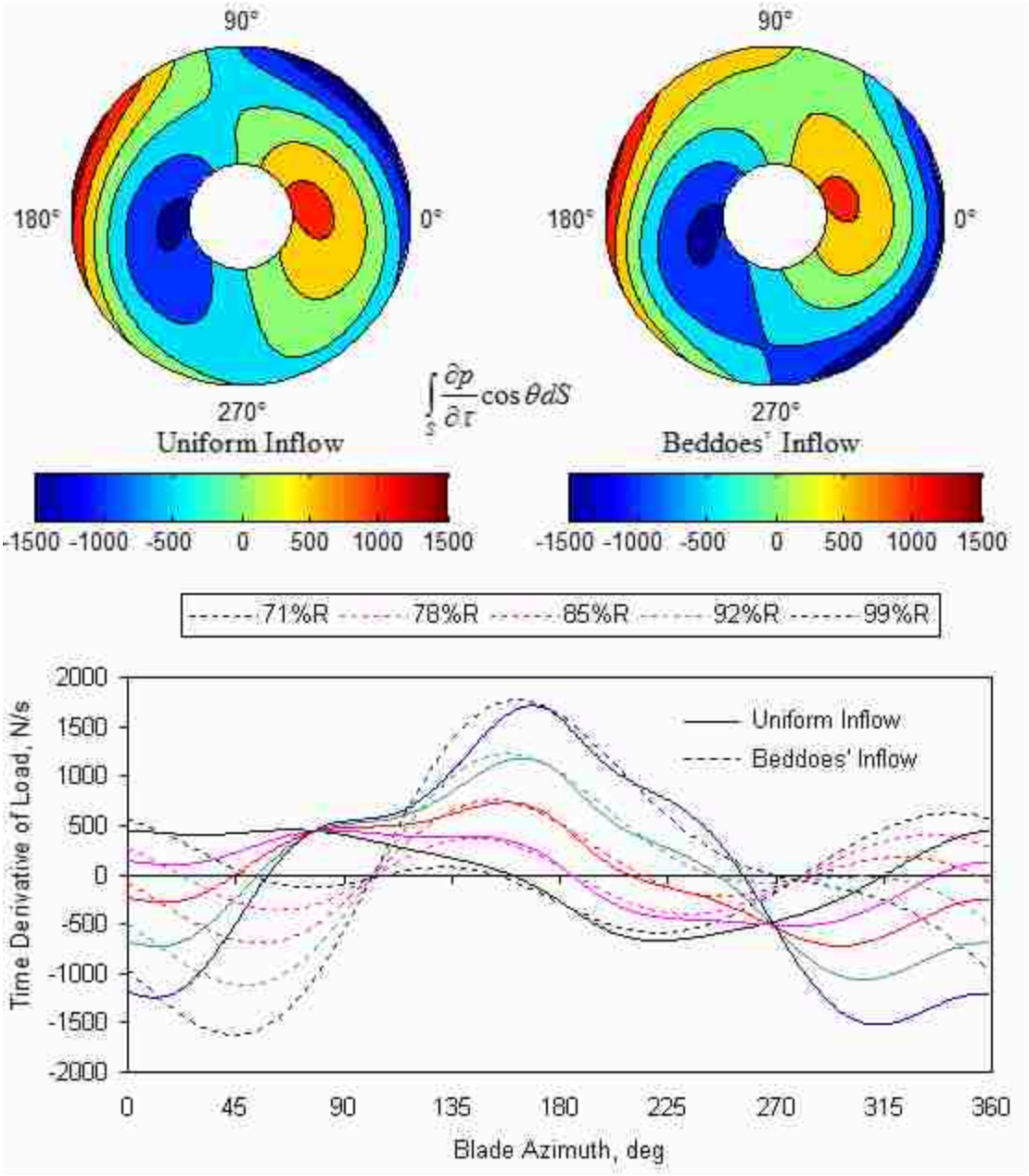

Figure G.6. Distribution of the time derivative of the load

References

[1] Ungar, Eric E., et al. "A Guide for Predicting the Aural Detectability of Aircraft." AFFDL-TR-71-22. AF Flight Dynamics Laboratory, Wright-Patterson AFB, OH, Mar. 1972.

[2] Hubbard, Harvey H., "Aeroacoustics of Flight Vehicles: Theory and Practice. Volume 1: Noise Sources." TR 90-3052. NASA Langley Research Center, Hampton, VA, 1991.

[3] Schmitz, F. H., and Yu Y., H., "Helicopter Impulsive Noise: Theoretical and Experimental Status." NASA Technical Memorandum 84390. USAAVRADCOM, Ames Research Center, Moffett Field, CA, Nov. 1983.

[4] Sickenberger, R., Gopalan, G., and Schmitz, F., "Helicopter Near-Horizon Harmonic Noise Radiation due to Cyclic Pitch Transient Control." *American Helicopter Society 67th Annual Forum*. Virginia Beach, VA, 3-5 May 2011.

[5] Watts, M. E., et al. "Maneuver Acoustic Flight Test of the Bell 430." *American Helicopter Society 68th Annual Forum,* Fort Worth, TX, 1-3 May 2012.

[6] Ffowcs Williams, J. E., and Hawkings, D. L., "Sound Generation by Turbulence and Surfaces in Arbitrary Motion," Philosophical Transactions of the Royal Society of London, Series A, Mathematical and Physical Sciences, Vol. 264, No. 1511, pp. 321-342, May 1969.

[7] Brentner, K. S., "Prediction of Helicopter Rotor Discrete Frequency Noise: A Computer Program Incorporating Realistic Blade Motions and Advanced Acoustic Formulation." NASA Technical Memorandum 87721. NASA Langley Research Center, Hampton VA, 1986.

[8] Brooks, T. F., et al. "Aeroacoustic Codes for Rotor Harmonic and BVI Noise – CAMRAD.Mod1/HIRES." *AIAA/CEAS 2nd Aeroacoustics Conference*, State College, PA, 6-8 May 1996.

[9] Lim, J. W., Yu, Y. H., and Johnson W. "Calculation of Rotor Blade-Vortex Interaction Airloads Using a Multiple-Trailer Free-Wake Model." *Journal of Aircraft*. Vol. 40, No. 6. (2003): 1123-1130.

[10] Brentner, K. S., et al. "Maneuvering Rotorcraft Noise Prediction: A New Code for a New Problem." *AHS Aerodynamics, Acoustics, and Test Evaluation Specialist Meeting*, San Francisco, CA, 23-25 Jan. 2002.

[11] Brentner, K. S., et al. "Noise Prediction for Maneuvering Rotorcraft." *AIAA/CEAS 6th Aeroacoustics Conference,* Lahaina, HI, 12-14 Jun. 2000.

[12] Brentner, K. S., et al. "A First Step Toward the Prediction of Rotorcraft Maneuver Noise." *Journal of the American Helicopter Society*. Vol. 50, No. 3. (2005): 230-237.

[13] Duque, E. P. N., et al. "Revolutionary Physics-Based Design Tools for Quiet Helicopters." AIAA Paper No. 2006-1068.

[14] Brentner, K. S., et al. "Near Real-Time Simulation of Rotorcraft Acoustics and Flight Dynamics." *American Helicopter Society 59th Annual Forum*. Phoenix, AZ, 6-8 May 2003.

[15] Hennes, C. C., et al. "Influence of Transient Flight Maneuvers on Rotor Wake Dynamics and Noise Radiation." *AHS 4th Decennial Specialist's Conference on Aeromechanics,* San Francisco, CA, 21-23 Jan. 2004.

[16] Forsyth, D. W., Guilding, J., and DiPardo, J. "Review of Integrated Noise Model (INM) Equations and Processes." NASA/CR-2003-212414. May 2003.

[17] Conner, D. A. and Page, J. A. "A Tool for Low Noise Procedures Design and Community Noise Impact Assessment: The Rotorcraft Noise Model (RNM)," *AHS International Technical Specialists' Meeting on Advanced Rotorcraft Technology and Life Saving Activities*, Utsunomiya, Japan, 11-13 Nov. 2002.

[18] Gopalan, G. "Quasi-Static Acoustic Mapping of Helicopter Blade-Vortex Interaction Noise," Ph.D. Dissertation, University of Maryland, 2004.

[19] Greenwood, E. "A Physics-Based Approach to Characterizing Helicopter External Noise Radiation from Ground-Based Noise Measurements," Masters Thesis, University of Maryland, 2008.

[20] Steidl, G. "Final Report for ECO HELI AP 4.1 Extraction and Analysis of Fenestron Noise from DLR PAVE Flight Test," Institute of Aerodynamics and Flow Technology, IB 124-2011/909, Braunschweig, Germany, Aug. 2011.

[21] Gervais, M., et al. "Validation of EC130 and EC135 Environmental Impact Assessment using Helena" *American Helicopter Society 66th Annual Forum*, Phoenix AZ, May 11-13, 2011.

[22] Greenwood, E. "Fundamental Rotorcraft Acoustic Modeling from Experiments (FRAME)," Ph.D. Dissertation, University of Maryland, 2011.

[23] Greenwood, E., Schmitz, F., and Sickenberger, R., "A Semi-Empirical Noise Modeling Method for Helicopter Maneuvering Flight Operations," *American Helicopter Society 68th Annual Forum*, Fort Worth, TX, May 1-3, 2012.

[24] Boxwell, D. A., et al. "Helicopter Model Rotor-Blade Vortex Interaction Impulsive Noise: Scalability and Parametric Variations" *Journal of the American Helicopter Society*, Vol. 32, No. 1 (1987): 3-12.

[25] Yamauchi, G. K., et al. "Flight Measurements of Blade-Vortex Interaction Noise Including Comparisons with Full-Scale Wind Tunnel Data," *American Helicopter Society 49th Annual Forum*, St. Louis, MO, 19-21, May 2993.

[26] Schmitz, F. H. and Boxwell, D. A, "In-Flight Far-Field Measurement of Helicopter Impulsive Noise," *Journal of the American Helicopter Society*, Vol. 21, No. 4 (1976): 2-16.

[27] Cross, J. L. and Watts, M. E., "In-Flight Acoustic Testing Techniques Using the Y0-3A Acoustic Research Aircraft," NASA Technical Memorandum 85895, NASA Langley Research Center, Hampton VA, Mar. 1984.

[28] Spiegel, P., Buchholz, H., and Splettstößer, W. "The "RONAP" Aeroacoustic Flight Tests with a Highly Instrumented BO 105 Helicopter," *American Helicopter Society 59th Annual Forum*, Phoenix, AZ, May 6-8, 2003.

[29] Spiegel, P., Buchholz, H., and Pott-Pollenske, M., "Highly Instrumented BO105 and EC135-FHS Aeroacoustic Flight Tests including Maneuver Flights," *American Helicopter Society 61st Annual Forum*, Grapevine, TX, Jun. 1-3, 3005.

[30] Schmitz, F. H., et al., "Measurement and Characterization of Helicopter Noise in Steady-State and Maneuvering Flight," *American Helicopter Society 63rd Annual Forum*, Virginia Beach, VA, May 1-3, 2007.

[31] Sickenberger, R. and Schmitz, F., "Longitudinal Tip-Path-Plane Measurement using an Optics-Based System," *American Helicopter Society 63rd Annual Forum,* Virginia Beach, VA, May 1-3, 2007.

[32] Sickenberger, R and Schmitz, F., "An Optics-Based Tip-Path Plane Tracking System for Rotorcraft Applications," *AIAA Guidance, Navigation and Control Conference,* Honolulu, HI, Aug. 18-21, 2008.

[33] Decker, W. A., et al. "Use of a Portable Programmable Guidance Display in Support of Helicopter Noise Testing," *American Helicopter Society 63rd Annual Forum*, Virginia Beach, VA, May 1-3, 2007.

[34] Schmitz, F. and Sim, B., "Acoustic Phasing, Directionality and Amplification Effects of Helicopter Blade-Vortex Interactions," *Journal of the American Helicopter Society*, Vol. 46, No. 4 (2001): 273-282.

[35] Schmitz, F. and Sim, B., "Radiation and Directionality Characteristics of Helicopter Blade-Vortex Interaction Noise," *Journal of the American Helicopter Society,* Vol. 48, No. 4 (2003): 253-269.

[36] Leishman, J. Gordon, "Principles of Helicopter Aerodynamics," 2nd ed. New York NY: Cambridge University Press, 2006.

[37] Widnall, Sheila, "Helicopter Noise due to Blade-Vortex Interaction," *Journal of the Acoustical Society of America*, Vol. 50, No. 1 (1971): 365-365.

[38] Martin, R. M., et al. "Advancing-Side Directivity and Retreating-Side Interactions of Model Rotor Blade-Vortex Interaction Noise," NASA-TP-2784, May 1988.

[39] Chen, Robert T. N., "A Simplified Rotor System Mathematical Model for Piloted Flight Dynamics Simulation," NASA Technical Memorandum 78575, Ames Research Center, Moffett Field, CA, May 1979.

[40] Chen, Robert T. N., "Effects of Primary Rotor Parameters on Flapping Dynamics," NASA Technical Paper 1431, Ames Research Center, Moffett Field, CA, Jan. 1980.

[41] Seckel, E. and Curtiss, H. C. Jr., "Aerodynamic Characteristics of Helicopter Rotors – Rotor Contributions to Helicopter Stability Parameters," Princeton University, Report No. 659, Dec. 1963.

[42] Prouty, Raymond W., "Helicopter Performance, Stability and Control," Malabar, FL: Krieger Publishing Company, Inc., 1989.

[43] Johnson, Wayne, "Helicopter Theory," New York, NY: Dover Publications, Inc., 1980.

[44] Weissten, Eric W., eds. "CRC Concise Encyclopedia of Mathematics," 2nd ed., New York, NY: CRC Press LLC, 1998.

[45] Anderson, John D. Jr., "Fundamentals of Aerodynamics," 4th ed., Boston, MA: McGraw-Hill, 2005.

[46] Bertin, John J., "Aerodynamics for Engineers," 4th ed., Upper Saddle River, NJ: Prentice Hall, 1979.

[47] Brentner, K. S. and Farassat, F., "Modeling Aerodynamically Generated Sound of Helicopter Rotors," *Progress in Aerospace Sciences*, Vol. 39, No 2-3 (2003): 83-120.

[48] Farassat, F., "Derivation of Formulations 1 and 1A of Farassat," NASA Technical Memorandum 2007-214853, NASA Langley Research Center, Hampton VA, Mar. 2007.

[49] Koushik, Sudarshan N., "A New Experimental Approach to Study Helicopter Blade-Vortex Interaction Noise," Ph.D. Dissertation, University of Maryland, 2007.

[50] Lee, S., Brentner, K. S., and Farassat, F., "Analytic Formulation and Numerical Implementation of an Acoustic Pressure Gradient Prediction," *Journal of Sound and Vibration*, Vol. 319, No. 3-5, (2009): 1200-1221.

[51] Kinsler, L. E., et al. "Fundamentals of Acoustics," 4th ed., New York, NY: John Wiley & Sons, Inc., 2000.

[52] Wiesel, W. E., "Spaceflight Dynamics," 2nd ed., Boston MA: McGraw-Hill, 1997.

[53] Etkin, B. and Reid, L. D., "Dynamics of Flight: Stability and Control," 3rd ed., New York, NY: John Wiley & Sons, Inc., 1996.